Les contacts atomiques : un banc d'essai pour la physique mésoscopique

Ronald Cron

Ronald Cron. Les contacts atomiques : un banc d'essai pour la physique mésoscopique. Physique [physics]. Université Pierre et Marie Curie - Paris VI, 2001. Français. NNT : . tel-00001329

HAL Id: tel-00001329
https://theses.hal.science/tel-00001329v1

Submitted on 29 Apr 2002

THESE de DOCTORAT de l'UNIVERSITE PARIS 6

Spécialité :

PHYSIQUE QUANTIQUE

présentée par Ronald Cron
pour obtenir le grade de DOCTEUR de l'UNIVERSITE PARIS 6.

Sujet de la thèse :

Les contacts atomiques : un banc d'essai pour la physique mésoscopique

Soutenue le 23 Novembre 2001
Devant le jury composé de :

R. Combescot (président)
M. H. Devoret
J. Lesueur
A. Levy Yeyati
J. M. van Ruitenbeek (rapporteur)
B. J. van Wees (rapporteur)

Table of Contents

Remerciements

Ce travail de thèse doit beaucoup à toutes les personnes qui font fonctionner au quotidien le Service de Physique de l'Etat Condensé (SPEC). Je les remercie pour les conditions de travail idéales qu'ils ont mises à ma disposition. Plus particulièrement, merci à Jacques Hamman et Louis Laurent de m'avoir accueilli au sein de leur service. Merci à Madame Marciano et à Sandrine Thunin très efficaces pour démêler les imbroglios administratifs dans lesquels je n'ai cessé de m'empêtrer. Merci aux techniciens du grand atelier, en particulier à Michel Juignet de m'avoir initié à la fraiseuse et à Vincent Padilla de m'avoir initié au tour et d'avoir fabriqué le dispositif de flexion de mon expérience. Merci à Jean-Michel Richomme et Patrice Jacques pour leur accueil toujours aimable et leurs conseils au petit atelier. Merci à Pierre Janvier de mettre à notre disposition le magasin et d'avoir toujours résolu avec le sourire mes problèmes d'hélium liquide.

Voilà bientôt quatre années que j'ai le plaisir de travailler avec les membres du groupe Quantronique. J'espère que tous sont conscients du bien que je pense de l'équipe compétente, enthousiaste et sympathique qu'ils forment. Merci de votre éternelle bonne humeur et de tout ce que, à votre contact, j'ai appris sur la physique, la littérature espagnole, les relations humaines, le football, le cinéma, le travail en équipe, le Chili, l'Argentine, la biologie, l'économie, les moteurs de voiture, les opérations à cœur ouvert …

Un grand merci à Cristiàn Urbina pour toute l'énergie qu'il a consacrée à diriger au jour le jour ce travail de thèse. Je le remercie pour sa disponibilité permanente et pour toutes les discussions très instructives sur la physique et sur l'élaboration des expériences que nous avons eues. Merci pour tout le temps passé au débrouillage puis au perfectionnement de mes exposés (notamment ceux en Anglais) et pour toutes les corrections et améliorations apportées à ce manuscrit. Merci enfin pour ce large sourire de bienvenue dispensé chaque matin qui redonnerait courage au plus désespéré des thésards.

Egalement un grand merci à Marcello Goffman. Merci de m'avoir initié à toutes les techniques expérimentales et d'avoir partagé avec moi deux ans de mesures, de refroidissements, de déjupages, de calculs, de fabrication, de fuites de gamelle, de rédaction

d’articles, de filtres EMI soudés-dessoudés-ressoudés, d’exposés, de réparations, de doutes (parfois). Merci également pour tous ces matchs de football de la coupe du monde des laboratoires de physique des environs d’Orsay.

Merci à Daniel Estève qui, grâce à ses dons d’ubiquité, a suivi de très près mon travail de thèse. Je le remercie pour ses encouragements dans les moments délicats, pour les nombreux conseils et nombreuses idées sur la théorie ainsi que sur l’interprétation des expériences qui ont démêlé de nombreuses situations. Merci pour tout le temps et l’enthousiasme consacrés à l’amélioration de mes exposés oraux et de ce manuscrit.

Merci à Michel Dévoret pour toutes les discussions instructives et exaltantes que j’ai eues avec lui, notamment concernant la supraconductivité et le phénomène de réflexion d’Andreev. Je le remercie également pour son aide et son soutien lors de ma recherche d’un post-doc même si finalement je n’ai pas choisi cette voie.

Merci à Philippe Joyez pour tous les conseils expérimentaux, théoriques et pédagogiques qu’il m’a prodigués et le soutien continuel qu’il m’a apporté. Merci plus particulièrement pour son aide précieuse lors de l’expérience sur le Blocage de Coulomb et lors de la rédaction de ce manuscrit.

Merci à Pief Orfila dont les talents ont mis à ma disposition, en permanence, des équipements informatiques, cryogéniques, de microfabrication et de mesure opérationnels. Merci de l’aide pour l’entretien de ma voiture, merci pour mon imprimante « perso » lors de la rédaction de cette thèse, pour les chocolats, les parties de badminton…

Merci à Hugues Pothier et Denis Vion pour leur soutien constant et pour l’intérêt qu’ils ont porté à mes expériences. Merci à Hugues pour ses conseils toujours avisés sur les transparents (notamment à propos des couleurs) et de m’avoir appris que : « Quand on travaille tout seul, on ne raconte que des co… ».

C’est avec plaisir que j’ai partagé ces trois années de thèse avec les autres chercheurs et thésards du SPEC. Plus particulièrement, j’ai apprécié de travailler avec Andy Steinbach et Abdelhanin Aassime. Merci à Frédéric Pierre de m’avoir initié au Reggae, et merci pour le trip top roots en Turquie. Merci à Valentin Rodriguez pour toutes les discussions sur nos états d’âme concernant la thèse et l’après thèse. Merci à Fabien Portier et Sophie Djordjevic pour toutes les soirées sympas passées ensemble. Merci à Franck Selva blagueur émérite, organisateur des repas thésards et futur requin des finances.

Au cours de ma thèse, j'ai eu le plaisir de travailler également avec Alfredo Levy Yeyati sur la théorie de nos expériences, Nicolas Agraït et Gabino Rubio Bollinger sur l'implémentation d'un STM à basse température, Elke Scheer et Patrice Brenner sur les contacts atomiques de zinc, ainsi qu'Adrien Fuchs sur l'expérience de blocage de Coulomb. Je remercie également Juan Carlos Cuevas, Georg Göppert, Takis Kontos, Yasunobu Nakamura, John Martinis, Yuli Pashkin, Hirotaka Tanaka, Hideaki Takayanagi, Shen Tsai, T. Yamamoto, pour les discussions à la fois instructives et agréables que j'ai eues avec eux.

Je remercie Jan van Ruitenbeek et Bart van Wees d'avoir accepté d'être les rapporteurs de ma thèse, et Roland Combescot, Jérôme Lesueur et Alfredo Levy Yeyati d'avoir bien voulu faire partie de mon jury. Merci à mes amis qui sont venus (ou souhaitaient venir) assister à ma soutenance de thèse.

Enfin, je remercie de tout cœur mon père Bernard, ma mère Monique, et ma sœur Emeline pour leur soutien permanent aux cours de toutes ces longues années d'études qui m'ont mené jusqu'au doctorat, ainsi qu'Anne qui maintenant partage ma vie. Cette thèse leur est dédiée.

Atomic Contacts:
a Test-Bed for Mesoscopic Physics

Transport through quantum coherent conductors

Although the behavior of electrons is governed by quantum mechanics, significant quantum effects appear in the transport properties of an electronic conductor only when one at least of its characteristic lengths is shorter than the so-called coherence length L_ϕ [1]. This length represents the distance over which an electron at the Fermi level propagates inside the conductor without loosing its quantum coherence. For example, quantum interference effects do modify the conductance of diffusive thin films and narrow wires [2], but only weakly. The most spectacular quantum effects, such as Aharonov-Bohm interferences [3] arising when electrons can follow two or more distinct paths in going from one point to another, appear when the whole circuit is smaller than L_ϕ. In this regime, a two-probe circuit behaves as a quantum scatterer for the electrons injected by the contact probes, which act as electron reservoirs (see Figure 1). This point of view, due to Rolf Landauer [4], is extremely powerful since all the transport properties of a quantum coherent circuit can be expressed in terms of its scattering matrix for the electron waves in the case of non interacting electrons. In particular, the conductance of the circuit is directly related to the transmission matrix [4], which is the part of the scattering matrix relating amplitudes of incoming waves on one end to outgoing waves on the other end. This transmission matrix has a set of eigenmodes, called conduction channels. Each channel contributes independently to the transport properties. As an example, each channel contributes $G_0\tau$ to the conductance, where τ, the transmission probability, is the modulus square of the corresponding eigenvalue and $G_0 = 2e^2/h$ is the conductance quantum. The total conductance is then given by the famous Landauer formula: $G = G_0\sum_{i=1}^{N}\tau_i$ where N is the number of channels and the τ_i's are the individual transmission probabilities.

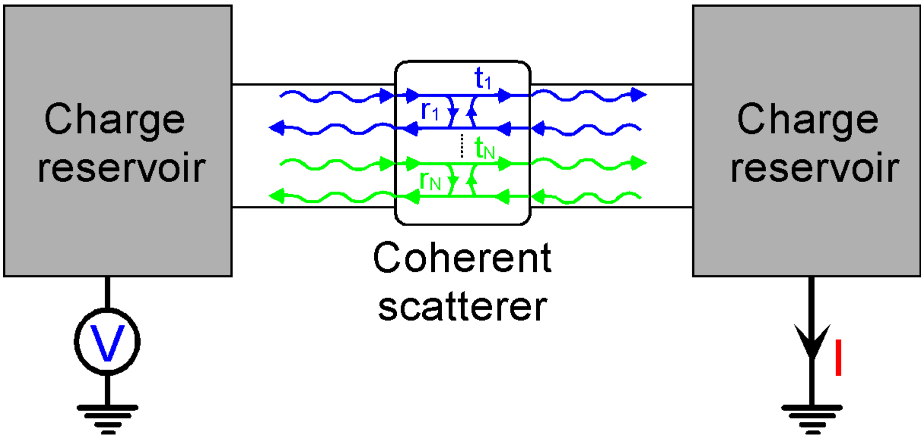

Figure 1: Transport experiment viewed as a scattering process. Electrons injected from a charge reservoir are scattered by the quantum coherent device. In each conduction channel i, an electron wave has a probability amplitude t_i to be transferred and r_i to be reflected. Its transmission probability τ_i is the modulus square of t_i.

The spectacular observation of steps in the conductance of 2D electron gas quantum point contacts [5] as the number of open channels is progressively increased by means of an external electrostatic gate, has beautifully confirmed the validity of the scattering formalism for the description of quantum coherent transport. Since that pioneering work, a large effort has been devoted to the investigation of quantum coherent transport in a wide range of situations, ranging from ballistic to diffusive conductors, connected to reservoirs in the normal (i.e. non-superconducting) or in the superconducting state [1,6]. On the theoretical side, the Landauer-Büttiker scattering formalism has been extended to multiterminal conductors, fluctuations, finite frequency, etc. Other transport properties, such as the shot-noise in the current or the supercurrent in the case of superconducting reservoirs, have been calculated within this formalism. Not surprisingly, all considered physical quantities can be expressed in terms of the transmission probability set $\{\tau_1,...,\tau_N\}$, which appears to be the mesoscopic "Personal Identity Number (PIN) code" of the conductor, regardless of other microscopic details.

On the experimental side, many interesting effects had indeed been observed before the beginning of this thesis work. However, most of the experiments had not achieved a quantitative comparison with the theoretical predictions because the mesoscopic codes of the structures were unknown, but for the already mentioned quantum point contact experiment [5], and for diffusive conductors with many channels, whose statistical distribution of channel transmissions is known theoretically [7].

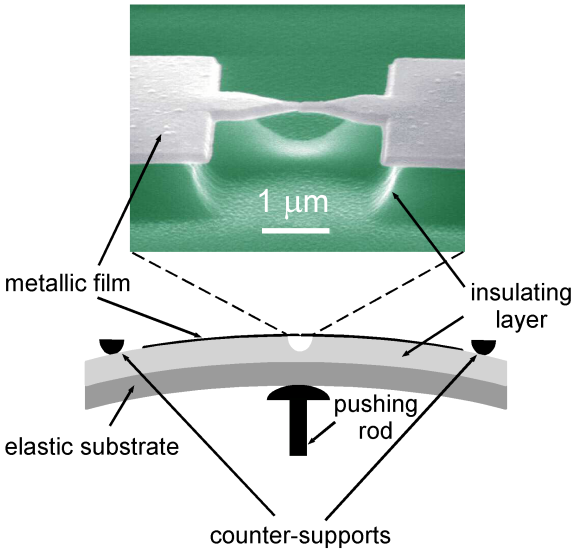

Figure 2 : Scanning electron microscope picture of an aluminum nanofabricated bridge and schematic drawing of the mechanically controllable break junction set-up. The pushing rod controls the bending of the substrate.

Atomic contacts as quantum coherent conductors

Among the various systems investigated, atomic-size contacts played an important role. These contacts were first obtained in the group of Jan van Ruitenbeek at Leiden using the break-junction technique [8]. Since all their characteristic dimensions are of the order of the Fermi wavelength, atomic contacts are perfect quantum conductors, even at room temperature, and accommodate only a small number of channels. The discovery that their mesoscopic code could be accurately decoded [9] paved a way to a new generation of quantum transport experiments, in which the measured transport quantities could be compared to the theoretical predictions without any adjustable parameters.

In this thesis, we report three experiments on atomic-size contacts used as a generic quantum coherent conductor for which this comparison is performed. These experiments concern

- the supercurrent flowing through a quantum coherent conductor placed between two superconducting reservoirs
- the shot-noise associated to the current when a voltage difference is applied between the reservoirs (normal or superconducting)
- the Coulomb blockade of the conductance, when the quantum coherent conductor is connected in series with an electromagnetic impedance.

Before discussing these experiments and their main results, we describe both the nanofabrication technique that has made possible the experiments, and the way to determine the mesoscopic code of atomic-size contacts.

We produce atomic-size contacts by means of the nanofabricated break-junction technique developed in the Quantronics group [10]. Using electron beam lithography and reactive ion etching, a metallic bridge clamped to an elastic substrate is suspended over a few micrometers between two anchors. The bridge presents in its center a constriction with a diameter of approximately 100 nm. In order to obtain an atomic-size contact, the substrate is first bent till the bridge breaks at the constriction (see Figure 2). The two resulting electrodes are then slowly brought back into contact. The high mechanical reduction ratio of the bending bench allows to control the number of atoms forming the contact one by one; in this way, single atom contacts can be produced in a controlled fashion. Compared to other techniques, nanofabricated break junctions present two major advantages essential to the realization of the experiments presented in this thesis. First, nanofabricated atomic-size contacts are extremely stable and can be maintained for days. Second, the versatility of this technique allows to embed contacts in an adequately tailored nanocircuit that insures appropriate dissipation and filtering.

Just before I started my thesis work, it had been shown that for one-atom contacts the number of conduction channels is directly related to the number of valence orbitals of the central atom [11]. For example gold one-atom contacts contain only one channel, while aluminum and lead have three, and niobium five. Moreover, it was shown that for such a small number of channels it is possible to determine with good accuracy the mesoscopic code [9] from the precise measurement of the current-voltage characteristic $I(V)$ in the superconducting state.

In the superconducting state the current results from Multiple Andreev Reflections (MAR) of all orders (see inset p. 7). The *n*-th order process involves the transfer of *n* electrons, and in a given channel its intensity varies as the *n*-th power of the transmission. Consequently, the $I(V)$ depends on all powers of every transmission coefficient in the code and therefore it carries all the information necessary to reconstruct it. Figure 3(a) shows the numerically calculated current-voltage characteristic $i(V,\tau)$ resulting from these MAR processes for a single channel of arbitrary transmission τ [12,13,14,15]. These elementary $i(V,\tau)$ curves are highly non-linear below twice the superconducting gap Δ and present current steps at voltages $2\Delta/ne$, which mark the onset of MAR of different orders. The determination of the code of any atomic-size contact is achieved by decomposing the measured total $I(V)$ into a series of such elementary characteristics, each of them corresponding to a well defined transmission probability. The individual transmission probabilities of the channels are adjusted so as to get the best fit of the measured current-voltage characteristic (see Figure 3(b)). We have used this procedure throughout this thesis.

We now briefly present the three experiments we have carried out and their main results.

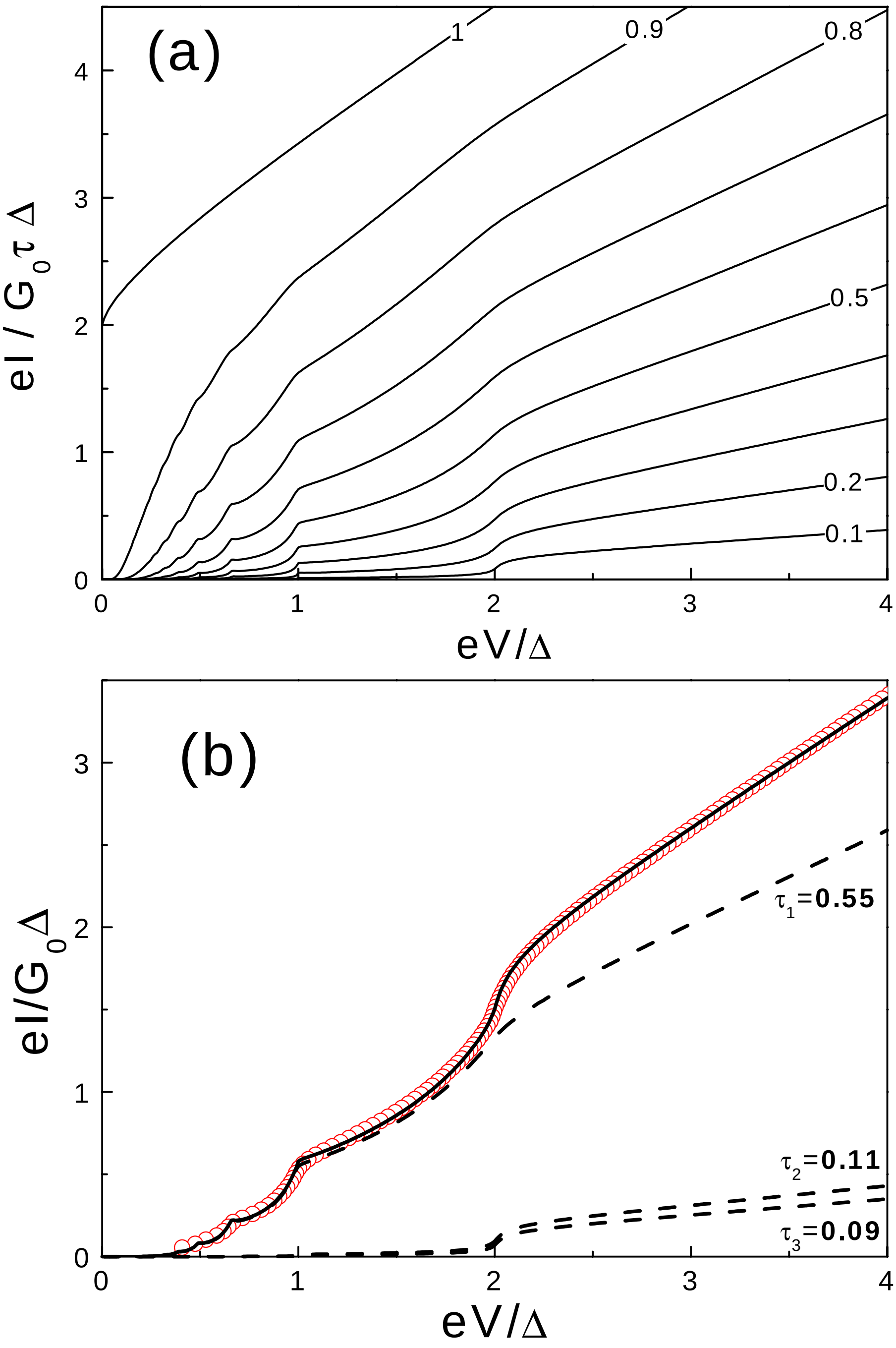

Figure 3: (a) Theoretical current-voltage characteristics (in reduced units) of a single conduction channel between two superconducting reservoirs, for a transmission probability τ ranging from 0.1 to 1 by steps of 0.1. The non linearities correspond to the onset of decreasing order multiple Andreev reflections processes as the voltage increases.

(b) Mesoscopic PIN code determination of a one-atom aluminum contact. The experimental $I(V)$ characteristic (open dots) is decomposed into the sum of independent single channel characteristics (dashed curves). This particular contact contains three channels with transmission probabilities $\tau_1 = 0.55$, $\tau_2 = 0.11$ and $\tau_3 = 0.09$. These probabilities were adjusted so as to get the best fit (continuous curve). These procedure gives a determination accurate to the % level for contacts containing up to five channels.

Andreev reflection at a normal-superconducting interface [20]

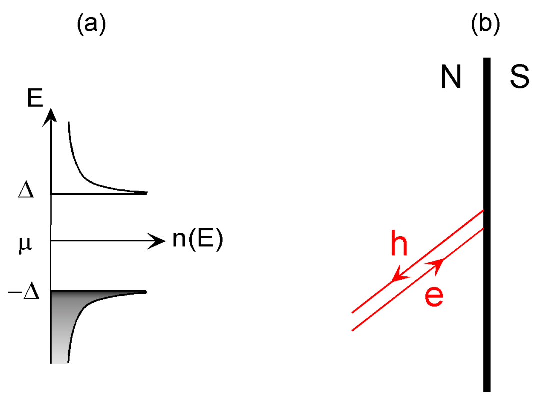

In the superconducting state, the coupling of electrons with opposite spin opens a gap in the quasiparticle density of states *n(E)* (dark regions correspond to occupied states) (a). Consequently, an electron coming from a normal electrode with an energy smaller than the superconducting gap cannot enter the superconductor. However, it can be reflected as a hole, leaving an extra charge 2e in the superconducting condensate (b). This process, called Andreev reflection, has emerged in the last decade as a central concept in our understanding of electrical transport at interfaces involving one or more superconductors an in particular in Josephson junctions.

Multiple Andreev Reflections (MAR) processes

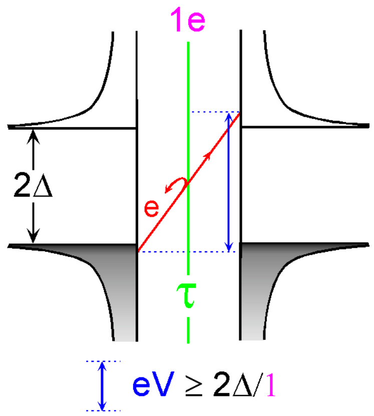

Single charge transfer process (from the left to the right superconducting electrode)

We have represented the density of states of both electrodes. An electron crossing the channel from the left to the right can be reflected back or transmitted. The transmission probability is τ. If transmitted, it gains an energy eV provided by the voltage source. Starting from the left electrode with an energy $\varepsilon < -\Delta$ an electron can find an empty state in the right electrode only if $eV \ge \Delta - \varepsilon \ge 2\Delta$. Consequently a gap occurs in the single electron transport for voltages $eV < 2\Delta$.

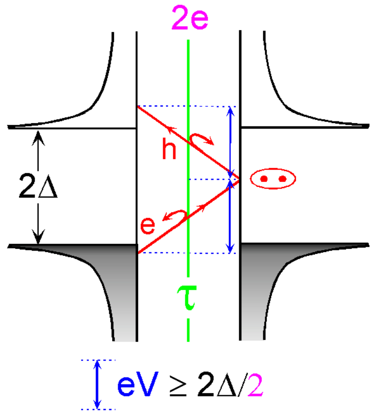

Two charge transfer process

For energies $eV < 2\Delta$, a transmitted electron can not find an empty state in the right electrode and is Andreev reflected as a hole. The hole crossing the channel in opposite direction but with opposite charge gains again an energy eV. The condition for the hole to find an empty state is no longer $eV \ge 2\Delta$ but $eV \ge \Delta$. During this process, which for small transmission has a probability τ^2, two electron charges are transferred from left to right.

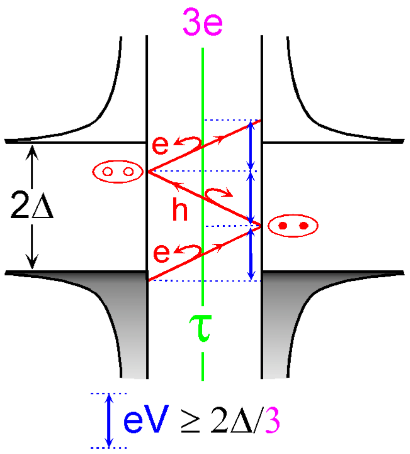

Three, four ,… charge transfer process

For voltages $eV \le \Delta$ the Andreev reflected hole can not find an empty state in the left electrode but can be Andreev reflected in turn as an electron. The threshold energy for this electron to find an empty state in the right electrode is $eV \ge 2\Delta/3$. Three charges are transferred in this process which, for small transmission, has a probability τ^3. For smaller voltages, Multiple Andreev Reflections (MAR) processes that transfer four or more electron charges carry the current. A process transferring *n* electron charges, called *n*-th order process, involves (*n*-1) Andreev reflections and has a probability τ^n (for small τ) and a threshold voltage $V = 2\Delta/en$.

Josephson supercurrent through a single atom

In 1962, Josephson predicted that a surprisingly large supercurrent could flow between two superconducting electrodes coupled by a tunnel barrier [16]. This current, driven by the superconducting phase difference δ between the two electrodes, flows at zero bias voltage. Since this spectacular prediction, the Josephson current has been observed in all kinds of systems involving two superconducting electrodes connected by a “weak link”[17]. A weak link can be for example an insulating layer, as originally proposed by Josephson, but also a short normal diffusive or ballistic metallic wire, or a point contact. A great deal of theoretical activity has been devoted to relate the maximum supercurrent I_0 that a weak link can sustain to its normal resistance R_N. In the case of tunnel junctions with a large number of very weakly transmitting channels, Josephson established that, for BCS superconductors, the product $R_N I_0$ only depends on the gap energy and is $R_N I_0 = \pi\Delta/2e$ [16]. For metallic links, Kulik and Omel’yanchuk, using a Green function approach, predicted that the $R_N I_0$ product is 1.32 and 2 times greater than for a tunnel junction with the same resistance, in the diffusive and ballistic limits respectively [18,19]. A unified theoretical framework, in which Andreev reflection [20] plays again a central role, has emerged only in the last decade and provided the answer for an arbitrary structure in terms of its transmission set [21,22].

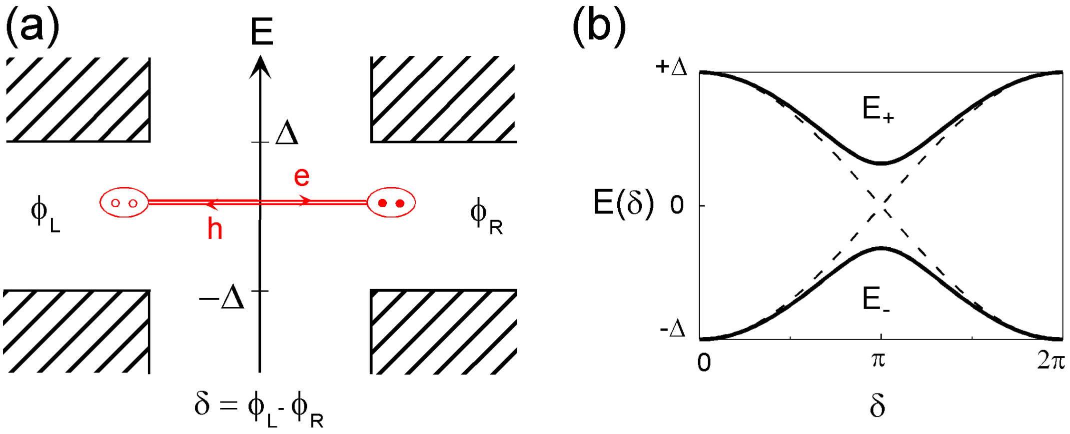

Figure 4: (a) Josephson coupling through a single ballistic channel between two superconducting electrodes with phase difference $\delta = \phi_L - \phi_R$. The hatched areas indicate energy intervals containing available states.

(b) Phase dependence of the energy of the two Andreev states. Dashed lines: Andreev spectrum for a ballistic channel. Full lines: For a channel with transmission τ a gap $2\Delta\sqrt{1-\tau}$ opens at $\delta = \pi$ in the Andreev spectrum.

This analysis is based on the concept of Andreev bound states, which we describe now. In the simplest case of two superconducting electrodes connected through a ballistic channel ($\tau = 1$), an electron with energy E smaller than Δ (in absolute value) moving to the right, is Andreev reflected with probability one by the right superconductor into a left moving hole at the same energy and a Cooper pair is transferred. This hole is in turn reflected back into a right moving electron with again the same energy (see Figure 4(a)). During one cycle, the electron acquires a phase shift, which depends on its energy and on the superconducting phase difference δ. At a given δ, a resonance occurs at an energy $-\Delta\cos(\delta/2)$ giving rise to a so-called Andreev bound state localized into the channel. Of course, the same picture applies with a left moving electron, giving rise to a second Andreev bound state with opposite energy: $+\Delta\cos(\delta/2)$ (see Figure 4(b)). The two levels cross each other at $\delta = \pi$. These Andreev bound states carry well defined opposite currents of Cooper pairs between the electrodes $I(\delta) = \varphi_0^{-1} dE(\delta,\tau)/d\delta = \pm e\Delta/\hbar \sin(\delta/2)$.

For a non ballistic channel ($\tau < 1$), these Andreev bound states still exist but they are coupled through the normal reflection of electrons into electrons and holes into holes. This coupling mixes the states and opens a gap $2\Delta\sqrt{1-\tau}$ at the crossing between these two states around $\delta = \pi$. The energy of the states becomes $E_\pm(\delta) = \pm\Delta[1-\tau\sin^2(\delta/2)]^{1/2}$ (Figure 4(b)). Since at a given phase these two Andreev bound states result in currents $I_\pm(\delta) = \varphi_0^{-1} dE_\pm(\delta,\tau)/d\delta$ equal in magnitude but in opposite directions, the net supercurrent results from the imbalance of their populations.

For an arbitrary quantum coherent conductor characterized by its code $\{\tau_i\}$, the phase-driven supercurrent is given by $I_J(\delta,\{\tau_i\},\{n_{i\pm}\}) = \sum_{i=1}^{N}(n_{i-} - n_{i+}) I_-(\delta,\tau_i)$ where $n_{i\pm}$ are the occupation numbers of the two Andreev bound states associated with the *i*th channel. The maximum supercurrent the conductor can sustain is obtained when in each channel only the Andreev bound state with the lower energy is populated (zero temperature). Its value is then: $I_0(\{\tau_i\}) = \max_\delta[I_J(\delta,\{\tau_i\}, n_{i+} = 0, n_{i-} = 1)]$.

We have performed an experiment on aluminum atomic contacts in which we compare the measured maximum supercurrent with the predictions of the mesoscopic Josephson effect theory described above. Since the contacts have to be connected to external leads in order to determine their code, measurements could not be performed by imposing the phase difference, which would require to short-circuit the contact with a superconducting coil. Instead, they have been done by dc-current biasing it, and detecting the maximum possible current at zero voltage. In such a set-up, the phase difference δ acquires a dynamical behavior which is very sensitive to the electrical circuit in which the contact is embedded [23,24]. Since the Josephson coupling introduced between the two electrodes has a small characteristic energy $E_J = \varphi_0 I_0 (\leq 1\, k_B \mathrm{K}$ for typical aluminum one-atom contacts), δ is prone to both quantum and thermal fluctuations. In order to observe a well-developed supercurrent close to its maximum possible value, these fluctuations have to be carefully controlled. For this reason, we have integrated an atomic-size contact in a suitable on-chip dissipative electrical circuit (see Figure 5). This circuit ensures that the phase fluctuations do not wash out the supercurrent.

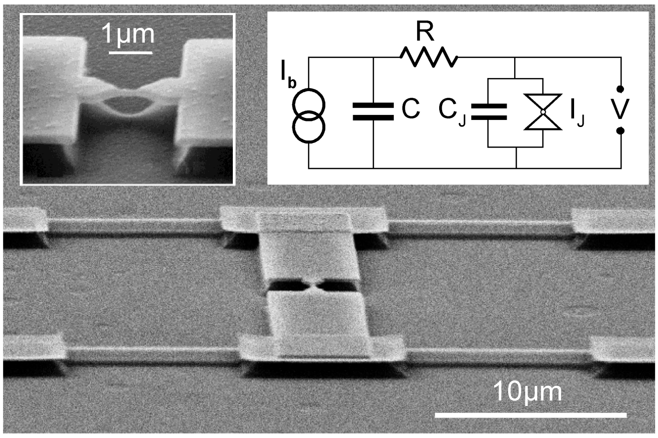

Figure 5: Micrograph of an Al microbridge in a dissipative environment. Each IV probe contains an AuCu resistor of the order of $150\,\Omega$ (10 µm long suspended bridge). Left inset: side view of the central bridge. Right inset: equivalent circuit. The atomic contacts (double triangle symbol) is connected to a current source through a resistor R. The total capacitance of measurement lines is C, and C_J is the total capacitance between the two sides of the bridge.

Assuming that Andreev states are thermally occupied, it is easy to calculate the maximum supercurrent a contact can sustain as a function of temperature. For atomic contacts with all transmissions smaller than 0.9, we find a quantitative agreement between predictions and measurements as can be seen in Figure 6 (a) for one particular contact.

The graph in Figure 6 (b) presents measurements on an atomic contact containing an almost ballistic channel ($\tau = 1$) compared to the predictions of this “equilibrium” theory: Measured maximum supercurrents are significantly higher than the predictions above 100 mK. We attribute this effect to a population of the upper Andreev bound states through Landau-Zener [25] transitions induced by the fast dynamics of the phase difference. As the transmission increases, the gap $2\Delta\sqrt{1-\tau}$ in the Andreev spectrum decreases, making such dynamical transitions plausible. Indeed, the predictions assuming a perfect Zener transition at each crossing are in good agreement with the data. However, if such a reasoning is justified for a ballistic channel, there is at present no rigorous treatment valid for arbitrary transmission. Thus, a quantitative understanding of our data in the high transmission range 0.90-0.99 is still lacking.

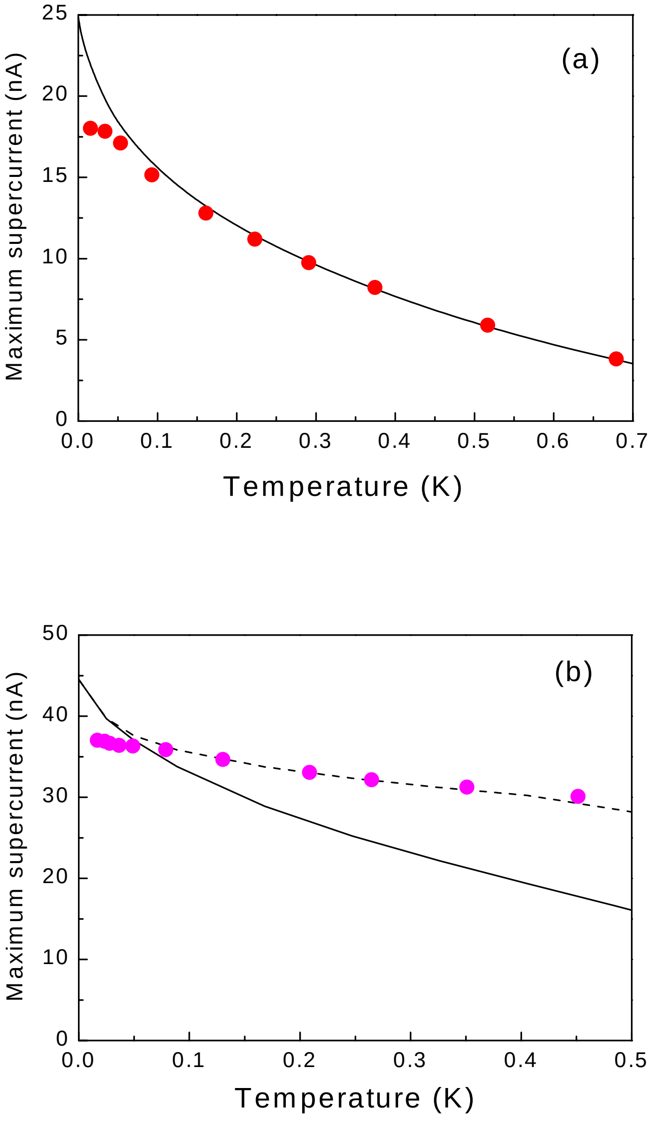

Figure 6 : Thermal equilibrium prediction (full lines) and measured (dots) maximum supercurrent for two one-atom aluminum contacts as a function of temperature. Mesoscopic PIN codes are {0.52,0.26,0.26} and {0.998,0.09,0.09,0.09} for the top and bottom panel respectively. Dashed line in right panel: prediction assuming $\tau = 1$ for the almost ballistic channel.

Shot noise in the current at finite voltage

The discreteness of electric charge and the stochastic character of electrical transport give rise to temporal fluctuations in the electrical current flowing through electronic devices. This so-called shot noise was predicted and first evidenced by Schottky in vacuum diodes [26], in which the current results from the random emission of electrons following a poissonian process. At low frequencies, the spectral density S_I of the current fluctuations is thus constant (white noise) and proportional to the mean current I and to the size e of the shot "pellets": $S_I = 2eI$.

In experiments with mesoscopic conductors the situation is quite different. Due to the Pauli principle, electrons incoming from a reservoir are completely correlated [27]. All current fluctuations are due to the random scattering of this perfectly correlated electron flux by the conductor. As a result, the noise is suppressed in the limit of a perfect ballistic channel ($\tau = 1$). In the opposite limit of a weakly transmitting channel, electron transmission follows a poissonian process and the Shottky result is recovered. For a channel with arbitrary transmission τ, the shot noise spectral density is predicted to be $S_I = 2eI(1-\tau)$, reduced from its poissonian value by the so-called Fano factor $(1-\tau)$. For a multichannel conductor characterized by a code $\{\tau_i\}_{i\in[\![1,N]\!]}$, the generalization is straightforward and one predicts at zero temperature [27,28]:

$$S_I = 2e\sum_{i=1}^{N} I_i(1-\tau_i) = 2eI(1-\sum_{i=1}^{N}\tau_i^{\,2} / \sum_{i=1}^{N}\tau_i), \qquad (1)$$

where I_i is the current through the i-th channel and the Fano factor is $(1-\sum_{i=1}^{N}\tau_i^{\,2} / \sum_{i=1}^{N}\tau_i)$.

The predicted noise reduction has already been observed in quantum point contacts tailored in 2DEG [29,30] where conduction channels open one by one. However, atomic contacts provide a larger palette of mesoscopic codes on which to test quantitatively the general multichannel noise formula (1). For all investigated contacts, the measured shot noise is sub-poissonian by a factor in agreement with the predicted one (see Figure 7).

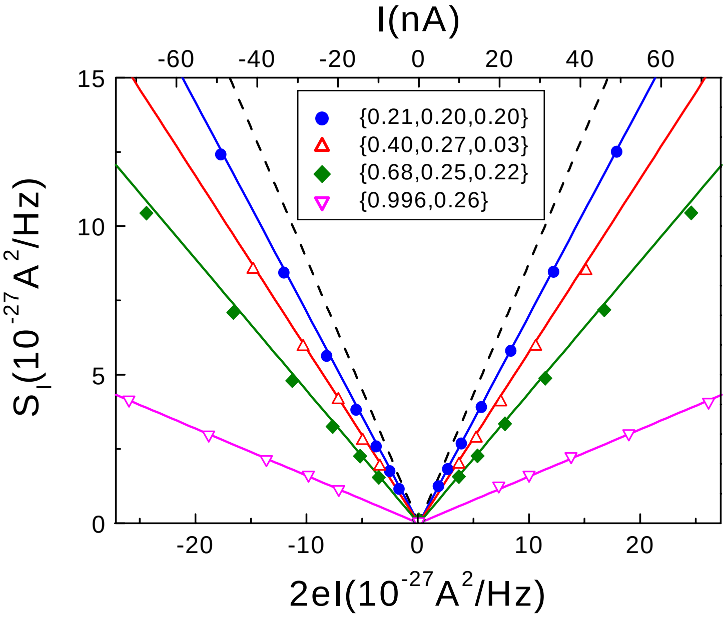

Figure 7: Symbols: measured low frequency spectral density of aluminum atomic-size contacts versus poissonian spectral density $2eI$. Solid lines are prediction of (1) for the corresponding mesoscopic codes. The dashed line is the poissonian limit.

In the tunnel limit, the ratio $Q^* = S_I / 2I$, called the effective charge, is simply equal to the charge e transferred by each elementary process. In the superconducting state, the current in the sub-gap region involves the transfer of multiple charge quanta. Is it possible to measure effective charges of $2e$, $3e$ or more? This question motivated our shot noise measurements in the superconducting state. In the weak transmission limit, the theoretical answer is indeed yes. At small transmissions τ , the probability of an n-th order MAR process is proportional to τ^n because n particles cross the channel during such a process (see the inset on MAR) [31]. As a consequence, since $\tau^n \ll \tau^{n-1}$ if $\tau \ll 1$, only one MAR process contributes significantly to the current at a given voltage and the effective charge is a multiple of the electronic charge (see Figure 8).

On the contrary, for larger transmissions different order MAR processes contribute to the current at a given voltage. Furthermore, as in the normal state, a Fano reduction factor is also at play, all this leading to an effective charge which is not forcely a multiple of e. The full quantum coherent MAR theory, which is able to compute its exact value, has been developed recently in the case of a single channel [31,32]. Once again, a quantitative test of this theory is possible using atomic contacts since conduction channels are independent.

Our results demonstrate that in the sub-gap region the carrying transport processes between two superconducting electrodes do carry large effective charges (see Figure 8). For not to high transmissions, the measured effective charge clearly exhibits a staircase pattern, as predicted, and all our measurements are in quantitative agreement with MAR theory.

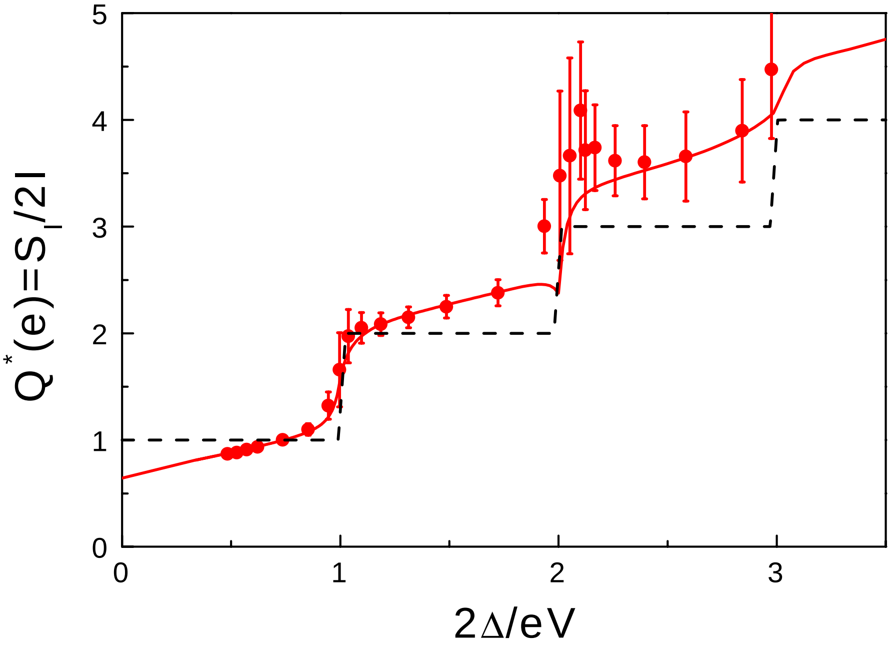

Figure 8: Effective size of the shot-noise “pellets”, in units of e, as a function of the inverse reduced voltage for a contact in the superconducting state. Dashed line : MAR theory prediction in the tunnel limit. As the voltage increases, MAR processes of lower order set-in one by one leading to this perfect staircase pattern. Dots : Data for an aluminum atomic contact with mesoscopic PIN code {0.40,0.27,0.03}. Full line : MAR theory prediction for this code.

Dynamical Coulomb blockade

The dynamical Coulomb blockade of single electron tunneling occurs when a small capacitance tunnel junction is placed in series with an impedance [33]. A tunnel event across the junction is accompanied by the passage of a charge *e* through the impedance. This can excite electromagnetic modes in the impedance and as a result electron tunneling is inelastic. Because of this loss of energy to the environment, the phase space for allowed electronic transitions is reduced. As a consequence, at low voltages and temperature, the transfer rate is reduced giving rise to a dip at zero voltage in the differential conductance as a function of voltage (see Figure 9). Coulomb blockade is a quantum effect, which is large when the series impedance is comparable to the resistance quantum h/e^2. Recently, A. Levy-Yeyati *et al.* proposed a connection between this phenomenon and shot noise in a generic quantum coherent structure [34]. Indeed, shot noise also results from the random current pulses due to tunneling of single electrons, and energy has to be dissipated in the impedance, thus retreiving the situation discussed above.

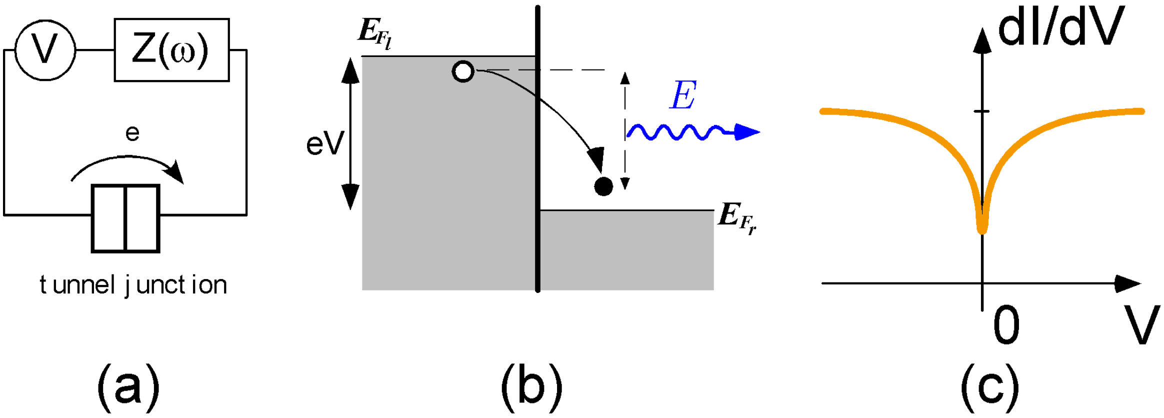

Figure 9 : (a) Dynamical Coulomb blockade occurs in circuits where a tunnel junction is in series with a non negligible impedance Z(ω).

(b) At a given voltage and zero temperature, electronic states on both side of the junction are filled up to the Fermi energies which are shifted by eV. When an electron tunnel through the junction, an amount of its energy E is transferred to the electromagnetic environment. The phase space allowed for electronic transitions is reduced.

(c) The inelastic tunneling rate is thus also reduced. This results in a dip in the differential conductance at low voltage.

This reasoning, which can be made rigorous, rises the question of the intensity of Coulomb blockade in a channel with arbitrary transmission. Would Coulomb blockade be suppressed, like shot noise, in a ballistic channel? Is the link between Coulomb blockade and shot noise generic? The theory of Coulomb blockade in this regime, in the case of an impedance small compared to the resistance quantum, predicts a suppression of the conductance dip by the same factor as for shot noise.

In order to test these new predictions, we have embedded an atomic contact in an on-chip electromagnetic environment with a similar design as for the Josephson supercurrent experiment. However, in this case the resistors are made out of aluminum. In the superconducting state the resistors have thus zero DC resistance, allowing the determination of the code of the contact[1]. In order to measure the dynamical Coulomb blockade, the sample is then brought into the normal state by applying a magnetic field of 200 mT perpendicular to the plane of the electrodes, in which case the resistors have a resistance $R \simeq 1\,\text{k}\Omega$, and the differential conductance is measured as a function of voltage.

Our results, depicted in Figure 10, demonstrate that Coulomb blockade is indeed suppressed when the transmission approaches one. Quantitatively, the measured conductance dip is in agreement with the predictions within the uncertainty on the channel content determination mentioned in the footnote.

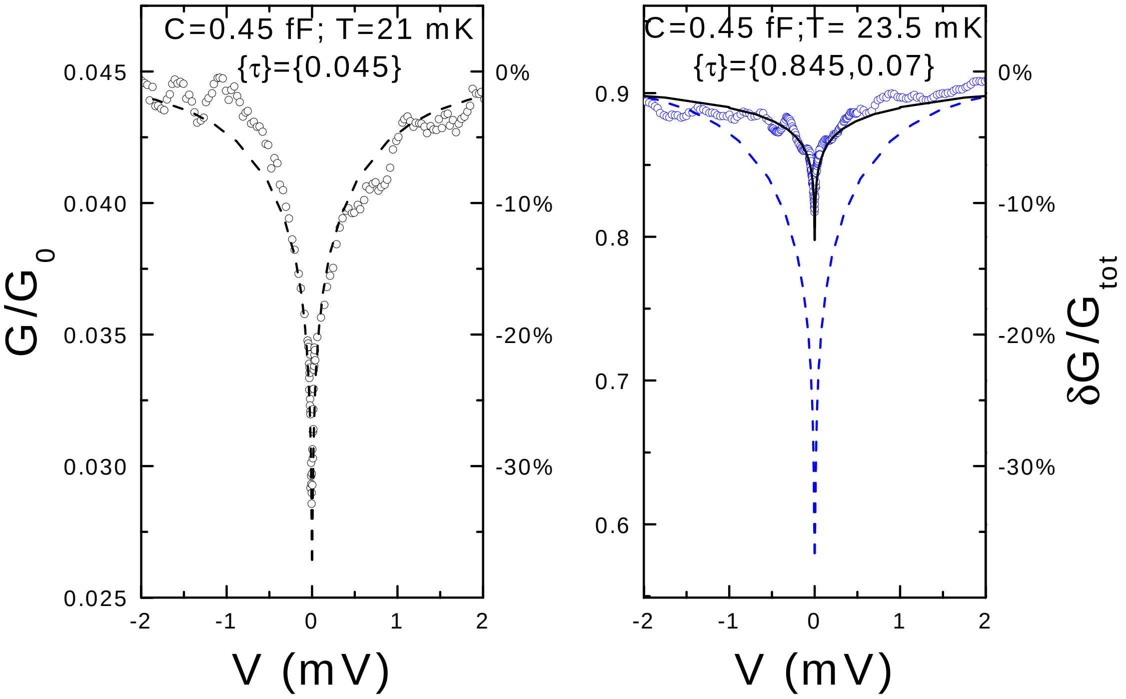

Figure 10: Measured differential conductance curves of two atomic contacts (symbols referred to the left axe), and comparison with the predictions for the dynamical Coulomb blockade (lines). Right axes, relative reduction of the conductance. Dashed lines are the predictions for the tunnel case. The wiggles and asymmetry appearing on the experimental curves are reproducible conductance fluctuations due to interference effects depending on the detailed arrangement of the atoms in the vicinity of the contact [35]. The left panel corresponds to the case of a contact with just a single weakly transmitting channel, and the experimental data are well described by the standard theory of dynamical Coulomb blockade valid for tunnel contacts, as expected. On the right panel, the contact has two channels, one with $\tau \sim 0.835$. In this case, the relative reduction of conductance is much less than in the tunnel case. The full line, which agrees reasonably well with the data, is the prediction of A. Levy-Yeyati et *al*. summing the contributions of the two channels of the contact.

---

[1] Note however that such resistors have an impedance with a non-zero real part above twice the gap frequency that is expected to slightly modify the shape of the current-voltage characteristic, in a way that is not yet quantitatively known. As a result, the channel decomposition is slightly less accurate than in previous experiments.

To conclude, the experiments described in this thesis show that besides being interesting objects by themselves, atomic contacts provide an ideal test-bed for mesoscopic physics. The accuracy of the mesoscopic PIN code determination and the integrability of these contacts into adequate mesoscopic environments allow quantitative test of theoretical predictions. Several mesoscopic phenomena other than those addressed in this thesis remain to be investigated. Some situations are even completely unexplored.

First, Coulomb blockade of Multiple Andreev Reflections remains an open problem both theoretically and experimentally. Are high-order processes, because of their larger associated charge, more strongly suppressed than lower order processes?

Second, it should be possible with these contacts to measure the basic object of the Josephson effect theory, namely the full current-phase relationship, and this for a wide range of transmissions. This experiment poses however a formidable technical challenge.

Third, the ac Josephson effect for arbitrary transmissions remains to be explored. Is it possible to observe the fractional Shapiro steps that have recently be predicted [36]?

Finally, the whole field of high-frequency dynamics remains *terra-incognita* from the experimental point of view. The usefulness of the dc $I(V)$ characteristics should not hide the extraordinary richness of the high frequency components of the current and of its fluctuations. Detailed predictions exist that await to be tested [13,14].

References of the introduction

[1] C. W. J. Beenaker and H. van Houten, in: "*Solid state Physics*", Vol. 44**,** Eds. H. Ehrenreich and D. Turnbull, Academic Press, Boston (1991).

[2] S. Chakravarty and A. Schmid, Phys. Rep. **140**, 193 (1986).

[3] S. Washburn and R. Webb, Adv. Phys. **35**, 375 (1986).

[4] R. Landauer, IBM J. Res. Dev. **1**, 223 (1957); Philos. Mag. **21**, 863 (1970).

[5] D. A. Wharam, T. J. Thornton, R. Newbury, M. Pepper, H. Ahmed, J. E. F. Frost, D. G. Hasko, D. C. Peacock, D. A. Ritchie, and G. A. C. Jones, J. Phys. C **21,** L209 (1988); B.J. van Wees, H. van Houten, C.W.J. Beenaker, J.G. Williamson, L.P. Kouwenhoven, D. van der Marel, and C.T. Foxon, Phys. Rev. Lett. **60**, 848 (1988).

[6] For reviews see: S. Datta, "*Electronic Transport in Mesoscopic Systems*", Cambridge University, Cambridge, England (1995); Y. Imry "*Introduction to mesoscopic physics*", Oxford university Press (1997); Ya. M. Blanter and M. Büttiker, Phys. Rep. **336**, 1 (2000).

[7] O.N. Dorokhov, Solid State Commun. **51**, 384 (1984).

[8] C.J. Muller, J.M. van Ruitenbeek, and L.J. de Jongh, Physica C **191**, 485 (1992).

[9] E. Scheer, P. Joyez, D. Esteve, C. Urbina, and M.H. Devoret, Phys. Rev. Lett. **78**, 3535 (1997).

[10] J.M. van Ruitenbeek, A. Alvarez, I. Piñeyro, C. Grahmann, P. Joyez, M.H. Devoret, D. Esteve, and C. Urbina, Rev. Sci. Instrum. **67**, 108 (1996).

[11] E. Scheer, N. Agraït, J.C. Cuevas, A. Levy Yeyati, B. Ludoph, A. Martin-Rodero, G. Rubio Bollinger, J. M. van Ruitenbeek, and C. Urbina, Nature **394**, 154 (1998).

[12] L.B. Arnold, J. Low Temp. Phys. **68**, 1 (1987).

[13] D. Averin and A. Bardas, Phys. Rev. Lett. **75**, 1831 (1995).

[14] J.C. Cuevas, A. Martin-Rodero, and A. Levy Yeyati, Phys. Rev. B **54**, 7366 (1996).

[15] E. N. Bratus, V. S. Shumeiko, E. V. Bezuglyi, and G. Wendin, Phys. Rev. B **55**, 12666 (1997).

[16] B. D. Josephson, Phys. Lett. **1**, 251 (1962).

[17] K. K. Likharev, Rev. Mod. Phys. **51**, 101 (1979).

[18] I.O. Kulik and A.N. Omelyanchuk, JETP Lett. **21**, 96 (1975).

[19] I.O. Kulik and A.N. Omelyanchuk, Fiz. Nizk. Temp. **3**, 945 (1977) [Sov. J. Low Temp. Phys.].

[20] A.F. Andreev, Zh. Eksp. Teor. Fiz. **46**, 1823 (1964) [Sov. Phys. JETP **19**, 1228 (1964)].

[21] C. W. J. Beenaker and H. van Houten, Phys. Rev. Lett. **66**, 3056 (1991); A. Furusaki, H. Takayanagi, and M. Tsukada, Phys. Rev. Lett. **67**, 132 (1991); A. Furusaki, H. Takayanagi, and M. Tsukada, Phys. Rev. B **45**, 10563 (1992).

[22] P. Bagwell, R. Riedel, and L. Chang, Physica (Amsterdam) **203B**, 475 (1994); V.S. Shumeiko and E.N. Bratus, J. Low Temp. Phys. **23**, 181 (1997); J.C. Cuevas, Superlattices Microstruct. **25**, 927 (1999).

[23] D. Vion, M. Götz, P. Joyez, D. Esteve, and M.H. Devoret, Phys. Rev. Lett. **77**, 3435 (1996).

[24] P. Joyez, D. Vion, M. Götz, M. Devoret, and D. Esteve, J. Supercond. **12**, 757 (1999).

[25] L.D. Landau, Phys. Z. Sow. **2**, 46 (1932); C. Zener, Proc. R. Soc. London, Ser. A **137**, 696 (1932).

[26] W. Schottky, Ann. Phys. (Leipzig) **57**,16432 (1918).

[27] Th. Martin and R. Landauer, Phys. Rev. B **45**, 1742 (1992).

[28] M. Büttiker, Phys. Rev. Lett. **65**, 2901 (1990).

[29] M. Reznikov, M. Heiblum, Hadas Shtrikm, and D. Mahalu, Phys. Rev. Lett. **75**, 3340 (1995).

[30] A. Kumar, L. Saminadayar, and D.C. Glattli, Phys. Rev. Lett. **76**, 2778 (1996).

[31] J.C. Cuevas, A. Martin-Rodero, and A. Levy Yeyati, Phys. Rev. Lett. **82**, 4086 (1999).

[32]Y. Naveh and D. Averin, Phys. Rev. Lett. **82**, 4090 (1999).

[33] G.-L. Ingold and Yu. V. Nazarov in *Single Charge Tunneling*, edited by H. Grabert and M.H. Devoret (Plenum Press, New York, 1992), p 21.

[34] A. Levy Yeyati, A. Martin-Rodero, D. Esteve, and C. Urbina, Phys. Rev. Lett. **87**, 046802 (2001).

[35] B. Ludoph, M. H. Devoret, D. Esteve, C. Urbina, and J. M. van Ruitenbeek, Phys. Rev. Lett. **82**, 1530 (1999).

[36] J.C. Cuevas, J. Heurich, A. Martin-Rodero, A. Levy Yeyati, and G. Schön cond-mat/0109152.

Chapter 1 Metallic atomic-size contacts: fully characterized quantum coherent conductors

The first experiments on small metallic point contacts were performed by bringing a metallic needle into contact with a metallic surface, usually using a differential screw mechanism to control the relative motion. This so-called spear-anvil technique pioneered by Yanson [1] in the 70's, and later developed by Jansen *et al.* [2] allowed to form stable metallic contacts with a diameter in the range 10-100 nm, but usually the mechanical control of the needle was not sufficiently stable to reach smaller sizes. Later on, mechanical set-ups were developed that did control the position of the tip at the atomic scale allowing the formation of stable contacts with diameters going all the way down to the atomic size. The Scanning Tunneling Microscope (STM) invented by Binnig and Rohrer in 1981 is the ultimate achievement of this technological progress. The STM as well as mechanical break-junctions are nowadays mature techniques to realize atomic-size contacts. We briefly present these techniques in the first part of this chapter.

Although the exact configuration of atomic-size contacts is generally not directly accessible, their electrical conductance provides some information about the number of atoms constituting the contact. By monitoring the conductance while withdrawing or driving in the metallic tip, atomic rearrangements of the contact are evidenced, and the smallest contact, namely a one-atom contact, can be adjusted. The second part of this chapter deals with the conductance of atomic-size contacts and the available evidence for one atom contacts.

Finally, as the coherence length of electrons in metals is larger than the atomic scale, even at room temperature, atomic-size contacts are quantum coherent conductors. Furthermore, as their transverse size is comparable to the Fermi wavelength, they accommodate a small number of conduction channels, and the complete mesoscopic code is amenable to measurement. This determination paved the way to experiments that established the link between the conduction properties of a single atom and its chemical valence. In the third part of this chapter, we describe how this determination is performed.[1]

1.1 Obtaining atomic-size contacts

1.1.1 The Scanning Tunneling Microscope

The first technique to reproducibly achieve atomic-size contacts was the Scanning Tunneling Microscope (STM) with which even a controlled atomic switch has been operated [3]. Presently, the widespread technique to produce contacts with a STM works as follows. The sharp metallic tip of a STM is first pressed against a metallic surface to form through a plastic deformation a large contact. Subsequently, an elongated contact is formed as the tip is withdrawn using a piezoelectric actuator. The conductance of the contact is monitored on-flight providing an indirect information on the size of the contact. Generally speaking, a

---

[1] Most of the material presented in this chapter covers work by other people, but it is presented for the sake of completeness and as a short introduction to the basic techniques.

conductance of the order of the conductance quantum $G_0 = 2e^2/h \simeq 1/12.9\ \mathrm{k}\Omega^{-1}$ indicates that the contact has an atomic size. This fast technique (one can pull out the tip in as short as 1ms, still slow compared to the atom dynamics), allows to perform statistical measurements of the properties of these contacts [4]. For this kind of experiments the STMs usually operate at room temperature in air, but in order to get accurate measurements of the properties of individual contacts it is better to work at cryogenic temperatures. When associated to an Atomic Force Microscope (AFM) that measures the force between the tip and the metallic surface, this technique allows to probe the internal mechanical strength and atomic rearrangements in atomic-size contacts simultaneously with conductance measurements [5,6]. In other experiments, the structure of the neck connecting the tip to the metallic surface has been directly observed with a transmission electron microscope, which allows to relate the atomic configuration to the conductance of the contact [7,8].

1.1.2 The Mechanical Controllable Break Junction technique (MCBJ)

This second technique used to obtain atomic size contacts was developed in 1992 by the team of J.M. van Ruitenbeek at Leiden University [9] as an extension of the “break junction technique” pioneered by Moreland and Ekin [10]. It consists essentially in breaking a thin metallic wire by bending the elastic substrate to which it is anchored. The two resulting electrodes are then slowly approached by controlling the strain on the substrate until a contact is recovered. Because this bending set-up is more compact and more rigid than the one of an usual STM, essentially by giving away the possibility of lateral scan, small contacts are significantly more stable with this technique. Furthermore, MCBJs are much easier to implement at low temperature and breaking the wire under cryogenic high vacuum prevents tip or surface contamination.

1.1.2.1 “Conventional” Mechanical Controllable Break Junctions

The schematic set-up of a MCBJ is depicted in Figure 1. A metallic wire is attached to an elastic substrate (bending beam) of thickness *t* between two anchors separated by a distance *u*. The metallic wire presents in between the two anchors a notch. The substrate is placed on two countersupports a distance L apart, and bent by pushing in its center with a pushing rod. The strain imposed on the wire by bending the substrate is geometrically concentrated at the notch. The distance between the two anchors is increased until the metallic wire breaks at the constriction. The two resulting electrodes are then slowly brought back into contact. A simple calculation assuming that the regime is elastic shows that a longitudinal displacement δx of the driving rod results in a change in the inter-electrode distance $\delta D = r\,\delta x$, where the reduction ratio $r = 6ut/L^2$ [11].

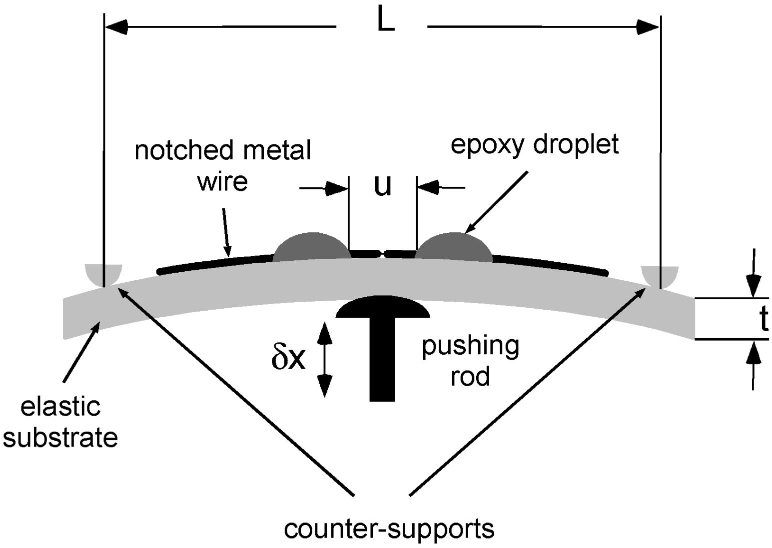

Figure 1 “Conventional” mechanically controllable break junction set-up. A notched wire is anchored to an elastic substrate by two droplets of epoxy. It is broken by bending the elastic substrate. For fine adjustment of the distance between electrodes the pushing rod is driven by a piezoelement.

In “conventional” MCBJ, the metallic wire, with a typical diameter between 20 and 200 µm, is notched with a knife and glued with two droplets of epoxy to the elastic substrate. Typical values are $t \approx 1\text{mm}$ and $L \approx 20\,\text{mm}$ and in practice the distance between the two epoxy anchors cannot be made much smaller than $u \approx 0.5\,\text{mm}$, giving rise to a reduction ratio of the order of $r \approx 7.10^{-3}$. After breaking the wire and reestablishing back a contact, the pushing rod is controlled by a piezoelectric actuator to achieve atomic scale control of the interelectrode distance.

The increased stability of the atomic contacts obtained through this technique allowed the team lead by Jan van Ruitenbeek to carry out a wide variety of elegant experiments [4].

1.1.2.2 Nanofabricated Mechanically Controllable Break Junctions

The technique of nanofabricated MCBJ developed in the Quantronics group at Saclay decreases the reduction ratio even further and thus improves the achievable stability [11]. Using nanofabrication techniques, a metallic film presenting in its center a constriction (see Figure 2) is deposited on an elastic substrate coated with an insulating polyimide layer (see Chapter 2 for the fabrication steps). The polyimide layer is then etched so as to suspend a metallic bridge around the constriction, the large metallic regions remaining anchored to the substrate. Typically the bridge is suspended over 3 μm and has a 100 nm diameter constriction. For nanofabricated MCBJ, the distance between the two anchors $u \approx 3\mu\text{m}$ is two orders of magnitude smaller than in conventional MCBJ. The much smaller reduction ratio, typically $r \approx 9.10^{-5}$ results in an improved stability, allowing to form atomic-size contacts that can be preserved identical for days. This point was essential to the realization of the experiments presented in this thesis because most of measurements required several hours to be completed.

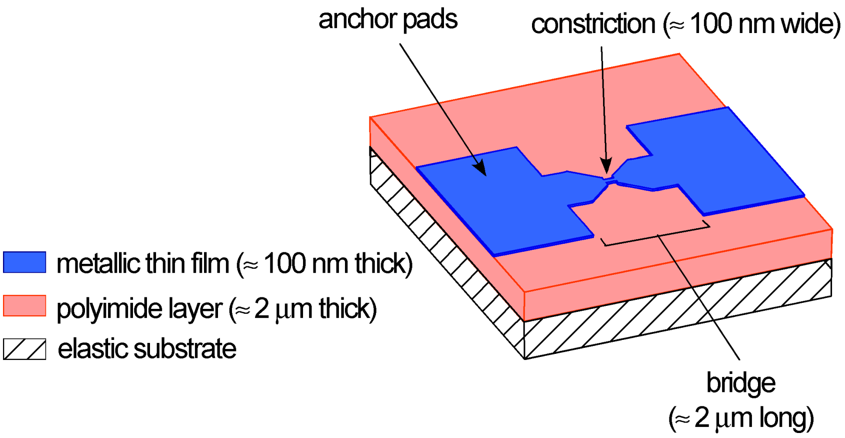

Figure 2: Schematic view of a sample fabricated using electron beam lithography and evaporation techniques. By carving the polyimide layer the bridge is released from the elastic substrate. The large-area metallic regions (anchor pads) remain fixed to the substrate.

1.2 Conductance of atomic-size contacts

1.2.1 Conductance steps and plateaus

Figure 3 presents a typical conductance trace obtained while bringing together at constant velocity the two electrodes of an aluminum nanofabricated MCBJ. Measurements were performed at 50 mK under a magnetic field of 200 mT to destroy superconductivity in the aluminum films.

The conductance first increases exponentially (see inset in Figure 3), revealing the tunnel regime in which there is a vacuum gap between the electrodes. This exponential dependence of the conductance allows a precise calibration of the mechanical set-up and a determination of its stability. The measured drift in the interelectrode spacing is of the order of 0.2 pm/h, to be compared to 30 pm/h for conventional MCBJ [11].

At some point the conductance shows a discontinuity that corresponds to a mechanical instability when the two electrodes jump into contact. Afterwards, the conductance evolves through a series of plateaus and sharp steps. The conductance on the first plateau is close to the conductance quantum G_0 and the height of the steps is also of the order of G_0. A similar staircase is observed while separating the two electrodes. Although a staircase pattern is observed every time the experiment is performed, the horizontal extension (of the order a fraction of nanometer) and the vertical position of the plateaus are not reproducible for subsequent compression-extension cycles.

To date, these general features have been observed in a large palette of metals [12]: Au, Ag, Cu, Zn, Na, K, Li, Al, Pb, Nb, Sn, …, and under a great variety of experimental conditions (temperature, technique to produce atomic size contacts, rate of compression and extension). The typical conductance on the first plateau, the typical lengths of the plateaus, and the behavior within the plateaus are characteristic of each material. For example, as can be seen in Figure 6 and 3, Al has generally plateaus with negative slope whereas Pb and Nb have mainly positive ones.

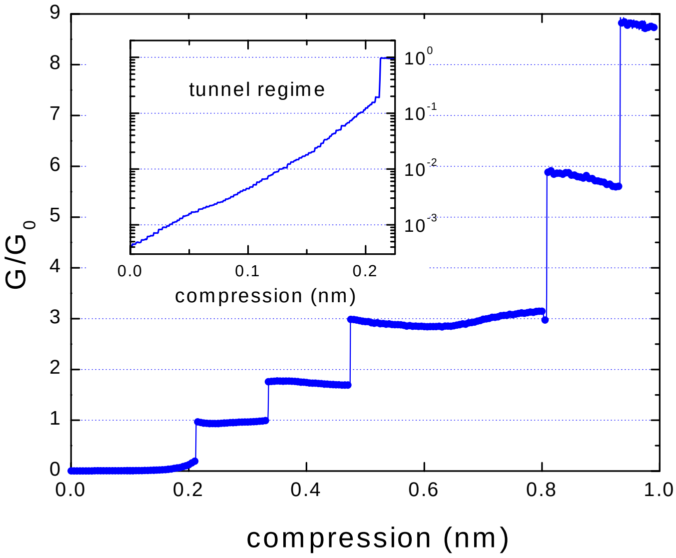

Figure 3: Conductance as a function of the relative displacement between the two electrodes while bringing them closer. Inset: Conductance in the tunnel regime on a logarithmic scale.

The succession of plateaus and conductance jumps is directly related to the dynamics of the atomic configuration of the contact. Combined STM-AFM experiments that measure the force between the tip and the surface simultaneously with the conductance, have beautifully evidenced that on a plateau the atomic configuration is only elastically deformed while a conductance jump results from an abrupt reconfiguration of the atoms at the contact accompanied by a stress relief (see Figure 4). The experimental set-up is depicted in the inset of Figure 4. A clean gold sample is mounted at the end of a cantilever beam. The force between the tip and the gold sample is obtained by measuring the deflection of the cantilever beam with an AFM working in the contact mode. At a conductance step, the contact switches from one atomic configuration to another one. In MCBJ experiments in which the contact is adjusted precisely at a conductance jump, temporal fluctuations between the two atomic configurations, revealed as two levels fluctuations in the conductance, have been observed [13,14].

Molecular dynamics simulations [15,16,17] confirm this interpretation of the staircase pattern. Starting with a perfectly ordered cylindrical metallic wire containing a few thousands atoms, the position of each atom is calculated while the wire is stretched. The atomic structure evolves through a series of stress accumulation phases, in which the relative positions of atoms remain almost constant, and abrupt stress relief phases corresponding to an atomic reconfiguration. During a reconfiguration the lateral dimensions of the contact changes abruptly resulting in a jump of its conductance. Just before breaking, the last and smallest contact corresponding to the last conductance plateau is formed by a single atom (or sometimes a several atom long chain), for which free electron calculations predict a conductance value of the order of G_0 [17].

In experiments, the exact conductance of the last plateau is not reproducible from one stretching to another but conductance histograms clearly show a peak at a particular value. In addition, for several metals this peak is very close to G_0. These facts were the first clues that the smallest contacts are indeed one-atom contacts. Other experiments described below have well established this point and provided a deeper insight into electrical transport through a single atom.

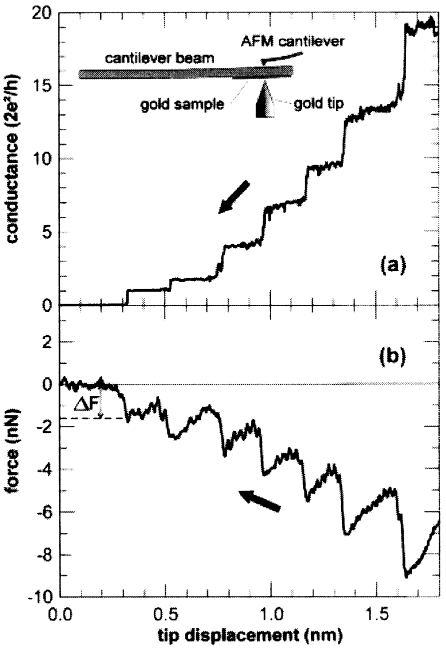

Figure 4 (reproduced from [5]): Inset: Schematic representation of the set-up combining an STM and an AFM. Main panel: Representative simultaneous recording of the measured conductance (a) and force (b) during the elongation of an atomic-sized constriction at 300 K. Conductance steps occurs simultaneously with relaxation of the force as a result of atomic rearrangements.

1.2.2 One-atom contacts

1.2.2.1 Direct observation of one-atom gold contact

In the case of gold, one-atom and chain contacts have indeed been observed directly with Ultra High Vacuum (UHV) high resolution Transmission Electron Microscopes (TEM) [7,8]. Contacts were formed at room temperature using an STM placed at the specimen stage of the UHV TEM. Video images of the atomic structure of the contact have been recorded at high magnification while withdrawing the tip (see Figure 5). They show that the last contact before breaking is constituted from a strand of gold atoms whose conductance is close to G_0.

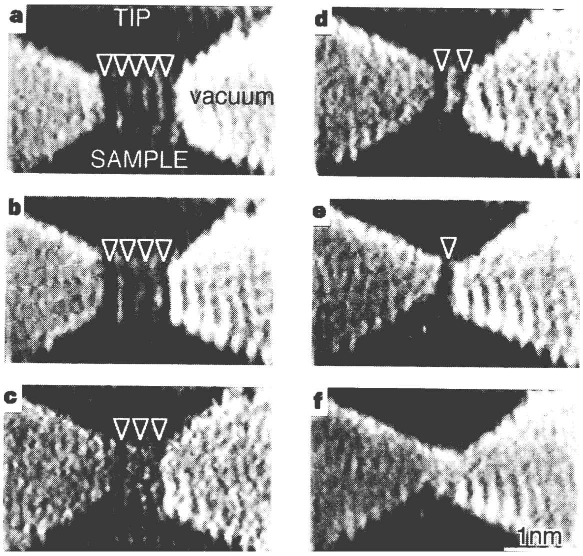

Figure 5 (reproduced from [7]): Electron microscope images of a contact while withdrawing the tip. A gold bridge formed between the gold tip (top) and gold substrate (bottom), thinned from a to e and rupture at f. Dark lines indicated by arrowheads are rows of gold atoms. The faint fringe outside each bridge and remaining in f is a ghost due to interference of the imaging electrons. The conductance of the contact is 0 at f and ~$2G_0$ at e.

This formation of a chain of a few gold atoms was also reported in "standard" STM experiments and MCBJ. By repeating at a high rate many compression-extension cycles, a chain containing up to four or five atoms was sometimes detected, as evidenced by an unusually long last conductance plateau before breaking [18]. The formation of such atomic chains is not completely understood from the molecular dynamics simulation point of view. Furthermore, this phenomenon has been observed only in gold samples and the specificity of this metal compared to others is not well understood.

1.2.2.2 Direct link between the conductance of a one-atom contact and its chemical valence

As already mentioned the typical conductance value for the smallest contact depends on the material. Conductance histograms, constructed from a large number of conductance traces like the one in Figure 3, show a peak at a particular value, which for monovalent metals like gold, silver, cooper and the alkali metals is close to G_0 whereas for lead it is centered at 1.8 G_0 and for niobium at 2.3 G_0 [12]. The position of this peak is related to the chemical valence of the material.

As described in the following, the number of conduction channels of the last contact can be determined using the highly non-linear current-voltage characteristics in the superconducting state. Experiments performed by three groups have shown that this number of conduction channels is directly related to the number of valence orbital of the metal involved [19]. Four metals, namely lead, aluminum, niobium and gold, were studied covering a large palette of valence structures. In the case of gold, the superconductivity was induced through the proximity effect by a thick aluminum layer in intimate contact with the metallic gold film everywhere but at the constriction [20]. It was found that for gold only one conduction channel contributes to the conductance on the lowest conductance plateau. However, for aluminum and lead, which have p-electrons at the Fermi level, three channels contribute. Niobium is a transition metal with s- and d-electrons, and five conduction channels were found to contribute (see Figure 6).

In order to gain a microscopic insight into the link between conduction channels and the atomic orbital structure, a tight-binding model of a one-atom constriction using an atomic orbital basis was constructed [21,22]. The model includes small random displacements of the atoms around their position in a perfect crystal, but neglects the atom dynamics. Remarkably, despite the fact that the transmission probability of each channel is very sensitive to the exact positions of the atoms in the vicinity of the contact and that the system is not at equilibrium, the number of conduction channels was found to be robust against disorder around the central atom. It is simply determined by its number of valence orbitals. The number of contributing channels predicted by this microscopic calculation is in agreement with experimental results [19].

These theoretical and experimental works firmly established that the smallest possible contact does consist of a single atom, and that the electrical transport properties of one-atom contacts are determined by the chemical nature of the involved atom.

We present now the method used to determine the number of channels. It extracts the complete mesoscopic code of atomic-size contacts from their current-voltage characteristic in the superconducting state.

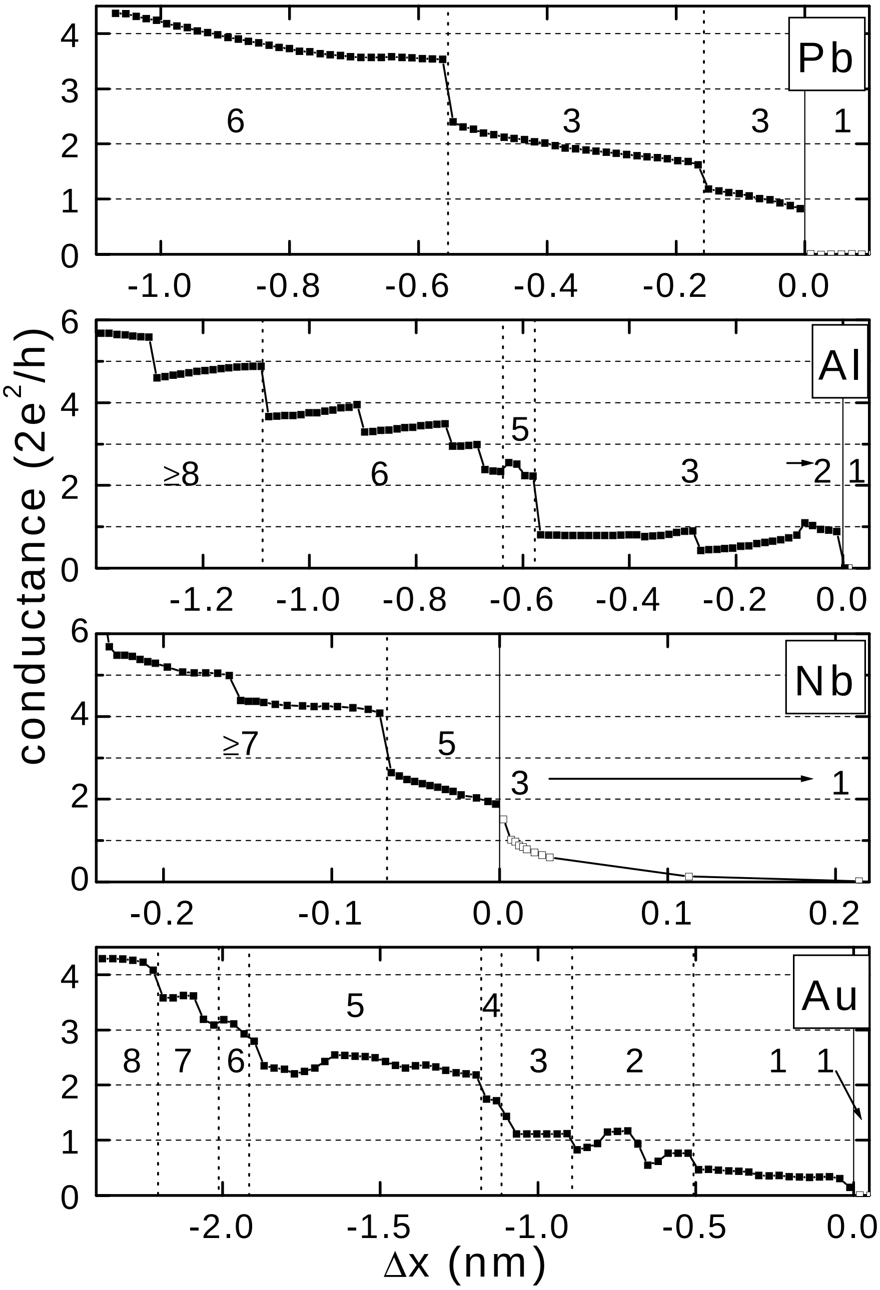

Figure 6: Conductance traces recorded while stretching atomic-size contacts as a function of the displacement Δx between the two electrodes for four different metals. Measurements on Pb were made using an STM. For Nb, conventional MCBJ have been employed while for Al and Au nanofabricated ones were used. Each point in these graphs is obtained by stopping the stretching of the contact and taking the current-voltage characteristic in the superconducting state. From the characteristic, the number of channels (indicated below and above the conductance traces) as well as the conductance of the contact are inferred.

1.3 Full characterization of atomic-size contacts as quantum coherent conductors

As explained in the Appendix B, in the superconducting state the transport through a quantum coherent conductor occurs at small voltages through MAR processes leading to highly non-linear current-voltage characteristics. These non-linearities strongly depend on the transmission of the channels. Since atomic-size contacts accommodate only a small number of channels, their current-voltage characteristic contains enough information to extract their mesoscopic code [23]. We present now the steps leading to the determination of the mesoscopic code and discuss the accuracy of the method.

1.3.1 Determination of the mesoscopic PIN code

The determination is achieved by breaking up the measured current-voltage characteristic *I(V)* into the contribution of independent channels: $I(V)=\sum_{i=1}^{N} i(V,\tau_i,\Delta)$ where N is the number of channels, Δ the superconducting gap of the metallic films and $i(V,\tau,\Delta)$ the current-voltage curve calculated for one channel with transmission probability τ. The latter were obtained from the numerical code developed by Cuevas, Martin-Rodero and Levy Yeyati [24]. A least-square fitting procedure is applied with χ^2 defined as:

$$\chi^2(\{\tau_1,...,\tau_N\})=(\frac{h}{2e\Delta})^2\int\frac{1}{D(V)}(I(V)-\sum_{i=1}^{N} i(V,\tau_i,\Delta))^2 dV$$

where D(V) is the density of data points at V in the measured current-voltage characteristic. As the characteristics are non-linear and we do not voltage bias the contact, this density is not at all uniform. One has to take it into account to ensure that the current-voltage characteristic is uniformly weighted. As the size of the voltage interval on which the n-th order MAR process dominates the current is roughly speaking of the order of $2\Delta/ne$, a uniform density gives more relative weight in χ^2 to the low order MAR processes. Note however that this imbalance would be worse if the density D(V) were not taken into account. Finally, the maximum voltage of the measured current-voltage characteristics determines the weight attributed to the first order process in the fits. In our fits this voltage is typically of the order of $4-5\,\Delta/e$.

1.3.1.1 Measurement of the superconducting gap of the metallic film

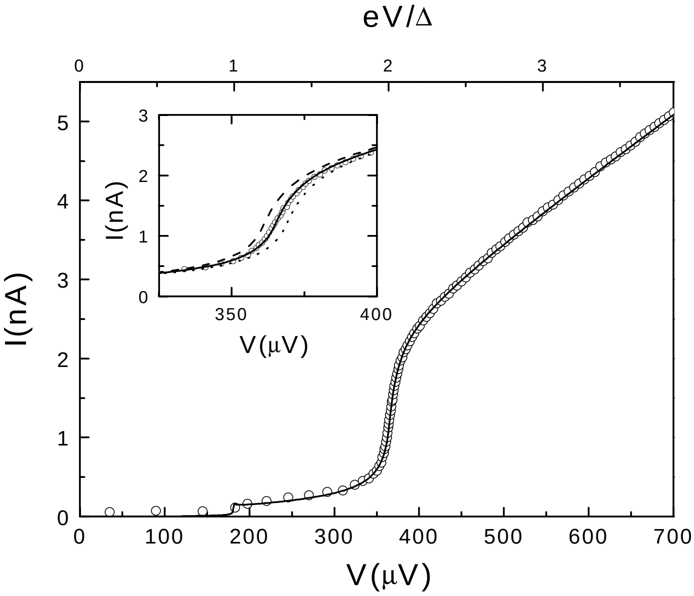

Figure 7: Circles: Measured current-voltage characteristic in the tunnel regime. Full line: best fit obtained by adjusting both the superconducting gap Δ and the transmission of the conduction channel: $\Delta = 182$ μeV and $\tau = 0.097$. Inset: zoom around the V=2Δ/e region. Full line: best fit of main panel. Dashed line: best fit with only the transmission as a fitting parameter, and the gap fixed at $\Delta = 180$ μeV. Dotted line: best fit with only the transmission as a fitting parameter, and the gap fixed at $\Delta = 184$ μeV.

For a given sample, the superconducting gap Δ of the metallic electrodes is determined prior to all other measurements. In the tunnel regime, only one conduction channel with $\tau \ll 1$ contributes to the current [25]. Taking a current-voltage characteristic in the tunnel regime, Δ is determined by adjusting its value as well as the transmission probability of the conduction channel in order to obtain the best fit (see Figure 7). All measurements performed during the course of this thesis were made on aluminum films. For all samples, the superconducting gap was between 175 and 200 μeV, the accuracy being of the order of 1 μeV. This is slightly larger than the bulk value, 175 μeV, as frequently observed in thin films. The value of Δ determined in the tunnel regime is subsequently used to determine the mesoscopic codes of all contacts obtained on the same sample, and is consequently no longer a fitting parameter.

1.3.1.2 Fitting procedure to determine the mesoscopic PIN code

For a given number n of channels,

$$\chi^2(n) = \underset{\{\tau_1,\ldots,\tau_n\}\in[0,1]^n}{\mathrm{Min}} \chi^2(\{\tau_1,\ldots,\tau_n\})$$

is determined by scanning all possible combinations of transmissions with a C++ program[2]. For transmission probabilities ranging from 0.1 to 0.99, the increment step is 0.01. From 0 to 0.1 and 0.99 to 1, the step is 0.001 so as to increase the precision in the tunnel and almost ballistic regime. This brute force complete scanning is possible in a reasonable time when considering up to 4 channels. For a larger number of channels, it is too much time consuming and in that case we use a steepest-descent minimization algorithm performed by a Mathematica code.

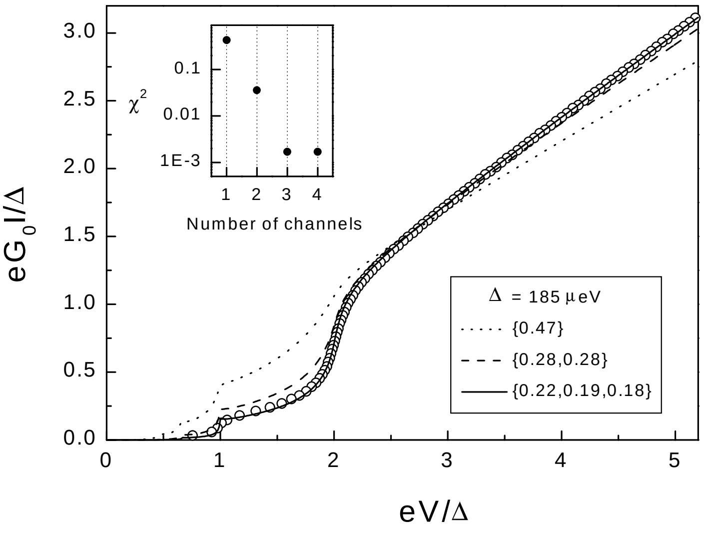

Figure 8: Dots: Current-voltage characteristic of a one-atom aluminum contact in reduced units. Lines: best fits using one, two and three conduction channels. Inset: $\chi^2(n)$ on a logarithmic scale. The number of channels n is increased as long as the χ^2 decreases significantly. For this particular contact, taking into account four channels does not improve the fit. The contact is thus considered as having three conduction channels. The best fit with three channels gives the mesoscopic PIN code: τ_1=0.22, τ_2=0.19, τ_3=0.18.

---

[2] Executable available upon request.

Of course, $\chi^2(n)$ is a decreasing function of n. The fitting procedure starts with n=1. Then n is incremented until $\chi^2(n)$ stops to decrease significantly. At this point increasing n corresponds to add channels that contribute in a negligible manner ($\tau \ll 1$) to the current-voltage characteristic and which can be taken as closed ($\tau = 0$). The final n is the number of conduction channels and the set of transmission probabilities corresponding to the minimum $\chi^2(n)$ is the mesoscopic code of the atomic-size contact. This fitting procedure is presented in Figure 8 in the typical case of a one-atom aluminum contact containing three channels.

In order to get some insight into how the individual transmission coefficients are deduced, we now demonstrate how they can be "manually" determined. For this purpose, we discuss the case of an atomic contact containing conduction channels with well-separated transmission probabilities, like the contact in Figure 9. This is a two-channel contact with one channel almost perfectly transmitted ($\tau_1 = 0.995$) and a weakly transmitted one ($\tau_2 = 0.26$). Two characteristics of the current-voltage curve determine the highest transmission. The current below Δ which is completely dominated by this well-transmitted channel and the excess current at large voltages (see Figure 9(a)). Fitting the low voltage region by imposing the highest transmission to be 1 gives too much current while with a transmission of 0.99 some is missing, as depicted in Figure 9(b). Finally, the transmission of the less transmitted channel is determined by getting the right total conductance, namely the correct slope at large voltages.

More generally, for an atomic-size contact with an arbitrary number of channels, the region of the current-voltage characteristic corresponding to the lowest voltages reveals the highest transmission probability. The following lower transmission probabilities are predominantly revealed by considering successive higher-voltage regions. The normal conductance, which is proportional to the sum of the transmission probabilities ($G = G_0 \sum_{i=1}^{N} \tau_i$), and the excess current impose two additional constraints on the mesoscopic code. For a number of channels equal or smaller than three, it is straightforward to determine "manually" the transmission probabilities.

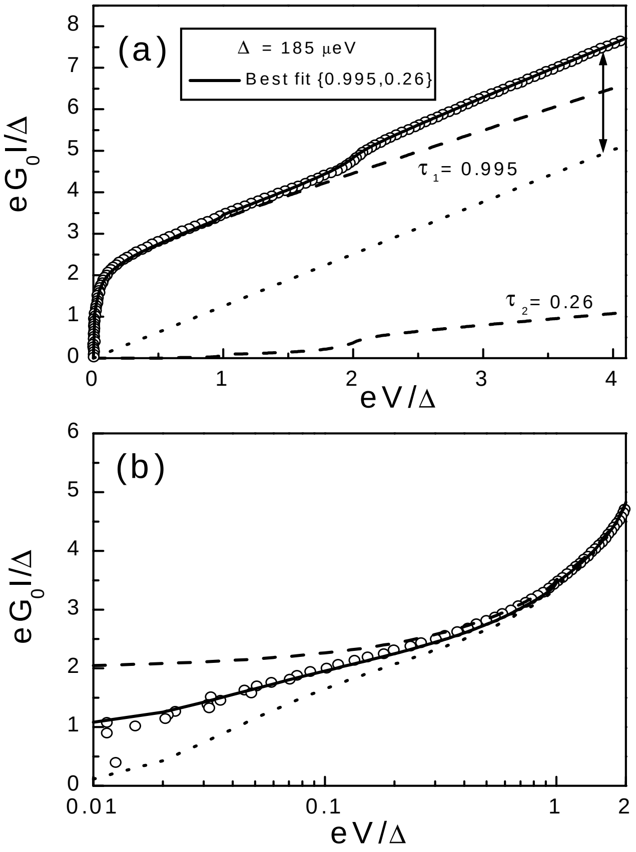

Figure 9: (a) Circles: measured current-voltage characteristic of a one-atom aluminum contact containing two conduction channels. Solid line: best two channels fit: $\tau_1 = 0.995$, $\tau_2 = 0.26$. Dashed lines: contribution of each channel. Dotted line: linear current voltage characteristic in the normal state, which for large voltages has the same slope as the characteristic in the superconducting state. The double arrow line indicates the excess current in the superconducting state. (b) Dots and full line: the same as in (a). Dotted line: best fit with τ_1=0.99 fixed. Dashed line: best fit with τ_1=1 fixed. Note the logarithmic scale on the horizontal axis in (b).

1.3.2 Accuracy of the mesoscopic PIN code determination

Three factors, both experimental and theoretical, contribute to the uncertainty in the determination of the individual transmission coefficients.

The first one is that currents and voltages are measured with a finite accuracy. The influence of these measurement uncertainties is well illustrated by the contact presented in Figure 9. Clearly, the current-voltage characteristic is noisy at low voltages (Figure 9 (b)). As this voltage region determines the highest transmission probability, the noise leads to an uncertainty on its value. This uncertainty relatively decreases as the transmission increases.

The second one is the thermal smoothing of the MAR steps. The theoretical current-voltage characteristics $i(V,\tau,\Delta)$ are calculated at zero temperature but current-voltage characteristics are typically measured at 20 mK. The MAR steps are thus smoothed on a voltage scale of the order of $20.10^{-3} k_B / e \simeq 2\ \mu\text{V}$. As this smoothing is not taken into account by the theoretical curves, the fit can not be perfect.

The last one are the possible deviations in a given sample from perfect BCS behavior, since the theoretical curves are calculated assuming an ideal BCS spectrum. Note however that our Aluminum samples are very close to ideal BCS, as observed in the tunnel regime.

Given all these factors the mesoscopic code can not be determined exactly. Within a given accuracy, we can only give a set of plausible mesoscopic codes. The criteria we use to distinguish between "possible" and "impossible" codes is the following:

$$\chi^2(\{\tau_1,...,\tau_N\}) \le (\frac{h}{2e\Delta})^2 \int \frac{1}{D(V)} (10^{-2} \times I(V))^2 dV$$

That is, "possible" mesoscopic codes are the set of transmission probabilities $\{\tau_1,...,\tau_N\}$ that fit the experimental current-voltage characteristic with an overall accuracy better than 1%, a conservative estimate of the actual experimental accuracy.

This inequality defines a volume Ω in the transmission probability space: the smaller this volume, the better the mesoscopic code determination. Generally speaking, the volume is an ellipsoid with its symmetry axis not along the τ_i, and a separated uncertainty can not be assigned to each individual transmission probability. However, for the particular case of Figure 9 of a contact having just two conduction channels with well-separated transmission probabilities, the envelope is almost a square and it is possible to ascribe an uncertainty to each individual transmission coefficient: $\tau_1 = 0.995 \pm 10^{-3}$ and $\tau_2 = 0.26 \pm 10^{-2}$.

The accuracy is better at larger transmission probability because the “distance” $\|i(V,\tau+0.01)-i(V,\tau)\|$ between two current-voltage characteristics with consecutive transmissions, defined as:

$$d(\tau)=\|i(V,\tau+0.01)-i(V,\tau)\|=\frac{h}{2e\Delta}\left(\int(i(V,\tau+0.01,\Delta)-i(V,\tau,\Delta))^2\,dV\right)^{1/2}$$

increases with transmission (see Figure 10). The discrimination between two adjacent transmissions is consequently much easier at the high transmission end.

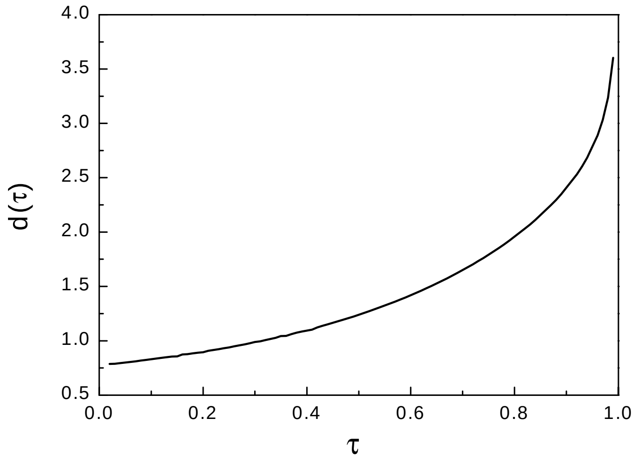

Figure 10: Distance between two theoretical current-voltage characteristics with transmission probabilities differing by 0.01 as a function of transmission probability τ.

1.3.3 Uncertainties propagation

After we determine the mesoscopic code of a particular contact, we use it to predict all the contact transport properties. Quantities like the maximum supercurrent for the DC Josephson effect, or the Fano factor for shot noise in the normal state are functions of the mesoscopic code. For example, the Fano factor for a given set of transmission probabilities $\{\tau_1,\ldots,\tau_N\}$ is equal to:

$$F(\{\tau_1,\ldots,\tau_N\})=1-\frac{\sum_{i=1}^{N}\tau_i^2}{\sum_{i=1}^{N}\tau_i}$$

The uncertainty in the prediction of these quantities from the mesoscopic code is evaluated by calculating them for all “possible” mesoscopic code. In the case of the Fano factor, this procedure defines an interval of “possible” Fano factors whose lower and upper bounds are respectively:

$$Min\ F\left(\{\tau_1,...,\tau_N\}\right) \text{ and } Max\ F\left(\{\tau_1,...,\tau_N\}\right) \text{ for } \{\tau_1,...,\tau_N\} \in \Omega$$

1.4 Conclusion

STM and MCBJ allow to routinely make atomic-size contacts between two metallic electrodes. Due to their small dimensions, these contacts are quantum coherent conductors that contain a small number of conduction channels. The great variety of the microscopic transport mechanisms in the superconducting state permits to extract from the current-voltage characteristic the mesoscopic code of atomic-size contacts. This determination has already allowed to relate the number of conduction channels of contacts containing only one atom to the chemical valence of this atom [19]. Now, we are in the position to use these fully characterized quantum coherent conductors to test quantitatively the predictions of mesoscopic physics. We present in the following chapters three different such tests.

References of Chapter 1

[1] I.K. Yanson, Zh. Eksp. Teor. Fiz. **66,** 1035 (1974) (Sov. Phys.-JETP **39,** 506 1974).

[2] A.G.M. Jansen, A.P. van Gelder, and P. Wyder, J. Phys. C: Solid St. Phys. B **13,** 6073 (1980).

[3] D. M. Eigler, C.P. Lutz, and W.E. Rudge, Nature **352**, 600 (1991).

[4] J.M. van Ruitenbeek, in *Mesoscopic electron transport*, L.L. Sohn, L.P. Kouwenhoven, and G. Schön, eds., NATO-ASI series E: Appl. Sci. **345**, 549 (Kluwer Academic Publishers, Netherlands, 1997).

[5] G. Rubio, N. Agraït, and S. Vieira, Phys. Rev. Lett. **76**, 2302 (1996).

[6] N. Agraït, G. Rubio, and S. Vieira, Phys. Rev. Lett. **74**, 3995 (1995).

[7] H. Onishi, Y. Kondo, and K. Takayanagi, Nature **395**, 780 (1998).

[8] V. Rodrigues and D. Ugarte, Phys. Rev. B **63,** 073405 (2001).

[9] C.J. Muller, J.M. van Ruitenbeek, and L.J. de Jongh, Physica C **191**, 485 (1992).

[10] J. Moreland and J.W. Ekin, J. Appl. Phys. **58**, 3888 (1985).

[11] J.M. van Ruitenbeek, A. Alvarez, I. Piñeyro, C. Grahmann, P. Joyez, M.H. Devoret, D. Esteve, and C. Urbina, Rev. Sci. Instrum. **67**, 108 (1996).

[12] A.I. Yanson, PhD thesis.

[13] C. J. Muller, J. M. van Ruitenbeek, and L. J. de Jongh, Phys. Rev. Lett. **69**, 140 (1992).

[14] H.E. van den Brom, PhD thesis.

[15] T.N. Todorov and A.P. Sutton, Phys. Rev. Lett. **70**, 2138 (1993).

[16] M. Brandbyge, J. Schiotz, M.R. Sorensen, P. Stoltze, K. W. Jacobsen, J.K. Norskov, L. Oleesen, E. Laegsgaard, and F. Besenbacher, Phys. Rev. B **52**, 8499 (1995); M.R. Sorensen, M. Brandbyge, and K. W. Jacobsen, Phys. Rev. B. **57**, 3283 (1998).

[17] Uzi Landman, W. D. Luedtke, Brian E. Salisbury, and Robert L. Whetten, Phys. Rev. Lett. **77**, 1362 (1996).

[18] A.I. Yanson, G. Rubio Bollinger, H.E. van den Brom, N. Agraït, and J.M. van Ruitenbeek, Nature **395**, 783 (1998).

[19] E. Scheer, N. Agraït, J.C. Cuevas, A. Levy Yeyati, B. Ludoph, A. Martin-Rodero, G. Rubio Bollinger, J. M. van Ruitenbeek, and C. Urbina, Nature **394**, 154 (1998).

[20] E. Scheer, W. Belzig, Y. Naveh, M.H. Devoret, D. Estève, and C. Urbina, Phys. Rev. Lett. **86**, 284 (2001)

[21] J.C. Cuevas, A. Levy Yeyati, and A. Martin-Rodero, Phys. Rev. Lett. **80**, 1066 (1998).

[22] A. Levy Yeyati, A. Martin-Rodero, and F. Flores, Phys. Rev. B **56**, 10369 (1997).

---

[23] E. Scheer, P. Joyez, D. Esteve, C. Urbina, and M.H. Devoret, Phys. Rev. Lett. **78**, 3535 (1997).

[24] J.C. Cuevas, A. Martin-Rodero, and A. Levy Yeyati, Phys. Rev. B **54**, 7366 (1996).

[25] N. van der Post, E. T. Peters, I. K. Yanson, and J. M. van Ruitenbeek, Phys. Rev. Lett. **73**, 2611 (1994).

Chapter 2 Experimental techniques

In this chapter, we describe in some details the basic techniques that were implemented to carry out the three experiments presented in the next chapters. The basic requirement is to obtain very stable and clean atomic contacts. To fulfill it, we use nanofabricated break-junctions operated at cryogenic temperatures. Furthermore, for two of the experiments the break-junction had to be integrated in specially designed on-chip environments, a goal achievable using the flexibility of electron beam lithography. Finally, one has to detect small signals arising from fragile microscopic mechanisms that correspond to very small energies (microelectronvolts). It is thus necessary to properly filter all the measurement lines to ensure that the devices are really at the low-temperatures provided by the dilution refrigerator.

2.1 Nanofabricated break junctions

The goal here is to fabricate a metallic bridge suspended over a few micrometers (see Figure 1). First, a metallic elastic substrate is covered with an insulating polyimide layer topped by an electrosensitive bilayer. Then, by exposing the bilayer to the electron beam of a scanning electron microscope, a mask with designed openings overhanging above the polyimide layer is obtained after development [1,2,3]. Metal is subsequently evaporated through this mask, in an electron gun or a Joule evaporator, leading after lift-off to a metallic structure narrowed in its center and deposited on the polyimide layer. In a final step, the narrow central region is freed from the polyimide layer by isotropic dry etching while the large-area metallic regions remain attached to the polyimide, thus giving rise to the suspended metallic bridge.

We now describe in detail the different steps of the fabrication process.

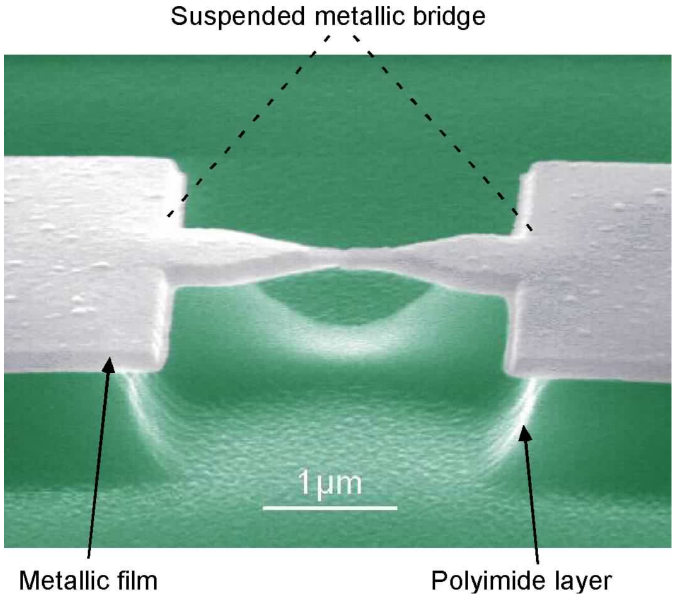

Figure 1 : SEM colorized micrograph of a nanofabricated suspended bridge.

2.1.1 Wafer preparation

A schematic cross section of the wafer consisting in an elastic metallic substrate covered with a polyimide insulating layer and a electrosensitive bilayer is shown in Figure 2.

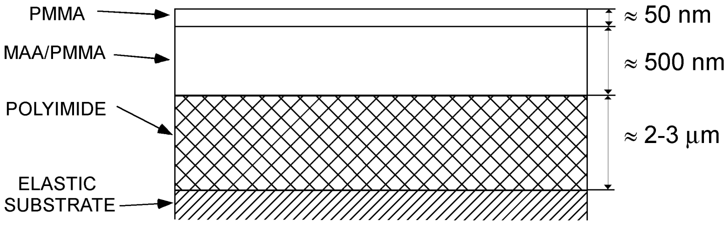

Figure 2 : Cross section of the wafer before nanofabrication steps.

Preparation recipe

As a metallic elastic substrate we use 0.3 mm-thick bronze sheets (Cu, Sn 3%,Zn 9%). A 7cm×7cm square substrate is polished using a manual polisher until the residual roughness is close to 1 μm. It is then cleaned in successive ultrasonic baths of RBS, water, acetone and ethanol. Care is taken to maintain the surface of the wafer wet between the polishing and the cleaning procedure. An adhesion promoter Ultradel A600 layer is first spread on the metallic sheet. It is spun for 30 s at 4000 rpm and dried for 1 min on a hot plate. A 2-3 μm thick layer of polyimide PI2610 from Dupond de Nemours is then spun for 1 min at 2000 rpm and baked for 30 min in an oven at 200 °C to remove the solvent. The polyimide layer is then annealed for 3 hours at 350°C in a vacuum chamber under a pressure lower than 10^{-3} Pa.

The electrosensitive bilayer consists of a layer of copolymer meta-acrylate acid/methyl-meta-acrylate (MAA/MMA) about 500 nm thick covered by a layer of PMMA about 50 nm thick. The copolymer MAA/MMA is diluted at 10% (by weight) in ethylactate. It is spun for 60s at 2000 rpm and dried for 2 min at 170°C on a hot plate. The PMMA polymer is diluted at 3% in anisole, spun 60s at 4000 rpm and baked 15 min at 170°C on a hot plate.

Comments

The polyimide layer plays three roles. First, it planarizes the substrate surface to a level compatible with the smallest dimension of the devices (100 nm). Second, it insulates the metallic thin films from the substrate. Finally, it can be carved to free the bridge. The annealing step is necessary for the polyimide layer to retain its elastic properties at low temperatures. The electrosensitive bilayer is the simplest way to realize suspended masks using electron beam lithography. The MAA/MMA layer, which has a greater electron sensitivity, sustains the suspended PMMA mask through which metals are evaporated. The thin bilayer we use allows to currently fabricate nanostructures with dimensions down to 50 nm.

The coated substrate is finally diced into 20 mm×5 mm chips and each chip is then processed separately.

2.1.2 Lithography and metal deposition

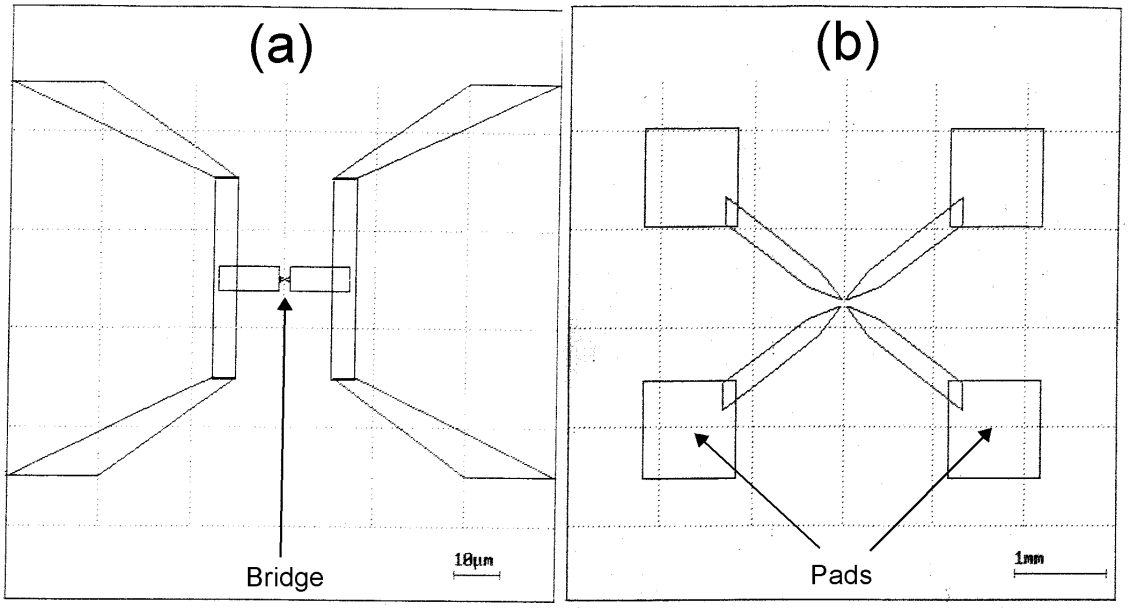

Figure 3 : Representative exposure patterns for the $120\,\mu m \times 90\,\mu m$ (a) and $6\,mm \times 4.5\,mm$ (b) exposure fields.

The sequence of steps leading to the fabrication of the metallic nanostructure on top of the polyimide layer is schematically represented in Figure 4.

Electron beam exposure

The electrosensitive bilayer is exposed using a JEOL-840A scanning electron microscope. The exposure pattern, dose and blanking of the electron beam are driven by the Proxy-writer system from Raith GmbH. We currently work with a 35 keV electron beam, for which the standard exposure dose is about $2\ pC.\mu m^{-2}$. The writing of the full mask is done in two steps. The first one ($120\ \mu m \times 90\ \mu m$ exposure field) with a 10 pA current beam patterns the fine details, i.e. mainly the geometry of the bridge (see Figure 3(a)). The second step ($6\ mm \times 4.5\ mm$ exposure field) patterns the leads (12 nA) and pads (30 nA) that connect the bridge to the measurement circuit (see Figure 3(b)). The electrons penetrate the bilayer and release their energy in the resin. In irradiated regions, PMMA and MAA are broken into fragments of smaller molecular weight. As depicted in Figure 4(a), the same beam affects a broader region in the copolymer layer than in the PMMA. This is due first to the greater sensitivity of the MAA resin and second to enhanced exposure dose of this bottom layer from electrons backscattered by the substrate. This undercut can be locally enhanced by an additional low dose electron beam exposure that affects only the bottom layer (Figure 4(b)).

Development

The irradiated regions of the bilayer are subsequently completely removed in a solvent while the non-exposed regions remain unaffected (Figure 4(c)). As a developer we use methyl-isobutyl-ketone (MIBK) diluted at 25% vol. in propanol-2. Resins are usually developed for 40s at 19°C and rinsed for 5s in propanol-2. The PMMA mask is then ready for the metal deposition step.

Metal deposition

Metals are evaporated through the mask in an electron-gun or in a Joule evaporator. The sample is positioned on a tiltable sample holder allowing evaporation at different angles. The metal evaporated at an angle through PMMA openings with not much undercut is deposited on the copolymer layer walls and not on the polyimide (Figure 4(d)).

A typical aluminum film was deposited at a pressure of 10^{-4} Pa and at a rate of 4 nm/s. Its resistance at 4 K was about 3 times lower than that at 300 K.

Lift-off

Once the metallic film is deposited, the PMMA mask and the copolymer ballast are removed in acetone at 50°C for a few minutes. The metal deposited on top of the bilayer and on the walls of the bottom copolymer are eliminated (Figure 4 (e)).

This completes the electronic lithography steps.

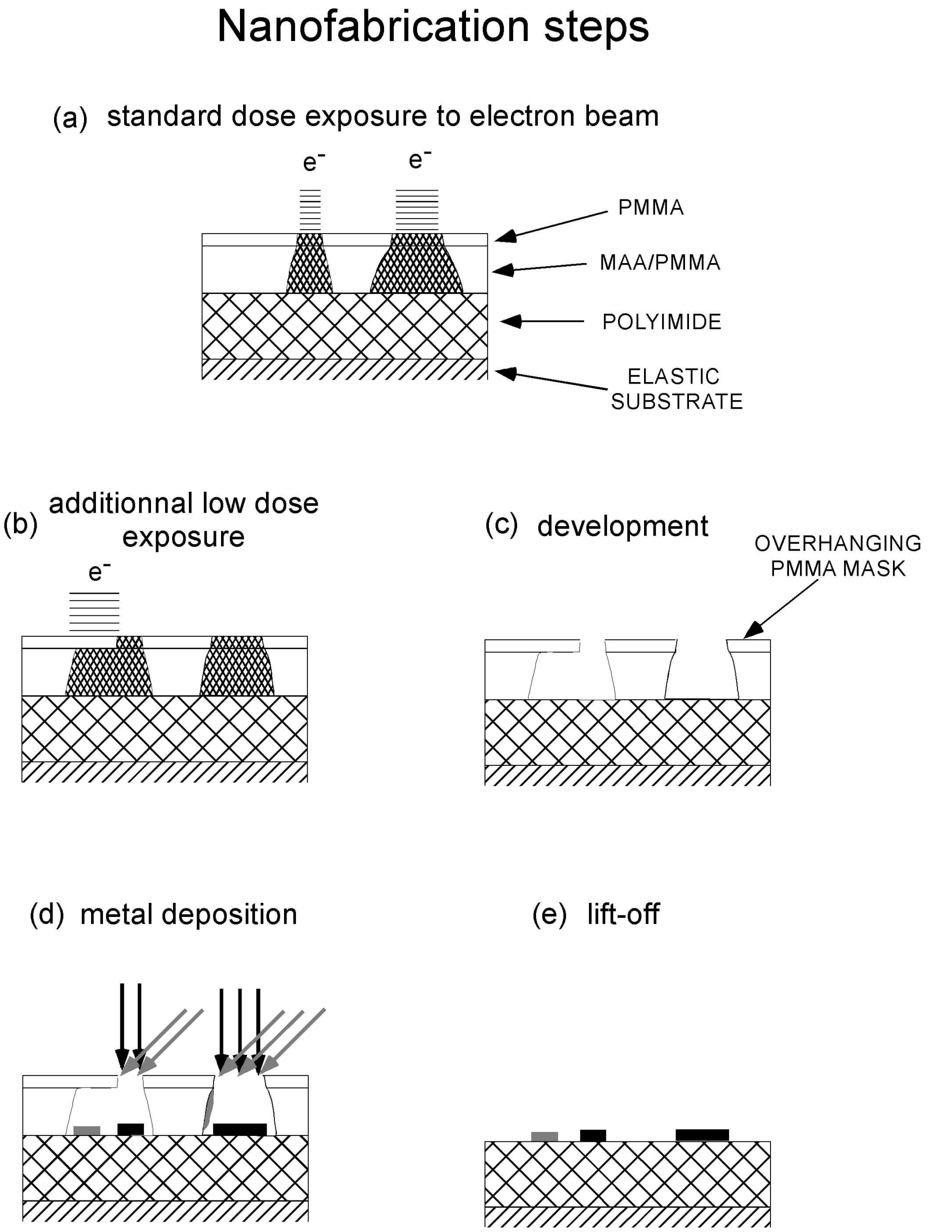

Figure 4 : Schematic representation of the nanofabrication steps based on the technique of deposition through a suspended PMMA mask.

2.1.3 Dry etching of the polyimide layer

The polyimide layer is then isotropically dried etched so as to suspend the bridge. The etching can be done either

- in a reactive ion etcher under the following rf plasma conditions: a flow of 50 sccm of O_2 and 1 sccm of SF_6 at a total pressure of 2.7 Pa and a bias voltage of 20 V, or
- in a downstream etching machine: 30 sccm of O_2 at a pressure of 28 Pa and a power of 100 W.

The vertical etching depth is monitored by means of a laser interferometer. Etching about $1\,\mu\text{m}$ vertically is sufficient to free from the substrate the metallic features having lateral dimensions lower than $2\,\mu\text{m}$. A SEM photograph of a resulting suspended bridge is shown in Figure 1.

2.1.4 Embedding a nanofabricated break-junction in an on-chip electromagnetic environment

The pattern of electron beam exposure can be designed so as to embed the break junction in an on-chip electrical circuit using metal evaporation at different angles or two steps fabrication procedures. This was essential to the realization of the experiments on the Josephson effect and on dynamical Coulomb blockade. In both cases, the circuit consisted of four small resistors and four large capacitors (see the “sample part” at the bottom of Figure 9).

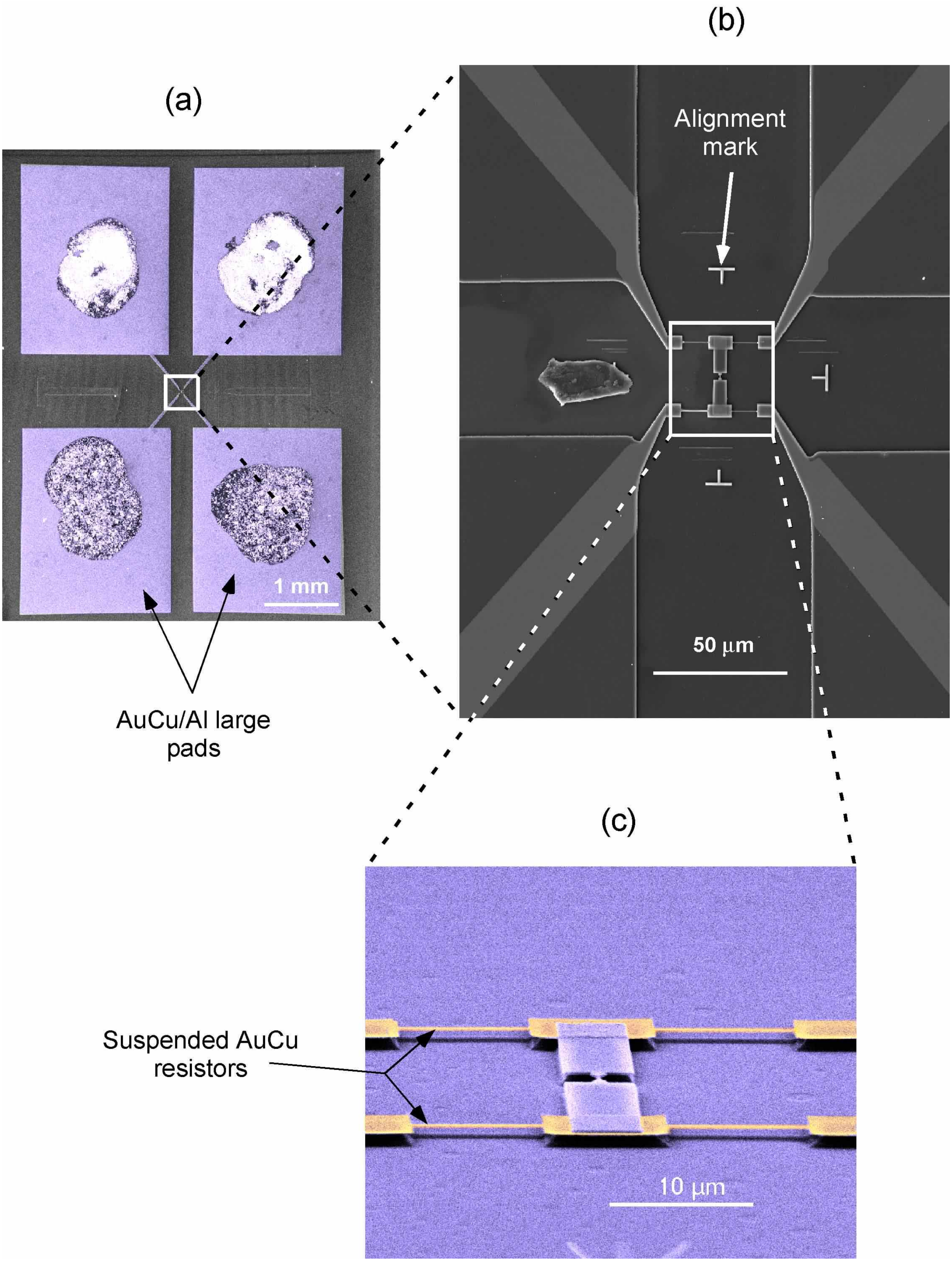

Figure 5 : SEM micrographs at different scales of one of the two samples measured in the experiments on Josephson supercurrent. (a) AuCu/Al large pads that forms with the metallic substrate large capacitors. (b) Large SEM micrograph of the central part : The layer superposition resulting from the two different fabrication stages is clearly visible. (c) Suspended bridge and AuCu resistors.

2.1.4.1 Samples measured in the Josephson supercurrent experiment

In the experiments on the Josephson supercurrent, the resistors were made out of an AuCu alloy (see Figure 5(b) et (c)) and the large capacitors were formed between large AuCu/Al pads and the substrate, the dielectric being the polyimide layer (see Figure 5(a)). This was obtained in two lithography stages, with an intermediate alignment procedure. First, the AuCu alloy (weight ratio 3:1) was deposited in a Joule evaporator to form the small resistors and the large pads with no interconnections, and four alignment marks. After lift-off, a new bilayer was deposited and another lithography cycle was performed to obtain the Al bridge, the anchor pads and the interconnections. The bilayer being almost transparent to electrons, it allows the alignment of the second pattern with respect to the previously fabricated AuCu structures. Before depositing aluminum, an ion-mill cleaning procedure is performed to ensure good contact between the two metallic layers. The AuCu/Al top plates of the capacitors were $2.5\,\mathrm{mm}\times 2\,\mathrm{mm}$ rectangles $180\,\mathrm{nm}$ thick. The measured capacitance was of the order of $140\,\mathrm{pF}$. The AuCu resistors were $10\,\mu\mathrm{m}$ long, $500\,\mathrm{nm}$ wide and 30 or $50\,\mathrm{nm}$ thick leading, respectively, to resistances of $170\pm 20\,\Omega$ and $125\pm 20\,\Omega$.

2.1.4.2 Sample measured in the Coulomb blockade experiment

In the experiment on dynamical Coulomb blockade, the resistors were thin aluminum leads and the capacitors were implemented by four large aluminum pads. Only one lithography stage was necessary in that case. Aluminum was evaporated at three different angles (0° and ± 40°) through a single mask. First, a 12 nm thick film of aluminum was evaporated perpendicularly to the substrate. This film is thus deposited on all polyimide regions facing the openings in the mask. The break junction and pads regions were subsequently thickened by two 75 nm depositions at ± 40°. The sample is tilted around an axis parallel to the long and narrow openings in the mask giving rise to the resistors. Consequently, as explained before (p. 47), these angle evaporations do not add any metal to them. The thin aluminum leads forming the resistors were $25\,\mu\mathrm{m}$ long and 200 nm wide (see Figure 6) with a resistance of the order of $920\,\Omega$ in the normal state. The resistance is essentially due to surface scattering and thus decreases rapidly when the leads are thickened.

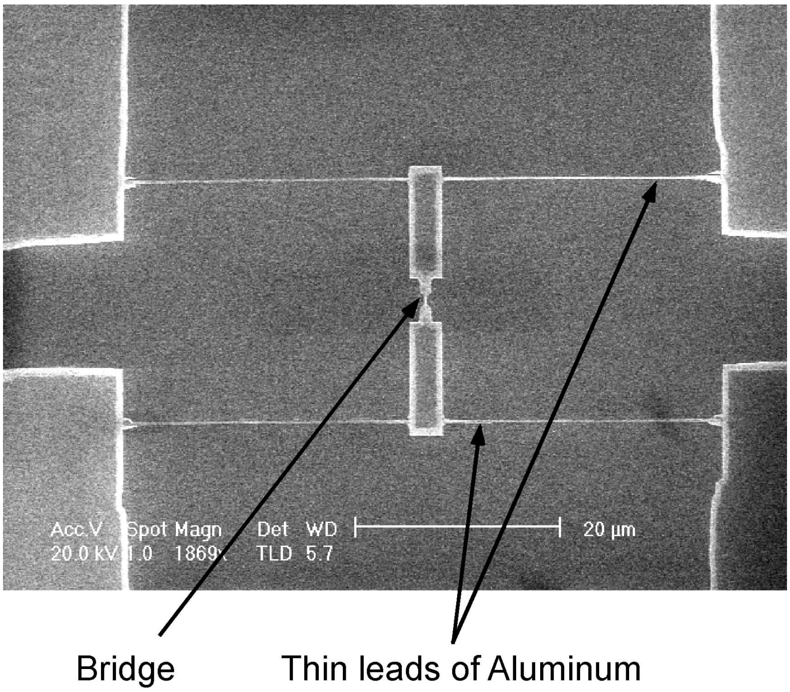

Figure 6: Sample measured in the experiment on dynamical Coulomb blockade. Both the bridge and the resistors are made out of aluminum.

2.2 Bending mechanism

The sample is placed on a three point bending bench that is thermally anchored to the mixing chamber of a He_3/He_4 dilution refrigerator (see Figure 7). The two countersupports are 14 mm apart. A differential screw, with a 100 µm pitch, controls the relative translation between the pushing rod and the two countersupports. The sample is mounted with the bridge centered with respect to the pushing rod. The nominal reduction ratio $r \simeq 9.2\times10^{-5}$ translates one turn of the screw into a 9.2 nm stretching of the suspended bridge[1]. The differential screw is driven by a DC electrical motor (controlled by a PC) through a series of three reduction gear boxes for a typical total reduction ratio of 16260:1 (see Figure 8). The motor speed can be continuously adjusted between 0.1 and 100 turns per seconds. The different stages are connected through axles made of thin-walled stainless steel tubes to reduce the thermal loads on the different parts of the fridge. The first gearbox is directly coupled to the motor and

---

[1] Note that as the substrates show some slight plastic deformation after the experiments are completed, the nominal reduction ratio (calculated assuming a perfectly elastic deformation) is probably smaller than the actual one.

drives a rotating vacuum feedthrough that enters into the vacuum can of the refrigerator. The second gearbox is thermally anchored at 4K and the third one to the 1K pot. From there, a last section of tube, 40 cm long, directly drives the differential screw.

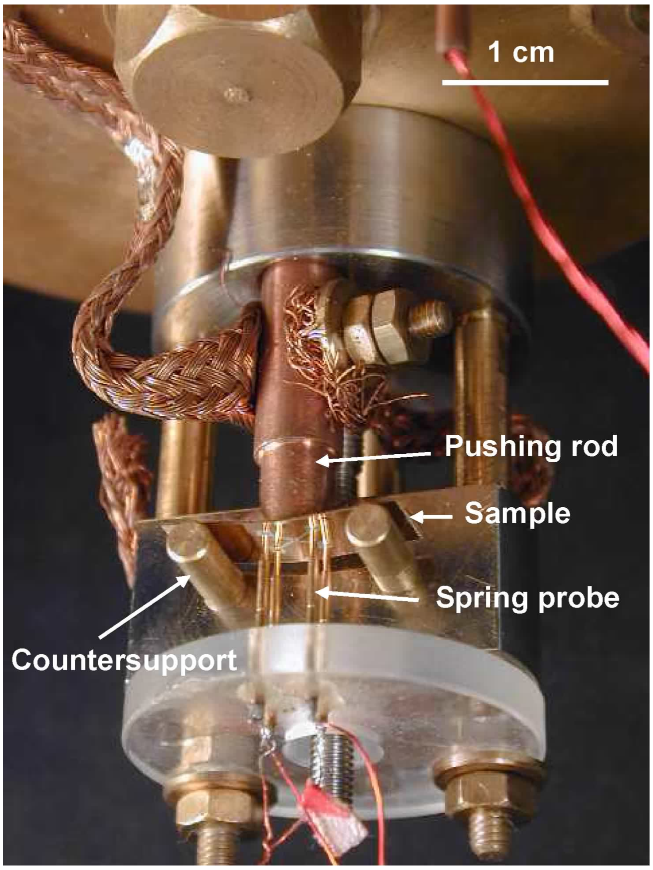

Figure 7 : Three point bending bench.

The bridge is broken at a typical stretching rate of 50-100 pm/s. Because of friction in the differential screw, the temperature during this step is not lower than 500 mK. The relative displacement between the two freshly fabricated electrodes is then controlled using the same mechanical set-up. The contacts are adjusted changing the interelectrode distance at speeds ranging from 5 pm/s down to 0.5 pm/s ($\simeq 0.9$ rps for the DC motor). At the lowest speeds, it is possible to keep the sample temperature below 50 mK.

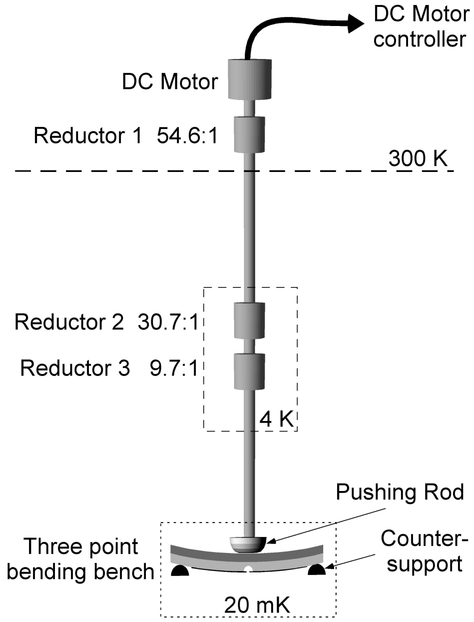

Figure 8 : Schematic representation of the whole mechanical bending set-up from room temperature down to the coldest part of the dilution fridge.

2.3 Measurements at low temperature

Measurements at low temperature are made in a Oxford He_3/He_4 dilution refrigerator. The temperature is adjustable between 1 K and its base value that with the mechanical set-up mounted is 17 mK. The elastic substrate is thermalized through contact with the two countersupports and the pushing rod. The full bending bench is enclosed in a copper shield thermally anchored to the mixing chamber. The cryostat is equipped with an 8 Tesla superconducting coil surrounding the experimental box.

The large area pads of the sample are connected to a four terminal measurement circuit by means of four spring contact probes. Silver paint is spread on top of the pads to avoid piercing them while bending the substrate. The measurement lines are home-made lossy shielded cables [4] to prevent high-frequency noise from reaching the sample. Microfabricated distributed RC filters shaped as meander lines [5] are inserted in the lines, just before they enter the copper shield. The lines are carefully thermally anchored at the different stages of the refrigerator.

The cryostat is equipped with shielded twisted-pair and coaxial lines. The inner conductors are polyimide coated manganin wires, and the shields are stainless steel capillaries. The coaxial cables going from 300K to 4K are made out of 0.1 mm diameter wire (~ 60 Ω/m), and those going from 4K to the mixing chamber out of .05 mm wire. The shields are $\Phi_{\text{int}} = 0.2\text{mm}, \Phi_{\text{ext}} = 0.7\text{mm}$ capillaries. These cables have a distributed capacitance of about 100 pF/m. The twisted pairs going from 300K to 4K are made out of 0.1 mm diameter wire inside a $\Phi_{\text{int}} = 0.4\text{mm}, \Phi_{\text{ext}} = 1.0\text{mm}$ shield, and those going from 4K to the mixing chamber out of .05mm wire inside a $\Phi_{\text{int}} = 0.2\text{mm}, \Phi_{\text{ext}} = 0.7\text{mm}$ shield.

The distributed RC filters have an attenuation in the [40 MHz, 20 Ghz] frequency window greater than 80 dB, when measured on 50 Ohm lines.

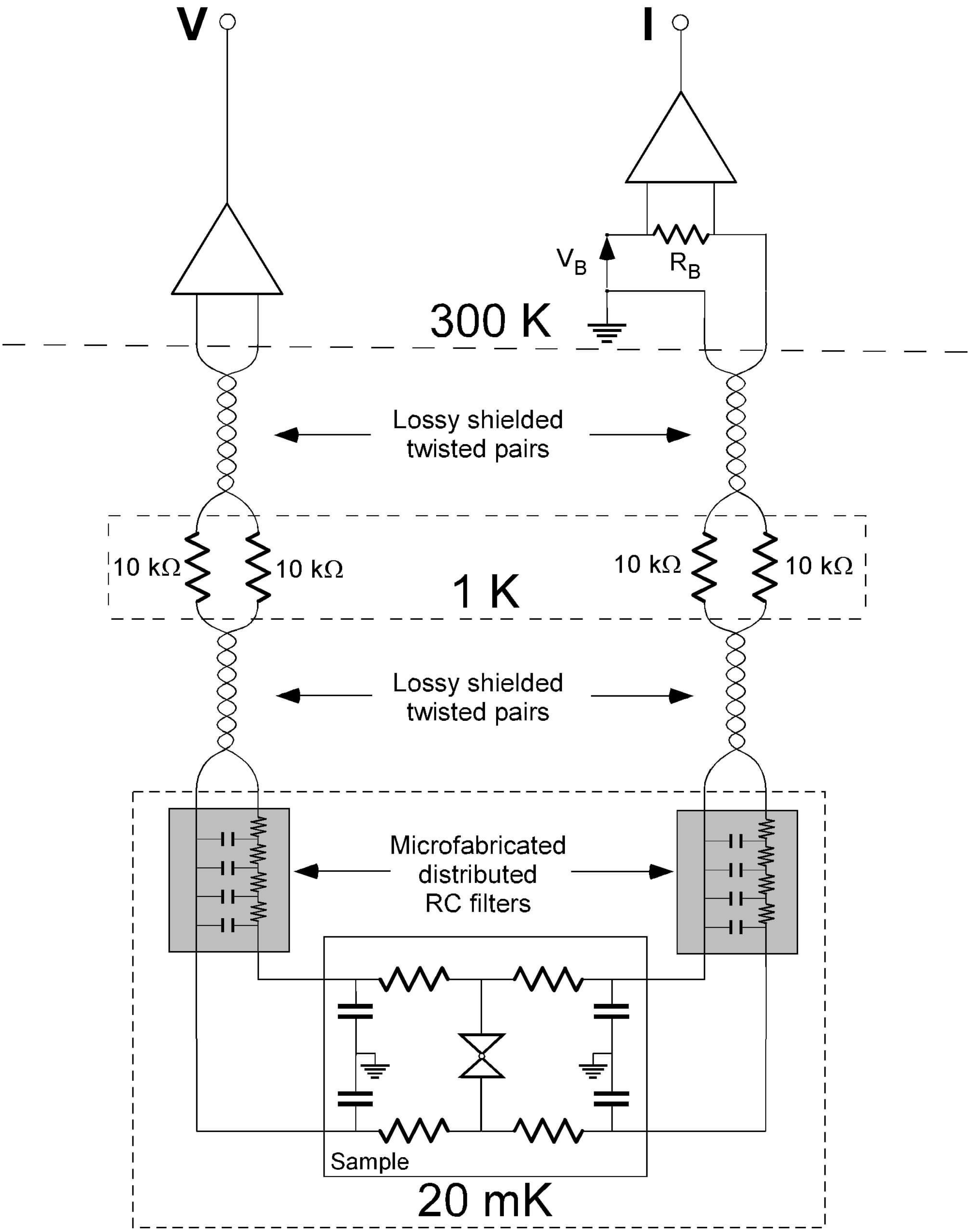

Figure 9 : Schematic representation of the four point measurement set-up and on-chip electrical circuit in experiments on Josephson supercurrent and dynamical Coulomb blockade. One bifilar line is used to current bias the sample while the another one allows to measure the voltage across the contact. To ensure the electronic thermalization at the lowest temperature of the fridge, 10 kΩ resistances are placed in between the two lossy lines stages. Together with the cable capacitance, they form a *RC* filter with a 1 MHz cut-off frequency.

A schematic representation of the measurement set-up used in the experiments on Josephson supercurrent and dynamical Coulomb blockade is depicted in Figure 9. The set-up for the shot-noise experiments will be described in Chapter 4. The voltage V across the contact is measured using two low-noise battery powered differential preamplifiers in series: a $\times 100$-gain NF-LI-75A followed by a Stanford-SR560 of selectable gain. The current I through the sample is produced by applying a voltage bias V_B to a biasing resistance R_B of the order of $50\,\mathrm{k}\Omega$ and measured by a low-noise differential preamplifier Stanford-SR560. The current-voltage characteristics are recorded on a digital oscilloscope Nicolet Pro44 and transferred through an IEEE data link to a PC for treatment.

References of Chapter 2

[1] G.J. Dolan and J.H. Dunsmuir, Physica B **152**, 7 (1988).

[2] J. Romijn and E. Van der Drift, Physica B **152**, 14 (1988).

[3] T.A. Fulton and G.J. Dolan, Phys. Rev. Lett. **59**, 109 (1987).

[4] D.C. Glattli, P. Jacques, A. Kumar, P. Pari, and L. Saminadayar, J. Appl. Phys. **81**, 7350 (1997).

[5] D. Vion, P.F. Orfila, P. Joyez, D. Esteve, and M. H. Devoret, J. Appl. Phys. **77**, 2519 (1995).

Chapter 3 Josephson supercurrent through one atom

3.1 The Josephson supercurrent

Josephson predicted in 1962 [1] that a supercurrent can flow between two superconducting electrodes even when they are weakly coupled. This so-called Josephson supercurrent results from the coherent transfer of Cooper pairs between the superconducting electrodes when a superconducting phase difference $\delta = \phi_L - \phi_R$ is applied between them.

This phase difference δ is a purely electrodynamic quantity related to the voltage difference V between the electrodes by the Josephson relation: $\varphi_0 \dot{\delta} = V$, where $\varphi_0 = \hbar/2e$ is the reduced flux quantum.

The Josephson effect was observed one year after its prediction by Anderson and Rowell [2], and later on in a large variety of weak coupling configurations (see Figure 1). Two large classes of Josephson elements can be distinguished: the “tunnel type” consisting of two superconducting electrodes coupled through a thin vacuum or insulating tunnel barrier, and the “weak link” type when the two electrodes are “directly” electrically connected through a metallic conducting region. A weak link can consist in a geometrical constriction like a narrow bridge or a point contact, or of a small non-superconducting lead (see [3] for a more extensive list).

How much supercurrent flows through a Josephson element for a given phase difference depends on its electrical and geometrical characteristics, and on external parameters like temperature or magnetic field. Many theoretical works have been devoted to the determination of the current-phase relation $I(\delta)$ for the various types of weak links, and in particular to the prediction of the maximum supercurrent that they can sustain, which is called the critical current I_0. In this chapter, we report measurements of the critical current of superconducting atomic contacts and compare to the theoretical predictions.

3.1.1 Current-phase relationship and critical current of various Josephson elements

For tunnel junctions with BCS superconducting electrodes, Josephson predicted a sinusoidal current-phase relationship and determined the critical current at zero temperature:

$$I(\delta) = I_0 \sin(\delta) \text{ with } I_0 = \frac{\pi\Delta}{2eR_N}, \tag{1}$$

where Δ is the modulus of the order parameter in the bulk superconducting electrodes and R_N the resistance of the tunnel junction in the normal state. The $R_N I_0$ product is constant for a given superconducting gap: the critical current is simply proportional to the normal state conductance of the junction. The transport properties in the superconducting state are related to those in the normal state in a simple manner. Ambegaokar and Baratoff have completed Josephson's work by determining the temperature dependence of the critical current:

$$I_0(T) = \frac{\pi\Delta(T)}{2eR_N}\tanh(\frac{\Delta(T)}{k_B T}). \tag{2}$$

The case of weak links is more complex, and various behaviors have been found depending on the type of weak link. Weak links are classified by comparing their length L to the coherence length ξ and to the elastic mean free path ℓ of the constitutive material: weak links with $L \ll \xi$ ($L \geq \xi$) are called short (long) weak links, and weak links with $L \gg \ell$ ($L \leq \ell$) are called dirty (clean) weak links. The current-phase relationship and the temperature dependence of the critical current are nowadays known for all these types of weak links (see Figure 2).

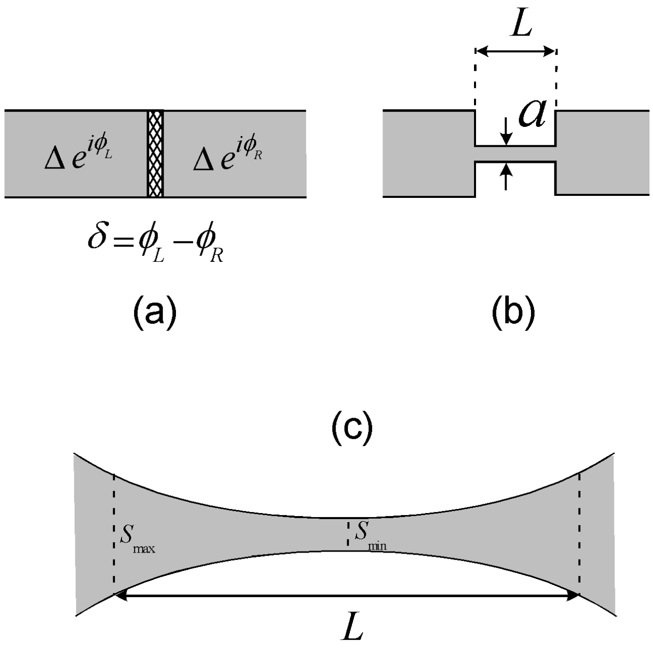

Figure 1: Examples of structures showing a Josephson effect and discussed in this section. (a) Tunnel junction. (b) Geometrical constriction considered by Kulik and Omel'yanchuk ($a \ll \xi, L$) both in the dirty $\ell \ll L$ and clean $\ell \gg L$ limit. (c): Superconducting adiabatic constriction considered by Beenakker and van Houten ($S_{\min} \ll S_{\max}$).

In 1969, Aslamanov and Larkin treated the case of a short and dirty weak link ($L \ll \xi$ and $L \gg l$)[4]. Their calculation, based on the Ginzburg-Landau equations, is valid only near the critical temperature of the superconducting electrodes. In this limit, independently of the material constituting the weak link, they established that the current-phase relationship is sinusoidal, like for tunnel junctions. In 1975, Kulik and Omelyanchuk extended the calculation to arbitrary temperatures by means of Usadel equations [5]. At temperatures much smaller than the critical temperature, they predicted a non-sinusoidal current-phase relationship:

$$I(\delta) = \frac{\pi\Delta}{eR_N}\cos\left(\frac{\delta}{2}\right)\operatorname{arcth}\left(\sin\left(\frac{\delta}{2}\right)\right). \qquad (3)$$

Compared to the tunnel case, the $R_N I_0$ product is at zero temperature increased by a factor 1.32.

In 1977, using the more general formalism of Eilenberger equations [6], the same authors solved the short and clean limit ($L \ll \xi$ and $L \ll l$)[7]. The current-phase relationship at low temperature is non-sinusoidal, and, at zero temperature, the phase dependence of the supercurrent is proportional to $\sin(\delta/2)$ with a $R_N I_0$ product twice larger than in the tunnel case:

$$I(\delta) = \frac{\pi\Delta}{eR_N}\sin\left(\frac{\delta}{2}\right) \quad \delta \in [-\pi;\pi]. \qquad (4)$$

In the beginning of the 90’s, motivated by the observation in 1988 of conductance quantization in quantum point contacts tailored in 2D electron gases [8], Beenaker and van Houten investigated the quantum regime which occurs when the width of the weak link becomes comparable to the Fermi wavelength. In this regime, the contact accommodates only a few conduction channels whose number increases with the point contact lateral size. They determined the current-phase relationship for an adiabatic impurity free superconducting constriction [9] by solving the Bogoliubov-de Gennes equations using the WBK method introduced by Bardeen *et al.* [10].

The main result is that, like the conductance in the normal state, the critical current of an adiabatic constriction increases stepwise as a function of its width, and that the current-phase relationship at zero temperature is given by:

$$I(\delta) = N\left(\frac{e\Delta}{\hbar}\right)\sin\left(\frac{\delta}{2}\right) \quad \delta \in [-\pi;\pi], \tag{5}$$

where N is the number of open conduction channels. This result is equivalent to the expression (4) since the contact conductance is directly related to the number of open channels by the Landauer relation (see Appendix A).

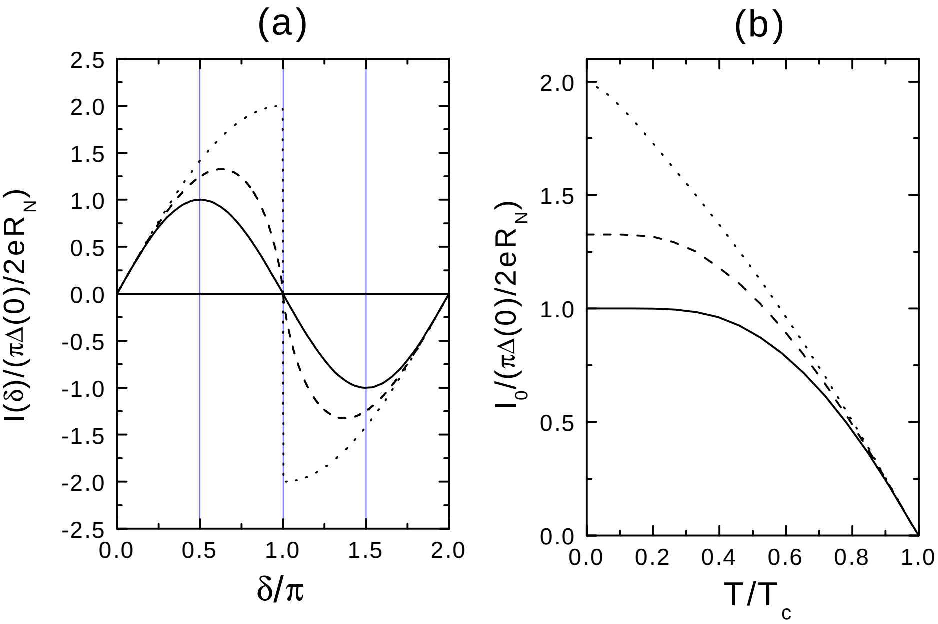

Figure 2: Current-phase relationships at zero temperature (a) and temperature dependence of the critical current (b) for different Josephson elements. Full lines: tunnel junction. Dashed lines: short dirty weak link. Dotted lines: short ballistic weak link.

3.1.2 Current-phase relationship of a quantum coherent conductor

In the mesoscopic regime, a unified theoretical picture covering all type of weak links from the tunnel to the ballistic limit has emerged in the last decade [11]. As explained in

Appendix B, Bagwell established that, in the generic case of a one dimensional conduction channel with arbitrary transmission τ and arbitrary length, the supercurrent is carried by Andreev bound states. In the short limit, when L is much smaller than the superconducting coherence length, there are only two such states with opposite energy $E_{\pm}(\delta,\tau)=\pm\Delta\sqrt{1-\tau\sin^2(\delta/2)}$ that carry current in opposite directions:

$$I_{\pm}(\delta,\tau)=\varphi_0^{-1}\frac{dE_{\pm}}{d\delta}(\delta,\tau)=\pm\frac{e\tau\Delta}{2\hbar}\frac{\sin(\delta)}{\sqrt{1-\tau\sin^2(\delta/2)}}. \tag{6}$$

The supercurrent through the channel depends thus on the population imbalance between the two Andreev bound states. At thermal equilibrium, the supercurrent at a given phase difference δ is given by:

$$I(\delta,\tau)=\frac{e^{\frac{-E_{-}(\delta,\tau)}{k_BT}}I_{-}(\delta,\tau)+e^{\frac{-E_{+}(\delta,\tau)}{k_BT}}I_{+}(\delta,\tau)}{e^{\frac{-E_{-}(\delta,\tau)}{k_BT}}+e^{\frac{-E_{+}(\delta,\tau)}{k_BT}}}=\frac{e\tau\Delta}{2\hbar}\frac{\sin(\delta)}{\sqrt{1-\tau\sin^2(\delta/2)}}\tanh\left(\frac{E_{+}(\delta,\tau)}{k_BT}\right). \tag{7}$$

The current-phase relationship of a quantum coherent conductor with a mesoscopic code $\{\tau_1,...,\tau_N\}$ is obtained by summing up the independent contribution of all conduction channels:

$$I_J(\delta,\{\tau_1,...,\tau_N\},\{n_{i\pm}\})=\sum_{i=1}^{N}(n_{i-}-n_{i+})I_{-}(\delta,\tau_i), \tag{8}$$

where the $n_{i\pm}$ are the occupation numbers of the two Andreev bound states associated with the *i*-th channel. It is assumed here that all channels share the same phase difference δ imposed by the superconducting electrodes that act as perfect superconducting phase reservoirs. At zero temperature and thermal equilibrium, $n_{i+}=0$ and $n_{i-}=1$ and :

$$I_J(\delta,\{\tau_i\})=\frac{e\Delta}{2\hbar}\sum_{i=1}^{N}\frac{\tau_i\sin(\delta)}{\sqrt{1-\tau_i\sin^2(\delta/2)}}. \tag{9}$$

Note that in the single channel case, the critical current is not simply proportional to τ and thus neither to the normal conductance. It is given by:

$$I_0(\tau)=\frac{e\Delta}{\hbar}(1-\sqrt{1-\tau}). \tag{10}$$

More generally, the expression (9) implies that transport properties in the superconducting state are not simply related to the normal state conductance. One recovers however a direct link with the normal conductance in the limit cases described before. In the tunnel limit, all transmission probabilities are small $\tau_i \ll 1$, so that the denominators $\sqrt{1-\tau_i \sin^2(\delta/2)}$ are equal to 1 and Exp. (9) becomes:

$$I_J(\delta,\{\tau_i\}) = \frac{e\Delta}{2\hbar}\left(\sum_{i=1}^{N}\tau_i\right)\sin(\delta) = \frac{\pi\Delta}{2e}\left(G_0\sum_{i=1}^{N}\tau_i\right)\sin(\delta)\,. \tag{11}$$

The Josephson result (1) is then recovered using the Landauer relation $1/R_N = G_0\sum_{i=1}^{N}\tau_i$. The ballistic limit corresponds to set all transmissions to one and Exp. (9) is in that case equivalent to the result (5) of Beenakker and van Houten. The short and dirty limit follows from (9) using the distribution function $P(\tau)$ of coherent diffusive wires derived by Dorokhov [12] using random matrix theory:

$$P(\tau) = \frac{\ell}{L}\frac{1}{\tau\sqrt{1-\tau}} \text{ for } 4e^{-2L/\ell} \le \tau < 1 \text{ and 0 otherwise.} \tag{12}$$

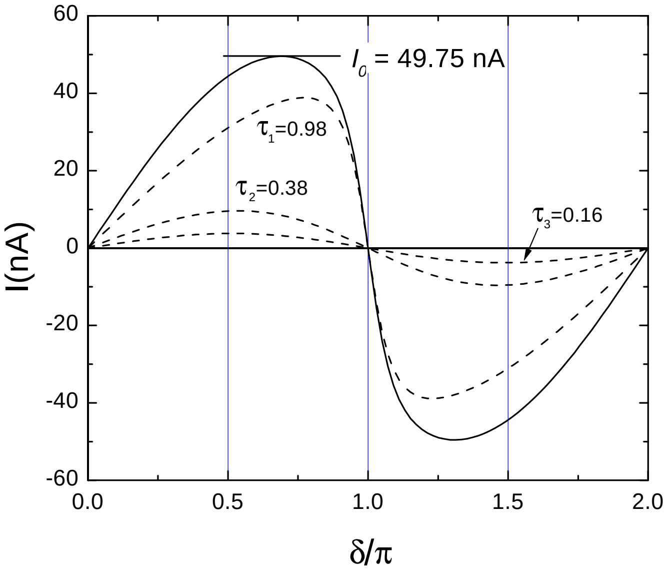

Figure 3: Full line: current-phase relationship of an atomic-size contact with mesoscopic code {0.98,0.38,0.16}. Dashed lines: Current-phase relationship of each conduction. The maximum of this curve is the critical current I_0 of the atomic size contact.

On the experimental side, one thus requires weak links whose channel content is known in order to test the prediction (9). Since quantum point contacts tailored in 2D-electron gas beautifully show quantum quantization in the normal state, this type of mesoscopic structure appears to be an ideal system for that purpose. Superconductivity can indeed be induced in those semiconductor heterostructures by depositing on top superconducting metallic pads. However, because of Shottky barriers, it is difficult to realize good interfaces between the pads and the 2D-electron gas, and the supercurrent through a point contact is then highly dependent on the interface resistance. This is why the first experiments aiming to test the predictions of Exp. (9) have been carried out using superconducting atomic-size contacts.

Figure 3 depicts the current-phase relationship predicted by Exp. (9) for a typical atomic-size contact accommodating three conduction channels. Previously to our work, two sets of experiments, described below, had been performed on superconducting atomic-size contacts [13,14,15].

3.1.3 Previous experiments on superconducting atomic-size contacts

Muller *et al.* [13,14] have measured the critical current I_0 of MCBJs made of several superconducting metals (Nb, Pb, In, Sn and Ta), and covering a wide range of contact sizes, from thousand atom contacts down to a few atom contacts. This corresponds to normal state resistances varying from a few ohms up to tenth of kiloohms. They have determined the effective critical current, defined as the largest supercurrent on the zero voltage branch of the current-voltage characteristics. They observed that, like the conductance, the effective critical current decreases by steps when the break-junction is stretched. The magnitude of the steps is of the order of $e\Delta/\hbar$, which is the predicted change when one channel closes (Exp. (5)). However, for contacts with resistance R_N exceeding $80\,\Omega$, they found in all materials that the $R_N I_0$ product decreases as a function of R_N well below the theoretical predictions (see Figure 4(a)).

Koops, van Duyneveldt and de Bryun Ouboter measured the current-phase relationship of atomic-size contacts by placing a MCBJ in a superconducting loop [15]. An external magnetic field was applied through the loop to induce a phase difference between the two superconducting electrodes of the break-junction. The self-induced magnetic flux $\left\langle \Phi_S \right\rangle = L\left\langle I_S \right\rangle$, where L is here the inductance of the loop containing the MCBJ, was then measured by means of a commercial SQUID magnetometer. Measurements were performed on niobium and tantalum atomic-size contacts. The results demonstrated for the first time the non-sinusoidal behavior of the current phase relationship (see Figure 4(b)). However, their experimental set-up did not allow to measure the current-voltage characteristic, and thus to determine the mesoscopic code of the atomic-size contacts. A quantitative comparison with the predictions (9) was thus impossible.

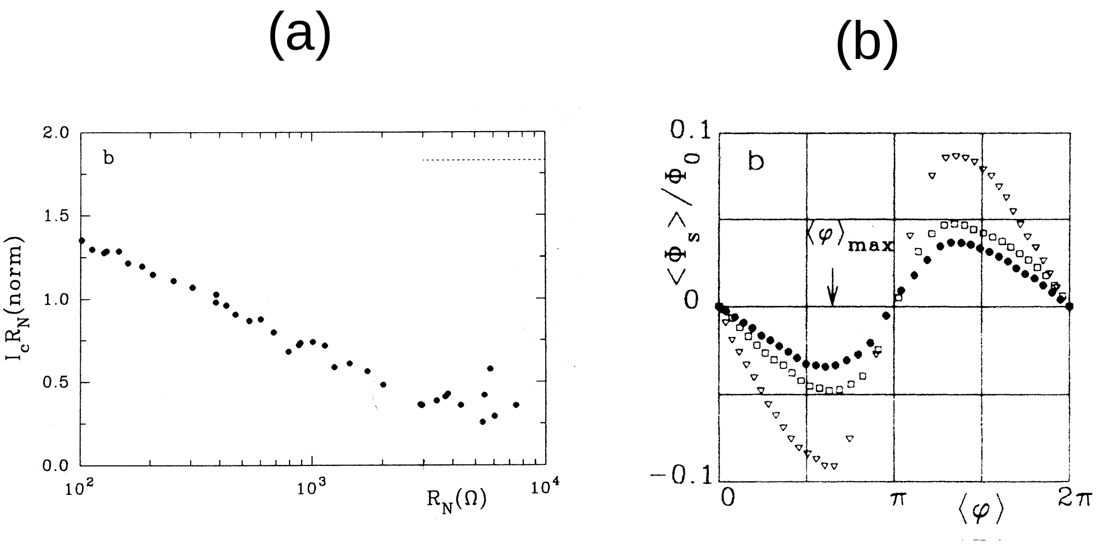

Figure 4: (a) (reproduced from [14]) Symbols: $I_C R_N$ product of niobium MCBJs with decreasing sizes. Dotted line: theoretical prediction of Kulik and Omel'yanchuk for a short ballistic weak link. (b) (reproduced from [15]) Self-induced flux $\langle \Phi_S \rangle = L\langle I_S \rangle$ as a function of the average phase difference $\langle \varphi \rangle$ for three different contact configurations of a niobium MCBJ.

3.1.4 Our experiment on Josephson supercurrent in aluminum atomic-size contacts

We have performed an experiment on aluminum atomic-size contacts in order to test quantitatively the predictions of Exp. (9) concerning the critical current. We made a set-up that allows both to determine the mesoscopic code of the contact and to measure accurately the critical current. We used a four point measurement technique and a current-bias configuration. Figure 5 depicts a typical current-voltage characteristic measured using this circuit. It consists of two distinct branches: a metastable “zero voltage” branch that corresponds to the Josephson supercurrent, and a finite voltage branch called the quasiparticle branch. When the bias-current is increased linearly, the system stays on the zero-voltage branch, till it switches at a current I_s to the quasiparticle branch. This switching is a stochastic process governed by the phase fluctuations controlled by the bias circuit. The switching current is smaller than the critical current, but approaches it if the phase fluctuations are small enough. In this case, the system can reach a stable phase state at a value close to the one that maximizes the supercurrent. For this purpose, we have embedded the break-junction in an on-chip dissipative electromagnetic environment which allows to control phase fluctuations, as previously demonstrated by Vion *et al.* [16,17] for small capacitance tunnel junctions. The measurement of the mean switching current then provides a quantitative test of Exp. (9).

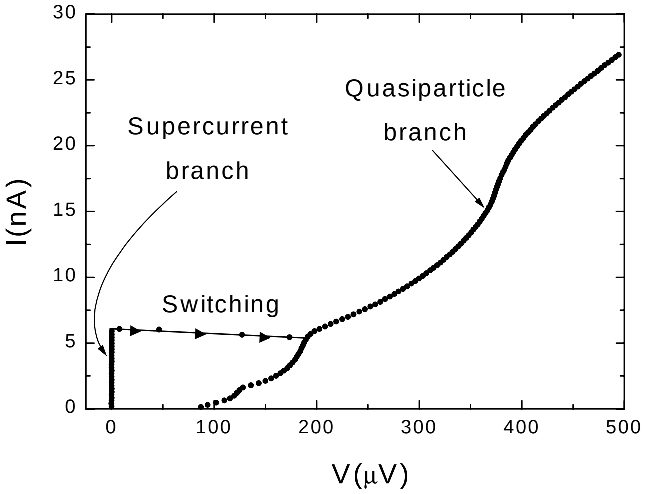

Figure 5: Typical experimental current-voltage characteristic of a superconducting current-biased atomic-size contact. It consists of two branches: the supercurrent branch at nearly zero voltage, and the quasiparticle branch at finite voltage. Upon increasing the bias-current through the contact, the voltage stays close to zero till it jumps to a large value. The current at which switching occurs is the switching current I_s.

3.2 Theoretical analysis of the switching process

The on-chip environment we fabricated consists on each lead of a small resistor, located as close as possible to the contact, and of a large capacitor to the ground plane formed with the metallic substrate (see Figure 5 in Chapter 2, Figure 7(a)). The atomic-size contact is thus unshunted at DC, which allows to measure the current-voltage characteristics. The resistors in series with the capacitors provide a dissipative impedance at finite frequency, which is necessary to observe a well developed supercurrent branch. We discuss in this section the dynamics of the phase in such a dissipative environment, and determine the relation between the switching current and the critical current.

3.2.1 Qualitative description of the phase dynamics of a DC unshunted atomic-size contact

The atomic-size contact in its measurement circuitry can be modeled as an ideal Josephson element characterized by the current-phase relationship (9) in parallel with its capacitance C_J. Using Norton's theorem, the bias-current line as well as the voltage measurement line can be modeled by an ideal current source I_b in parallel with a frequency dependent admittance $Y(\omega)$ which produces a Johnson-Nyquist noise current I_n (see Figure 7(b)). The application of Kirchhoff's laws to this electrical circuit leads to the following Langevin integro-differential equation for the phase difference δ:

$$C_J \varphi_0 \ddot{\delta} + \varphi_0 \int_0^\infty \dot{\delta}(t-\tau) y(\tau) d\tau + I_J(\delta) = I_b + I_n(t) \qquad (13)$$

where $y(\tau)$ is the inverse Fourier transform of $Y(\omega)$. The dynamics of the system is identical to that of a particle with position δ and mass $C_J \varphi_0^2$, in the tilted washboard-like potential $U_0(\delta) = \varphi_0 (I_b \delta - \int_0^\delta I_J(x) dx)$. The amplitude of the oscillating part $-\varphi_0 \int_0^\delta I_J(x) dx$ is the Josephson energy $E_J = \varphi_0 I_0$, and the tilt of the potential is proportional to the bias current I_b. The particle is also submitted to the retarded friction force described by the kernel $\varphi_0^2 y(t)$, and to the random force $\varphi_0 I_n(t)$ resulting from thermal fluctuations in the admittance. We treat here the phase and the current as classical degrees of freedom, and we further assume that the static current-phase relationship can be used when the phase evolves. The classical description for the phase is valid as far as quantum fluctuations are negligible, i.e. when the admittance across the Josephson element is large enough compared to the conductance quantum, as recently proved by Grabert and Ingold [18]. The adiabatic approximation is valid as long as the phase velocity is small enough and will be discussed later on.

In order to get some insight into the dynamics of δ in this classical adiabatic regime, let us first consider the zero temperature case. At zero temperature, the random force $\varphi_0 I_n(t)$ vanishes, and the dynamics of δ is deterministic. If I_b is smaller than I_0, the tilted washboard potential presents locally stable minima in which the particle can be trapped. The phase stays constant, and the voltage is consequently zero. Upon increasing the bias-current I_b, the tilt of the potential increases. When I_b becomes larger than I_0, the wells disappear and the particle runs away. Because the Josephson element is unshunted at DC, the limit velocity is not fixed by the dissipation into the environment, but by the production of quasiparticles.

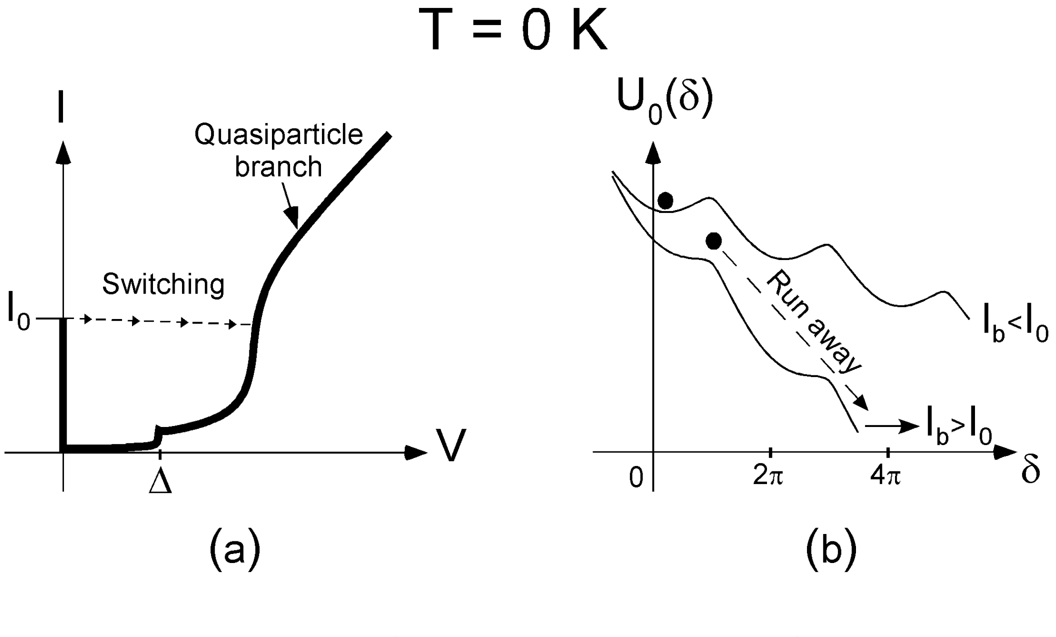

Figure 6: (a) Schematic representation of the current-voltage characteristic of atomic-size contacts at zero temperature. Upon increasing the bias current I_b, the operating point stands on the supercurrent branch for $I_b < I_0$ and on the quasiparticle branch for $I_b > I_0$. (b) Mechanical analog of the two possible dynamical states of the phase at zero temperature. If $I_b < I_0$ (supercurrent branch), the particle is trapped in one of the potential well , while for $I_b > I_0$ (quasiparticle branch) the particle runs away down the potential at constant velocity.

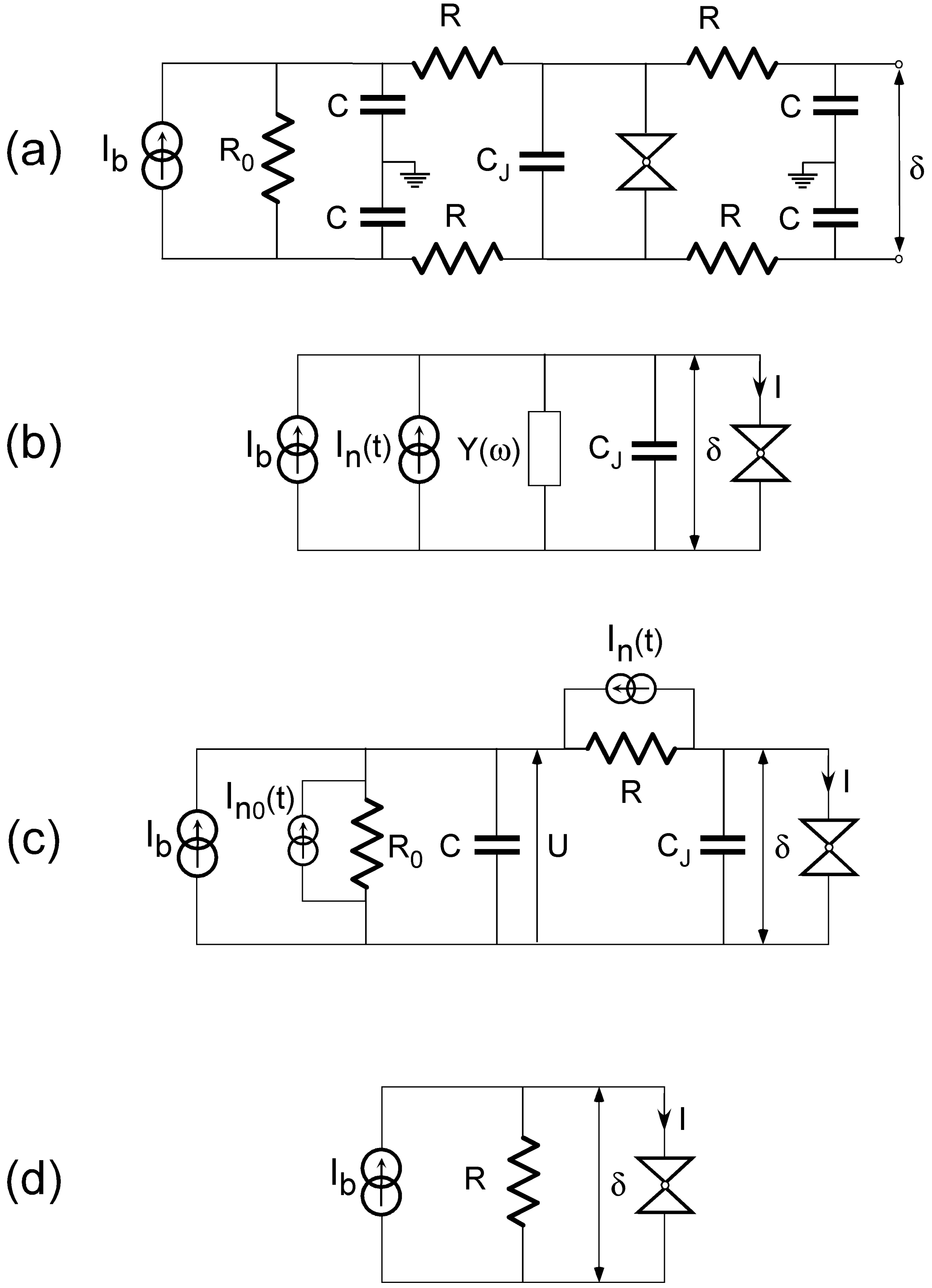

Figure 7: (a) Schematic representation of the atomic-size contact (double triangle symbol) in its on-chip electromagnetic environment characterized by a resistance R and a large capacitor C in each line; R_0 is the impedance of the current source. (b) Using Norton's theorem, the circuit can be modeled by the junction capacitance C_J in parallel with an admittance $Y(\omega)$, a bias current source and a noise current source. Circuit (c), equivalent to circuit (a) , was used for the theoretical calculations. (d) Resistively shunted model for a Josephson element.

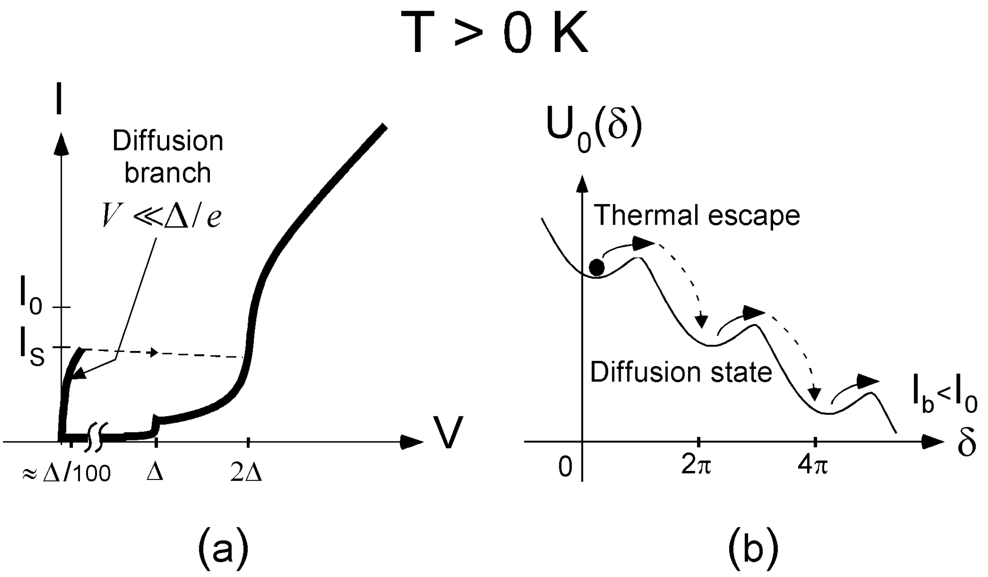

Figure 8: (a) Schematic representation of the current-voltage characteristic of dc-unshunted atomic-size contacts at finite temperature. Due to thermal excitations, the operating point switches from the supercurrent branch to the quasiparticle one at a current I_S smaller than I_0. (b) Mechanical analog of the phase dynamics corresponding to the diffusion branch. The particle being constantly ejected out of the potential wells by thermal excitation, and getting retrapped in a different one because of dissipation, hops diffusively down the potential.

At finite temperature, the phase dynamics is more complex and depends on the dissipation. For atomic-size contacts with a typical critical current of $I_0 \approx 10\,\mathrm{nA}$, the Josephson energy, which sets the scale of the potential wells, is $E_J = \varphi_0 I_0 \approx 0.25\,\mathrm{k_B K}$. Thermal fluctuations play thus an important role in the temperature range 20 mK-1K accessible to the experiment (see Figure 8). In particular, thermal activation of the particle out of the potential well at $I_b < I_0$ occurs on a time-scale shorter than the measurement time. In absence of dissipation, the particle would then run-away, and the system would switch to the quasiparticle branch well before I_b reaches the critical current I_0. However, if dissipation is sufficiently large, the particle can be retrapped in the next potential well. Subsequently, the particle is re-ejected, retrapped in the next well, and so on. This dynamical state in which the particle hops diffusively from a local minimum to next one down the potential is called the diffusion state. The average phase velocity is non zero, but still small: $0 < V = \varphi_0 \langle \dot{\delta} \rangle \ll 2\Delta / e$. Furthermore, this dynamical state is metastable. Indeed, if thermal fluctuations allow the particle to reach a large enough velocity, dissipation is then unable to retrap the particle, and switching to the voltage state occurs. This new switching process is also a thermally activated random process, but with an effective barrier which is much larger than for the escape out of a the potential wells. We have determined the switching rate out of the diffusion state by extending the model of Vion *et al.* [19,20] to atomic contacts.

3.2.2 Solving the phase dynamics

Our measurement set-up can be modeled by the electrical circuit depicted in Figure 7(c). The atomic-size contact, modeled as a pure Josephson element with capacitance C_J, is connected to a current source I_b with internal resistance R_0 through an R-C circuit. The resistances R and R_0 are the sources of thermal fluctuations represented by the Johnson-Nyquist current noise sources I_n and I_{n0}. Introducing the reduced voltage u defined as the ratio between the voltage U across the capacitance C and RI_0, Eq. (13) is equivalent to the following set of dimensionless second order differential equations:

$$\frac{1}{\alpha_0}\frac{d^2\delta}{d\tau}+\frac{d\delta}{d\tau}=u-i_J(\delta)-i_n(t) \tag{14}$$

$$\frac{1}{\alpha_0}\frac{d^2\delta}{d\tau}+\alpha\frac{du}{d\tau}=i_b-\frac{R}{R_0}u-i_J(\delta)+i_{n0}(t), \tag{15}$$

where $\tau = tRI_0/\varphi_0$ is the reduced time, and i_J, i_b, i_n and i_{n0} are reduced currents in units of I_0. The noise currents i_n and i_{n0} are random gaussian variables characterized by their correlation functions $\langle i_n(\tau)i_n(0)\rangle = 2\Theta\delta(\tau)$ and $\langle i_{n0}(\tau)i_{n0}(0)\rangle = 2\Theta R/R_0\ \delta(\tau)$, where $\delta(\tau)$ denotes here the Dirac function, and $\Theta = k_BT/\varphi_0 I_0 = k_BT/E_J$ is the reduced temperature. The parameters $\alpha_0 = \varphi_0/R^2I_0C_J$ and $\alpha = R^2I_0C/\varphi_0$ characterize the damping and control the dynamics of the switching process. Their typical values in our experiment make it possible to greatly simplify Eqs. (14)-(15).

3.2.2.1 Overdamped junction : $\alpha_0 \gg 1$

For atomic-size contacts with I_0 of the order of 10 nA and C_J in the pF range, connected to on-chip resistances of the order of $150\,\Omega$, one has $\alpha_0 \simeq 1300 \gg 1$. In this limit, the $1/\alpha_0 \, d^2\delta/d\tau^2$ terms in Eqs. (14)-(15) can be neglected, which corresponds to neglecting the current flowing through the capacitance compared to that flowing through the admittance $Y(\omega)$. The equations (14) and (15) then become first-order equations:

$$\frac{d\delta}{d\tau} = u - i_J(\delta) - i_n(t) \tag{16}$$

$$\alpha \frac{du}{d\tau} = i_b - \frac{R}{R_0} u - i_J(\delta) + i_{n0}(t). \tag{17}$$

This regime is called the overdamped regime.

3.2.2.2 Adiabatic regime : $\alpha \gg 1$

When the damping is such that $\alpha \gg 1$, the time evolution of *u* is much slower than that of δ. This limit can only be reached by taking C as large as possible since R has to be much smaller than R_Q to avoid quantum fluctuations of the phase. In our experiments, $C = 140\,\text{pF}$ and $R = 125\,\Omega$ or $170\,\Omega$, which results in a typical value $\alpha = 64$ in the first case ($R = 125\,\Omega$) and $\alpha = 80$ in the second case ($R = 170\,\Omega$). The separation between characteristic time scales for δ and u is then large enough to allow for an adiabatic approximation : First, the dynamics of the phase is determined at constant *u*. Then, the dynamics of *u* is calculated using the statistical properties of the phase previously determined. When *u* is constant, the dynamics of δ is governed only by the Langevin equation (16), the dissipative circuit consisting of a pure resistor (see Figure 7 (d)). In the overdamped regime, this model is called the RSJ model and is solvable.

3.2.3 Solving the RSJ model in the overdamped regime

3.2.3.1 Occupation factors of Andreev bound states

For atomic-size contacts, the potential is not the usual tilted sinusoidal potential but has the more general form that follows from the expression of the Andreev state energies:

$$U_p(\delta, \{\tau_i\}) = -u\delta + \frac{\Delta}{E_J} \sum_{i=1}^{N} (n_{i+} - n_{i-}) \sqrt{1 - \tau_i \sin^2(\delta/2)} \,. \tag{18}$$

It is assumed here that the Andreev bound states evolve adiabatically as the phase varies. We will see later that this adiabatic approximation breaks down when the dynamics of the phase is fast enough to induce Landau-Zener transitions between Andreev bound states. The potential depends on the mesoscopic code of the atomic-size contact and on the occupation numbers of the Andreev bound states. Several mechanisms can change these occupation numbers, but they are not very efficient, except one. The relaxation induced by phonons has been addressed in [21]. Following the same hamiltonian approach as in [21] and performing a calculation to first order in the environment impedance, we have found that the relaxation of the upper state by creation of an electromagnetic excitation in the environment is extremely slow, except for highly transmitted channels and at $\delta \sim \pi$. On the other hand, relaxation by exchange of quasiparticles with states in the bulk electrodes is very fast, but only at $\delta = 0$. This process is the dominant thermalization process of Andreev states.

We first consider a simplified model in which the populations of the Andreev bound states are treated in average using their thermal equilibrium values at $\delta = 0$. The corresponding potential U_p is then:

$$U_p(\delta, \{\tau_i\}, T) = -u\delta + \frac{\Delta(T)}{E_J} \tanh(\frac{\Delta}{k_B T}) \sum_{i=1}^{N} \sqrt{1 - \tau_i \sin^2(\frac{\delta}{2})}. \tag{19}$$

We first solve the dynamics of the phase in this potential. We have checked that this time-averaged potential yields results equivalent to those of the full numerical simulations of the Langevin equation (16).

3.2.3.2 Ambegaokar-Halperin like calculation

We have solved Eq. (16) by solving the associated Fokker-Planck equation. We have generalized the procedure introduced by Ambegaokar and Halperin in the case of overdamped Josephson tunnel junctions [22]. In this ensemble formalism, the phase dynamics is described by a probability density $\sigma(\delta, t)$ of finding the value δ for the phase at time *t*. This probability density $\sigma(\delta, t)$ verifies the normalization condition $\int_0^{2\pi} \sigma(\delta, t)\, d\delta = 1$, and the average supercurrent through the Josephson element is $\int_0^{2\pi} \sigma(\delta, t)\, I_J(\delta) d\delta$. When the thermal fluctuations of the phase are large, the probability density is almost constant

($\sigma(\delta) = \text{constant} = 1/2\pi$), and the supercurrent $1/2\pi \int_0^{2\pi} I_J(\delta)d\delta$ is zero because the current-phase relationship is 2π-periodic and even. The conservation of the probability density provides the Fokker-Planck evolution equation [23] for $\sigma(\delta,t)$:

$$\frac{\partial\sigma(\delta,t)}{\partial t} = \frac{\partial}{\partial\delta}\left(\frac{dU_p}{d\delta}(\delta)\sigma(\delta,t) + \Theta\frac{\partial\sigma(\delta,t)}{\partial\delta}\right) \equiv -\frac{\partial J}{\partial\delta}(\delta,t), \tag{20}$$

where J is the probability current. In this equation, the term $dU_p/d\delta\,\sigma$ arises from the deterministic drift, and the term $\Theta\partial\sigma/\partial\delta$ from diffusion. In the steady state, the probability density is time-independent and fulfills the boundary condition $\sigma(0) = \sigma(2\pi)$.

In this case, the solution of Eq. (20) can be explicitly written down:

$$\sigma(\delta) = \frac{J}{\Theta}\frac{S(\delta)}{S(2\pi) - S(0)}\left(S(0)\int_0^{\delta}\frac{dx}{S(x)} + S(2\pi)\int_{\delta}^{2\pi}\frac{dx}{S(x)}\right), \tag{21}$$

where $S(\delta) = \exp(-U_p(\delta)/\Theta)$. The current J is now deduced from Exp. (21) using the normalization condition $\int_0^{2\pi}\sigma(\delta)\,d\delta = 1$.

The mean value of the reduced voltage across the contact $\langle v\rangle = \langle V/RI_0\rangle = \langle \varphi_0\dot{\delta}/RI_0\rangle$ $= \langle d\delta/d\tau\rangle$ is then:

$$\langle v\rangle(u) = 2\pi J = 2\pi\Theta\frac{\exp(2\pi u/\Theta) - 1}{\int_0^{2\pi} S(\delta)\left[\int\limits_0^{\delta}\frac{dx}{S(x)} + \exp(2\pi u/\Theta)\int\limits_{\delta}^{2\pi}\frac{dx}{S(x)}\right]d\delta}. \tag{22}$$

The average supercurrent flowing through the contact is given by $\langle i_J\rangle(u) = u - \langle v\rangle(u)$.

3.2.3.3 Numerical simulation

The dynamics of the phase can also be solved by performing a brute-force numerical simulation of the Langevin equation (16), taking into account the full time dependence of the potential due to changes in the population of the Andreev bound states. The Langevin equation is integrated during a finite time T using a discrete time algorithm with a time-step of length $\tau = T/N$. The stochastic variable δ at time $\tau_{n+1} = (n+1)\,\Delta\tau$ is calculated from its value at time $\tau_n = n\,\Delta\tau$ according to [23]:

$$\delta_{n+1} = \delta_n + [u - i_J(\delta)]d\tau + \sqrt{2\Theta d\tau}\,w_n, \tag{23}$$

where the w_n are independent Gaussian-distributed random variables with $\langle w_n \rangle = 0$ and $\langle w_n w_{n'} \rangle = 2\delta_{nn'}$. The occupation numbers of the Andreev bound-states are drawn according to a thermal distribution when the phase reaches a multiple of 2π. At the end of the simulation, the average velocity of the phase, and thus the mean reduced voltage v, is defined by $\langle v \rangle(u) = \delta_N / T$. The simulation time T is taken long enough in such a way that $\langle v \rangle(u)$ reaches a steady value. The average supercurrent is then $\langle i_J \rangle(u) = u - \langle v \rangle(u)$.

3.2.3.4 Current-voltage characteristic of a resistively shunted atomic contact

We have calculated the current-voltage characteristic of a resistively shunted superconducting atomic contact using the two procedures previously described. A set of characteristics at different temperatures obtained by solving the Fokker-Planck equation is shown in Figure 9 in the particular case of a three channel contact. Note that in this resistively shunted scheme, no switching occurs. The results closely reproduce the characteristics of Josephson tunnel junctions: The supercurrent branch is a supercurrent peak which is progressively washed out and widened as the temperature is increased. In particular, the maximum supercurrent I_{MAX} decreases progressively starting from the critical current at zero temperature. These general features are independent of the mesoscopic PIN code $\{\tau_1, ..., \tau_N\}$. Numerical simulations that take into account the evolution of the Andreev bound-states occupation numbers, lead to almost perfectly identical results.

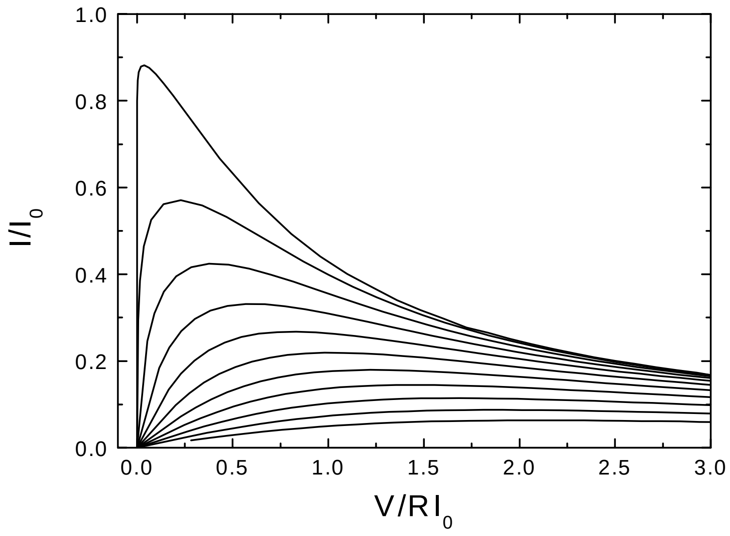

Figure 9: Calculated current-voltage characteristics of an atomic-size contact with mesoscopic PIN code {0.46,0.18} for equally spaced temperatures ranging from (from top to bottom) 10 mK to 800 mK. The maximum supercurrent is $I_0 = 16\ \text{nA}$ and the Josephson energy $E_J = 0.381\, k_B \text{K}$.

3.2.3.5 Temperature dependence of the supercurrent peak height

The maximum supercurrent I_{MAX} as a function of temperature is plotted in reduced units in Figure 10 for the set of current-voltage characteristics shown in Figure 9. We have similarly determined the temperature dependence of the maximum supercurrent for a large palette of mesoscopic codes, and compared to the case of tunnel junctions with the same critical current. The deviations are very small: the current-voltage characteristic mainly depends on the critical current, and is not very sensitive to the potential shape.

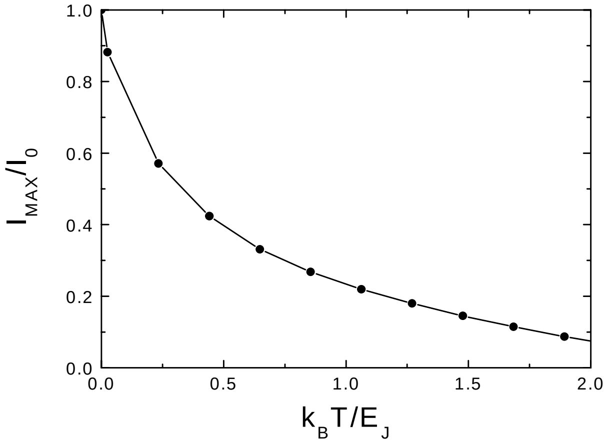

Figure 10: Dots: Maximum of the supercurrent peak I_{MAX} of the characteristics presented in Figure 9 as a function of temperature. The critical current is $I_0 = 16\ \mathrm{nA}$ and the Josephson energy $E_J = 0.381\,\mathrm{k_B K}$. The line connecting the dots is just a guide for the eyes.

3.2.4 Current-voltage characteristics of RC shunted atomic contacts in the overdamped regime

In the overdamped regime $\alpha \gg 1$, the voltage across the large capacitor evolves slowly and the current through the atomic contact is at a given time determined by the parameterized current-voltage characteristic solution of Eq. (16). If one neglects the fluctuations of u, a static solution can be determined graphically. From Eq. (17), it follows that such a static solution satisfies the equation $i_b - R/R_0\,u - \langle i_J\rangle(u) = 0$. Since $u = \langle i_J\rangle(u) + \langle v\rangle(u)$, the average current and voltage thus verify the equation $i_b - R/R_0\langle v\rangle = (1 + R/R_0)\langle i_J\rangle(u)$. In the current bias mode, $R_0 \gg R$ and thus the static solution can be graphically determined by the intersection between the load line defined by $i_b - R/R_0\langle v\rangle = \langle i_J\rangle$ and the current-voltage characteristic solution of Eq. (16). When the slope of the load line R/R_0 is small and the bias-current large enough, there are three solutions, as shown in Figure 11. The stable solutions labeled (S) and (M) correspond respectively to the running state (large voltage) and to the diffusion state (small voltage). The solution at intermediate voltage (U) is unstable. In this model, the maximum supercurrent is obtained when the load-line is tangent to the current-voltage characteristic.

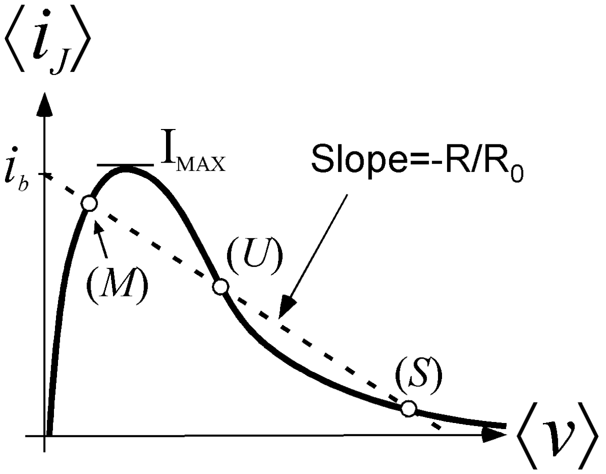

Figure 11: Geometric construction yielding the average current and voltage for a given current bias. Full line: Schematic representation of an *IV* characteristic corresponding to the RSJ model. Dashed line: load line defined by $\langle i_J \rangle = i_b - R/R_0 \langle v \rangle$.

When fluctuations are taken into account, the diffusion state (M) becomes metastable, and the system can switch out of the diffusion state prior to reaching the maximum supercurrent I_{MAX} of the static solution. The switching rate can be inferred from the slow evolution of u. For that purpose, the supercurrent $i_J(\delta)$ in Eq. (17) is decomposed into a mean value $\langle i_J \rangle(u)$ and a fluctuating part $\eta(u,t)$, whose statistical properties are calculated assuming the voltage u is constant. One then obtains the following Langevin equation for u:

$$\alpha \frac{du}{d\tau} = i_b - \frac{R}{R_0} u - \langle i_J \rangle(u) - \eta(u,t) + i_{n0}(t). \qquad (24)$$

This equation corresponds to the motion of a massless particle at position u, submitted to a deterministic force $F(u) = i_b - R/R_0\, u - \langle i_J \rangle(u)$, a drag force $-\alpha\, du/d\tau$, and to a position dependent random force $\xi(u,t) = -\eta(u,t) + i_{n0}(t)$. The problem is then reduced to the escape of a diffusing particle above an effective potential barrier $-\int F(u)du$. At a given bias-current i_b, the escape rate $\Gamma(i_b)$ of u above this barrier follows a Kramers law [24]:

$$\Gamma(i_b) = \frac{D(u_t)}{2\pi} \sqrt{\left(\frac{-F}{\alpha D}\right)'_{u_b} \left(\frac{-F}{\alpha D}\right)'_{u_t}}\ \exp(B), \qquad (25)$$

where $D(u) = 1/\alpha^2 \int_0^\infty \xi(u,0)\xi(u,t)dt$ is a position-dependent diffusion coefficient associated to the random force and $B = \int_{u_b}^{u_t} F(u)/\alpha D(u)du$, u_b and u_t corresponding respectively to the bottom and to the top of the effective potential barrier. In the case of a sinusoidal current-phase relationship, the escape rate is easily computed because both the average current $\langle i_J \rangle (u)$ and the diffusion coefficient $D(u)$ are known analytically [20]. The main result of the calculation is that the exponent B is proportional to the damping coefficient: $B \propto \alpha$. As expected, the static solution corresponds to the infinite α limit.

The switching histograms obtained when a bias-current ramp is applied are then easily determined. The probability to switch at a given current $P(I)$, is related to the escape rate $\Gamma(I)$ and to the sweeping rate $S = dI_b/dt$ by the relation:

$$P(I) = S^{-1} \frac{\Gamma(I)}{1 - \int_0^I P(u)du}. \qquad (26)$$

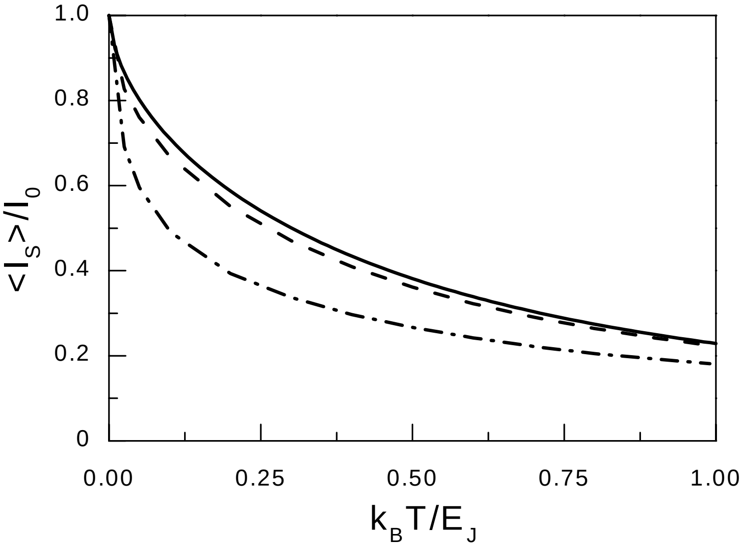

Figure 12: Predicted average switching current $\langle I_S \rangle$ as a function of temperature for three values of the damping parameter. The curves are calculated at $dI_b/I_0dt = 500\ s^{-1}$. Full curve: RSJ model corresponding to the $\alpha = \infty$ limit. Dashed curve: $\alpha = 100$. Dashed-dotted curve: $\alpha = 10$.

The mean value $\langle I_S \rangle$ of the switching histograms is plotted in Figure 12 for three values of the damping parameter α. For $\alpha = 100$, the mean switching current is close to the maximum supercurrent in absence of fluctuations (infinite damping limit), whereas, for $\alpha = 10$, it is significantly reduced. The average switching current thus provides non-ambiguous informations on the maximum supercurrent only in the large α regime.

For atomic-size contacts containing only weakly transmitted channels (typically all transmissions smaller than 0.5), the energies of the Andreev bound states are very close to be a cosine function, and thus the above calculation provides a good approximation for the switching rate. In the more general case of the non-cosinusoidal potential shape, no such quasi-analytical solution is available. However, since the dynamics of the phase in the RSJ model is not really sensitive to the deviation from the cosinusoidal behavior, we expect even smaller corrections for the slow dynamics of u. Furthermore, the typical sweeping rates used of to measure the switching histograms, and the typical damping parameters of our atomic-size contacts (see Table 1 in the following section) are close to the parameters used to calculate the dashed curve in Figure 12: $dI_b / I_0 dt = 500\ s^{-1}$ and $\alpha = 100$. Our measurements were thus taken in the strong damping regime, where the mean switching current is close to the maximum value I_{MAX} of the RSJ model, and the switching histograms narrow. In this regime, the small effect of thermal fluctuations on the switching can be accurately estimated using an effective cosinusoidal potential approximation.

3.3 Measurement of the maximum supercurrent

3.3.1 Measuring switching current histograms

We have measured the mean value of the switching current $\langle I_S \rangle$, obtained from switching current histograms, as a function of temperature and for different contact configurations. We have performed two runs on two different aluminum break-junction samples whose characteristics are presented in the left column of Table 1.

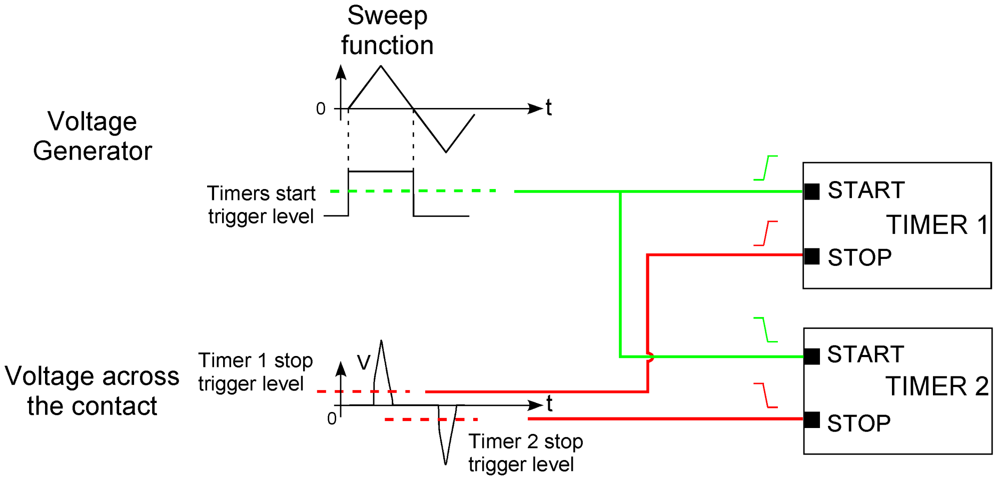

Figure 13: Schematic representation of switching current measurement set-up. The TTL synchronization signal of the voltage generator sets the start of both timers. The stop signal is provided by the voltage across the sample after amplification.

Histograms of the switching current I_S were obtained from 7640 switching events. The contact was current-biased using a HP3325 voltage source in series with a bias resistor R_0. The sweeping function had a triangular shape and the typical sweep frequency was $100\,\mathrm{Hz}$. The typical reduced sweep rate was $dI/I_0dt = 500\,s^{-1}$. Two timers (Philips PM6654C and Fluke PM6680B) measured the elapsed time between the beginning of the ramp and the switching event characterized by a sudden and strong change of the voltage across the contact. Both polarities: $I > 0$ and $I < 0$ were measured to compensate for offsets in the bias-current line. The start signal was the TTL synchronization signal of the voltage source, and the stop signal the voltage across the contact (see Figure 13) after amplification by a low-noise pre-amplifier (NF). The timers can store 764 events, and a series of ten such packets was measured to produce histograms. Simultaneously, the average time evolution of the current $I(t)$ through R_0 was measured. The averaging was done over 100 traces on a Nicolet Pro 44 oscilloscope. The $I(t)$ curve as well as the switching time records were transferred through a IEEE data link to a PC for post-treatment. From the linear fit of the $I(t)$ curve part before the switching event, the two time records were converted into two current records. The mean value of the two corresponding current histograms were equalized, leading to the average switching current $\langle I_S \rangle$. The standard deviation ΔI_S was calculated from the standard deviation of the two histograms.

The following table reviews, for each sample, the selected atomic-size contacts whose switching current measurements are presented and discussed in this chapter as well as their main characteristics: critical current I_0, corresponding Josephson energy E_J, and damping parameter α.

	Mesoscopic PIN code	$\boldsymbol{I_0}$**(nA)**	$\boldsymbol{E_J/k_B}$**(mK)**	$\boldsymbol{\alpha = R^2 I_0 C/\varphi_0}$
Sample #1 $\Delta = 178 \pm 1\ \mu\text{eV}$ $R = 125 \pm 10\ \Omega$ $C = 140 \pm 10$ pF	{0.21,0.07,0.07}	8.0 ± 0.1	190 ± 2	$55 \pm 20\%$
	{0.52,0.26,0.26}	25 ± 0.4	600 ± 10	$170 \pm 20\%$
	{0.95,0.09,0.09,0.09}	39 ± 0.2	925 ± 5	$260 \pm 20\%$
	{0.98,0.21,0.15,0.14}	46 ± 0.4	330 ± 10	$300 \pm 20\%$
	{0.998,0.09,0.09,0.09}	44 ± 0.9	1050 ± 20	$294 \pm 20\%$
Sample #2 $\Delta = 184.5 \pm 1\ \mu\text{eV}$ $R = 170 \pm 20\ \Omega$ $C = 140 \pm 10$ pF	{0.33,0.13,0.12}	14 ± 0.2	330 ± 5	$170 \pm 30\%$
	{0.78,0.12,0.12}	29 ± 0.4	690 ± 10	$360 \pm 30\%$
	{0.92,0.02,0.02}	33 ± 0.4	800 ± 10	$410 \pm 30\%$

Table 1: Characteristic parameters of the atomic size contacts discussed in this chapter. Two runs involving two different samples have been performed. The first column indicates the superconducting gap Δ of the aluminum electrodes and the environment parameters R and C. The uncertainties on the critical current I_0 are evaluated following the procedure described at the end of Chapter 1.

3.3.2 Atomic contacts with not too high transmission probabilities ($\tau < 0.9$)

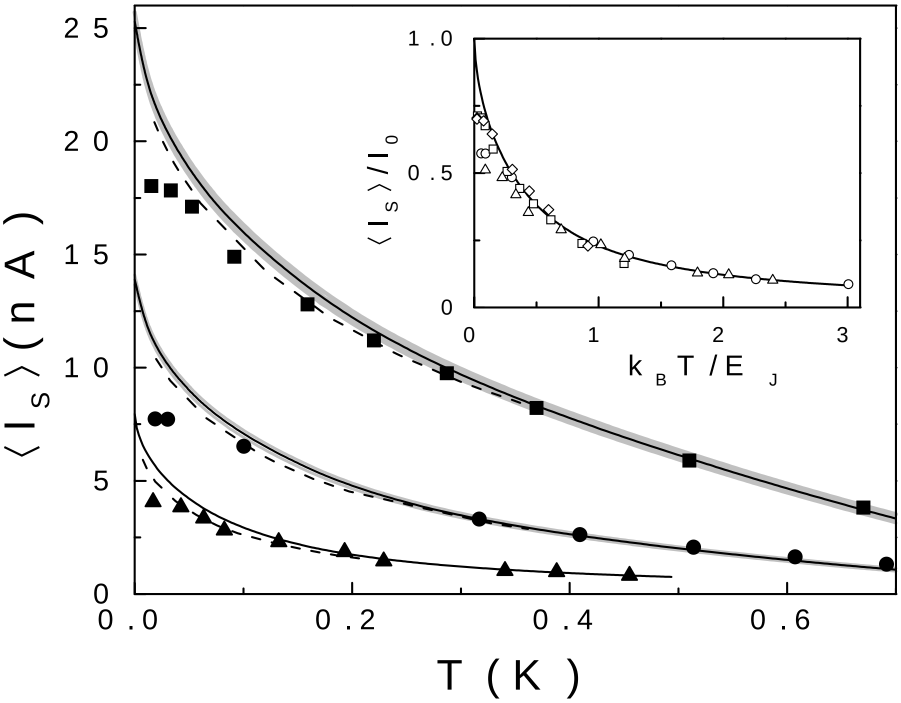

Figure 14: Main panel: Mean switching current as a function of temperature for three atomic size contacts (symbols) . Mesoscopic PIN codes: {0.52,0.26,0.26} (squares), {0.33,0.13,0.12} (circles), {0.21,0.07,0.07} (up-triangles). The full lines are the prediction of the $\alpha \to \infty$ adiabatic theory described above, and the dashed line that of the finite α theory using the independently measured mesoscopic codes. The grey area represent the fuzziness on the theoretical curves due to the uncertainties in the determination of the mesoscopic code (too thin to be visible for the lowest curve). Inset: same contacts plus contact {0.78,0.12,0.12} (diamonds). Mean switching current in units of I_0 versus $k_B T / E_J$. Full curve: Ambegaokar-Halperin result (RSJ model in the tunnel limit).

The mean switching current is plotted in Figure 14 as a function of temperature for three atomic-size contacts, together with the theoretical predictions of the adiabatic theory described in the preceding section. All those contacts have channels with transmissions probabilities smaller than 0.9. The data at high temperature are well explained by the $\alpha \to \infty$ limit of the theory that corresponds to the RSJ model. Moreover, the finite α corrections calculated assuming a cosinusoidal potential shape explain the small deviations at intermediate temperature. We found a similar quantitative agreement for all measured contacts provided no well transmitted channel ($\tau > 0.9$) is present. At the lowest temperatures, the data deviate markedly from the predictions. As explained in the article (see the Annex), we attribute this deviation to the saturation of the electronic temperature in the resistors.

The inset in Figure 14 depicts the same data in reduced units (I_0 for the currents, and E_J / k_B for the temperatures). In this reduced plot, the temperature dependence appears universal and very close to the Ambegaokar and Halperin maximum current for the RSJ model. This means that the non-cosinusoidal shape of the potential does not affect quantitatively the dynamics of the phase. Indeed, the thermal escape rate from a potential well mainly depends on the energy barrier height rather than on its exact shape.

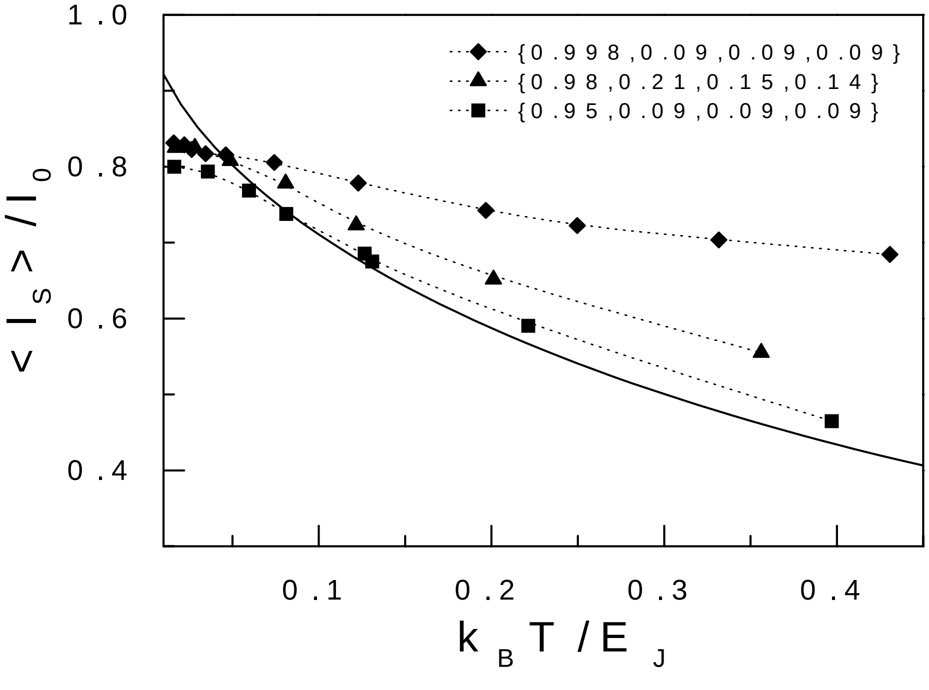

Figure 15: Symbols: Average reduced switching current as a function of reduced temperature $k_B T / E_J$ for three atomic-size contacts containing a well transmitting channel ($\tau > 0.9$). The dotted curves are guide for the eyes. Full curve: Ambegaokar-Halperin result (RSJ model in the tunnel limit).

3.3.3 Atomic contacts with high transmitting channels ($\tau > 0.9$): the ballistic limit

For atomic-size contacts containing well transmitted conduction channels $\tau > 0.9$, the data deviate markedly from an universal behavior, as depicted in Figure 15 for three such contacts. One of them contains an almost ballistic channel with transmission probability $\tau = 0.998$ (subsequently called “0.998 contact”). A second one has a highest transmission of 0.98 (“0.98 contact”). The last one has a highest transmission $\tau = 0.95$ (“0.95 contact”). The mean switching current of these three contacts is more temperature resilient and, but at very low temperature, larger than predicted by the adiabatic model for the Andreev states. The higher the transmission probability, the tougher the resistance to thermal fluctuations is: Over the whole range of explored temperatures, the switching current of the 0.998 contact is larger than that of the 0.98 contact, which is larger than that of the 0.95 contact.

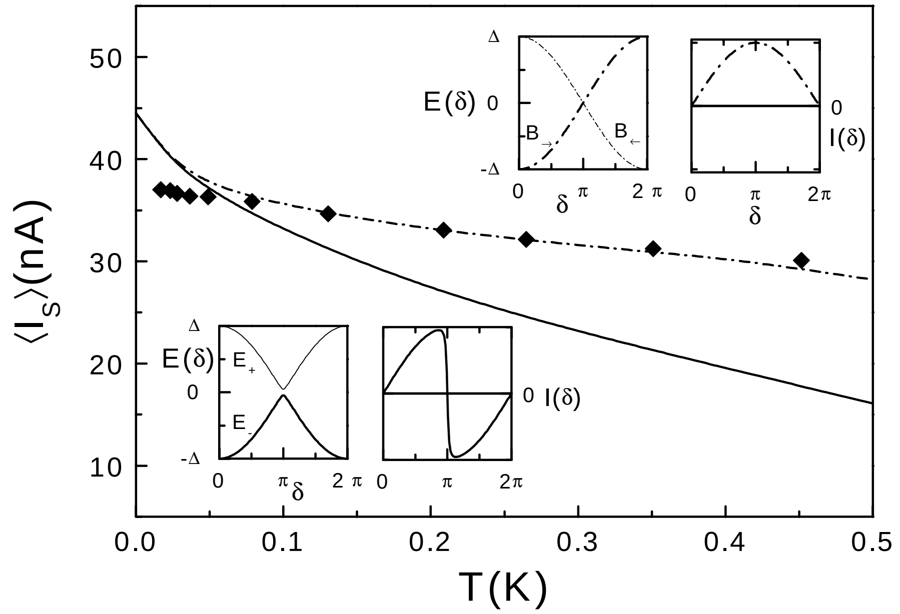

Figure 16: Diamonds: measured mean switching current of the 0.998 contact (Mesoscopic PIN code: {0.998,0.09,0.09,0.09}). Full curve: prediction of the adiabatic theory. Dashed-dotted curve: prediction assuming a perfect transmission $\tau = 1$. Insets: Andreev bound states energy spectrum and current-phase relationship at zero temperature of one conduction channel with transmission probability 0.998 (bottom) and 1 (top).

The experimental results on the 0.998 contact are well explained by assuming a perfect transmission for this conduction channel. At perfect transmission, the potential is qualitatively modified since the lower Andreev state E_- at zero phase evolves adiabatically into the upper energy Andreev E_+ when the phase goes through the level crossing. This state is a ballistic state $B_\rightarrow$ (see Appendix B and the upper inset in Figure 16) whose current flows in the same direction for all values of the phase. As a result, the maximum supercurrent is strongly resilient to thermal fluctuations, as long as the other ballistic Andreev state $B_\leftarrow$ is not equally populated. Quantitatively, the shape of the potential is modified as shown in the insets of Figure 16. The average switching current, calculated in the overdamped regime for this potential, is then in good agreement with our experimental results as can be seen in the main panel of Figure 16.

The perfect transmission hypothesis is in fact not strictly speaking necessary, since the assumption that the system undergoes at $\delta = \pi$ a transition from the lower Andreev bound state E_- up the upper one E_+ with probability one would be equivalent. This transition could be interpreted in terms of a Landau-Zener like transition [25] induced by the fast dynamics of the phase at the level crossing.

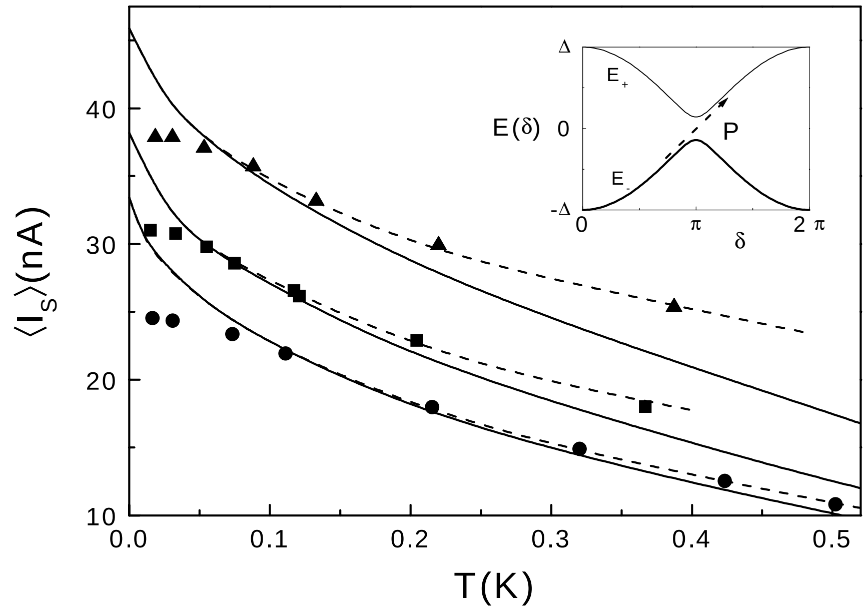

Figure 17: Mean switching current as a function of temperature. Symbols: experimental results for three atomic-size contacts. Mesoscopic PIN codes: {0.98,0.21,0.15,0.14} (up-triangles), {0.95,0.09,0.09,0.09} (squares), {0.92,0.02,0.02} (circles). Full curves: adiabatic theory. Dashed curves: theoretical predictions assuming a Landau-Zener transition at π with probability P between the two Andreev bound states of the high transmitting channel. From top to bottom: $P = 0.80, 0.40, 0.15.$ Inset: schematic representation of the Landau-Zener transition.

We have tried to fit the measurements for atomic-size contacts containing a highly transmitting channel by introducing a Zener-like transition rate at the level crossing occurring at $\delta = \pi$. When the transmission decreases, the minimum energy gap $2\Delta\sqrt{1-\tau}$ between the two Andreev bound states increases, and the transition probability is lower. In the numerical simulations discussed in section 3.2.3, we have implemented a temperature independent transition probability P between the two levels at $\delta = \pi$. Each time δ crosses π , the Andreev state occupations are refreshed according to this transition probability. The experimental results for the 0.98 contact are well fitted assuming a transition probability $P = 0.80$. For the 0.95 contact, we found $P = 0.40$, and for the 0.92 contact presented in Figure 4 of the article (see the Annex) $P = 0.15$.

The standard Landau-Zener theory can be used to determine the transition probability at a level crossing when a parameter of the hamiltonian is swept at constant velocity. In our set-up, the phase is a dynamic variable whose evolution depends on the current through the contact. One can nevertheless use the Landau-Zener theory to check if the adiabaticity hypothesis is valid. Assuming indeed that no transition occurs at a level-crossing, the phase evolution can be simulated, and the adiabaticity criterion checked. The transition probability p_z between the two Andreev bound states of a single conduction channel with transmission τ is:

$$p_z = \exp\left(-\pi\Delta\left(1-\tau\right)/\hbar v\right) \tag{27}$$

where v is the phase sweep velocity. The relevant velocity is the velocity of the phase at $\delta = \pi$ for the bias current at which the switching event occurs, which is of the order of $\varphi_0^{-1} R I_0(\tau)$ where $I_0(\tau)$ is given by Exp. (10). When this velocity is injected in (27), one finds that the adiabaticity criterion is not fulfilled for the 0.98 contact: the adiabatic approach is thus non valid, and a full dynamical approach is necessary. The probability p_Z one estimates assuming that the phase dynamics is the same as in absence of Zener transitions is nevertheless of the same order of magnitude than the probability P injected by hand. For the $\tau = 0.95$ contact, one finds at the opposite that the adiabaticity criterion is fulfilled, and that no Zener transitions should occur. The observation of a large transition probability in this contact is thus in contradiction with the model. A rigorous theory, in which the phase and the internal degrees of freedom of the contact would be treated together, is clearly lacking. Our results have already inspired a reinvestigation of the Zener effect [26], but the problem is presently beyond reach of existing theories. Experimentally, a direct measurement of the current through the contact with a phase imposed would probe the Andreev states at equilibrium, which would circumvent the difficulties arising from the complex dynamics of the system in a current-bias configuration.

3.4 Conclusions

The maximum supercurrent through current-biased superconducting atomic-size contacts embedded in a dissipative circuit is in quantitative agreement with the theoretical predictions based on the Andreev bound states, for a large palette of mesoscopic codes, over a wide temperature range. The departures from the theoretical predictions lie within the error bar due to the imperfect determination of the mesoscopic codes. When highly transmitted channels are present, we could probe quantitatively the predictions only for the perfectly transmitted ballistic channel case because the relationship between the critical current and the measured switching current is not well established when the Andreev state dynamics departs from adiabaticity. In the non-adiabatic regime, we have accounted for the experiments by introducing a transition probability at the level crossing which remains to be explained.

Annex: Article published in Physical Review Letters

We reproduce here an article published in Physical Review Letters presenting our measurements of the supercurrent through atomic-size contacts.

Supercurrent in Atomic Point Contacts and Andreev States

M. F. Goffman,[1] R. Cron,[1] A. Levy Yeyati,[2] P. Joyez,[1] M. H. Devoret,[1] D. Esteve,[1] and C. Urbina[1]
[1]*Service de Physique de l'Etat Condensé, CEA-Saclay, F-91191 Gif-sur-Yvette Cedex, France*
[2]*Departamento de Física Teórica de la Materia Condensada C-V, Universidad Autónoma de Madrid, E-28049 Madrid, Spain*

(Received 13 December 1999)

We have measured the supercurrent in aluminum atomic point contacts containing a small number of well characterized conduction channels. For most contacts, the measured supercurrent is adequately described by the opposite contributions of two thermally populated Andreev bound states per conduction channel. However, for contacts containing an almost perfectly transmitted channel $0.9 \leq \tau \leq 1$ the measured supercurrent is higher than expected, a fact that we attribute to nonadiabatic transitions between bound states.

PACS numbers: 73.40.Jn, 73.20.Dx, 74.50.+r

In 1962, Josephson predicted that a surprisingly large supercurrent could flow between two weakly coupled superconducting electrodes when a phase difference δ is applied across the whole structure. This phase-driven supercurrent $I(\delta)$ has subsequently been observed in a variety of weak coupling configurations such as thin insulating barriers, narrow diffusive wires, and ballistic point contacts between large electrodes. However, a theoretical framework powerful enough to predict the current-phase relation $I(\delta)$ in all configurations has emerged only during the last decade [1]. It applies in the mesoscopic regime, when electron transport between the electrodes is a quantum coherent process. Such transport is described by a set of N transmission coefficients $\{\tau_i\}$ corresponding to N independent conduction channels. In the normal state, the conductance is given by $G_0 \sum_{i=1}^{N} \tau_i$ where $G_0 = 2e^2/h$ is the conductance quantum. In the superconducting state, electrons (holes) transmitted in one channel are Andreev reflected at the electrodes into holes (electrons) in the same channel. After a cycle involving two reflections at the electrodes, they acquire at the Fermi energy an overall phase factor $\pi + \delta$ (Fig. 1). In a "short" coupling structure, these cycles give rise to two electron-hole resonances per channel, called Andreev bound states (AS) [2] with energies $E_{\pm}(\delta, \tau_i) = \pm\Delta[1 - \tau_i \sin^2(\delta/2)]^{1/2}$ (Δ is the energy gap in the electrodes). These two AS carry current in opposite directions, $I_{\pm}(\delta, \tau) = \varphi_0^{-1}\, dE_{\pm}(\delta, \tau_i)/d\delta$ (where $\varphi_0 = \hbar/2e$), and the net supercurrent results from the imbalance of their populations. A quantitative comparison of the predictions of this "mesoscopic superconductivity" picture of the Josephson effect with experimental results is usually hindered by the fact that in most devices the current flows through a very large number of channels with unknown τ_i. However, an atomic-size constriction between two electrodes, referred to hereafter simply as an atomic contact [3], is an extreme type of weak coupling structure which accommodates just a few channels. Because their set $\{\tau_i\}$ is amenable to a complete experimental determination and because it can be controlled in a certain range [4], atomic contacts are ideal systems on which to test quantitatively the concepts of mesoscopic physics. The knowledge of $\{\tau_i\}$ allows in principle the calculation of all transport quantities. In particular, the phase-driven supercurrent is given by

$$I_J(\delta, \{\tau_i\}, \{n_{i\pm}\}) = \sum_{i=1}^{N} (n_{i-} - n_{i+}) I_{-}(\delta, \tau_i), \quad (1)$$

where $n_{i\pm}$ are the occupation numbers of the two AS associated with the ith channel. The critical current of the contact is the maximum of this current-phase relationship at zero temperature $I_0(\{\tau_i\}) = \max_{\delta}[I_J(\delta, \{\tau_i\}, n_{i+} = 0, n_{i-} = 1)]$. In this Letter, we present an

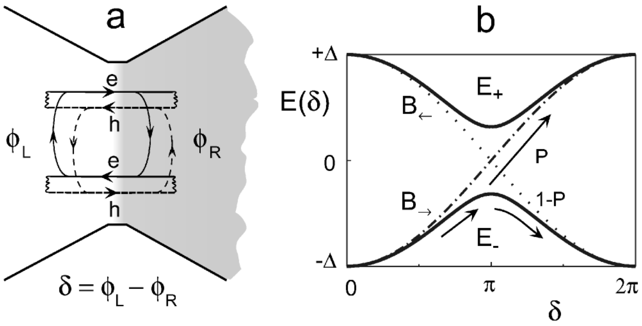

FIG. 1. (a) Josephson coupling through a single channel of transmission τ between two superconducting electrodes with phase difference $\delta = \phi_L - \phi_R$. Wavy lines represent Andreev scattering mechanism: electrons (holes) are reflected as holes (electrons) at the electrodes. Upward and downward arrows represent normal scattering, which couples electron (hole) states with backward electron (hole) states. (b) Combination of both scattering mechanisms results in two "Andreev bound states" with phase dependent energies $E_{\pm}$ (full lines). Gap at $\delta = \pi$ is $2\Delta\sqrt{1 - \tau}$. P is interlevel nonadiabatic transition probability at $\delta = \pi$. Dash-dotted (dotted) line is $B_{\rightarrow}(B_{\leftarrow})$ ballistic state for $\tau = 1$, carrying current towards the right (left).

experiment on aluminum atomic contacts in which we compare the measured supercurrent with the predictions of this mesoscopic Josephson effect theory.

In practice the measurement of a supercurrent is not done by imposing a phase difference across the device [5] but by biasing it with a dc current and detecting the maximum current at zero voltage. As the Josephson coupling introduced between the two electrodes by a single channel of transmission τ has a small characteristic energy $E_J = \varphi_0 I_0(\tau) \leq \varphi_0 I_0(\tau = 1) = \Delta/2$ (for Al, $E_J \leq 1 k_B K$), the phase difference δ is prone to both quantum and thermal fluctuations, which depend not only on the parameters of the contact but also on the circuit in which the contact is embedded. In fact, unless this electromagnetic environment is carefully designed so as to damp phase fluctuations [6], the supercurrent time averages to nearly zero and the observed maximum supercurrent is much smaller than I_0 [3]. We have thus integrated microfabricated mechanically controllable break junctions [7] into an adequate on-chip dissipative environment (see Fig. 2). Current-voltage characteristics (IV) were measured using a four-probe geometry. Each line contains a small resistor close to the atomic contact, and also a large capacitor to the underlying ground plane formed by the substrate. The equivalent circuit of the setup is shown in the right inset of Fig. 2. The atomic contact is characterized by (1) and its capacitance C_J. It is connected through a resistor R to a current source I_b in parallel with a capacitance C. We now concentrate on one-atom aluminum contacts which typically accommodate three channels and have a conductance of order G_0 [4]. A typical IV measured at the lowest temperature is shown in Fig. 3. The strong nonlinearities in the finite voltage (dissipative) branch are associated [8] with multiple Andreev reflection processes and allow the determination of $\{\tau_i\}$ [4]. The supercurrent branch appears on large voltage scales as a vertical line at $V \sim 0$. However, the upper inset of Fig. 3 shows that for finite current there is always a finite voltage across the contact. When the bias current is ramped repeatedly, the system switches to the dissipative branch at a value I_s which fluctuates from cycle to cycle. The slope of the supercurrent branch and the average switching current $\langle I_s \rangle$ both decrease when increasing the temperature.

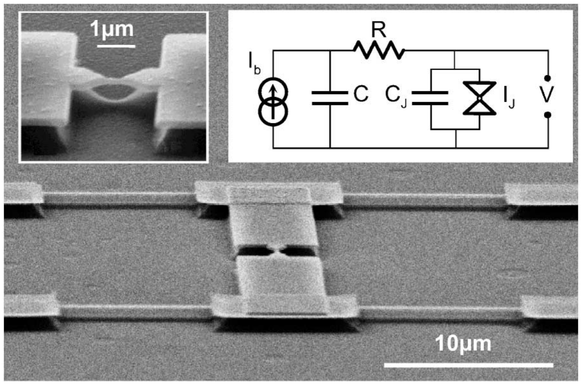

FIG. 2. Micrograph of Al microbridge in a dissipative environment. Each IV probe contains a AuCu (weight ratio 3:1) resistor (10 μm-long, 500 nm wide, and 30 or 50 nm thick) and a large (2.5 mm$)^2$, 180 nm thick AuCu/Al pad (not shown) that forms with the metallic substrate a large capacitor. Substrate is phosphor-bronze covered by a 2 μm thick layer of polyimide. Left inset: side view of bridge (150 nm thick Al layer with 100 nm wide constriction in the middle) suspended by selective etching of polyimide. Bridge is broken by controlled bending of the substrate at low temperatures ($T < 1$ K) and under cryogenic vacuum to prevent contamination of the two resulting electrodes. Right inset: equivalent circuit. The atomic contact (double triangle symbol) is connected to a current source through a resistor R. The capacitors on each line combine into the capacitor C. Total capacitance between the two sides of the bridge is C_J. The voltage V across the contact is related to the phase velocity through the Josephson relation $\varphi_0 \dot{\delta} = V$.

Given the simplicity of the biasing circuit, the exact shape of the supercurrent branch can be calculated. Following the analysis of [6] the circuit is described by two dynamical variables, δ and u (the ratio between the voltage across the capacitor C and RI_0), and three environment parameters: a characteristic time $t_J = \varphi_0/RI_0$ and the damping factors $\alpha_0 = \varphi_0/R^2 I_0 C_J$ and $\alpha = R^2 C I_0/\varphi_0$. For all the measured contacts the environment parameters were chosen such that $\alpha_0 \gg 1$ [9], and the current through C_J can thus be neglected. In this classical regime, the time evolution of the circuit is governed by two dimensionless equations,

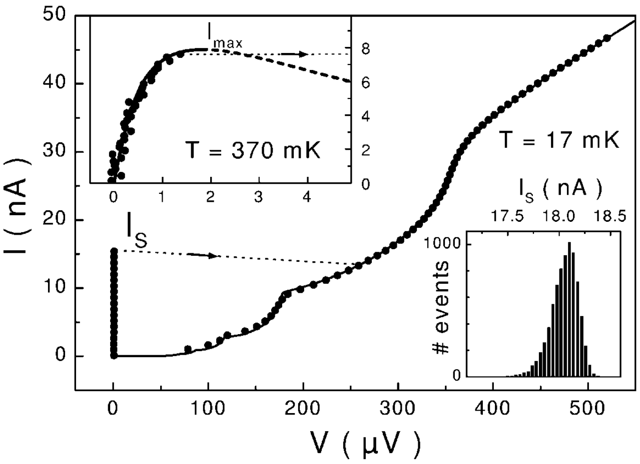

FIG. 3. Large scale IV characteristic of atomic contact, measured at 17 mK (dots). Switching at current I_s from supercurrent branch (almost vertical branch near zero voltage) to dissipative branch is a stochastic process. Full line is the best fit of this branch, obtained by decomposing the total current into contributions of 3 independent channels, giving $\{\tau_i\} = \{0.52, 0.26, 0.26\}$ and $I_0 = 25.3 \pm 0.4$ nA. Top inset: expanded view of experimental (dots) and theoretical (lines) diffusion branch at 370 mK (thick dashed line shows negative differential resistance region). Bottom inset: I_s histogram measured at $T = 17$ mK and $dI/I_0\,dt = 581$ s^{-1}.

$$\frac{d\delta}{dt} = u - i_J(\delta) + i_n(t), \tag{2}$$

$$\alpha \frac{du}{dt} = i_b - i_J(\delta). \tag{3}$$

Here, time is in units of t_J, $i_J(\delta) = I_J(\delta)/I_0$, and $i_b = I_b/I_0$. The thermal current noise source $i_n(t)$ associated with the resistor obeys the fluctuation-dissipation theorem. If R and C are large enough to achieve $\alpha \gg 1$ (keeping, however, $R \ll h/4e^2$ to avoid quantum fluctuations of δ [10]), the time evolution of u is much slower than that of δ. One then first solves (2) with a constant u and afterwards solves (3) for the slower dynamics of u. The first step is equivalent to solving the resistively shunted junction model [11] with a voltage source u. As in the well-known case of tunnel junctions, the dynamics of the phase in this circuit is equivalent to the Brownian motion of a massless particle in a tilted washboardlike "potential," governed by the Langevin equation (2). However, here the potential is not the usual tilted sinusoid but has instead the more general form [12]

$$U_p = -u\delta + \sum_{i=1}^{N} (n_{i+} - n_{i-}) E_-(\delta, \tau_i), \tag{4}$$

which depends on $\{\tau_i\}$ and the time dependent $n_{i\pm}$. Several mechanisms can make these $n_{i\pm}$ change, but in general none is very efficient. The relaxation induced by phonons has been addressed in [13]. We have found that the relaxation of the upper state through the emission of photons in the environment is extremely slow except for highly transmitted channels at $\delta \sim \pi$ [14]. However, relaxation by the exchange of quasiparticles with states in the bulk electrodes can be very fast, but only at $\delta = 0$ (Fig. 1). We have solved (2) by making a straightforward generalization of the procedure introduced by Ambegaokar and Halperin [15] for overdamped tunnel junctions. In this adiabatic model the "particle" moves in a constant potential obtained by replacing in (4) the $n_{i\pm}$ by their thermal equilibrium values at $\delta = 0$ [16].

The upper inset of Fig. 3 shows a comparison of the measured supercurrent branch for a particular contact with the predictions of this adiabatic model. The supercurrent branch is, in fact, a current peak. The equivalent particle is constantly thermally activated over the potential barriers between the wells and undergoes a classical diffusion motion with a small, friction-limited drift velocity. The only inputs of the calculation are the temperature, R, and the measured values of $\{\tau_i\}$, which determine the zero temperature supercurrent I_0 [17]. The value of R, which is measured independently, sets only the voltage scale of the supercurrent peak. In our RC biasing scheme, which keeps the atomic contact unshunted at dc, the negative differential resistance region of the IV is unstable, and the system switches to the dissipative branch before reaching the maximum $I_{\max}$ of the current peak. The capacitor was designed large enough ($C = 140$ pF) for all the samples to be in the overdamped limit $\alpha \gg 1$, in which case I_s is predicted to be close to $I_{\max}$. The fluctuations of I_s are also small, as shown by the narrow switching current histogram in the bottom inset of Fig. 3.

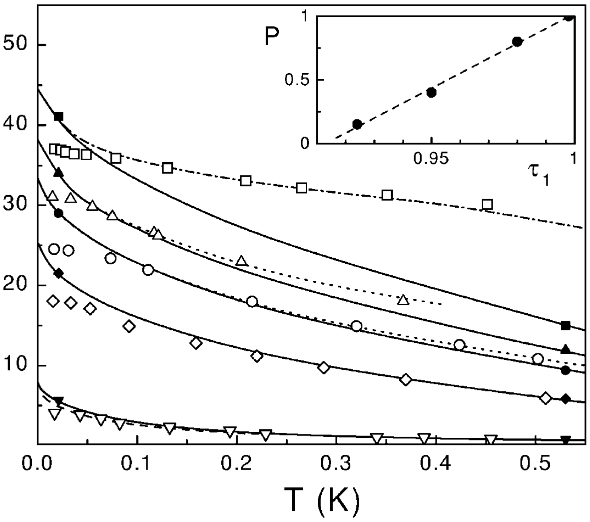

FIG. 4. Experimental (open symbols) and theoretical (lines) average switching current $\langle I_s \rangle$ as a function of temperature for different contacts on two samples. (▽) $\{\tau_i\} = \{0.21, 0.07, 0.07\}$, $I_0 = 8.0 \pm 0.1$ nA [17]. (◇) $\{\tau_i\} = \{0.52, 0.26, 0.26\}$, $I_0 = 25.3 \pm 0.4$ nA. (∘) $\{\tau_i\} = \{0.925, 0.02, 0.02\}$, $I_0 = 33.4 \pm 0.4$ nA. (△) $\{\tau_i\} = \{0.95, 0.09, 0.09, 0.09\}$, $I_0 = 38.8 \pm 0.2$ nA. (□) $\{\tau_i\} = \{0.998, 0.09, 0.09, 0.09\}$, $I_0 = 44.2 \pm 0.9$ nA. Contacts (▽), (◇), (△), and (□) from sample with $\Delta/e = 178 \pm 1$ μV, $R = 125 \pm 10$ Ω. Contact (∘) from sample with $\Delta/e = 184.5 \pm 1.0$ μV, $R = 170 \pm 20$ Ω. Full lines (with solid symbols): predictions of adiabatic theory for $\alpha \to \infty$, for which $\langle I_s \rangle \to I_{\max}$. Dashed line: finite α corrections for contact (▽). Dash-dotted line: predictions of adiabatic theory for contact (□), assuming the highest transmitted channel to be ballistic. Dotted lines: predictions of extended model including empirical interlevel nonadiabatic transition probability P at $\delta = \pi$ ($P = 0.4$ for upper curve, $P = 0.15$ for lower one). Inset: probability P as a function of transmission coefficient τ_1 of highest transmitted channel for different contacts displaying extra supercurrent. Symbols are best fits values from simulation. Dotted line is guide for the eye.

The temperature dependence of $\langle I_s \rangle$ measured for five contacts is shown in Fig. 4 together with the predictions of the adiabatic model sketched above. For every contact having all channels such that $\tau_i \lesssim 0.9$ the $\alpha \to \infty$ limit of the theory describes well the data at high temperature. Moreover, in the case of very low τ, finite α corrections can be calculated [6] and explain the small deviations at intermediate temperatures. We attribute the remaining low temperature deviations to the saturation of the electronic temperature in the resistors [18]. The uppermost data points in Fig. 4 correspond to a contact in which one of the channels had $\tau = 0.998$. The measured $\langle I_s \rangle$ are larger than predicted by the adiabatic theory for this τ. However, if we assume this channel to be perfectly transmitted ($\tau = 1$), a reasonable assumption given our accuracy in the determination of the τ's, we recover a very satisfactory fit of the data. This is due to the fact that this small change in τ has a profound impact on the shape of the potential. For $\tau = 1$ the AS singularly become the ballistic $B_{\rightleftarrows}$ states (Fig. 1), which have no extrema at $\delta = \pi$. In this case the current flows always in the same direction, thus leading to a much larger average value. For contacts having at least one channel with $\tau_i \geq 0.9$, but definitely not ballistic within the experimental accuracy, the measured $\langle I_s \rangle$ is also larger than the predictions of the adiabatic theory, which corresponds in principle to the maximum observable $\langle I_s \rangle$. A possible explanation of this excess supercurrent could be the existence of transitions between the adiabatic $E_{\pm}$ states (Fig. 1), induced by the fast dynamics of δ. In the case of an almost perfectly transmitted channel ($\tau \simeq 1$), the energy gap $2\Delta\sqrt{1 - \tau}$ at $\delta = \pi$ is very small. If the system starts a $[\delta : 0 \rightarrow 2\pi]$ cycle in the lower adiabatic state E_-, there is a finite probability P for finding it in the excited adiabatic state E_+ after δ has diffused across the region around π at finite speed (Fig. 1). For a large P the system would follow most of the time just the ballistic state $B_{\rightarrow}$, making the time-averaged supercurrent resistant to thermal fluctuations, as observed experimentally. Note that this strong nonequilibrium occupation of the AS marks the uprising of the dissipative current [19]. We have extended our model in a minimal way by adding to the boundary conditions of thermal equilibrium at $\delta = 0$, the possibility of interlevel transitions at $\delta = \pi$, with an empirical, temperature independent probability P. As shown in Fig. 4, this modified model allows fitting the experimental data reasonably well. The inset of Fig. 4 shows the best-fit value of P obtained using this procedure, as a function of the τ of the highest transmitted channel. We note that the standard Landau-Zener theory [19] predicts much too small values of P given the small drift velocity of the phase. In fact, the Landau-Zener theory is not directly applicable to the present situation in which the phase is not an external parameter swept at a constant rate, but is instead a dynamical variable undergoing a driven diffusive motion. A rigorous theory of this dissipative nonadiabatic mechanism, valid for arbitrary transmission, remains to be developed for our system, along the lines of [20] or [21], for example.

In conclusion, superconducting atomic contacts can sustain supercurrents close to that predicted solely from their mesoscopic transmission set. The value of the supercurrent is thus related to the dissipative branch of the IV characteristics, like in usual macroscopic Josephson junctions, although in the latter the contribution of the different channels cannot be disentangled. More generally, our findings strongly support the idea of the supercurrent being carried by Andreev bound states and show that the concepts of mesoscopic superconductivity can be applied down to the level of single atom contacts.

We acknowledge the technical assistance of P. F. Orfila and discussions with D. Averin, J. C. Cuevas, M. Feigel'man, A. Martín-Rodero, Y. Naveh, H. Pothier, and A. Shytov. M. F. G. acknowledges support by FOMEC.

[1] Entry points into the literature: P. Bagwell, R. Riedel, and L. Chang, Physica (Amsterdam) **203B**, 475 (1994); V. S. Shumeiko and E. N. Bratus, J. Low Temp. Phys. **23**, 181 (1997); A. Martín-Rodero, A. Levy Yeyati, and J. C. Cuevas, Superlattices Microstruct. **25**, 927 (1999).

[2] A. Furusaki and M. Tsukada, Solid State Commun. **78**, 299 (1991); C. W. J. Beenakker and H. van Houten, Phys. Rev. Lett. **66**, 3056 (1991).

[3] J. M. van Ruitenbeek, in *Mesoscopic Electron Transport,* edited by L. L. Sohn, L. P. Kouwenhoven, and G. Schön, NATO ASI, Ser. E, Vol. 345 (Kluwer, Dordrecht, 1997).

[4] E. Scheer *et al.,* Phys. Rev. Lett. **78**, 3535 (1997); E. Scheer *et al.,* Nature (London) **394**, 154 (1998).

[5] With one remarkable exception: M. C. Koops, G. V. van Duyneveldt, and R. de Bruyn Ouboter, Phys. Rev. Lett. **77**, 2542 (1996).

[6] D. Vion *et al.,* Phys. Rev. Lett. **77**, 3435 (1996); P. Joyez *et al.,* J. Supercond. **12**, 757 (1999).

[7] J. M. van Ruitenbeek *et al.,* Rev. Sci. Instrum. **67**, 108 (1996).

[8] These nonlinearities follow the temperature and magnetic field dependence of the gap and are not related to spurious electromagnetic resonances in the external circuit. See E. Scheer *et al.,* Physica (Amsterdam) **280B**, 425 (2000).

[9] We estimate $C_J \lesssim 2$ fF from the measured capacitance between a metallic pad and the ground plane (28 aF/μm^2).

[10] G.-L. Ingold and H. Grabert, Phys. Rev. Lett. **83**, 3721 (1999).

[11] D. E. McCumber, J. Appl. Phys. **39**, 3113 (1968).

[12] D. V. Averin, A. Bardas, and H. T. Imam, Phys. Rev. B **58**, 11 165 (1998).

[13] D. A. Ivanov and M. V. Feigel'man, JETP Lett. **68**, 890 (1998).

[14] Values of δ are given modulo 2π throughout this paper.

[15] V. Ambegaokar and B. I. Halperin, Phys. Rev. Lett. **22**, 1364 (1969).

[16] A numerical simulation of Langevin equation (2), with $n_{i\pm}$ selected according to a thermal equilibrium probability each time δ goes through 0, gives the same results.

[17] The set $\{\tau_i\}$ is determined by probing all possible combinations with a transmission step of 10^{-3}. The uncertainty on I_0 is obtained taking into account all $\{\tau_i\}$ fitting the IV with an accuracy better than 1%, a conservative estimate of the actual experimental accuracy.

[18] For the power levels dissipated in the resistors we do not expect them to cool much below 100 mK. See M. Henny *et al.,* Appl. Phys. Lett **71**, 773 (1997).

[19] D. Averin and A. Bardas, Phys. Rev. Lett. **75**, 1831 (1995); Phys. Rev. B **53**, R1705 (1996).

[20] E. Shimshoni and A. Stern, Phys. Rev. B **47**, 9523 (1993).

[21] A. V. Shytov, cond-mat/0001012.

References of Chapter 3

---

[1] B. D. Josephson, Phys. Lett. **1**, 251 (1962).

[2] P.W. Anderson and J.M. Rowell, Phys. Rev. Lett. **10**, 230 (1963).

[3] K. K. Likharev, Rev. Mod. Phys. **51**, 101 (1979).

[4] L.G. Aslamazov and A.I. Larkin, JETP Lett. **9**, 87 (1969).

[5] I.O. Kulik and A.N. Omelyanchuk, JETP Lett. **21**, 96 (1975).

[6] G. Eilenberger, Z. Phys. **214**, 195 (1968).

[7] I.O. Kulik and A.N. Omelyanchuk, Fiz. Nizk. Temp. **3**, 945 (1977).

[8] B.J. van Wees, H. van Houten, C.W.J. Beenaker, J.G. Williamson, L.P. Kouwenhoven, D. van der Marel, and C.T. Foxon, Phys. Rev. Lett. **60**, 848 (1988).

[9] C.W.J. Beenaker and H. van Houten, Phys. Rev. Lett. **66**, 3056 (1991).

[10] J. Bardeen, R. Kümmel, A. E. Jacobs, and L. Tewordt, Phys. Rev. **187**, 556 (1969).

[11] Entry points into the literature: P. Bagwell, R. Riedel, and L. Chang, Physica (Amsterdam) **203B**, 475 (1994); V.S. Shumeiko, and E.N. Bratus, J. Low Temp. Phys. **23**, 181 (1997); J.C. Cuevas, Superlattices Microstruct. **25**, 927 (1999).

[12] O.N. Dorokhov, Solid State Commun. **51**, 384 (1984).

[13] C. J. Muller, J. M. van Ruitenbeek, and L. J. de Jongh, Phys Rev. Lett. **69**, 140 (1992).

[14] C. J. Muller, M.C. Koops, B.J. Vleeming, R. de Bruyn Ouboter, and A.N. Omelyanchouk, Physica C **220**, 258 (1994).

[15]M. C. Koops, G. V. van Duyneveldt, and R. de Bruyn Ouboter, Phys. Rev. Lett. **77**, 2542 (1996).

[16] D. Vion, M. Götz, P. Joyez, D. Esteve, and M.H. Devoret, Phys. Rev. Lett. **77**, 3435 (1996).

[17] P. Joyez, D. Vion, M. Götz, M. Devoret, and D. Esteve, J. Supercond. **12**, 757 (1999).

[18] G.-L. Ingold and H. Grabert, Phys. Rev. Lett. **83**, 3721 (1999).

[19] D. Vion, M. Götz, P. Joyez, D. Esteve, and M.H. Devoret, Phys. Rev. Lett. **77**, 3435 (1996).

[20] P. Joyez, D. Vion, M. Götz, M. Devoret, and D. Esteve, J. Supercond. **12**, 757 (1999).

[21] D.A. Ivanov and M.V. Feigel'man, JETP Lett. **68**, 890 (1998).

[22] V. Ambegaokar and B.I. Halperin, Phys. Rev. Lett. **22** , 1364 (1969).

[23] H. Risken, *The Fokker-Planck Equation* (Springer-Verlag, Berlin, 1984).

[24] V.I. Mel'nikov, Phys. Rep. **209**, 1 (1991).

[25] L.D. Landau, Phys. Z. Sow. **2**, 46 (1932); C. Zener, Proc. R. Soc. London, Ser. A **137**, 696 (1932).

---

[26] A. V. Shytov, cond-mat/0001012.

Chapter 4 Shot noise in atomic-size contacts

The discreteness of the electronic charge and the stochastic character of electrical transport give rise to temporal fluctuations, known as shot noise, in the current flowing through electronic devices. Schottky first evidenced these current fluctuations in vacuum diodes as early as in 1918 [1]. Many electronic devices, like metal-insulator-metal tunnel junctions, tunnel diodes, bipolar and FET transistors for example, also show shot noise that usually limits their performances [2].

In vacuum diodes, the electrical current is made up of electrons emitted by the polarized cathode. This stochastic electron emission is a poissonian process and the time correlation function of the current $I(t)$ is then δ-correlated and equal to:

$$\left\langle I(t)I(t')\right\rangle = e\left\langle I(t)\right\rangle \delta(t-t'), \tag{1}$$

where $\langle ... \rangle$ symbolizes time average. The corresponding spectral density $S_I(\omega)$ defined for positive pulsation as twice the correlation function Fourier transform is given by:

$$S_I(\omega) = 2\,\mathcal{F}\left(\left\langle I(t)I(t')\right\rangle\right) = 2e\left\langle I(t)\right\rangle \quad (\omega > 0). \tag{2}$$

This expression reveals the general features of shot noise. The spectral density is frequency independent[1] (white noise). It is proportional to the average current $\left\langle I(t)\right\rangle$, denoted simply I in the following, and to the charge of the current carriers, namely here the electronic charge e. The exact value $2eI$ is however specific to a perfectly random poissonian process, commonly referred as poissonian noise, and any correlation in the electronic flow reduces this value.

Shot noise amplitude is thus sensitive to the charge of the current carriers and to any physical process that eliminates, generates or modifies randomness in the electronic flow like statistical correlations, scattering or interactions. Consequently, it reveals transport properties inaccessible through simple conductance measurements and has been widely investigated in mesoscopic conductors during the last decade, both theoretically and experimentally (see [3] for a review).

For example, experiments [4,5] and theoretical calculations [6,7,8,9] on diffusive wires of various length L connecting two normal charge reservoirs, reveal how shot noise can be modified by interactions among electrons and between electrons and phonons. At low temperature, the length L_{e-e} over which electrons reach thermal equilibrium among themselves through inelastic e-e collisions is typically smaller than the length L_{e-ph} over which electrons relax to the phonon temperature, but higher than the coherence length L_ϕ of

---

[1] Here the emission process is supposed to be instantaneous and the current is consequently $\delta-$correlated . A finite emission time *t* would introduce a natural cut-off at frequency 1/*t* for the spectral density.

electrons. Following [4] one can distinguish several regimes. In the "macroscopic" regime $L_{e-ph} \ll L$, the electrons are always in equilibrium at the lattice temperature and the noise does not depend on the current. In other words there is only equilibrium (Johnson) noise and no shot-noise, which is essentially an out-of equilibrium phenomenon. In the "interacting hot-electron" regime $L_{e-e} \ll L \ll L_{e-ph}$, electrons are still at equilibrium among themselves but at a (non-uniform) higher temperature than the phonons. There is then an out of equilibrium component to the noise, which at high voltages $eV / k_B T \gg 1$ is equal to $\left(\sqrt{3}/4\right)2eI$, i.e. below the full Poisson value. In the "independent hot-electron" regime, $L_\phi \ll L \ll L_{e-e}$, shot noise is reduced to a value of $\left(1/3\right)2eI$. Finally, the same noise is obtained in the "mesoscopic" regime, $\ell \ll L \ll L_\phi$, where ℓ is the elastic mean-free-path.

As another example of the insight gained on electronic correlations through shot noise measurements, we mention the detection of quasiparticles of fractional charges in a 2D electron gas under high magnetic field in the highly correlated N-body state of the fractional quantum hall effect [10]. The size of the charge "pellets" that make up the current was directly evidenced in the value of the spectral density of the noise.

The superconducting state is another N-body state which displays subtle electronic correlations. As already mentioned, the current between two superconductors proceeds through multiple Andreev reflections (MAR), for which large charge pellets are predicted. We have carried out experiments on aluminum atomic contacts to evidence these correlations. Along the way, as the measurement set-up had to be calibrate with enough accuracy, we tested extensively the basic predictions for the noise in a coherent conductor between normal charge reservoirs.

In the following, we first present the basic theoretical predictions and some existing experimental results for shot noise in mesoscopic conductors in the normal (section 4.1) and superconducting (section 4.2) state, before describing our experimental results (section 4.3).

4.1 Shot noise in a quantum coherent conductor connecting normal charge reservoirs

4.1.1 Brief review of the theoretical results

We present in Appendix A the derivation within the framework of the scattering theory of the fluctuations in a quantum coherent conductor.

The basic ideas are the following. At zero temperature, due to the Pauli principle, there should be no fluctuations in the occupation numbers of the states in the reservoirs. The flow emitted by the reservoirs (considered as emitters) towards the conductor should thus be noiseless. However, at the scattering conductor, coherent superpositions of transmitted and reflected states are created. At the opposite reservoir, considered this time as a detector, these superpositions have to collapse, thus leading to fluctuations on the occupation numbers of the outgoing and incoming fluxes. Only in the case of perfect transmission, the conditions imposed by the reservoirs and the conductor are compatible. In all other cases, there is shot-noise across the full structure.

For a quantum coherent conductor characterized by the code $\{\tau_1,...,\tau_N\}$, the spectral density at voltage V and temperature T is constant at low frequency and equal to [11,12]:

$$S_I(V,T,\{\tau_1,...,\tau_N\}) = 2eV\coth\left(\frac{eV}{2k_BT}\right)G_0\sum_{i=1}^{N}\tau_i(1-\tau_i) + 4k_BTG_0\sum_{i=1}^{N}\tau_i^{\,2}. \qquad (3)$$

In the low voltage or high temperature limit $eV/2k_BT \ll 1$, (3) reduces to the equilibrium Johnson-Nyquist spectral density: $S_I = 4k_BTG_0\sum_{i=1}^{N}\tau_i = 4k_BTG$. On the contrary, in the large voltage or low temperature limit $eV/2k_BT \gg 1$, the spectral density increases linearly with the average current:

$$S_I(V,T,\{\tau_1,...,\tau_N\}) \simeq 2eI\left(1-\sum_{i=1}^{N}\tau_i^2 / \sum_{i=1}^{N}\tau_i\right). \qquad (4)$$

This is shot noise but reduced from its poissonian value $2eI$ by the so-called Fano factor

$$F\left(\{\tau_1,...,\tau_N\}\right)=1-\sum_{i=1}^{N}\tau_i^{\,2}/\sum_{i=1}^{N}\tau_i\,, \tag{5}$$

which depends only on the mesoscopic code. In the ballistic limit, the Fano factor vanishes, and so does shot noise, as the noiseless electronic steady stream emitted by the reservoirs is undisturbed by the coherent scatterer. In the opposite limit $\tau_i \ll 1$, electrons are randomly transmitted like electrons are emitted in vacuum diodes. In this case the Fano factor is close to unity and full shot noise $S_I = 2eI$ is recovered.

4.1.2 Shot noise in quantum point contacts tailored in 2D electron gas

Experimentally, the predictions of (3) were first tested at the beginning of the 90's in quantum point contacts tailored in 2D electron gas. The observation of conductance quantization in 1988 established that conduction channels open one by one as the width of these point contacts is enlarged by means of an electrostatic gate [13]. In other words, for all settings of the gate the code contains only 1's and 0's, but for one channel whose transmission can be continuously adjusted between 0 and 1. A comparison without any adjustable parameter between theory and experiment is then possible. First indications of sub-poissonian noise were first obtained in 1990-91 by Li *et al.* and Washburn *et al.* [14,15]. Measurements were done at low frequency and suffered of a large $1/f$ noise. Quantitative conclusions were thus hard to draw. In particular, the measured spectral density was not proportional to the average current but to its square, probably because the working voltage bias was too high. Subsequently, experimental techniques were much improved following different strategies to get rid of $1/f$ noise. In 1995, Reznikov *et al.* [16] measured shot noise in the microwave frequency range of 8-18 GHz, where $1/f$ noise is negligible, by implementing a cryogenic microwave amplifier. They observed the linear dependence of the spectral density on the average current but not full poissonian shot noise in the pinch-off regime ($\tau \ll 1$). Applying a constant bias current and varying the gate voltage, the spectral density oscillates and shows minima at integer values of the conductance in units of G_0 where all conduction channels are supposed to be perfectly open. The agreement with (3) was however only qualitative. The first measurements in quantitative agreement were performed in the group of Glattli in 1996 [17], who measured shot noise at low bias voltage and low frequency, getting rid of $1/f$ noise by means of a cross-correlation technique [18]. Their results on a single conduction channel for different transmission probabilities as well as the crossover from thermal to shot noise for a particular transmission probability are presented in Figure 1.

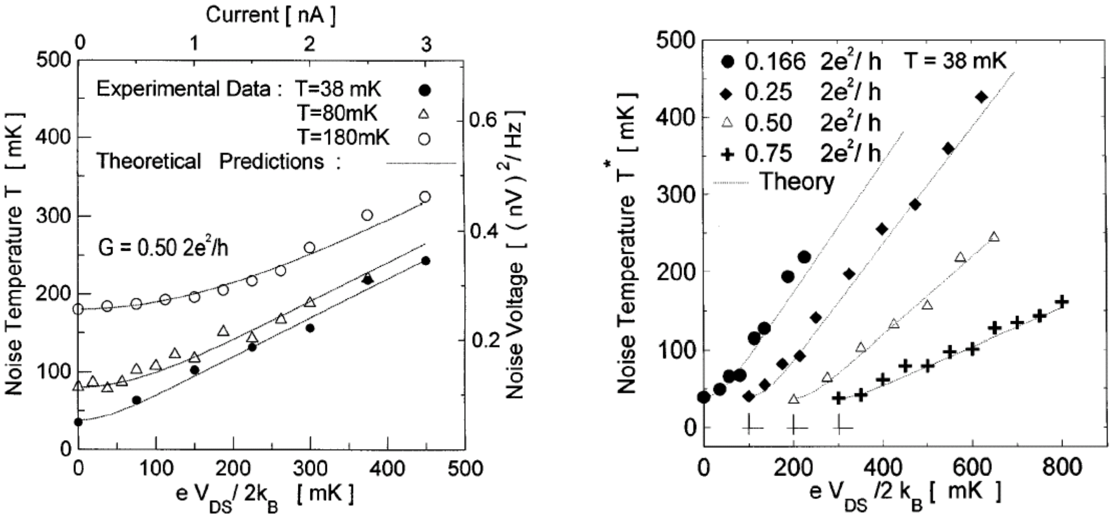

Figure 1: (reproduced from [17]) Left: Spectral density of the QPC voltage fluctuations S_V, also expressed as noise temperature $T^* = GS_V / 4k_B$, for one conduction channel with transmission probability $\tau = 0.5$ at T=38, 80, and 180 mK, as a function of the current or the average voltage expressed in relevant temperature units. The dotted lines are predictions of (3) with no adjustable parameters. Right: Noise temperature versus bias in temperature units for conductances G=1/6,1/4,1/2, and 3/4 G_0 at 38 mK. For clarity, data for different G are offset by 100 mK. Theory corresponds to (3) with one conduction channel.

4.1.3 Shot noise in gold atomic-size contacts

Considering (3) has well established, van den Brom and van Ruitenbeek reversed the point of view and performed shot noise measurements in atomic-size contacts in order to get information about the number of conduction channels and their transmission probabilities, that is about scattering process by the atomic size-contact [19]. For 27 different gold contacts with conductances ranging from $0.7\,G_0$ up to $4.1\,G_0$, they measured a spectral density well below the poissonian value, indicating that current is mostly carried by well transmitting channels. The values of the conductance and the shot noise density are related respectively to the first and second moment of the transmission probability distribution. Because from two parameters the code can be disentangled only if the contact contains no more than two conduction channels, their results were quantitative only for conductances below $2\,G_0$. For a single gold atom contact, the conductance is about G_0 and their shot noise measurements established that the contribution of partially transmitted conduction channels is only a few percent.

4.2 Shot noise in a quantum coherent conductor when superconducting reservoirs are involved

4.2.1 Double electronic charge transfer at a NS interface

For voltages smaller than the superconducting gap $2\Delta/e$, the microscopic mechanism of transport through a normal-superconducting interface is Andreev reflection, in which an electron is reflected as a hole at the interface and a cooper pair is transferred [20,21]. For a long diffusive normal wire, it has been demonstrated that independently of the transparency of the normal-superconducting interface, the noise is increased by a factor two with respect to the fully normal case, i.e. $S_I = 2\times 2/3 eI$. This doubling of shot noise as well as the crossover between thermal and shot noise at $2eV = 2k_B T$ was experimentally evidenced by Jehl *et al.* in Cu/Nb junctions [22].

4.2.2 SNS junction

In a SNS junction, Andreev reflections occur at both NS interfaces. As presented in Appendix B, in the limit where the length of the normal region is much smaller than the coherence length L_ϕ, the current at voltages smaller than $2\Delta/e$ proceeds through MAR processes. The MAR process of order n, which has a threshold voltage of $2\Delta/ne$, transfers a charge ne between the two superconducting electrodes. However, for a given voltage many such processes contribute coherently to the current. The calculation of the effective charge $q^* = S_I/2I$ as a function of voltage for arbitrary transmission [23,24] leads to a staircase pattern. As the transmission increases, the staircase pattern is progressively washed out. The effective charge increases as the voltage decreases and diverges at low voltage like $q^* \sim 2\Delta / eV$.

In 1997, Dieleman *et al.* observed a divergence of the effective charge at low voltages in NbN/MgO/NbN superconductor/ insulator/superconductor tunnel junctions [25]. It is believed that the measured junctions consisted in fact of parallel SNS point contacts because the 1 nm thick MgO barrier presented small pinholes. From the relative height of the differential conductance peaks at subharmonic values of 2Δ, Dieleman and coworkers determined that the mean transmission of these point contacts was $\tau = 0.17$. They explained their results developing a semi-empirical theory, but the agreement with the full theory presented above is only qualitative.

4.3 Shot noise measurements in aluminum atomic-size contacts both in the normal and in the superconducting state

In the normal state, all our measurements of shot noise as a function of temperature and bias current are in quantitative agreement with the predictions of the scattering theory (see Eq. (3)) using the code determined from the current-voltage characteristics in the superconducting state. Expression (3) was, as presented in 4.1, already tested in 2DEG quantum point contacts where conduction channels open one by one. However, as one-atom aluminum contacts contain typically three conduction channels they provide a larger palette of codes with arbitrary values, and our results can be considered as a broader test of the general multichannel formula (3).

In the superconducting state we do observe, for contacts containing no high transmitting channels, that the effective charge $q^* = S_I / 2I$ increases by steps as the voltage decreases revealing the transfer of multiple charge quanta through MAR processes in the sub-gap region. For larger transmission probabilities the staircase pattern progressively washes out, but the effective charge still strongly increases like $q^* \sim e(2\Delta / eV)$ as the voltage decreases. In all cases, our measurements are in quantitative agreement with the full quantum theory of MAR [23,24] using the code determined independently from the current-voltage characteristics in the superconducting state.

All these results were reported in “Multiple-Charge-Quanta Shot noise in Superconducting Atomic Contacts” by R. Cron, M.F. Goffman, D. Esteve, and C. Urbina, Phys. Rev. Lett. **86**, 1078 (2001), which we reproduce in section 4.3.2. Some complementary analysis is performed in section 4.3.3, and in section 4.3.1, we describe in detail the measurement set-up and its calibration.

4.3.1 Measurement of shot noise in atomic-size contacts

The set-up used to measure shot noise is depicted in Figure 2. It consists basically of one coaxial line, used to bias the on-chip grounded break-junction, and of two bifilar lines used to obtain two independent measurements of the voltage across with two sets of low-noise amplifiers. With this set-up current fluctuations are thus not directly measured, but instead inferred from the fluctuations of the voltage across the contact. The current and voltage fluctuations spectral densities, S_I and S_V respectively, are related, at a given voltage V through $S_V(V) = R_D^2 S_I(V)$, where $R_D\left(V\right) = \partial V \big/ \partial I\left(V\right)$ is the differential resistance. In the normal state, this differential resistance is essentially constant in the voltage range in which the experiments are carried out[2], and equals R_N, the normal resistance of the contact. In the superconducting state, the differential resistance can be highly non-linear.

All noise sources along the measurement lines, like the Johnson-Nyquist thermal noise of the resistors or the current and voltage noise of the amplifiers input stages, induce fluctuations that poison the shot noise signal. Because of that, the measurement lines and the bias line were carefully designed and built so as to limit and keep under control this additional

---

[2] Actually, the differential resistance presents small amplitude fluctuations (typically less than 1%) as a function of voltage. These fluctuations are well understood as arising from quantum interference effects.

noise. In the following, we first describe the details of the measurement set-up. Then we explain how we characterize it taking into account all noise sources and the attenuation along the lines. This characterization allows us to extract from the measured total voltage fluctuations, the fluctuations of the current through the atomic-size contact.

4.3.1.1 Description of the measurement set-up

The bias current is obtained using a $1\,\mathrm{M\Omega}$ resistor thermally anchored to the “$1\,\mathrm{K}$ pot”, whose actual temperature is between 1.2 and 1.5 K. The room temperature part of the bias line is simplified as much as possible to avoid picking up from external sources. Except for the power line harmonics, the voltage background noise on the sample was checked to be identical with or without this part of the bias line, independently of the contact resistance. Two voltage sources produce the bias: a low-noise Yokagawa voltage source provides the dc bias, and a Stanford Research SR830 lock-in amplifier provides an ac voltage used to measure the differential conductance. These signals are added using an operational amplifier summing circuit whose ground is decoupled from the power line ground. The resulting signal is fed to the biasing resistor through a $50\,\Omega$ adjustable attenuator. The latter is placed as close as possible to the feed-through connection on top of the cryostat (which acts as a Faraday cage), to avoid picking up too much noise through the cables. The bias current (both dc and ac) is deduced from the values of the input voltage, the voltage measured on the sample and the total resistance of the filters and resistors in the bias line.

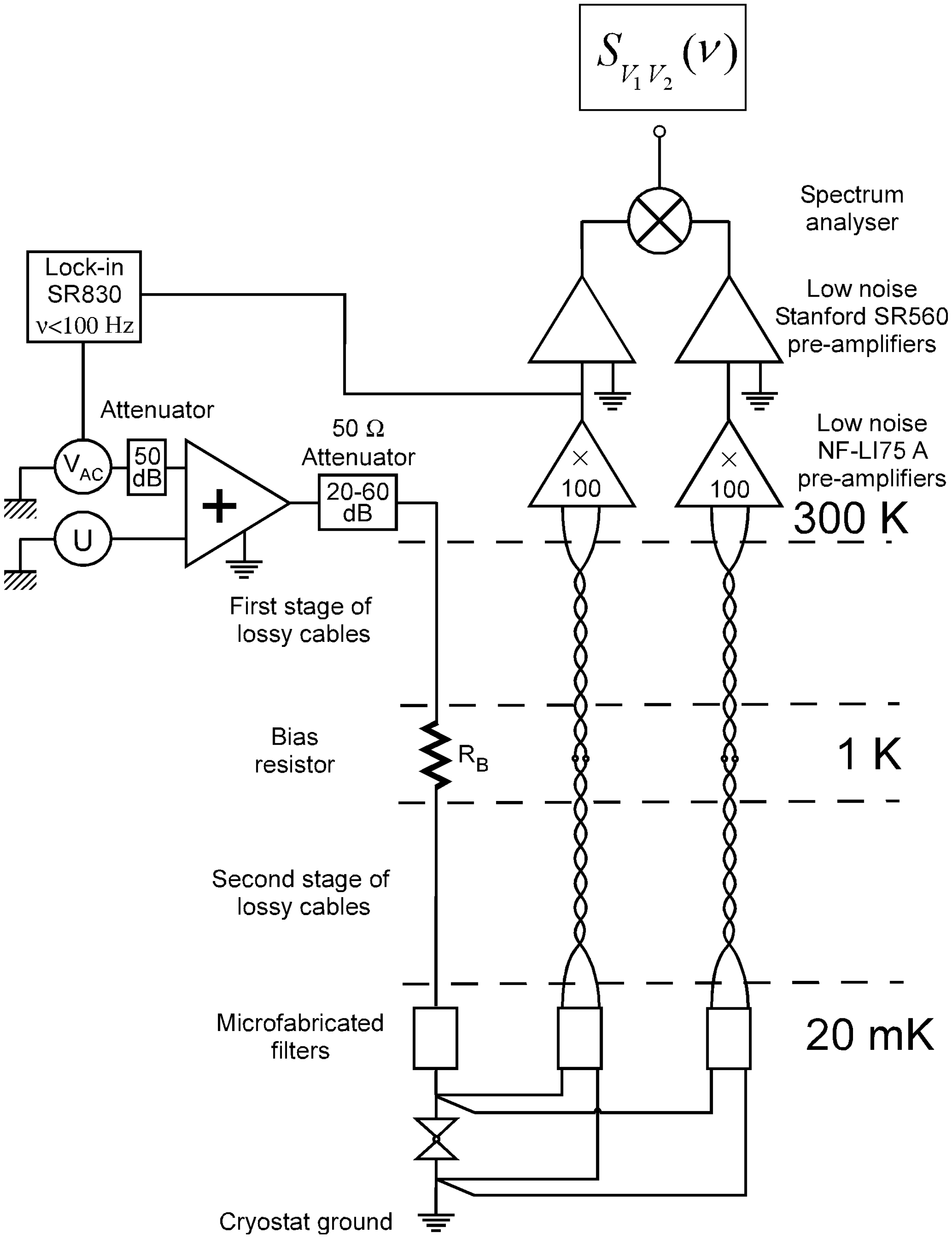

Figure 2: Schematic representation of the measurement set-up consisting of a coaxial line to bias the atomic-size contact (two triangle symbol) and of two bifilar lines to measure twice the voltage across it. The spectrum analyzer calculates the cross-correlation of these two signals.

The voltage across the atomic-size contact is measured twice using two bifilar lines. As close as possible to the feedthroughs that take these two lines out of the cryostat, the signals are amplified by identical cascades of two low-noise battery-powered pre-amplifiers: a x100 fixed gain NF LI75A, followed by a Stanford SR560 of adjustable gain. The connections from the top of the dilution refrigerator to the pre-amplifiers are made out of semi-rigid coaxial cables. The real part of the cross-correlation spectrum $S_{V_1 V_2}(\nu)$ of the two amplified signals $V_1(t)$ and $V_2(t)$ is calculated in real time by a spectrum analyzer SR780:

$$S_{V_1 V_2}(\nu) = \mathrm{Re}\left\langle \overline{\mathcal{F}(V_1(t))(\nu)} \cdot \mathcal{F}(V_2(t))(\nu) \right\rangle . \tag{6}$$

where $\mathcal{F}$ is the fast Fourier transform and $\langle ... \rangle$ refers to the vector averaging over successive temporal traces. This cross-correlation technique allows one to get rid of the $1/f$ noise coming from the preamplifiers and the measurement lines that poison the white noise signal. Typically, the spectra were measured over 800 points in a frequency window $[360, 3560\,\mathrm{Hz}]$ and averaged 1000 times in 4 min. At the same time, the lock-in measures the ac voltage signal from which the differential resistance is deduced.

4.3.1.2 Characterization of the measurement set-up

Using the broadband chirp source of the spectrum analyzer, we measured for frequencies up to 100 kHz the transfer function of each measurement line. Essentially, they behave as one-pole RC filters with R and C being respectively the total resistance and the total capacitance of the lines. The microfabricated filter provides most of this resistance, whereas the lossy lines account for most of the capacitance. The electrical circuit depicted in Figure 3, where all measurement lines contain a RC filter, is thus a good model for the measurement set-up. The noise introduced by the line resistances R_L and r_B is negligible as compared to the other noise sources and is thus not taken into account. Furthermore, the capacitance of the first lossy cable stage (from 300K to 1K) on the bias line is not taken into account because the bias resistance is much higher than all other resistances in the line.

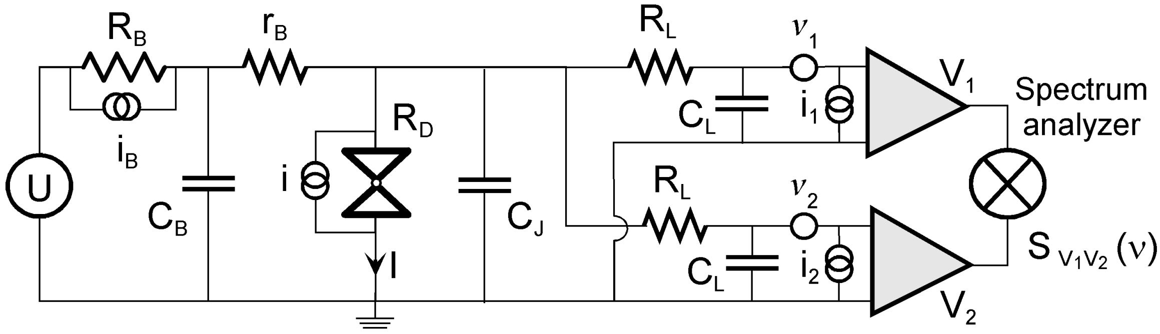

Figure 3: Model of the measurement set-up. The contact is characterized by its differential resistance $R_D(V) = \partial V/\partial I(V)$, its capacitance C_J dominated by the capacitance of the on-chip connection pads, and the noise source i, which is the signal to measure. The bias line is characterized by the bias resistor R_B, its current noise source i_B, and the total resistance r_B and capacitance C_B of the second lossy cable stage and microfabricated filter. The total resistance and capacitance along the voltage lines are respectively R_L and C_L. The current noise sources of the NF preamplifiers are denoted i_1 and i_2. The total voltage noise sources of the pre-amplifiers and of the measurement lines are denoted υ_1 and υ_2.

The exact expression of V_1 and V_2 is a somewhat cumbersome combination of $RC\omega$ like terms of all resistances (except R_B) and capacitances involved in the model. However, in all our measurements the atomic-size resistance R_D was larger than R_L and r_B and thus $R_DC\omega$ terms are dominant. Neglecting all terms two orders of magnitude smaller than these ones leads to a relatively simple expressions for V_1 and V_2:

$$\begin{aligned}
V_1(\omega) &= \frac{R_D\left(i(\omega)+i_B(\omega)+i_1(\omega)+i_2(\omega)\right)+R_Li_1(\omega)}{1+\dfrac{R_D}{R_B}+\dfrac{r_B}{R_B}+j\omega\left[R_D(C_J+2C_L+C_B)+2R_LC_L+r_BC_B\right]}+\upsilon_1 \\
V_2(\omega) &= \frac{R_D\left(i(\omega)+i_B(\omega)+i_1(\omega)+i_2(\omega)\right)+R_Li_2(\omega)}{1+\dfrac{R_D}{R_B}+\dfrac{r_B}{R_B}+j\omega\left[R_D(C_J+2C_L+C_B)+2R_LC_L+r_BC_B\right]}+\upsilon_2,
\end{aligned} \tag{7}$$

where only the fluctuating part of V_1 and V_2 is taken into account. The vector averaging of the cross correlation $\overline{V_1}V_2$ eliminates components of the two voltage signals that do not have a constant phase relationship between them. Consequently, only $\left\langle \overline{X}X \right\rangle$ like terms do not vanish and the contribution of the voltage noise sources of the amplifiers and measurement lines, which contain an awkward $1/f$ component, are consequently averaged to zero.

The cross-correlation thus writes:

$$S_{V_1V_2}(\nu)=\left\langle \mathrm{Re}\left[\overline{V_1}V_2\right]\right\rangle=\frac{R_D^2\left(S_I+S_B+2S_{Amp}\right)+2R_DR_LS_{Amp}}{\left(1+\frac{R_D}{R_B}+\frac{r_B}{R_B}\right)^2+\left(2\pi\nu\right)^2\left(R_D(C_J+2C_L+C_B)+2R_LC_L+r_BC_B\right)^2},\ (8)$$

where $S_I=\left\langle \bar{i}(\omega)i(\omega)\right\rangle$, $S_B=\left\langle \overline{i_B}(\omega)i_B(\omega)\right\rangle$ and $S_{Amp}=\left\langle \overline{i_1}(\omega)i_1(\omega)\right\rangle=\left\langle \overline{i_2}(\omega)i_2(\omega)\right\rangle$ are the spectral densities of the various noise sources. The contact differential resistance and the resistances of the voltage lines bring out these current noise sources as fluctuations of V_1 and V_2 whose amplitude is attenuated through the RC filters of the lines.

In the measurement frequency window $\left[360, 3560\,\mathrm{Hz}\right]$, the terms R_LC_L and r_BC_B in the denominator are usually negligible. Indeed, they are of the same order of magnitude as the R_DC dominant terms only when the contact resistance is below a few kiloohms. But in this low resistance regime, all these terms are negligible in the whole frequency range. The same argument works for r_B/R_B and (8) simplifies into:

$$S_{V_1V_2}\left(V,T,\{\tau_1,...,\tau_N\},\nu\right)=\frac{R_\parallel^2}{1+\left(2\pi\nu R_\parallel C_{tot}\right)^2}\left(S_I\left(V,T,\{\tau_1,...,\tau_N\},\nu\right)+S_B+2\left(1+\frac{R_L}{R_\parallel}\right)S_{Amp}\right),(9)$$

where $R_\parallel=R_BR_D/(R_B+R_D)$ is the resistance of the parallel combination of R_B and R_D, and $C_{tot}=\left(C_J+2C_L+C_B\right)$ is the total capacitance. This simplified expression retains the relevant parameters of the set-up within the contact resistance range and frequency window corresponding to the measurements. The current fluctuation spectrum, which depends on the DC bias voltage, the temperature and the mesoscopic code of the involved atomic-size contact, can thus be extracted from the measured cross-correlation spectrum $S_{V_1V_2}$ provided that the prefactor $R_\parallel^2/(1+(2\pi\nu R_\parallel C_{tot})^2)$ and the spectral densities S_{Amp} and S_B are well known. The determination of these factors, and the accuracy on their determination, is described in the Annex.

4.3.1.3 Current fluctuations spectrum deduced from the measured voltage spectrum

The spectrum of the fluctuations of the current through the atomic-size contact is thus related to the measured $S_{V_1V_2}\left(V,T,\{\tau_1,...,\tau_N\},\nu\right)$ by:

$$S_I\left(V,T,\{\tau_1,...,\tau_N\},\nu\right)=\frac{1+\left(2\pi\nu R_{\|}C_{tot}\right)^2}{R_{\|}^2}S_{V_1V_2}\left(V,T,\{\tau_1,...,\tau_N\},\nu\right)-S_B-2\left(1+\frac{R_L}{R_{\|}}\right)S_{Amp}.(10)$$

Figure 4 shows for one particular contact a raw spectrum $S_{V_1V_2}\left(\nu\right)$ together with the corresponding $S_I\left(\nu\right)$. The values of the parameters used for the data treatment as well as the uncertainty in their determination are recapitulated in the following table.

Data treatment parameter	**Value and incertitude**
Bias resistance	$R_B=\left(1.065\pm 5\,10^{-3}\right)$ MΩ
Spectral density of the Johnson-Nyquist current source of the bias resistor	$S_B=\left(7\pm 1\right)10^{-29}$ A^2/Hz
Total Capacitance	$C_{tot}=(1.16\pm 0.05)$ nF
Resistance of the voltage measurement lines.	$R_L=(1.60\pm 0.05)$ kΩ
Spectral density of the current noise source of the NF-preamplifiers.	$S_{Amp}\left(\nu\right)=\left(2.3\pm 0.2\right)10^{-28}$ $+\left(9.06\pm 0.06\right)10^{-32}\times\nu$ A^2/Hz

Table 1: Measured values of the parameters used to extract the spectrum of the current fluctuations $S_I\left(\nu\right)$ from the raw spectrum $S_{V_1V_2}\left(\nu\right)$.

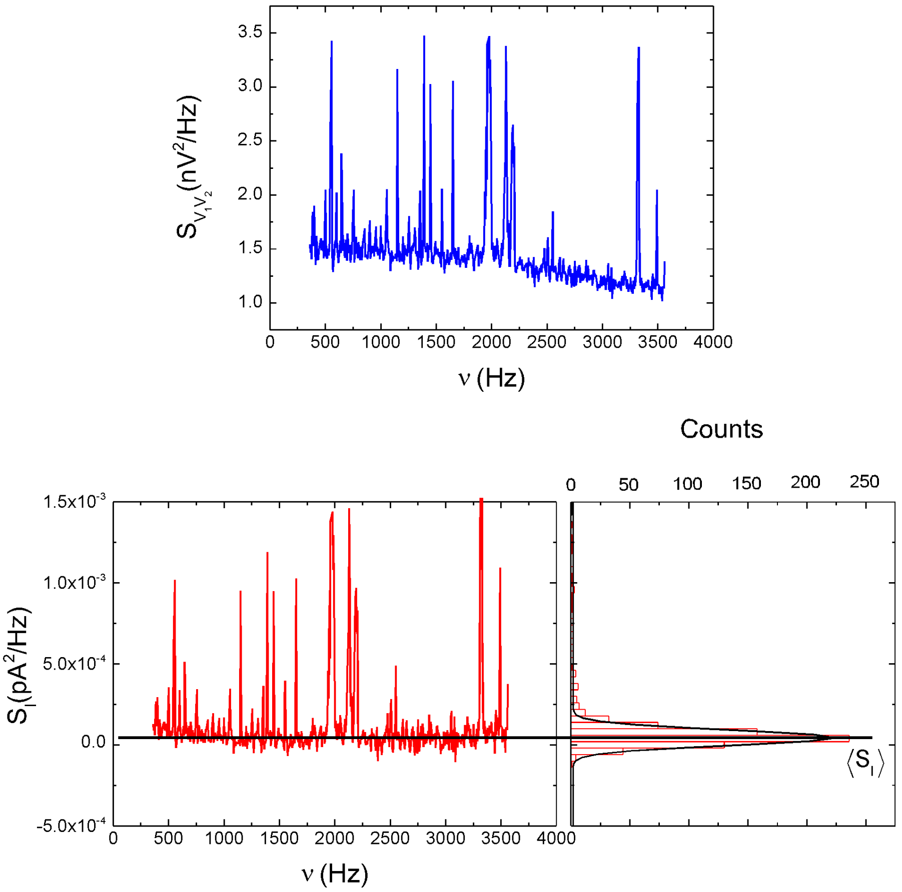

Figure 4: (Top) Raw cross-correlation spectrum[3] of the fluctuations of the voltage across an atomic-size contact with $R_D = 48270 \pm 1\%\ \Omega$ at 20 mK in the normal state. The sharp peaks correspond to harmonics of the power line while the wider ones (around 2 kHz and 3.25 kHz) correspond to microphonics. (Bottom left) Corresponding current fluctuations spectrum calculated using Eq. (10). (Bottom right) Spectrum histogram and its gaussian fit from which the average value of the current fluctuation spectrum $\langle S_I \rangle$ is determined.

Except for the peaks due to the power line harmonics and to microphonics, the current fluctuations spectra are white within our experiment accuracy. The average value $\langle S_I \rangle (V, T, \{\tau_i\})$ is determined as the mean value of the gaussian fit of the spectrum $S_I(\nu)$. This mean value is affected by both statistical and systematic errors. The latter arise from the uncertainties in the determination of the data treatment parameters. To provide the bounds of the systematic errors, the raw spectrum $S_{V_1V_2}(\nu)$ is treated choosing the set of parameters, within their uncertainty range, which maximize and minimize the current spectral density. The two resulting average values, $\langle S_I \rangle_{MAX}$ and $\langle S_I \rangle_{MIN}$, give respectively the upper and the lower bounds for $\langle S_I \rangle$ due to the systematic uncertainties. Taking also into account the

---

[3] The highest peaks have been removed for clarity.

statistical error, the uncertainty $\delta\langle S_I\rangle$ on $\langle S_I\rangle$ is equal to:

$$\delta\langle S_I\rangle = \frac{\langle S_I\rangle_{MAX} - \langle S_I\rangle_{MIN}}{2} + \frac{\Delta S_I}{\sqrt{N_{bin}}}, \tag{11}$$

where ΔS_I is the standard deviation of the current spectrum gaussian fit and N_{bin} the number of points in the spectrum that do not correspond to the spurious peaks (a lower bound for this number is $N_{bin} \simeq 700$).

Figure 5 shows the mean value $\langle S_I\rangle$ measured in the normal state, at $20\,\mathrm{mK}$ and zero bias voltage, for ten contacts with resistance ranging from $5\,\mathrm{k\Omega}$ up to $65\,\mathrm{k\Omega}$. We also show the predictions of Eq. (3) that corresponds to the Johnson-Nyquist thermal noise $4k_BT/R_D$. The agreement is quantitative within our measurement accuracy for the whole range of contact resistance, and the uncertainty is almost constant. Note however that for contact resistances less than one kiloohm the voltage fluctuations become very small and the measured voltage spectrum and consequently $\langle S_I\rangle$ is larger than expected from Exp. (9). Furthermore, for resistances much larger than a hundred kiloohms the attenuation along the measurement lines becomes very large and the measured thermal equilibrium $\langle S_I\rangle$ deviates also from the $4k_BT/R_D$ value.

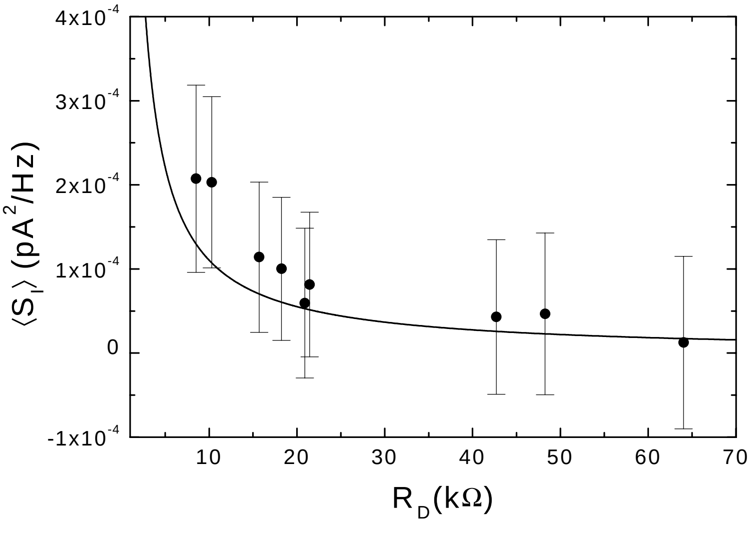

Figure 5: Average equilibrium noise $\langle S_I\rangle$ (dots), measured at 20 mK, for several contacts in the normal state. The full line corresponds to the predicted Jonhson-Nyquist thermal noise.

Nevertheless almost all of our measurements were in the $5-100\,\mathrm{k}\Omega$ contact resistance range, for which the predictions of Exp. (9) are in quantitative agreement with the equilibrium spectra. Therefore, we will use this expression also in the non equilibrium case ($V \neq 0$) to extract from the measured spectrum $S_{V_1V_2}(\nu)$ the current fluctuation spectrum $S_I(\nu)$.

4.3.2 Multiple-Charge-Quanta Shot Noise in Superconducting Atomic contacts (reproduced from Phys. Rev. Lett. 86, 4104 (2001))

Multiple-Charge-Quanta Shot Noise in Superconducting Atomic Contacts

R. Cron, M. F. Goffman, D. Esteve, and C. Urbina
Service de Physique de l'Etat Condensé, Commissariat à l'Energie Atomique, Saclay, F-91191 Gif-sur-Yvette Cedex, France

(Received 21 December 2000)

We have measured shot noise in aluminum atomic point contacts containing a small number of conduction channels of known transmissions. In the normal state, we find that the noise power is reduced from its Poissonian value and reaches the partition limit, as calculated from the transmissions. In the superconducting state, the noise reveals the large effective charge associated with each elementary transfer process, in excellent agreement with the predictions of the quantum theory of multiple Andreev reflections.

DOI: 10.1103/PhysRevLett.86.4104 PACS numbers: 74.50.+r, 73.23.–b, 73.40.Jn, 74.40.+k

As shown already in 1924 by Shottky, the granularity of electricity gives rise to fluctuations, known as "shot noise," in the electrical current through electronic devices. Lately, a great deal of activity has been devoted to this nonequilibrium noise in coherent nanostructures connecting two charge reservoirs. It is by now evident that even its low-frequency power spectrum carries a wealth of information on the interactions and quantum correlations between the electrons [1,2] in both the charge reservoirs and the nanostructure itself. When the current I is made up from perfectly independent shots, the white noise power spectrum assumes the well-known Poissonian form $S_I = 2qI$, where q is the "effective charge" transferred at each shot. In the case of normal, i.e., nonsuperconducting, metal reservoirs, the charge of the shots is simply the electron charge e. Interactions and correlations lead to large deviations from this value. One of the most striking examples is the fractional charge of quasiparticles in the highly correlated electronic state achieved in two-dimensional electronic systems under very high magnetic fields, which was recently evidenced through noise measurements [3]. The mechanism giving rise to superconductivity is another source of correlations among electrons. How big are the shots in the current when superconducting reservoirs are involved? The current between a superconducting reservoir and a normal one connected by a short normal wire proceeds through the process of Andreev reflection in which charge is transferred in shots of $2e$, thus resulting in a doubling of the noise with respect to the normal case [4]. When two superconducting electrodes connected through structures such as tunnel junctions or short weak links are voltage biased on an energy scale eV smaller than the superconducting gap Δ, the current proceeds through multiple Andreev reflections (MAR) [5]. In a MAR process of order n, which has a threshold voltage of $V = 2\Delta/ne$, two elementary excitations are created in the electrodes while a charge ne is transferred. For a given voltage many such processes can contribute to the current, but roughly speaking, "giant" shots, with an effective charge $q \sim e(1 + 2\Delta/eV)$, are predicted at subgap energies [6]. The exact value of q, like all other transport properties of a coherent nanostructure, depends on its "mesoscopic pin code," i.e., the set of transmission coefficients $\{\tau_i\}$ characterizing its conduction channels. A full quantum theory has been developed for the fundamental case of a single conduction channel connecting two superconducting electrodes [7,8] which predicts the voltage and temperature dependence of the current noise power spectral density $s_I(V, T, \tau)$, and therefore the size of the shots, for arbitrary transmission τ. In this Letter, we present an experiment on well-characterized coherent nanostructures, namely, atomic point contacts between two superconducting electrodes, which tests quantitatively these theoretical predictions.

Using nanofabricated break junctions, we produce aluminum atomic point contacts whose sizes can be adjusted *in situ* through a mechanical control system [9]. The samples are mounted in a vacuum can and cooled below 1 K. Figure 1 shows schematically the setup used to measure both the IVs and the noise. The contact is current biased (at low frequency) through a cold resistor R_B. The bias and the voltage measurement lines are filtered by a series of microwave cryogenic distributed lossy filters, an

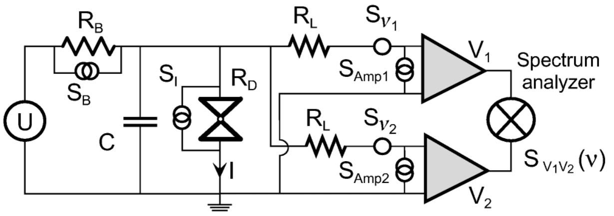

FIG. 1. Schematic experimental setup. An atomic contact (double triangle symbol), of dynamic resistance R_D, is current biased through $R_B = 1.065\ \text{M}\Omega$. The voltage V across the contact is measured by two low noise preamplifiers through two nominally identical lossy lines. $R_L = (1.60 \pm 0.05)\ \text{k}\Omega$ is the total resistance of each line. $C = (1.16 \pm 0.05)$ nF is the total capacitance introduced by the setup across the contact. The spectrum analyzer measures the cross-correlation spectrum of the two voltage lines. The $S_i (i = B, \text{Amp1}, \text{Amp2})$ are the known current noise sources associated with the bias resistor and the two amplifiers. S_I represents the signal of interest, i.e., the shot noise associated with the current through the contact. S_{v_1} and S_{v_2} represent the voltage noise sources of each line (amplifier + connecting leads).

essential requirement in order to observe MAR processes. After establishing a contact, which can be held for days, its IV characteristic is measured in the superconducting state (see inset of Fig. 4). Its code $\{\tau_i\}$ is then determined by decomposing this "mesoscopic fingerprint" [10] into the contributions of independent channels as calculated by the theory of quantum coherent MAR [11]. We work with the smallest possible contacts, which typically accommodate in aluminum three channels for a total conductance $G = G_0 \sum_i \tau_i$ of the order of the conductance quantum $G_0 = 2e^2/h$ [10]. Experiments in the normal state are done after applying a magnetic field of 50 mT, which does not affect the transmissions.

The voltage noise across the contact is measured simultaneously by two identical cascades of low noise amplifiers, and the cross spectrum $S_{V_1V_2}(\nu)$ of these two noise signals is calculated by a spectrum analyzer. This "four-point" noise measurement technique eliminates the voltage noise contributions of the resistive leads and of the preamplifiers [12]. We show in Fig. 2a examples of raw spectra $S_{V_1V_2}(\nu)$ [13] of the total noise measured at equilibrium ($I = V = 0$) and at the lowest temperature ($T = 20$ mK) for several contacts in the normal state. The spectra were measured over 800 points in a frequency window from 360 to 3560 Hz, and averaged 1000 times in typically 4 min. In this low-frequency window, the measurement lines behave as one-pole RC filters, and the cross spectrum $S_{V_1V_2}(\nu)$ adopts the form

$$S_{V_1V_2}(\nu) = \frac{R_\parallel^2}{1 + (2\pi\nu R_\parallel C)^2} \times \left[S_I + S_B + 2\left(1 + \frac{R_L}{R_\parallel}\right) S_{\mathrm{Amp}} \right]. \quad (1)$$

Here $R_\parallel = R_B R_D/(R_B + R_D)$, where $R_D(V) = \partial V/\partial I(V)$ is the dynamic resistance of the contact, which is measured simultaneously with the noise using a lock-in technique. C is the total capacitance introduced by the setup across the contact, and R_L is the total resistance of each measurement line. Besides the noise of interest, i.e., the intrinsic current noise of the contact S_I, two sources of background current noise contribute to the signal: the preamplifiers current noise $S_{\mathrm{Amp}}(\nu)$ and the white thermal current noise S_B of the bias resistor, both of which were measured independently. $S_{\mathrm{Amp}}(\nu)$ presents a linear frequency dependence almost identical for the two lines. The solid lines in Fig. 2a correspond to (1) for $V = 0$, in which case the contact contributes just its equilibrium or Johnson-Nyquist white current noise $S_I(0,T) = 4k_BT/R_D$. All measured equilibrium spectra are in agreement with what we expect from the independent characterization of our measurement setup. Therefore, in what follows we use (1) to extract from the measured $S_{V_1V_2}(\nu)$ the shot noise spectral density $S_I(V,T)$, for all contacts in both the normal and the superconducting states. We show in Fig. 2b a typical result of this analysis, as well as the two background contributions which are subtracted from the raw data according to (1). Within the experimental accuracy, we find that shot noise is indeed white. The average value $\langle S_I \rangle$ is the mean value of a Gaussian fit of the spectrum histogram.

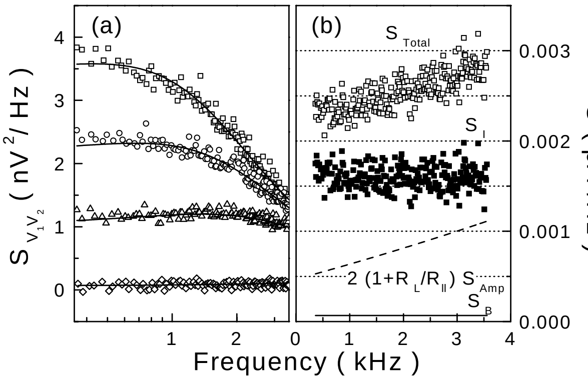

FIG. 2. (a) Measured (symbols) and calculated (solid lines) equilibrium ($V = I = 0$) cross spectra $S_{V_1V_2}(\nu)$ for four different atomic contacts in the normal state (from top to bottom: $R_D = 85.2, 64, 42, 8.5$ kΩ). The calculated spectra include the Johnson-Nyquist noise of the contacts, and the independently measured contributions of preamplifiers and bias-line current noise. They also take into account the calibrated low-pass filtering of the lines. (b) The shot noise power spectrum S_I (■) of the contact is obtained by subtracting from the total measured current noise S_{Total} (□) the two experimental sources of noise S_{Amp} and S_B. For these data, $R_D = 40.8$ kΩ and $I = 2.4$ nA.

The measured voltage dependence of $\langle S_I \rangle$ is shown in Fig. 3a for a typical contact in the normal state, at three different temperatures, together with the predictions of the theory of noise for quantum coherent structures [14,15],

$$S_I(V,T,\{\tau_i\}) = 2eV \coth\left(\frac{eV}{2k_BT}\right) G_0 \sum_i \tau_i(1 - \tau_i) + 4k_BTG_0 \sum_i \tau_i^2, \quad (2)$$

using the independently measured mesoscopic pin code $\{\tau_i\}$. The effective noise temperature is defined as $T^* = S_I/4k_BG$. At $V = 0$, the noise temperature is equal to T. For $eV \gg k_BT$, the noise is dominated by the nonequilibrium part, i.e., shot noise, and becomes linear in V. At $T = 0$, the predicted effective noise temperature reduces to

$$T^* = \frac{eV}{2k_B}\left(1 - \frac{\sum_i \tau_i^2}{\sum_i \tau_i}\right), \quad (3)$$

which is lower than the Poisson limit $eV/2k_B$ by the Fano factor $F(\{\tau_i\}) = 1 - \sum_i \tau_i^2/\sum_i \tau_i$. The noise measured at the lowest temperature for four contacts having different mesoscopic pin codes is shown in Fig. 3b, together with the theoretical predictions of (2). For all contacts the noise measured in the normal state is sub-Poissonian by a Fano factor, in agreement with the $\{\tau_i\}$ determined in the superconducting state. This reduction of the noise, which reflects the absence of fluctuations in the occupation

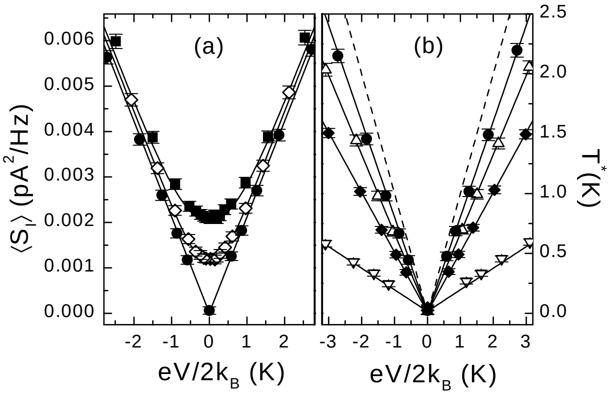

FIG. 3. (a) Symbols: measured average current noise power density $\langle S_I \rangle$ and noise temperature T^* as a function of reduced voltage, for a contact in the normal state at three different temperatures (from bottom to top: 20, 428, 765 mK). The solid lines are the predictions of (2), for the mesoscopic pin code $\{0.21, 0.20, 0.20\}$ as measured independently from the IV in the superconducting state. (b) Symbols: measured effective noise temperature T^* versus reduced voltage for four different contacts in the normal state at $T = 20$ mK. The solid lines are predictions of (2) for the corresponding mesoscopic pin codes (from top to bottom: $\{0.21, 0.20, 0.20\}$, $\{0.40, 0.27, 0.03\}$, $\{0.68, 0.25, 0.22\}$, $\{0.996, 0.26\}$). The dashed line is the Poisson limit.

numbers in the reservoirs, has already been observed in quantum point contacts tailored in 2DEG [16]. In those systems the noise originates essentially from a single channel, all the others being perfectly closed or perfectly open. On the contrary, in atomic contacts, one can have a large palette of mesoscopic pin codes, and our results constitute a first test of the general multichannel formula [17].

Having checked in the normal state the consistency between the measured shot noise reduction factor and the mesoscopic pin code determined from the IV's in the superconducting state, we then measured the noise in the superconducting state. We compare in Fig. 4, for one typical contact, the measured and the predicted $\langle S_I \rangle (V)$, in both the normal and the superconducting states. In the latter the noise is markedly nonlinear, and for high enough voltages it is above the one measured in the former. Note that these nonlinearities are not an artifact due to the voltage dependence of the dynamical resistance $R_D(V)$ entering (1), since $R_D(V)$ is measured with sufficient accuracy. The only ingredient injected into the calculated curves, $S_I(V, T, \{\tau_i\}) = \sum_i s_I(V, T, \tau_i)$, is the mesoscopic pin code $\{\tau_i\}$ extracted from the IV (see inset of Fig. 4). The agreement between experiment and the theory of MAR shot noise [7,8] is quantitative. The excess noise observed at high voltages ($V \gg 2\Delta$) in the superconducting state with respect to the normal state arises from the well-known excess current resulting from MAR processes [18].

The highly nonlinear dependence of the noise for $V < 2\Delta$ reveals the richness of the electronic transport in the superconducting state. This is visualized in Fig. 5, where the measured and the calculated effective charge $q = S_I/2I$ of the "shots" is shown as a function of inverse voltage, for four contacts spanning a large variety of mesoscopic pin codes. As can be seen, q/e does not necessarily correspond to an integer, and for a given voltage it strongly depends on the transmission of the different channels. This is due to the interfering contributions of many MAR processes of different orders. Only for very small τ's, i.e., in the tunnel regime, one expects the shots to correspond to an integer number of electrons [7,8]. Although the sensitivity of this measurement scheme does not allow us to reach this limit, the emergence of a staircase pattern shows the successive predominant role of increasing order MAR processes as the voltage decreases. Note that, for some parameters, one can have $q/e < 1$. This illustrates the fact that, as defined, the shot size not only reflects the superconducting correlations, but also the more trivial dependence of partition noise on transmissions. In other words, the Fano factor is also at play in the superconducting state. Indeed, in the limit $V \to \infty$, one expects $q/e \to F(\{\tau_i\})$. At low voltages, the effective charge diverges (see inset of Fig. 5 for contacts containing an almost ballistic channel), as has already been observed in tunnel junctions containing small defects in the insulating barrier [19] and in diffusive normal weak links [20].

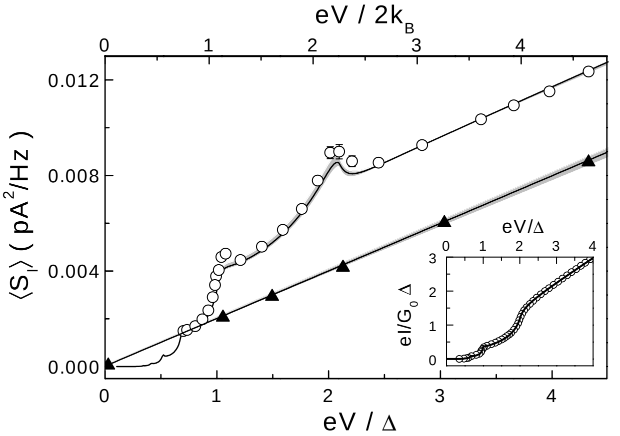

FIG. 4. Symbols: measured average current noise power density versus voltage, for a typical contact both in the normal state (triangles) and in the superconducting state (circles). Voltage is normalized to the measured superconducting gap $\Delta/e \simeq 185$ μV. The solid lines are theoretical predictions, using (2) for the normal state, and using MAR noise theory for the superconducting state. The gray areas represent the fuzziness on the predicted curves due to uncertainties in the determination of the mesoscopic pin code. Inset: superconducting state IV in reduced units. The solid line is a fit to measurements (circles) using [11] and provides the mesoscopic pin code $\{0.40, 0.27, 0.03\}$ and its uncertainty used in the main panel.

We draw the following conclusions from our results. First, shot noise measurements in the normal state are in

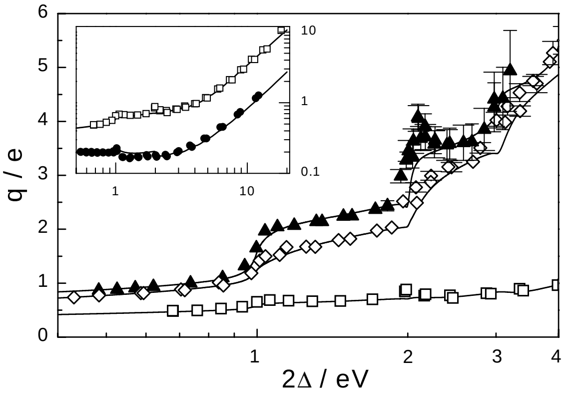

FIG. 5. Symbols: effective size $q/e = S_I/2eI$ of the noise shots versus reduced inverse voltage, for three different contacts in the superconducting state. These symbols are experimental results and the lines are predictions of the MAR theory for noise, using the mesoscopic pin codes determined from fits of the $IV's$. From top to bottom: $\{0.40, 0.27, 0.03\}$, $\{0.68, 0.25, 0.22\}$, $\{0.98, 0.55, 0.24, 0.22\}$. Inset: data for two contacts containing an almost ballistic channel (top $\{0.98, 0.55, 0.24, 0.22\}$, bottom $\{0.996, 0.26\}$) shown on a larger scale.

quantitative agreement with the independent electron multichannel theory using the $\{\tau_i\}$ determined in the superconducting state. Second, our results directly show that at finite bias voltage the microscopic current carrying processes between two superconductors do carry large effective charges. Furthermore, our results are in quantitative agreement with the predictions of the full quantum theory of MAR through a single channel. More generally, these findings, together with our previous measurements of Josephson supercurrents [21] and current-voltage characteristics [10] of superconducting atomic contacts, constitute a comprehensive positive test of the microscopic theory of superconducting transport, and firmly establish the central role of multiple Andreev reflections.

We thank M. Devoret, P. Joyez, P. F. Orfila, and H. Pothier for helpful discussions and permanent assistance. We are grateful to D. C. Glattli and P. Roche for introducing us to the subtleties of noise measurements. We also acknowledge illuminating discussions with D. Averin, J. C. Cuevas, T. M. Klapwijk, A. Levy-Yeyati, A. Martín-Rodero, Y. Naveh, V. Shumeiko, and C. Strunk. This work was partially supported by MAE through PICASSO, le Bureau National de la Métrologie, and the EU NANOMOL IST-1999-12603 project. M. F. G. acknowledges support by FOMEC.

[1] R. Landauer, Nature (London) **392**, 659 (1998).
[2] Ya. M. Blanter and M. Büttiker, Phys. Rep. **336**, 1–166 (2000).
[3] L. Saminadayar *et al.,* Phys. Rev. Lett. **79**, 2526 (1997); R. de-Picciotto *et al.,* Nature (London) **389**, 162 (1997); M. Reznikov *et al.,* Nature (London) **399**, 238 (1999).
[4] X. Jehl *et al.,* Nature (London) **405**, 50 (2000).
[5] T. M. Klapwijk, G. E. Blonder, and M. Tinkham, Physica (Amsterdam) **109B,C–110B,C**, 1657 (1982).
[6] D. Averin and H. T. Imam, Phys. Rev. Lett. **76**, 3814 (1996).
[7] J. C. Cuevas *et al.,* Phys. Rev. Lett. **82**, 4086 (1999).
[8] Y. Naveh and D. Averin, Phys. Rev. Lett. **82**, 4090 (1999).
[9] J. M. van Ruitenbeek *et al.,* Rev. Sci. Instrum. **67**, 108 (1996).
[10] E. Scheer *et al.,* Phys. Rev. Lett. **78**, 3535 (1997); E. Scheer *et al.,* Nature (London) **394**, 154 (1998).
[11] D. Averin and A. Bardas, Phys. Rev. Lett. **75**, 1831 (1995); J. C. Cuevas, A. Martín-Rodero, and A. Levy Yeyati, Phys. Rev. B **54**, 7366 (1996); E. N. Bratus’ *et al.,* Phys. Rev. B **55**, 12 666 (1997).
[12] D. C. Glattli *et al.,* J. Appl. Phys. **81**, 7350 (1997).
[13] About 20 of the 800 points in the spectra corresponded to strong peaks arising from microphonics and from the power line harmonics, and are not shown for clarity.
[14] G. B. Lesovik, Sov. Phys. JETP Lett. **49**, 592 (1989).
[15] Th. Martin and R. Landauer, Phys. Rev B **45**, 1742 (1992); M. Büttiker, Phys. Rev. B **46**, 12 485 (1992).
[16] M. Reznikov *et al.,* Phys. Rev. Lett. **75**, 3340 (1995); A. Kumar *et al.,* Phys. Rev. Lett. **76**, 2778 (1996).
[17] This reduction below Poissonian noise has already been used to obtain partial information on the mesoscopic pin code of normal atomic contacts [H. E. van den Brom and J. M. van Ruitenbeek, Phys. Rev. Lett. **82**, 1526 (1999)].
[18] J. P. Hessling *et al.,* Europhys. Lett. **34**, 49 (1996).
[19] P. Dieleman *et al.,* Phys. Rev. Lett. **79**, 3486 (1997).
[20] T. Hoss *et al.,* Phys. Rev. B **62**, 4079 (2000).
[21] M. F. Goffman *et al.,* Phys. Rev. Lett. **85**, 170 (2000).

4.3.3 Complementary analysis

4.3.3.1 Normal state

To be quantitative, we present in the following table the Fano factor predicted from the mesoscopic PIN code using Exp.(5) and the measured one for the atomic-size contacts presented in Figure 3 of the article. The measured Fano factor is defined as the slope of the curve $(\langle S_I \rangle / 2e)[I]$ at large current, its uncertainty being negligible compared to the one of the calculated factor. The measured factor is in agreement with the predicted one within our experimental accuracy.

Mesoscopic PIN code	**Calculated Fano factor**	**Measured Fano factor**
{0.21,0.20,0.20}	0.80 ± 0.02	0.79
{0.40,0.27,0.03}	0.66 ± 0.02	0.65
{0.68,0.25,0.22}	0.50 ± 0.01	0.49
{0.996,0.26}	0.16 ± 0.01	0.17

4.3.3.2 Superconducting state

We plot in Figure 6 the same data as in Figure 5 of the article for three of the four atomic-size contacts, but presented in terms of the current fluctuation spectral density $\langle S_I \rangle$ as a function of the reduced voltage eV / Δ. The shape of the curves and the intensity of the fluctuations strongly depend on the mesoscopic code. The “circle contact” that contain one almost ballistic channel and one poorly transmitting one ($\tau = 0.26$) has almost for all voltages a spectral density much smaller than the two others. Indeed, the spectral density in both channels is small: for the first one ($\tau = 0.996$) because of its high transmission, and for the second one because it carries a small part of the current. The “square contact” present also one channel with high transmission ($\tau = 0.98$), but in addition three not so well transmitting ones. Together, they contribute with a slightly larger weight to the conductance and thus carry almost the same amount of current which leads to a total spectral density even larger than the “diamond contact” that contains no ballistic channel. However, both the circle and square contacts display a strong increase at low voltages, the signature of their highly transmitting channel. The predictions of the MAR theory account well for this richness.

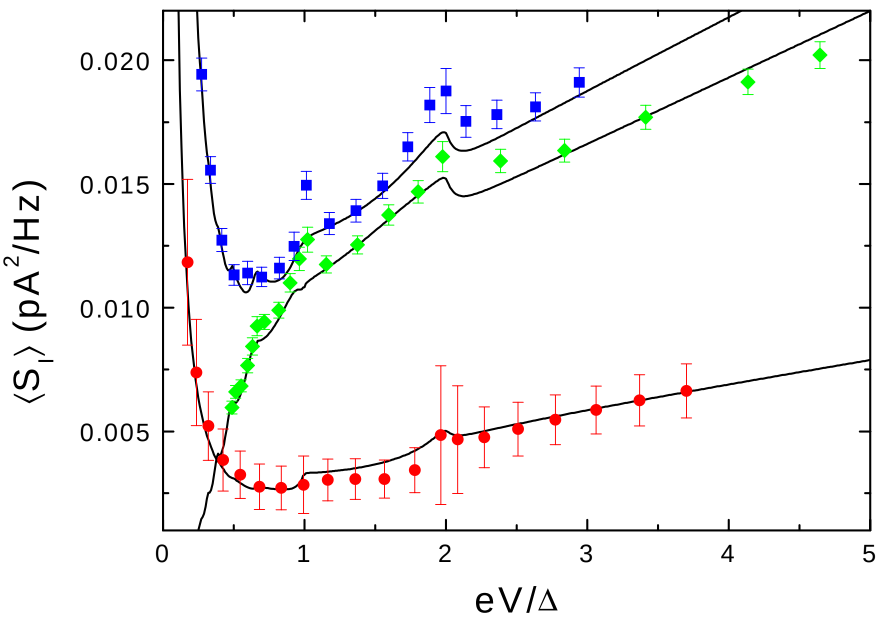

Figure 6: Dots: Measured current fluctuation spectral density as a function of reduced voltage of three atomic-size contacts. Mesoscopic PIN codes: {0.98,0.55,0.24,0.22} (squares), {0.68,0.25,0.22} (diamonds), {0.996,0.26} (circles). Full curves: theoretical predictions of the MAR theory using the mesoscopic code.

Annex Determination of the measurement set-up parameters used in the treatment of the noise spectra

Five parameters enter the procedure used to extract the spectrum of the current fluctuations $S_I(\nu)$ from the raw spectrum $S_{V_1V_2}(\nu)$:

1) <u>The bias resistance</u> R_B:

The bias resistance was measured at low temperature: $R_B = 1.065 \pm 5\times10^{-3}\,\mathrm{M\Omega}$.

2) <u>The spectral density of the bias resistor current fluctuation</u> S_B:

The bias resistor is thermally anchored to the 1K pot of the refrigerator. Its temperature is thus expected to be $T_B = 1.3 \pm 0.2\ \mathrm{K}$ leading to $S_B = 4k_BT_B / R_B = (7\pm1)\ 10^{-29}\ \mathrm{A^2/Hz}$.

3) <u>The total capacitance</u> C_{tot}: The total capacitance is equal to $C_{tot} = C_J + 2C_L + C_B$. The capacitances of the different lines were measured at room temperature, $C_L = 450 \pm 10\ \mathrm{pF}$ and $C_B = 165 \pm 10\ \mathrm{pF}$, and are not expected to change a lot at low temperature. The on-chip capacitance across the junction was measured to be $C_J = 60 \pm 5\ \mathrm{pF}$. On the other hand, one can determine C_{tot} from fits of the frequency dependence of the $S_{V_1V_2}(\nu)$ spectra for various values of the contact resistance and of the bias current (within the model described by Eq.(9)). We found $C_{tot} = 1.16 \pm 0.05\ \mathrm{nF}$, in reasonable agreement with the values measured independently.

4) <u>The voltage line resistance</u> R_L:

The voltage lines resistance was measured at low temperature: $R_L = 1600 \pm 50\ \Omega$.

5) <u>Spectral density of the current noise source of the NF-preamplifiers</u> S_{Amp}:

The input current noise of the NF preamplifiers is determined by measuring the output voltage fluctuations when the preamplifier is loaded with a high resistance. The preamplifier input stage is characterized by its gain G, input resistance R_{in}, and capacitance C_{in}, and its current i_n and voltage υ_n noise sources (see Figure 7).

If a voltage source V_S with output impedance R_S is connected to the preamplifier, the output voltage is equal to:

$$V_{out} = G\left(\upsilon_n + \frac{R_{par}}{1+jR_{par}C_{in}\omega}\left(i_n + \frac{V_S}{R_S}\right)\right), \tag{12}$$

where $R_{par} = R_{in}R_S/(R_{in}+R_S)$. If V_S is just the Johnson-Nyquist voltage noise source of R_S, the output spectral density S_{out} is:

$$S_{out} = G^2\left(S_V + \frac{R_{par}{}^2}{1+\left(R_{par}C_{in}\omega\right)^2}\left(S_{Amp} + \frac{4k_BT}{R_S}\right)\right). \tag{13}$$

Here S_V is the spectral density of υ_n. It is measured by short circuiting the input, in which case $S_{out} = G^2S_V$. The measured spectral density S_V is almost identical for the two NF preamplifiers. It contains a white noise component and a $1/f$ one. A best fit gives for the relevant frequency window the function:

$$S_V(\nu) = (2.20 \pm 0.05\,10^{-18}) + \frac{(4.5 \pm 0.5)10^{-16}}{\nu}\ \mathrm{V^2/Hz}\ .$$

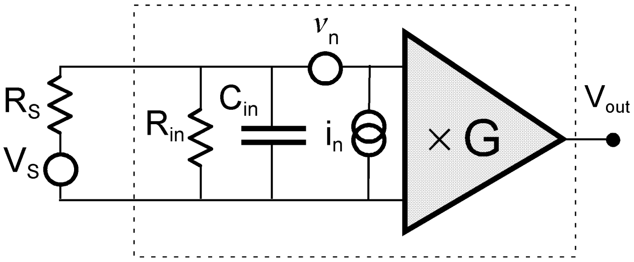

Figure 7: Model of the input stage of the NF preamplifier (dashed rectangle). The input resistance is $R_{in} \simeq 100\ \mathrm{M\Omega}$ and the input capacitance is $C_{in} \simeq 30\ \mathrm{pF}$. In order to measure the current noise source, a high source resistance R_S is connected.

The current noise spectral density is deduced from (13) in two steps. First the transfer function $R_{par}^2/1+\left(R_{par}C_{in}\omega\right)^2$ is measured using a broadband chirp source in series with R_S. In a second time, the spectral density S_{out} of the output voltage V_{out} is measured by the spectrum analyzer SR780 with just the source resistance R_S connected to the preamplifier.

Two source resistances were used, $R_S = 1.522\ \text{M}\Omega$ and $2.714\ \text{M}\Omega$, leading to the same value of S_{Amp}. It is almost identical for both preamplifiers and increases roughly linearly with frequency. A linear fitting procedure leads to the value:

$$S_{Amp}(\nu) = (2.28 \pm 0.2)10^{-28} + (9.06 \pm 0.06)10^{-32}\nu\ \text{A}^2/\text{Hz}\,.$$

This linear frequency dependence arises from the white voltage noise in the channel of the input transistors, which is converted into an input current noise source through a capacitive coupling.

References of Chapter 4

---

[1] W. Schottky, Ann. Phys. (Leipzig) **57**,16432 (1918).

[2] A. van der Ziel, Noise in solid state devices and circuits, Wiley, New York (1986).

[3] Ya. M. Blanter and M. Büttiker, Phys. Rep. **336**, 1 (2000).

[4] A. H. Steinbach, J.M. Martinis, and M.H. Devoret, Phys. Rev. Lett. **76**, 3806 (1996).

[5] M. Henny, S. Oberholzer, C. Strunk, and C. Schönenberger, Phys. Rev. B **59**, 2871 (1999)

[6] C.W.J. Beenaker and M. Büttiker, Phys. Rev. B **46**, 1889 (1992).

[7] K.E. Nagaev, Phys. Lett. A **169**, 103 (1992).

[8] A.H. Steinbach, J.M. Martinis, and M.H. Devoret, Bull. AM. Phys. Soc. **40**, 400 (1995); M.J.M. de Jong, Ph. D. thesis, Leiden University (1995); K.E. Nagaev, Phys. Rev. B **52**, 4740 (1995); V.I. Kozub and A.M. Rudin, Phys. Rev. B **52**, 7853 (1995).

[9] D.E. Prober, M.N. Wybourne, and M. Kansakar, Phys. Rev. Lett. **75**, 3964 (1995).

[10] L. Saminadayar, D.C. Glattli, Y. Jin, and B. Etienne, Phys. Rev. Lett. **79**, 2526 (1997); R. de-Picciotto, M. Reznikov, M. Heiblum, V. Umansky, G. Bunin, and D. Mahalu, Nature (London) **389**, 162 (1997); M. Reznikov, R. de Picciotto, T.G. Griffiths, M. Heiblum, and V. Umansky, Nature (London) **399**, 238 (1999).

[11] M. Büttiker, Phys. Rev. Lett. **65**, 2901 (1990).

[12] Th. Martin and R. Landauer, Phys. Rev. B **45**, 1742 (1992).

[13] B.J. van Wees, H. van Houten, C.W.J. Beenaker, J.G. Williamson, L.P. Kouwenhoven, D. van der Marel, and C.T. Foxon, Phys. Rev. Lett. **60**, 848 (1988).

[14] Y.P. Li, D. C. Tsui, J. J. Heremans, J. A. Simmons, and G. W. Weimann, Appl. Phys. Lett. **57**, 774 (1990).

[15] S. Washburn, R. J. Haug, K. Y. Lee, and J. M. Hong, Phys. Rev B. **44**, 3875 (1991).

[16] M. Reznikov, M. Heiblum, Hadas Shtrikm, and D. Mahalu, Phys. Rev. Lett. **75**, 3340 (1995).

[17] A. Kumar, L. Saminadayar, and D.C. Glattli, Phys. Rev. Lett. **76**, 2778 (1996).

[18] D.C. Glattli, P. Jacques, A. Kumar, P. Pari, and L. Saminadayar, J. Appl. Phys. **81**, 7350 (1997).

[19] H.E. van den Brom and J.M. van Ruitenbeek, Phys. Rev. Lett. **82**, 1526 (1999).

[20] A.F. Andreev, Sov. Phys. JETP **19**, 1228 (1964).

[21] G.E. Blonder, M. Tinkham, and T.M. Klapwijk, Phys. Rev. B **25**, 4515 (1982).

[22] X. Jehl, M. Sanquer, R. Calemczuk, and D. Mailly, Nature (London) **405**, 50 (2000).

[23] J.C. Cuevas, A. Martin-Rodero, and A. Levy Yeyati, Phys. Rev. Lett. **82**, 4086 (1999).

[24] Y. Naveh and D. Averin, Phys. Rev. Lett. **82**, 4090 (1999).

---

[25] P. Dieleman, H.G. Bukkems, T.M. Klapwijk, M. Schicke, and K.H. Gundlach, Phys. Rev. Lett. **79**, 3486 (1997).

Chapter 5 Dynamical Coulomb blockade

Dynamical Coulomb blockade is a quantum effect which appears when a quantum coherent conductor is connected in series with an electromagnetic impedance [1]. It manifests itself as a reduction of the conductance of the conductor at small bias voltages and low temperatures. Dynamical Coulomb blockade was first observed and understood within the framework of single electron tunneling in small capacitance metallic tunnel junctions with a large number of weakly transmitting channels. When an electron tunnels through the insulating barrier, an electronic charge e is transferred very suddenly because the barrier is short (a few nanometers at most), and the electron energy several eV below the potential barrier. This current pulse can excite the electromagnetic environment of the junction, which takes in that case a fraction of the energy available from the voltage source for tunneling: electron tunneling is inelastic, and the reduced phase space available for the transmitted electron results in a reduction of the tunneling rate. This quantum effect is large when the impedance becomes comparable to the resistance quantum.

Recently, a connection between this blockade phenomenon and shot noise has been put forward by Levy-Yeyati *et al.* [2]. Indeed, shot noise in a tunnel junction also results from the random current pulses due to tunneling of single electrons. How deep this relation is? One might wonder in particular if Coulomb blockade is also suppressed, like shot noise is, in an element with perfectly transmitting channels. By treating Coulomb blockade as the response of the current to the insertion of a small impedance in the tunnel junction circuit, Levy-Yeyati *et al.* could solve the case of a single channel tunnel contact with arbitrary transmission. Their main prediction is that Coulomb blockade is suppressed by precisely the same factor $(1-\tau)$ as shot noise, which points to an intimate relationship between Coulomb blockade and shot noise.

In this Chapter we present a first and somewhat preliminary experimental investigation of Coulomb blockade in the high transmission regime. It is organized as follows: first, the standard theory of Coulomb blockade is summarized, and the recent predictions for a single channel with arbitrary transmission are given. Our results on dynamical Coulomb blockade in aluminum atomic-size contacts are then presented and compared to these predictions.

5.1 Coulomb blockade of single electron tunneling

Here we briefly overview the calculation of dynamical Coulomb blockade in tunnel junctions. For detailed calculations, the reader is referred to Ref. [1].

5.1.1 Hamiltonian of a tunnel junction embedded in an electromagnetic environment

The generic circuit displaying Coulomb blockade is sketched in Figure 1. A tunnel junction is placed in series with an electromagnetic impedance $Z_{series}(\omega)$ and a voltage source V. The hamiltonian of this system writes:

$$\hat{H} = \hat{H}_{qp} + \hat{H}_{env} + \hat{H}_{T} - eVN_T \,. \tag{1}$$

● The first term $\hat{H}_{qp}$ describes the two uncoupled electrodes:

$$\hat{H}_{qp} = \sum_{k,\sigma} \varepsilon_k \; c^{+}_{L,k,\sigma} c_{L,k,\sigma} + \sum_{k,\sigma} \varepsilon_k c^{+}_{R,k,\sigma} c_{R,k,\sigma} \,, \tag{2}$$

where $c^{+}_{L(R),k,\sigma}$ and $c_{L(R),k,\sigma}$ denote respectively the creation and annihilation operator of a quasiparticle labeled by the quantum number k and spin σ in the left (L) and right (R) electrodes, and ε_k their energy.

● The second term $\hat{H}_{env}$ is the hamiltonian of the electromagnetic environment of the tunnel element. This environment is fully described by the impedance $Z_{env}(\omega)$, which is is the parallel combination of $Z_{series}(\omega)$ with the junction capacitance C_J (see Figure 1):

$$Z_{env}(\omega) = \frac{Z_{series}(\omega)}{1 + jZ_{series}(\omega)C_J\omega} \,. \tag{3}$$

This impedance can be decomposed in a series combination of *LC* circuits, with a density determined by its real part. The hamiltonian of the environment is then obtained by associating an harmonic oscillator to each one of these modes [3].

● The tunneling term $\hat{H}_T$ couples the two electrodes:

$$\hat{H}_T = \sum_{k,q,\sigma} T_{k,q} c^{+}_{R,q,\sigma} c_{L,k,\sigma} e^{-i\varphi} + \sum_{k,q,\sigma} T^{*}_{k,q} c^{+}_{L,k,\sigma} c_{R,q,\sigma} e^{+i\varphi} \,. \tag{4}$$

Besides the usual operator products $\hat{c}^{+}\hat{c}$ that transfer one quasiparticle from an electrode to the other one [4], it contains the operators $e^{-i\varphi}$ and $e^{i\varphi}$, in which the phase φ, which acts on the environment, is canonically conjugated with the number of transferred electrons: $[\varphi, N_T] = i$. These operators describe the sudden transfer of a single electron charge through the environment impedance.

● The last term is the electrostatic energy associated to the number of electrons gone through the voltage source.

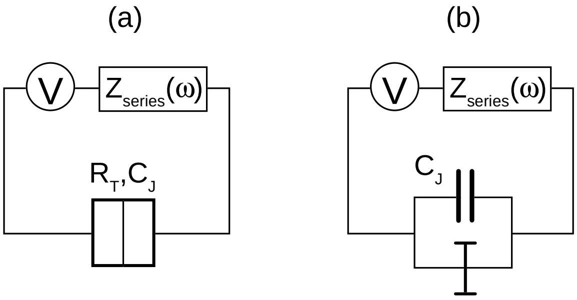

Figure 1: (a) Generic circuit displaying Coulomb blockade of tunneling. A tunnel junction characterized by its resistance R_T and capacitance C_J is connected in series with an impedance $Z_{series}(\omega)$ and a DC voltage source. (b) The tunnel junction is divided into two functional elements: the capacitance of the junction and a pure tunnel element symbolized by the double T symbol. The relevant impedance for the Coulomb blockade of tunneling is the parallel combination of $Z_{series}(\omega)$ and C_J .

5.1.2 Tunneling rates

For a tunnel junction with a large number of channels, the matrix elements $T_{k,q}$ are all very small and the tunnel hamiltonian can be treated as a perturbation. The current at a given voltage V is deduced from the tunneling rates of electrons going from the left to the right $\overrightarrow{\Gamma}(V)$ and from the right to the left $\overleftarrow{\Gamma}(V)$:

$$I(V) = e(\overrightarrow{\Gamma}(V) - \overleftarrow{\Gamma}(V)). \tag{5}$$

The tunnel hamiltonian induces transitions between states of the uncoupled hamiltonian. These states are of the form $|k\rangle \otimes |\Sigma\rangle \otimes |N_T\rangle$, where $|k\rangle$ is a short notation for a quasiparticle state, $|\Sigma\rangle$ is an environment state, and $|N_T\rangle$ a state with a given number of transferred electrons. The transition rates are evaluated with the Fermi golden rule. By example, for the transition rate $\overrightarrow{\Gamma}(V)$, only the first part of the tunneling hamiltonian that transfers electrons from left to right contributes:

$$\sum_{k,q,\sigma} T_{k,q} c^{+}_{R,q,\sigma} c_{L,k,\sigma} e^{-i\varphi} . \tag{6}$$

The calculation then follows the standard tunneling rate calculation, but with a contribution from the environment:

$$\vec{\Gamma}(V)=\frac{2\pi}{\hbar}\int_{-\infty}^{+\infty}d\varepsilon_k d\varepsilon_q\sum_{kq\sigma}\left|T_{kq}\right|^2 f(\varepsilon_k)(1-f(\varepsilon_q))$$
$$\times\sum_{\Sigma,\Sigma'}\overline{\left|\left\langle\Sigma'\right|e^{-i\varphi}\left|\Sigma\right\rangle\right|^2}\,\delta\left(\varepsilon_k+eV+E_\Sigma-\varepsilon_q-E_{\Sigma'}\right), \tag{7}$$

where $E_{\Sigma(\Sigma')}$ is the energy of $\left|\Sigma\right\rangle(\left|\Sigma'\right\rangle)$, $f(\varepsilon)=1/(1+e^{\beta\varepsilon})$ is the Fermi function at temperature T ($\beta=1/k_BT$), and the environmental average is over thermal states.

The term $f(\varepsilon_k)(1-f(\varepsilon_q))$ is the probability that in the initial state the quasiparticle state $\left|k\right\rangle$ is occupied in the left electrode, and the quasiparticle state $\left|q\right\rangle$ empty in the right electrode. The average over the channels leads to:

$$\vec{\Gamma}(V)=\frac{1}{e^2R_T}\int_{-\infty}^{+\infty}\int_{-\infty}^{+\infty}dEdE'f(E)(1-f(E'))$$
$$\times\sum_{\Sigma,\Sigma'}\overline{\left|\left\langle\Sigma'\right|e^{-i\varphi}\left|\Sigma\right\rangle\right|^2}\,\delta\left(E+eV+E_\Sigma-E'-E_{\Sigma'}\right). \tag{8}$$

The environment part can be expressed [1] as a function of the phase correlation function in the Heisenberg representation:

$$J(t)=\left\langle\left[\varphi(t)-\varphi(0)\right]\varphi(0)\right\rangle=\mathrm{Tr}\left(\left[\varphi(t)-\varphi(0)\right]\varphi(0)\rho_\beta\right),$$

in which the time evolution is due to the environment hamiltonian only. Here, ρ_β is the equilibrium density matrix of the environment. One obtains:

$$\sum_{\Sigma,\Sigma'}\overline{\left|\left\langle\Sigma'\right|e^{-i\varphi}\left|\Sigma\right\rangle\right|^2}\,\delta\left(E+eV+E_\Sigma-E'-E_{\Sigma'}\right)$$
$$=\int_{-\infty}^{+\infty}\frac{dt}{2\pi\hbar}\exp(\frac{i}{\hbar}(E-E'+eV)t)\exp(J(t)). \tag{9}$$

The expression of the rate can be recast in the following form:

$$\vec{\Gamma}(V)=\frac{1}{e^2R_T}\int_{-\infty}^{+\infty}\int_{-\infty}^{+\infty}f(E)\left(1-f(E'+eV)\right)P(E-E')dEdE', \tag{10}$$

where $P(\varepsilon)$ is the Fourier transform of $\exp[J(t)]$:

$$P(\varepsilon)=\frac{1}{2\pi\hbar}\int_{-\infty}^{+\infty}dt\exp[J(t)+\frac{i}{\hbar}\varepsilon t]. \tag{11}$$

It can be calculated from the impedance using the following expression of the phase correlation function $J(t)$:

$$J(t)=2\int_0^{+\infty}\frac{d\omega}{\omega}\frac{\mathrm{Re}[Z_{env}(\omega)]}{R_K}\left\{\coth(\frac{1}{2}\beta\hbar\omega)[\cos(\omega t-1)]-i\sin(\omega t)]\right\} \qquad \text{with } R_K=\frac{h}{e^2}\simeq 25.8\ \mathrm{k}\Omega. \tag{12}$$

Physically, $P(\varepsilon)$ is the probability for an electron tunneling through the tunnel barrier to give an amount ε of its energy to the environment.

5.1.3 The distribution function $P(\varepsilon)$

As expected for a probability density, the integral over energy of $P(\varepsilon)$ is normalized to 1:

$$\int_{-\infty}^{+\infty}P(\varepsilon)d\varepsilon=e^{J(0)}=1.$$

Furthermore, $P(\varepsilon)$ verifies the so-called detailed balance symmetry:

$$P(-\varepsilon)=e^{-\beta\varepsilon}\,P(\varepsilon)\,, \tag{13}$$

which means that the probability to excite the environment is larger than the probability to draw energy from it by a Boltzmann factor.

In absence of an environment, the phase does not fluctuate, and one has $J(t)=0$ and $P(\varepsilon)=\delta(\varepsilon)$. Tunneling is elastic, and one recovers the usual expression for the tunneling rate:

$$\vec{\Gamma}(V)=\frac{1}{e^2R_T}\int_{-\infty}^{+\infty}f(E)\left(1-f(E+eV)\right)dE\ . \tag{14}$$

In presence of an electromagnetic environment, the probability to find an occupied state in the left electrode with energy E and an empty state in the right electrode with energy $E'+eV$ is convoluted with the probability $P(\varepsilon)$ to give an energy $\varepsilon=E-E'$ to the environment (see Figure 2).

The perturbative limit

The calculation of $P(\varepsilon)$ is simplified when the real part of the environment impedance is much smaller than the resistance quantum $\mathrm{Re}[Z_{env}(\omega)] \ll R_K$, so that the exponential of $J(t)$ can be approximated by $1+J(t)$ in Exp.(11). At zero temperature, the inelastic part of $P(\varepsilon)$ then writes:

$$P_{inel}(\varepsilon) = \frac{2}{\varepsilon}\frac{\mathrm{Re}[Z_{env}(\varepsilon/\hbar)]}{R_K}. \tag{15}$$

This approximation consists in neglecting all multi-photon excitations of the environment.

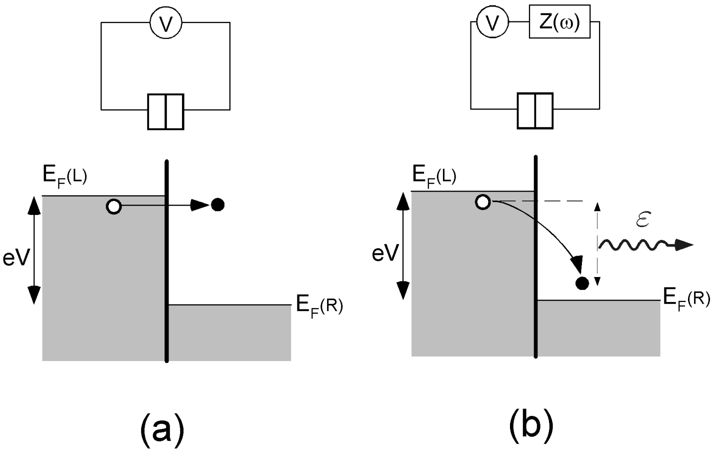

Figure 2: Schematic representation of a tunnel event without (a) and with (b) an impedance in series at zero temperature. Electronic states on both side of the junction are filled up to the Fermi energies, which are shifted by *eV*. In absence of environment, the tunneling is elastic. An electron in the left electrode with energy higher then $E_{F(R)}$ finds an empty state in the right electrode. In presence of an environment, tunneling is inelastic. An electron has a probability $P(\varepsilon)$ to give an amount of its energy ε to the environment. As in the right electrode, states with energy below $E_{F(R)}$ are not available, the phase space for electronic transitions is reduced, and so is the tunneling rate.

5.1.4 Conductance

The conductance is derived from the expression for the current:

$$G(V) = \frac{dI}{dV}(V) = \frac{1}{R_T}\int_{-\infty}^{+\infty}\int_{-\infty}^{+\infty} f(E)\left(-\frac{\partial f}{\partial E}(E'-eV) - \frac{\partial f}{\partial E}(E'+eV)\right)P(E-E')dEdE'. \tag{16}$$

Using the detailed balance relation (13) for $P(\varepsilon)$, this expression can be considerably simplified. In particular, at zero temperature, it can be shown that [1]:

$$G(V)=\frac{1}{R_T}\int_{-\infty}^{e|V|}d\varepsilon P(\varepsilon)\,, \tag{17}$$

which corresponds to a relative conductance change:

$$\frac{\delta G}{G}(V)\equiv\frac{G(V)-G(\infty)}{G(\infty)}=-\int_{e|V|}^{+\infty}d\varepsilon P(\varepsilon). \tag{18}$$

This expression shows that the conductance reduction is simply due to missing transitions: inelastic tunnel events with an energy transfer to the environment larger than eV are forbidden because states below the Fermi energy are fully occupied at zero temperature.

The temporal representation

Starting from $Z_{env}(\omega)$, the calculation of the conductance using Exp. (11),(12) and (16) necessitates three successive integrals. This number of integrations can be reduced to two since the conductance change can be directly related to $J(t)$, without calculating $P(\varepsilon)$ [5]:

$$\frac{\delta G}{G}(V)=2\int_0^{+\infty}\frac{dt}{\hbar\beta}\frac{\pi t}{\hbar\beta}\operatorname{Im}\left[\exp\left[J(t)\right]\right]\cos\left(\frac{eVt}{\hbar}\right)/\sinh^2[\frac{\pi t}{\hbar\beta}]. \tag{19}$$

5.1.5 The *RC* environment

The electromagnetic environment implemented in our experiment is close to a simple RC circuit with impedance:

$$Z_{env}(\omega)=\frac{R}{1+jRC\omega}. \tag{20}$$

This particular case is simple and amenable to analytic calculations. The relative reduction of the conductance predicted by Exp. (19) is plotted in Figure 3 for different temperatures, with values of the resistance and of the capacitance close to the experimental ones.

The dynamical Coulomb blockade manifests itself as a conductance dip at zero voltage. The dip shows up when the temperature is less than E_C/k_B, where $E_C=e^2/2C$ is the charging energy, and gets deeper and steeper as the temperature is lowered. The relative conductance change depends on the temperature and capacitance only through the ratio $k_B T / E_c$. At the base temperature ~ 10 mK of a dilution fridge, the capacitance has to be much smaller than $e^2 / 2k_B 10^{-2} \simeq 90\,\mathrm{fF}$ to observe a well developed conductance dip. For the particular values of the resistance and capacitance taken in Figure 3, at the lowest temperature and at zero voltage, the conductance is reduced by $38\,\%$. This maximum reduction would be larger for a larger resistance. The representation on a logarithmic scale (see inset in Figure 3) reveals three regimes: two saturations at small and large voltages, with an almost logarithmic behavior at intermediate voltages. At large voltages, the conductance tends asymptotically to the bare tunnel conductance in absence of any environment. At low voltages, the dip is smeared on a voltage scale of the order of $k_B T / e$.

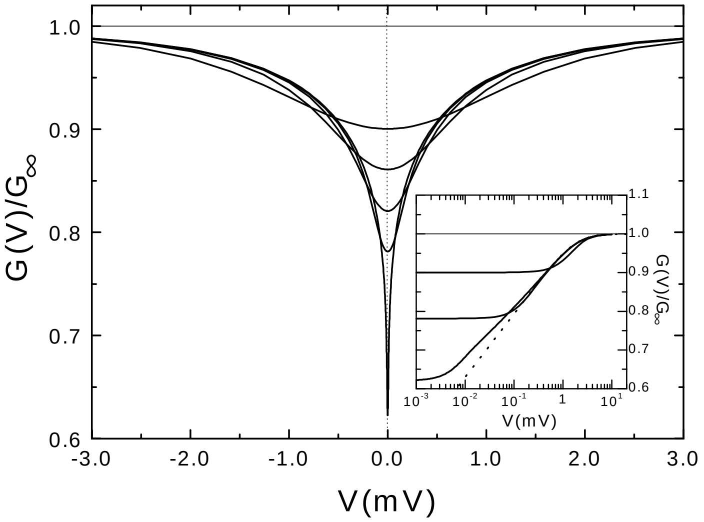

Figure 3: Normalized conductance of a tunnel junction placed in series with a resistance $R = 920\,\Omega$ as a function of voltage, at different temperatures. Main panel: from top to bottom, T=4 K, 2 K, 1 K, 500 mK, and 20 mK. Junction capacitance is $C_J = 0.40\,\mathrm{fF}$. Inset: From top to bottom, T= 4 K, 500 mK, and 20 mK. Dotted line is the zero temperature perturbative expression (21). Note the log scale on horizontal axis.

The zero temperature perturbative limit

The logarithmic behavior appears clearly in the zero temperature perturbative limit. For the RC environment impedance given by (20), Exp. (18) yields:

$$\frac{\delta G}{G}(R,C,T=0\,\mathrm{K},V)=-G_0R\ln\left(\sqrt{1+\left(\frac{\hbar}{eRCV}\right)^2}\right). \tag{21}$$

In the limit $(\hbar/eVRC)^2 \gg 1$, the relative conductance change can be written as:

$$\frac{\delta G}{G}(R,C,T=0\,\mathrm{K},V)\simeq 2.3G_0R\log(V)+\mathrm{K} \tag{22}$$

The predictions of this perturbative and zero temperature expression are compared to the exact result in the inset of Figure 3. For the value of the resistance considered, the perturbative calculation reproduces quite well the intermediate voltage behavior.

However, the finite temperature perturbative calculation (not shown in Figure 3) does not account quantitatively for the thermal rounding at small voltages: the zero voltage conductance reduction is systematically overestimated. The environment impedance is too large for the perturbative theory to be quantitative at small voltages.

5.2 Coulomb blockade in a single conduction channel contact

In the calculations completed by Yeyati *et al.* [2], a contact with a single conduction channel in series with an impedance is described by the same type of hamiltonian as in the tunnel case, but for the tunnel term which now takes the form:

$$\hat{H}_T=\sum_{\sigma}T_0(c^+_{L\sigma}c_{R\sigma}e^{-i\varphi}+c^+_{R\sigma}c_{L\sigma}e^{+i\varphi}), \tag{23}$$

with a hopping term which transfers an excitation between two localized states that are not eigenstates of the uncoupled hamiltonian. In absence of environment, T_0 is related to the channel transmission probability by the relation $\tau=4(T_0/W)^2/(1+(T_0/W)^2)^2$, where $1/W$ is proportional to the density of states in the electrodes. When T_0 varies from 0 to W, the channel transmission goes from 0 to 1. Contrary to the tunnel case, the hopping term is not small, and the hamiltonian $\hat{H}_T$ cannot be treated as a perturbation. The current is not evaluated from transition rates, but from the average value of the current operator:

$$\hat{I} = \frac{ie}{\hbar}\sum_{\sigma} T_0 (c^{+}_{L\sigma} c_{R\sigma} e^{-i\varphi} - c^{+}_{R\sigma} c_{L\sigma} e^{+i\varphi}) , \tag{24}$$

which is calculated using the Keldysh formalism [6]. The perturbative series expansion in the hopping term T_0 is resummed. The calculation has been worked out in the perturbative limit in impedance ($\mathrm{Re}[Z_{env}(\omega)] \ll R_K$).

The Coulomb blockade dip is simply reduced from its tunnel value by the same factor $(1-\tau)$ as shot noise and that at any temperature *T*:

$$\frac{\delta G}{G}(\tau, T) = (1-\tau)\frac{\delta G}{G}(Tunnel, T) \tag{25}$$

At zero temperature, the conductance variation then writes (see Exp. (15) and (18)):

$$\frac{\delta G}{G}(\tau, T = 0\,\mathrm{K}) = -G_0 (1-\tau)\int_{e|V|}^{+\infty} dE\, \frac{\mathrm{Re}[Z_{env}(E/\hbar)]}{E} . \tag{26}$$

The relation between Coulomb blockade and shot noise is thus the same for a contact with an arbitrary transmission as for a tunnel junction.

The *RC* environment

In the case of an RC environment, the relative reduction of the channel conductance is, at zero temperature:

$$\frac{\delta G}{G}(\tau, R, C, T = 0\,\mathrm{K}, V) = -G_0 R (1-\tau)\ln\sqrt{1+\left(\frac{\hbar}{eVRC}\right)^2} , \tag{27}$$

and in the case of several channels with transmission probabilities $\tau_1, ..., \tau_N$:

$$\frac{\delta G}{G}(\{\tau_1, ..., \tau_N\}, R, C, T = 0\,\mathrm{K}, V) = -G_0 R F(\{\tau_1, ..., \tau_N\})\ln\sqrt{1+\left(\frac{\hbar}{eVRC}\right)^2} , \tag{28}$$

where $F(\{\tau_1, ..., \tau_N\}) = 1 - \sum_i \tau_i^2 / \sum_i \tau_i$ is the Fano factor already encountered in the expression of shot noise (see Chapter 4). The effect of the Fano factor is to reduce the amplitude of the logarithmic term in the intermediate voltage regime, and is equivalent to a reduction of the impedance. The relative conductance change is plotted in Figure 4 for different Fano factors, and for the same values of the resistance and of the capacitance as in the previous paragraph. At finite temperature, the expression is modified like in the tunnel case.

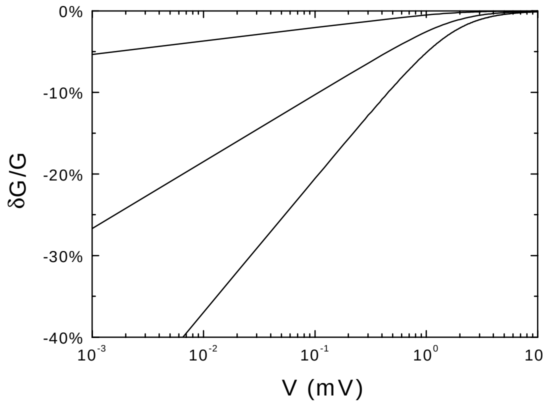

Figure 4: Relative reduction of the conductance of a quantum coherent conductor with capacitance $C_J = 0.40\ \text{fF}$ placed in series with a resistance $R = 920\ \Omega$, at zero temperature, for different Fano factors. From top to bottom, $F = 0.1$, $F = 0.5$, $F = 1$ (tunnel regime).

5.3 Measuring dynamical Coulomb blockade in atomic-size contacts

In order to measure the dynamical Coulomb blockade in atomic-size contacts, we have implemented a resistive on-chip environment as close as possible to the break-junction. This environment consists of four thin aluminum leads as discussed in Chapter 2 (section 2.1.4). The measurements proceed in two steps. First, the current-voltage characteristic of the atomic-size contact is measured in the superconducting state, when the DC resistance of the aluminum leads is zero, in order to determine the mesoscopic code. Then, a $200\ \text{mT}$ magnetic field is applied perpendicularly to the plane of the sample to drive the aluminum in the normal state. The lead resistance is then about $900\ \Omega$. The differential conductance G of the atomic-size contacts is measured as a function of the DC bias voltage using lock-in techniques.

We first discuss the on-chip electromagnetic environment provided by the thin aluminum leads and the capacitance of the junction.

5.3.1 Characteristics of the on-chip electromagnetic environment

The design of the electrical circuit close to the break junction is constrained by several factors. On one hand, Coulomb blockade should be large enough to be distinguished from conductance fluctuations, of the order of one percent [7], even in the high transmission limit. On the other hand, the lead resistance has to be kept small enough to avoid heating, and to allow for a comparison with the perturbative calculation.

With these factors in mind, we fabricated aluminum leads $25\,\mu\mathrm{m}$ long, $200\,\mathrm{nm}$ wide and $12\,\mathrm{nm}$ thick. The resistance of each lead was about $920\,\Omega$, which corresponds to a resistance per unit length $r = 36.8\,\Omega.\mu\mathrm{m}^{-1}$. The value of the resistance is small enough to allow a comparison with the perturbative theory and avoid spurious heating. We calculated that the Coulomb blockade dip is not significantly modified by electron heating in resistors with these parameters, essentially because the Coulomb blockade dip is sensitive to the electronic temperature only in the low voltage region where the current and consequently the heating are small.

The capacitance per unit length of each lead to the underlying ground plane, calculated from the lead geometry, is $c \simeq 5.10^{-2}$ fF.µm^{-1} (Note that, after partial etching of the polyimide insulating layer, the leads are lying onto the polyimide surface). The anchoring pads that sustain the metallic bridge (see Chapter 2) are $12\,\mu\mathrm{m}$ long, $3\,\mu\mathrm{m}$ wide and $160\,\mathrm{nm}$ thick. We estimate their mutual capacitance to be about $0.10\,\mathrm{fF}$. The capacitance between the two electrodes forming the atomic-size contact is difficult to evaluate because the geometry of the contact is not known. However, it is expected to be smaller than that of the pads. The total contact capacitance should thus be about the same for all contacts with the same design.

5.3.2 Environment impedance

The environment impedance $Z_{env}(\omega)$ consists of the impedance of the thin resistive aluminum leads Z_{lead} in parallel with the contact capacitance $C_{contact}$:

$$Z_{env}\left(\omega\right)=\frac{Z_{lead}\left(\omega,r,c,L,Z_{\ell oad}\right)}{1+jZ_{lead}\left(\omega,r,c,L,Z_{\ell oad}\right)C_{contact}\omega}. \tag{29}$$

The aluminum leads can be modeled by a RC transmission line terminated by an impedance Z_{load}. The impedance of this transmission line $Z_{lead}\left(\omega,r,c,L,Z_{load}\right)$ depends on its resistance r and capacitance c per unit length, on its length L, and on the load that closes the transmission line. In our measurement set-up, the load impedance is provided by the large capacitor formed by the connecting pads $C_{pads}\simeq 150\,\mathrm{pF}$. These large capacitors ensure that the environment impedance is well defined by the on-chip electrical circuit, and not by the remaining part of the measuring lines.

The impedance $Z_{lead}\left(\omega,r,c,L\right)$ of the transmission lines writes [1]:

$$Z_{lead}\left(\omega,r,c,L\right)=\sqrt{\frac{r}{j\omega c}}\frac{e^{2ik(\omega,r,c)L}-\lambda(\omega,r,c,Z_{\ell})}{e^{2ik(\omega,r,c)L}+\lambda(\omega,r,c,Z_{\ell})}, \tag{30}$$

where

$$k(\omega,r,c)=\left(-jrc\omega\right)^{1/2}$$

is the wave vector, and

$$\lambda(\omega,r,c,Z_{\ell})=\left(\sqrt{r/jc\omega}-Z_{\ell}\right)/\left(\sqrt{r/jc\omega}+Z_{\ell}\right)$$

is the reflection coefficient. The frequency dependence of $\mathrm{Re}[Z_{env}\left(\omega\right)]$ is shown in Figure 5.

Although the precise frequency dependence differs from that of a single pole RC circuit, the departure is small as far as Coulomb blockade is concerned. In the following, we thus make the approximation:

$$\mathrm{Re}[Z_{env}(\omega)]=\frac{R}{1+(RC\omega)^{2}}\ , \tag{31}$$

where the effective capacitance C takes into account the capacitance of the aluminum leads and of the junction capacitance.

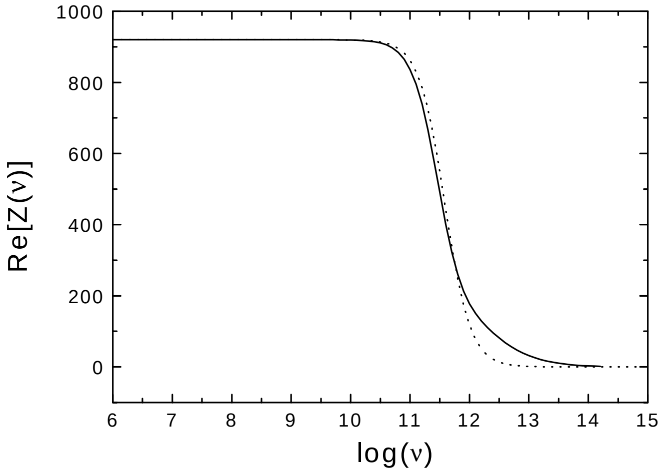

Figure 5: (Full line) Real part of $Z_{env}(\omega)$ calculated from (29) with $r = 36.8\ \Omega.\mu\mathrm{m}^{-1}$, $c = 5\,10^{-2}\ \mathrm{fF}.\mu\mathrm{m}^{-1}$, $L = 25\ \mu\mathrm{m}$, and $Z_{load} = 1/\,jC_{pads}\omega$ with $C_{pads} = 150\ \mathrm{pF}$, and $C_J = 0.10\ \mathrm{fF}$ as a function of the frequency logarithm. The –3dB point is at 300 GHz. (Dotted line) Real part of the impedance calculated from (31) (RC model) with $R = 920\ \Omega$ and $C = 0.45\ \mathrm{fF}$. This simplified model describes reasonably well the overall shape of the real part of the impedance.

5.4 Experimental results

We first discuss the determination of the mesoscopic code in presence of the superconducting aluminum leads.

5.4.1 Mesoscopic code determination

The current-voltage characteristic in the superconducting state (see Figure 6) presents two evident unusual features that make the code determination less accurate than in the case in which there is no environment. First, a current rounded peak shows up at a voltage around $170\ \mu\mathrm{V}$, which corresponds to $eV \simeq 1.3\,\Delta$. This voltage decreases with the magnetic field like the gap energy. The origin of this current peak is not known, but it might involve a resonance in the circuit involving the inductance of the aluminum leads.

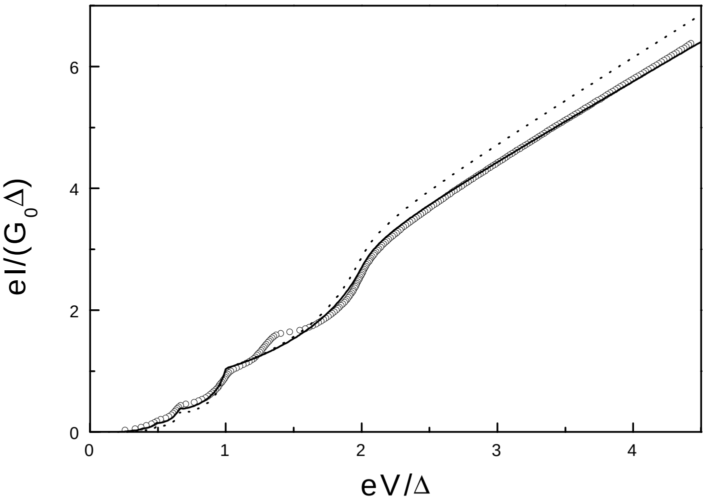

Figure 6: Measured current-voltage characteristic of a single atom aluminum contact embedded in the environment described in 5.3.1(circles) and best fit by the standard MAR theory (full line) with the mesoscopic PIN code {0.60,0.35,0.31}. The measured current-voltage characteristic presents a strong current peak around $V \simeq 1.3\,\Delta/e$, which is not accounted for. The dotted line is the best fit obtained when the correct conductance at large voltages is imposed. Clearly, this leads to an overestimated excess current.

Second, some current at large voltages ($V > 2\Delta/e$) is "missing". This point is particularly clear in the tunnel regime, as shown in Figure 7. In the contact regime, this makes impossible to fit correctly both the conductance and the excess current at large voltage (see Figure 6). We attribute these features to the residual Coulomb blockade resulting from the impedance of the superconducting thin aluminum leads at finite frequency.

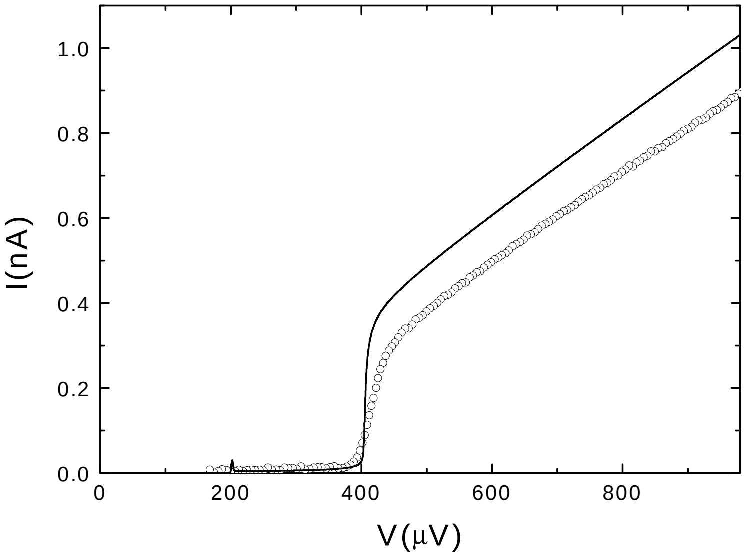

Figure 7: Circles: Current-voltage characteristic in the tunnel regime ($G \simeq 0.0136\,G_0$). Full line: Theoretical current-voltage characteristic of one channel with transmission probability $\tau = 0.0136$. For voltages larger than 2Δ, the measured current is substantially smaller than expected.

5.4.1.1 Impedance of the superconducting aluminum leads at finite frequency

At low frequency $\nu < 2\Delta/h$, the aluminum films behave like pure inductors. However, at frequencies above $2\Delta/h$, Cooper pairs can be broken into two quasiparticles, and the aluminum leads become dissipative. The admittance $Y(\omega)$ per unit length of a diffusive superconducting wire has been calculated within the framework of the BCS theory [8]. At zero temperature, the real and imaginary parts are given by:

$$Y_1(\omega) = \frac{1}{R}\left[\left(1+\frac{2\Delta}{\hbar\omega}\right)E(k(\omega)) - \frac{4\Delta}{\hbar\omega}K(k(\omega))\right] \text{ for } \hbar\omega \geq 2\Delta.,$$

$$Y_2(\omega) = -\frac{1}{R}\left[\frac{1}{2}\left(1+\frac{2\Delta}{\hbar\omega}\right)E(k') - \frac{1}{2}\left(1-\frac{2\Delta}{\hbar\omega}\right)K(k')\right],$$

where $k(\omega) = \left|(2\Delta - \hbar\omega)/(2\Delta + \hbar\omega)\right|$, E and K are complete elliptic integrals, and where $k'(\omega) = (1-k(\omega)^2)^{1/2}$. The frequency dependence of these functions is shown in Figure 8, in units of the normal state admittance.

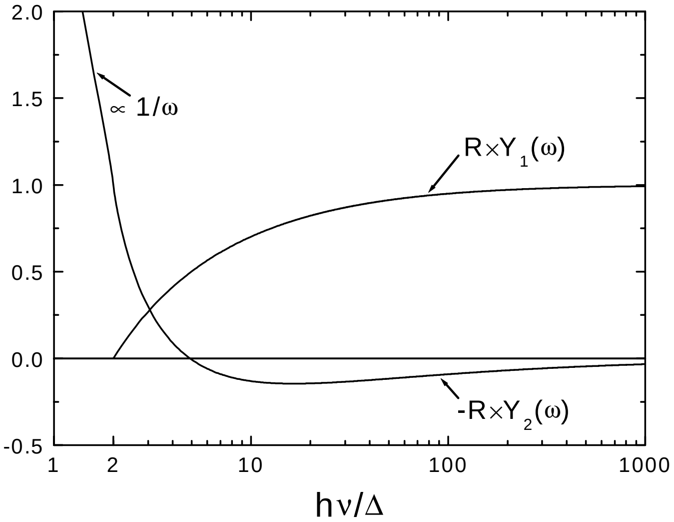

Figure 8: Real and imaginary part of the admittance of a superconducting lead as a function of the reduced frequency. The gap frequency is $\Delta/h \simeq 49\text{ GHz}$ for aluminum. The real part tends asymptotically to the normal state admittance $1/R$.

In the superconducting state, the environment impedance of the contact is thus:

$$Z_{env}^{S}\left(\omega\right)=\frac{1}{Y_1(\omega)+jY_2\left(\omega\right)+jC\omega}. \tag{32}$$

5.4.1.2 Coulomb blockade of the tunnel superconducting current-voltage characteristic

The calculation of Coulomb blockade in normal tunnel junctions, whose key lines were presented in Sec. 5.1, can be almost directly transposed to the case of quasiparticle tunneling in the superconducting state. At zero temperature, the current-voltage characteristic in presence of an electromagnetic environment $I_{env}(V)$ is just the convolution of the current-voltage characteristic without any environment $I(V)$ with the function $P(E)$ associated to the environment impedance $Z_{env}^{S}\left(\omega\right)$[9,1]:

$$I_{env}(V)=\int_{-\infty}^{+\infty}dE\;P(eV-E)\;I\left(E/e\right). \tag{33}$$

The function $P(E)$ presents two parts: a delta function at zero energy corresponding to elastic transitions, and an inelastic part for energies larger than 2Δ. The weight of the zero energy peak is in this case:

$$W_{el}=\exp\left(-2\int_{0}^{+\infty}\frac{\mathrm{Re}[Z_{env}^{S}(\omega)]}{R_K}\frac{d\omega}{\omega}\right).$$

For our particular environment parameters, the elastic contribution is reduced to about 80% of its bare value. The inelastic contribution to $I_{env}(V)$ is non zero only for voltages larger than $4\Delta/e$ as the inelastic part of $P(E/e)$ and the bare current-voltage characterictic $I(V)$ are non zero only for voltages larger than $2\Delta/e$. Up to $4\Delta/e$, $I_{env}(V)$ is simply given by:

$$I_{env}(V)=W_{el}\;I(V)\quad(V<4\Delta/e).$$

As can be seen in Figure 9, this model for $I_{env}(V)$ explains the observed reduction of the current quite well. We have also extended this Coulomb blockade model to the first MAR process in the weak transmission regime, and reached a satisfactory agreement between experiment and theory, using the same parameters.

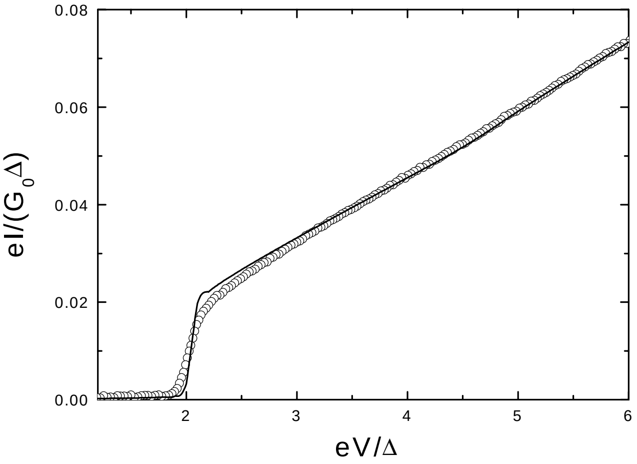

Figure 9: Circles: measured current-voltage characteristic in the tunnel regime: $G \simeq 0.0136\, G_0$ (same data as in Figure 7). Full line: characteristics calculated using Exp. (33) with the perturbative value of $P(\varepsilon)$ associated to the environment impedance $Z^S_{env}(\omega)$. The capacitance in $Z^S_{env}(\omega)$ is taken equal to $0.43\,\mathrm{pF}$.

5.4.1.3 Conclusion

The residual Coulomb blockade resulting from the high frequency impedance of the superconducting aluminum leads is thus well understood in the tunnel regime. However, the way in which Coulomb blockade modifies MAR processes is not known in general. At intermediate transmissions $0.05 \lesssim \tau \lesssim 0.6$ these modifications are appreciable, and excellent fits with the standard theory are not possible, as shown in Figure 6. For higher transmissions however, satisfactory fits become again possible, as shown in Figure 10. The unexplained current peak around $1.3\,\Delta$ progressively washes out, and the fits better account for the slope at voltages larger than 2Δ. In the ballistic limit, we think that the code determination becomes precise enough to allow possible a comparison between Coulomb blockade measurements in the normal state and the predictions of Exp. (28).

Note that Coulomb blockade of MAR processes, presented here as a drawback, is a very interesting phenomenon by itself. Indeed, one could expect for MAR processes of order *n*, which correspond to the transfer of *n* electron charges, a blockade n^2 times stronger than for single charge tunneling in the weak transmission limit. The connection between Coulomb blockade and shot noise could be tested here more deeply than for contacts in the normal state. To our knowledge, this subject has not yet been investigated, neither theoretically nor experimentally.

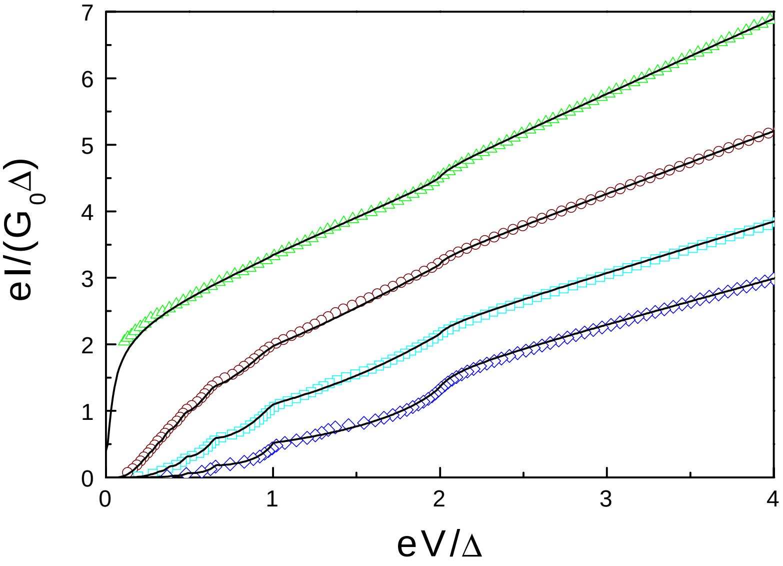

Figure 10: Superconducting current-voltage characteristics of four atomic-size contacts together with the best theoretical fits of the standard MAR theory. Mesoscopic PIN codes: {0.993,0.06,0.05} (up-triangles), {0.85,0.07} (circles), {0.70, 0.05} (squares), {0.52,0.14} (diamonds).[1]

5.4.2 Coulomb blockade in the normal state: the tunnel regime

The conductance of a tunnel contact in the normal state is shown in Figure 11 at different temperatures, together with the predictions of the full Coulomb blockade theory (Exp. (19)) for an RC environment (the capacitance was used as the only free parameter). As can be seen, reproducible conductance fluctuations are superposed onto the Coulomb blockade dip. These fluctuations result from quantum interference effects that depend on the

---

[1] Notice that the last three contacts are somewhat uncommon, in that they only have two conduction channels whereas the smallest aluminum contacts usually have three. In fact, all these contacts correspond to almost the same atomic configuration and were all obtained on the same conductance plateau while stretching the contact. One channel is weakly transmitting and the second one has a much higher transmission probability. The highest transmission is adjusted by stretching elastically this particular configuration, the lowest one remaining almost unchanged.

detailed arrangement of the atoms in the vicinity of the contact [7]: transmitted electronic waves interfere with the part of themselves that is back-scattered towards the contact by different impurities in the electrode. Since the phase accumulated in these random paths depends on the electron energy, the interference term depends on the bias voltage resulting in a modulation of the conductance.

Beside these fluctuations, the theoretical curves describe quite well the conductance dip. In particular, the thermal rounding of the dip is quantitatively reproduced for the three highest temperatures. At the lowest temperature of 20 mK, the observed rounding corresponds in fact to a temperature of 40 mK (see inset). We attribute this excess temperature to electron heating by spurious noise. Note that the capacitance value $C = 0.40\,\mathrm{fF}$ that comes out from these fits, is in close agreement with the estimated value given in section 5.3.2.

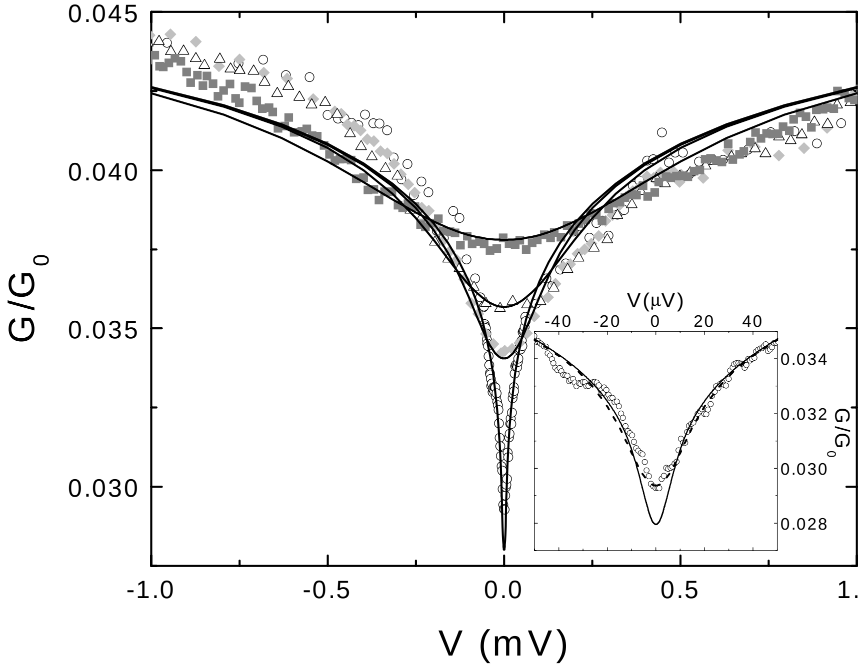

Figure 11: Main panel : Symbols: Differential conductance in units of G_0 of a tunnel contact at four different temperatures as a function of bias voltage; from top to bottom: T=1.39 K, 615 mK, 318 mK, and 20 mK. The asymptotic conductance at large voltages is $0.045\,G_0$ corresponding to a resistance of $290\ \mathrm{k}\Omega$. Full lines: theoretical curves calculated using Exp. (19) with an RC environment ($R = 920\ \Omega$ and $C = 0.40\ \mathrm{fF}$). Inset: Zoom around zero voltage for the lowest temperature T=20 mK. Dotted line is the prediction for T= 40 mK.

5.4.3 Coulomb blockade in the normal state: the ballistic regime

5.4.3.1 Coulomb blockade vanishes in the high transmission limit

We have measured the conductance of a series of contacts in the normal state whose codes had been determined previously. The relative conductance change of three of them, ranging from the tunnel regime to the almost ballistic regime, is shown in Figure 12. The main observation is a strong reduction of the Coulomb blockade dip when the transmission increases. At intermediate transmission $\tau \simeq 0.63$, the Coulomb dip is already significantly reduced compared to the tunnel case. For the contact containing an almost ballistic channel with $\tau = 0.992$, the dip has almost completely disappeared, the remaining small dip arising from the second weakly transmitting channel ($\tau = 0.11$).

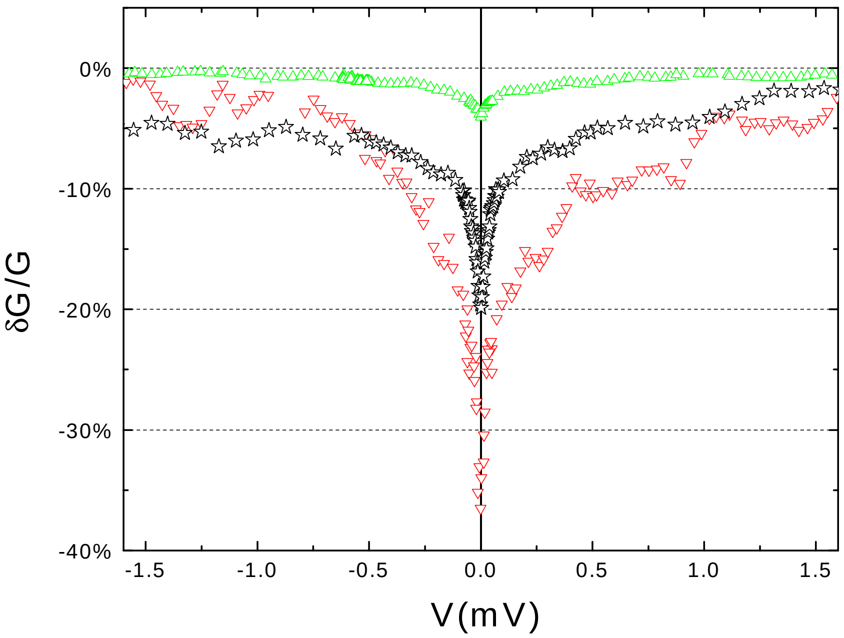

Figure 12: Relative conductance reduction of three atomic-size contacts at 20 mK. Mesoscopic PIN codes are {0.993,0.06,0.05} (up-triangles, same as in Figure 10), {0.63,0.06} (stars), and {0.045} (down-triangles, tunnel contact presented in section 5.4.2).

5.4.3.2 Comparison with the perturbative theory for arbitrary transmission

Our experimental results for five contacts are compared to the zero temperature prediction of Exp. (28) in Figure 13. The corresponding current-voltage characteristics in the superconducting state, used to determine the codes, can be seen in Figure 10.

The theoretical curves correspond to the predictions of Exp. (28) with the capacitance used to fit the data in the tunnel regime (section 5.4.2) and the Fano factor calculated from the mesoscopic codes. We restrict ourselves to the zero temperature predictions because, as already mentioned in section 5.1.5, the environment impedance is too high for the perturbative theory to account well for the thermal rounding at small voltages. The predicted conductance reduction in the logarithmic region is in relative good agreement with the experimental data for all Fano factors, but in all cases too large. We attribute this systematic deviation to the deficiency of the perturbative theory. Indeed, a better agreement is reached in the tunnel regime if one uses the full non-perturbative theory (dotted line in Figure 13).

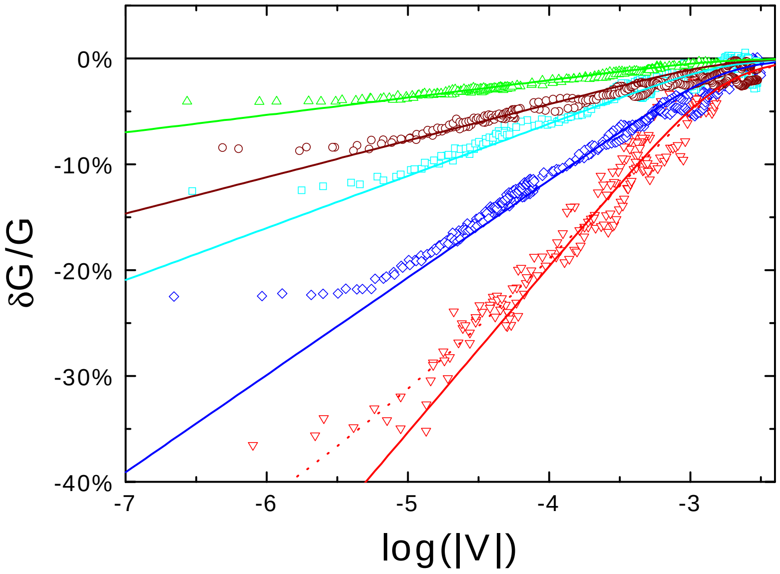

Figure 13: Relative conductance reduction for five different contacts at 20 mK. Down-triangles: tunnel contact; other symbols, same contacts as in Figure 10: {0.993,0.06,0.05} (up-triangles), {0.85,0.07} (circles), {0.70, 0.05} (squares), {0.52,0.14} (diamonds). Full lines represent Exp. (28) with $R = 920\,\Omega$, $C_J = 0.40$ pF, and the Fano factor calculated from the measured PIN codes. Dotted line: non-perturbative prediction of Exp. (19) at zero temperature for the same *RC* environment.

As discussed previously (section 5.4.1.3), it is presently difficult to evaluate the systematic error arising from the determination of the Fano factor. We think however that the good agreement we have observed is not fortuitous because the determination of large transmissions, which predominantly contribute to the Fano factor, is only weakly affected by Coulomb blockade.

5.4.3.3 Comparison with the extension of the perturbative result to the non perturbative case

The theoretical calculation by Levy Yeyati *et al.* reveals that, in the low environment impedance limit, the relative conductance reduction for a single conduction channel with transmission probability τ is simply given by the relative conductance reduction in the tunnel limit times the factor $(1-\tau)$ (Exp. (25)):

$$\frac{\delta G}{G}(\tau,T)=\left(1-\tau\right)\frac{\delta G}{G}(Tunnel,T).$$

Despite the difficulties we encountered in the interpretation of our measurements, it seems reasonable to conclude that they agree with this simple relationship. Does this relationship remain valid in the non-perturbative case in which the real part of the environment impedance is not much smaller than the resistance quantum R_K ?

As illustrated in the previous paragraph concerning the tunnel regime, the environment impedance in our experiment is too high for the perturbative theory to account well for the conductance at the lowest voltages. The exact theory is necessary to explain the thermal rounding. Expecting the same for larger transmissions, we may get a first insight into the validity of Exp. (25) in the non-perturbative limit by comparing its predictions with our experimental results.

This comparison is made in Figure 14 and Figure 15 for Coulomb blockade measurements on two atomic-size contacts with measured mesoscopic codes {0.993,0.06,0.05} (“0.993 contact”) and {0.70,0.05} (“0.70 contact”) at four different temperatures.

More precisely, the full theoretical curves for a contact characterized by the mesoscopic code $\{\tau_1,...,\tau_N\}$ are calculated from the expression:

$$G(\{\tau_1,...,\tau_N\},R,C,T,V)=G_0(\sum_i \tau_i + \tau_i(1-\tau_i)\ \delta G/G(\mathit{Tunnel},R_i,C,T,V)), \qquad (34)$$

where $\delta G/G(\mathit{Tunnel},R_i,C,T,V)$ is given by Exp. (19) with $Z_{env}(\omega)=R_i/(1+jR_iC\omega)$. The resistance R_i is the parallel combination of R and the resistance of all channels but the *i*-th. As viewed from the *i*-th channel, the other conduction channels are included in the environment.

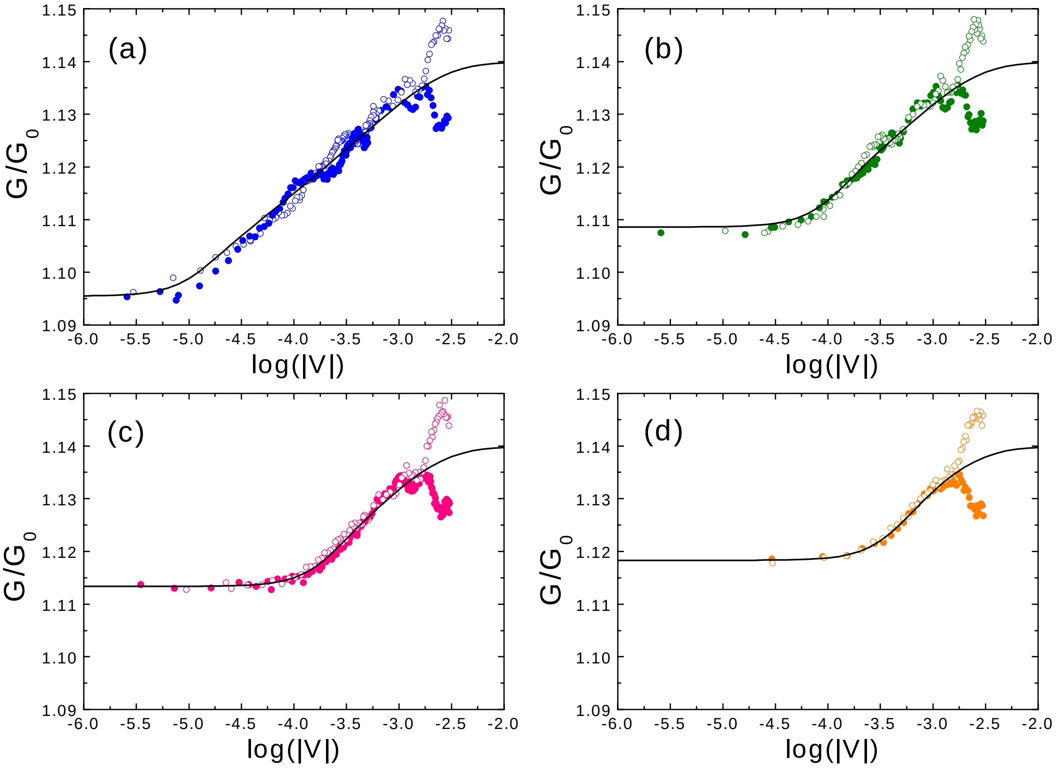

Figure 14: Circles: Conductance in units of G_0 as a function of the logarithm of the DC voltage bias absolute value for positive (full circles) and negative voltages (open circles) at four different temperatures: 24 mK (a), 330 mK (b), 665 mK (c), 1.35 K (d). The data are taken on the contact with mesoscopic PIN code $\{0.993,0.06,0.05\}$. Full lines: predictions of Exp. (34) for a mesoscopic PIN code $\{0.99,0.08,0.07\}$, $R=920\,\Omega$, $C=33\,\mathrm{pF}$, and the measured temperature (but for (a) where the temperature was taken to be 40 mK, instead of the measured value of 24 mK).

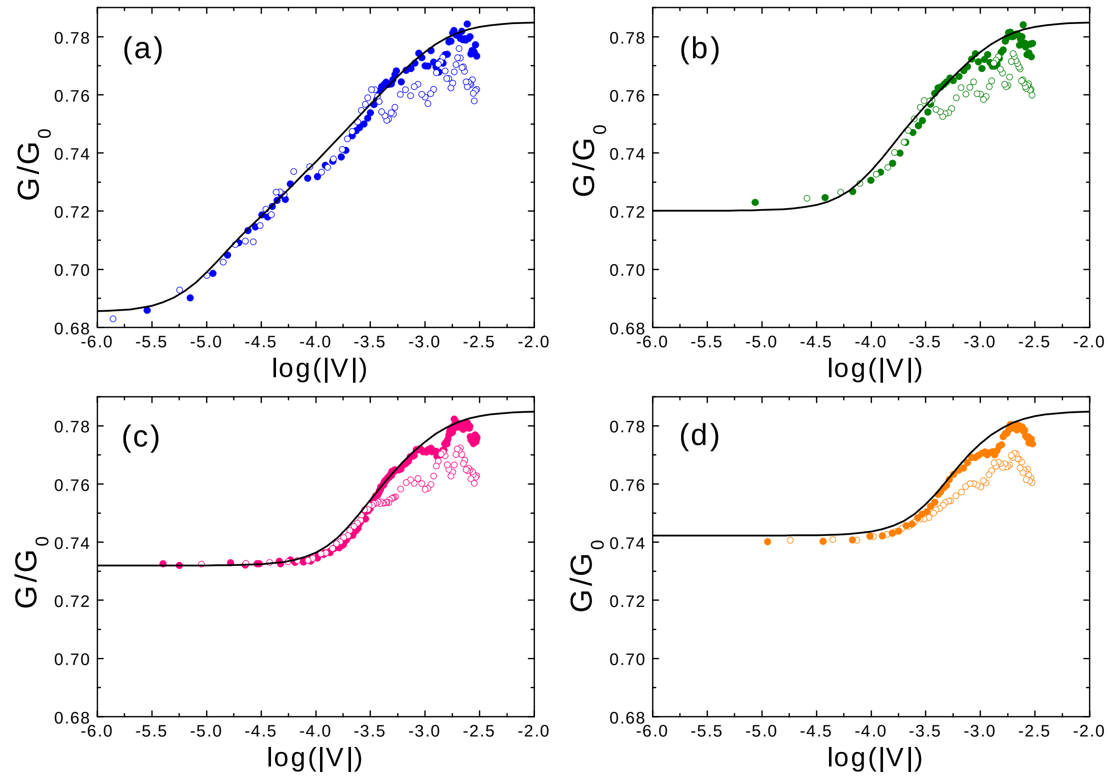

Figure 15: Circles: Conductance in units of G_0 as a function of the logarithm of the DC voltage bias absolute value for positive (full circles) and negative voltages (open circles) at four different temperatures: 26 mK (a), 295 mK (b), 620 mK (c), 1.16 K (d). The data are taken on the contact with mesoscopic PIN code {0.70,0.05}. Full lines: predictions of Exp. (34) for a mesoscopic PIN code {0.70,0.085}, $R = 920\,\Omega$, $C = 57\text{ pF}$, and the measured temperature.

The parameters adjusted so as to get a good agreement with the experimental data are the transmission of the low-transmitting channels and the total capacitance *C*. The errors in the determination of the channel transmission probabilities due to Coulomb blockade in the superconducting state are expected to be small for high transmissions. The highest transmission of the two contacts is thus assumed to be well determined from the fit of the current voltage in the superconducting state. However the lowest transmissions are corrected in order to get the “right” conductance in the large voltage limit. For example, in Figure 14, the measured mesoscopic code was {0.993,0.06,0.05} while the one used to fit the Coulomb blockade data was {0.99,0.08,0.07}. The capacitance value basically sets the zero voltage conductance limit.

Using reasonable capacitance values (section 5.3.2) and corrections to the small transmissions, the theoretical curves fit quite well the experimental data for the 0.993 contact, but less accurately for the 0.70 contact. Unfortunately, it is not possible to conclude whether or not Exp. (34) is quantitatively correct, because of conductance fluctuations and of the uncertainty in the mesoscopic code determination. Troubles due to conductance fluctuations are well illustrated in both cases. For the 0.993 contact, the conductance at large voltages differs between the positive and the negative voltage branches by about one percent, leading to a large uncertainty on the asymptotic conductance at high voltages. For the 0.70 contact the situation is even worse as conductance fluctuations completely hide the Coulomb blockade signal in the lower conductance branch corresponding to negative DC bias voltages (open circles in Figure 15). Concerning the uncertainties on the mesoscopic code, it should be noticed that for the 0.70 contact, better fits can be obtained by slightly increasing the highest transmission (mesoscopic code {0.72,0.065} and $C = 40\,\mathrm{pF}$). However, for the time being, such an assumption can not be justified quantitatively.

5.5 Conclusion

We have found that the dynamical Coulomb blockade of the conductance of a channel progressively disappears when the transmission approaches unity, as recently predicted. Within the experimental accuracy, the reduction of Coulomb blockade is the same as for shot noise. However, a quantitative comparison with theoretical predictions is hindered by the uncertainty in the determination of the codes, and by conductance fluctuations.

This preliminary experiment could thus be improved in two respects:

- The determination of the codes could be made more accurate by using for the thin connecting wires a metal with a larger gap than the one of the contact. Dissipation in the superconducting wires would not occur in the frequency range of interest for the contact, and the environment would not affect significantly the current-voltage characteristics in the superconducting state. For this purpose, the sample fabrication would require two steps, the aluminum contact being deposited onto niobium wires and pads for example.

- Conductance fluctuations could be averaged out by measuring the same contact at different magnetic fields. Indeed, the interference pattern responsible for the conductance fluctuations is significantly dephased by an applied field when the flux through the interference loops is of the order of the flux quantum.

The experiment described in this chapter is just one simple example in the exploration of Coulomb blockade in a quantum coherent conductor. Different and richer situations could be investigated. In particular, A. Levy Yeyati has recently considered the case of a single channel connecting a normal metal to a superconductor [10], in which case transport occurs through Andreev reflection. The blockade of MAR processes remains an open problem.

References of Chapter 5

---

[1] G.-L. Ingold and Yu. V. Nazarov in *Single Charge Tunneling*, edited by H. Grabert and M.H. Devoret (Plenum Press, New York, 1992), p 21.

[2] A. Levy Yeyati, A. Martin-Rodero, D. Esteve, and C. Urbina, Phys. Rev. Lett. **87**, 046802 (2001).

[3] A.O. Caldeira and A.J. Leggett, Ann. Phys. (N.Y.) **149**, 374 (1983).

[4] M. Tinkham, *Introduction to superconductivity* (McGraw-Hill, New York, 1975).

[5] A.A. Odinstov, G. Falci, and G. Schön, Phys. Rev. B **44**, 13089 (1991).

[6] L.V. Keldysh, Sov. Phys. JETP **20**, 1018 (1965).

[7] B. Ludoph, M. H. Devoret, D. Esteve, C. Urbina, and J. M. van Ruitenbeek, Phys. Rev. Lett. **82**, 1530 (1999).

[8] M. Tinkham in *Introduction to superconductivity*, McGraw-Hill international editions Sec. 3.9 and 3.10.

[9] G. Falci, V. Bubanja, and G. Schön, Europhys. Lett. **14**, 109 (1991); Z. Phys. B **85**, 451 (1991).

[10] Private communication.

Appendix A Scattering approach of conductance and shot noise

The scattering approach was introduced by Landauer [1] to describe the electrical transport through a quantum coherent conductor in terms of scattering of incoming electronic waves. It applies if the electrons form a fluid of non-interacting quasiparticles, i.e. when the "independent electron" picture is valid. In this approach, the quantum coherent conductor is described by a set of conduction channels whose transmissions determine all its transport properties. In this Appendix, we explain this formalism, and derive the expressions of the conductance and of the shot noise in terms of the transmission set in the case of a two-probe circuit.

A.1 The scattering model

The scattering model is formulated as follows: Electrons emitted from reservoirs are guided through leads to the quantum coherent conductor where they are scattered (see Figure 1). The incoming and outgoing propagating modes of the leads constitute the scattering state basis. The reservoirs play the double role of perfect source and sink for electrons. Here, perfect means that no scattering occurs at the reservoir-lead interface: electrons are emitted from the reservoir into the leads and absorbed from the leads into the reservoirs with probability one. As a consequence, the statistical properties of the scattering states are completely determined by the temperature and chemical potential of the reservoirs [2].

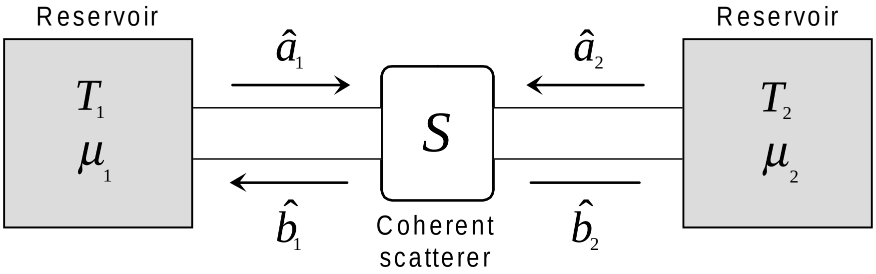

Figure 1: Scattering approach to electrical transport through a quantum coherent conductor.

We restrict ourselves to the case where the number of propagating modes N is the same on both sides of the conductor. Let us denote $\hat{a}^{+}_{1,i}(E)\,(\hat{a}_{1,i}(E))$ and $\hat{a}^{+}_{2,i}\left(E\right)(\hat{a}_{2,i}\left(E\right))$ with $i\in[\![1,N]\!]$ the creation (annihilation) operators for the electronic mode i with energy E incident upon the conductor respectively from the left and from the right, and $\hat{b}^{+}_{1,i}\left(E\right)(\hat{b}_{1,i}\left(E\right))$ and $\hat{b}^{+}_{2,j}\left(E\right)(\hat{b}_{2,j}\left(E\right))$ the outgoing ones (see Figure 1). The mean value of the occupation operators is imposed by the temperature and chemical potential of the reservoirs:

$$\left\langle \hat{a}^{+}_{\alpha,i}(E)\hat{a}_{\alpha,i}(E)\right\rangle = \left\langle \hat{b}^{+}_{\alpha,i}(E)\hat{b}_{\alpha,i}(E)\right\rangle = \frac{1}{1+e^{(E-\mu_\alpha)/k_B T_\alpha}} \equiv f_\alpha(E) \text{ with } \alpha = 1,2. \tag{1}$$

The incoming and outgoing operators are linked together by the $2N\times 2N$ scattering matrix S:

$$\begin{bmatrix}\hat{b}_1\\ \hat{b}_2\end{bmatrix} = S\begin{bmatrix}\hat{a}_1\\ \hat{a}_2\end{bmatrix}, \tag{2}$$

where

$$\hat{b}_1 = \begin{bmatrix}\hat{b}_{1,1}\\ \vdots\\ \hat{b}_{1,N}\end{bmatrix}, \hat{b}_2 = \begin{bmatrix}\hat{b}_{2,1}\\ \vdots\\ \hat{b}_{2,N}\end{bmatrix}, \hat{a}_1 = \begin{bmatrix}\hat{a}_{1,1}\\ \vdots\\ \hat{a}_{1,N}\end{bmatrix} \text{ and } \hat{a}_2 = \begin{bmatrix}\hat{a}_{2,1}\\ \vdots\\ \hat{a}_{2,N}\end{bmatrix}.$$

Because of particle conservation, the scattering matrix is unitary $S^{+}S = SS^{+} = \boldsymbol{1}$. It can be decomposed into four square $N \times N$ blocks:

$$S = \begin{bmatrix} s_{11} & s_{12} \\ s_{21} & s_{22} \end{bmatrix}. \tag{3}$$

The two off-diagonal blocks s_{12} and s_{21}, which describe the transmission of the waves respectively from the right to the left, and from the left to the right, are called the transmission matrices. The two diagonal ones s_{11} and s_{22} are the reflection matrices. They describe the reflection of electronic waves arriving respectively from the left and from the right. We assume here that the scattering matrix is independent of energy[1] in the small energy range probed by transport around the Fermi level.

A.2 Reduction of the scattering problem to independent conduction channels

The scattering problem can be decomposed into a set of N independent conduction channels by changing the basis of the propagating states in the leads. In this new basis, the propagating states are arranged in groups of four states, one for each propagation direction in each lead, which are connected only among themselves through the scattering process. This channel decomposition is unique[2] up to permutations[6]. Denoting $U_1\,(U_2)$ the unitary matrices describing the basis transformations for the states incoming from the left (right) and $V_1\,(V_2)$ that for the states outgoing to the right (left), the scattering matrix in the new basis writes:

$$S' = \begin{bmatrix} V_1^{+} & 0 \\ 0 & V_2^{+} \end{bmatrix} \begin{bmatrix} s_{11} & s_{12} \\ s_{21} & s_{22} \end{bmatrix} \begin{bmatrix} U_1 & 0 \\ 0 & U_2 \end{bmatrix} = \begin{bmatrix} -iR^{1/2} & T^{1/2} \\ T^{1/2} & -iR^{1/2} \end{bmatrix}, \tag{4}$$

where R and T are real, diagonal, and positive matrices which are independent of the initial

---

[1] Typically in metals the Fermi energy is of the order of the electronvolt: for example 11.7 eV for aluminum and in the experiments presented in this thesis the maximum measurement voltage is of the order of a meV.

[2] In Ref. [6], it is pointed out that such transformation is possible if the matrix $s_{11}^{+}s_{11}$ has no eigenvalue equal to 0 or 1. We disregard here this mathematical difficulty.

basis. They are indeed related to the transmission and reflection matrices, respectively s_{11} and s_{12} by the relations:

$$s_{11} = -iV_1R^{1/2}U_1^+,\ s_{12} = V_1T^{1/2}U_2^+ \ , \tag{5}$$

which lead to:

$$s_{11}^+s_{11} = U_1RU_1^+,\ s_{12}^+s_{12} = U_2TU_2^+ . \tag{6}$$

The unitary transformation U_2 (U_1) thus diagonalizes $s_{12}^+s_{12}$ $(s_{11}^+s_{11})$. The coefficients of R and T, which represent the reflection and transmission probabilities of the independent conduction channels, are thus the eigenvalues of $s_{11}^+s_{11}$ and $s_{12}^+s_{12}$ and consequently intrinsic to the scatterer. This set of eigenvalues forms the mesoscopic PIN code of the quantum coherent conductor.

Since the conduction channels are independent, the multichannel expression of any transport property thus simply writes as a sum over the contributions of the different channels. We now consider the case of the conductance and of the shot noise, treating first the case of a single conduction channel with arbitrary transmission probability τ. The notations $\hat{a}_\alpha^+, \hat{a}_\alpha, \hat{b}_\alpha^+$ and $\hat{b}_\alpha$ with α=1,2 now represent simple operators, and s_{11}, s_{12}, s_{21}, and s_{22} complex numbers, related to the transmission τ by the relations $|s_{12}|^2 = |s_{21}|^2 = 1 - |s_{11}|^2 = 1 - |s_{22}|^2 = \tau$.

A.3 The Landauer formula for the conductance

The current operator[3] can be expressed in terms of the creation and annihilation operators in the leads. Its Heisenberg representation is given by [3]:

$$\hat{I}(t) = \frac{e}{h}\iint dE\ dE'(\hat{a}_1^+(E)\hat{a}_1(E') - \hat{b}_1^+(E)\hat{b}_1(E'))\ e^{i(E-E')t/\hbar}. \tag{7}$$

---

[3] In the derivation of this expression, it is assumed that the variation of the group velocity with energy can be neglected.

Using Exp. (2), the operators $\hat{b}_1^+(E)$ and $\hat{b}_1(E')$ can be expressed in terms of the incoming waves operators, yielding:

$$\hat{I}(t) = \frac{e}{h} \sum_{\alpha,\beta=1,2} \iint dE dE' A_{\alpha\beta} \hat{a}_\alpha^+(E) \hat{a}_\beta(E') e^{i(E-E')t/\hbar} \tag{8}$$

where $A_{\alpha\beta} = \delta_{\alpha 1}\delta_{\beta 1} - s_{1\alpha}^* s_{1\beta}$. The current flowing through the quantum coherent conductor is the average value of the current operator:

$$\left\langle \hat{I}(t) \right\rangle = \frac{e}{h} \sum_{\alpha,\beta=1,2} \iint dE dE' A_{\alpha\beta} \left\langle \hat{a}_\alpha^+(E) \hat{a}_\beta(E') \right\rangle e^{i(E-E')t/\hbar}. \tag{9}$$

From (1), it follows that $\left\langle \hat{a}_\alpha^+(E)\hat{a}_\beta(E') \right\rangle = \delta_{\alpha\beta} f_\alpha(E)\delta(E-E')$. The average current results from the imbalance of the populations of propagating states with opposite directions:

$$\left\langle \hat{I}(t) \right\rangle = \frac{e}{h} \int dE \sum_{\alpha=1,2} A_{\alpha\alpha} f_\alpha(E) = \frac{e\tau}{2\pi\hbar} \int dE \,(f_1(E) - f_2(E)) = \frac{e^2}{h}\tau V. \tag{10}$$

Then, taking into account the spin degeneracy, one obtains the famous Landauer formula for the conductance G: $G = G_0 \tau$, where $G_0 = 2e^2/h \simeq 77\ \mu\text{s} \simeq 1/12927\ \Omega^{-1}$ is the conductance quantum. For a quantum coherent conductor characterized by the mesoscopic code $\{\tau_1, ..., \tau_N\}$, the Landauer formula writes:

$$G = G_0 \sum_{i=1}^{N} \tau_i. \tag{11}$$

A.4 Calculation of the shot noise spectral density

We present now the main lines of the calculation of the spectral density of the current fluctuations at low frequency. Denoting $\Delta\hat{I}(t) = \hat{I}(t) - \left\langle \hat{I}(t) \right\rangle$ the operator associated to the current fluctuations around the mean value $\left\langle \hat{I}(t) \right\rangle$, the spectral density is defined as [4]:

$$2\pi\delta(\omega+\omega')S(\omega) \equiv \left\langle \Delta\hat{I}(\omega)\Delta\hat{I}(\omega') + \Delta\hat{I}(\omega')\Delta\hat{I}(\omega) \right\rangle, \tag{12}$$

where $\Delta\hat{I}(\omega)$ is the Fourier transform of $\Delta\hat{I}(t)$:

$$\Delta\hat{I}(\omega) = \int_{-\infty}^{+\infty} \Delta\hat{I}(t) e^{+i\omega t} dt. \tag{13}$$

Exp. (8) of the current operator yields:

$$\Delta\hat{I}(\omega) = e\int dE \sum_{\alpha,\beta=1,2} A_{\alpha\beta}\left[\hat{a}^{+}_{\alpha}(E)\hat{a}_{\beta}(E+\hbar\omega) - \left\langle \hat{a}^{+}_{\alpha}(E)\hat{a}_{\beta}(E+\hbar\omega)\right\rangle\right] \tag{14}$$

and

$$\begin{aligned}\left\langle \Delta\hat{I}(\omega)\Delta\hat{I}(\omega')\right\rangle = e^{2}\int\int dEdE' \sum_{\alpha,\beta,\gamma,\delta=1,2} A_{\alpha\beta}A_{\gamma\delta}[\left\langle \hat{a}^{+}_{\alpha}(E)\hat{a}_{\beta}(E+\hbar\omega)\hat{a}^{+}_{\gamma}(E')\hat{a}_{\delta}(E'+\hbar\omega')\right\rangle \\ -\left\langle \hat{a}^{+}_{\alpha}(E)\hat{a}_{\beta}(E+\hbar\omega)\right\rangle\left\langle \hat{a}^{+}_{\gamma}(E')\hat{a}_{\delta}(E'+\hbar\omega')\right\rangle].\end{aligned} \tag{15}$$

The quantum and statistical average value of the four operator product in Exp.(15) is equal to [3]:

$$\begin{aligned}\left\langle \hat{a}^{+}_{\alpha}(E)\hat{a}_{\beta}(E+\hbar\omega)\hat{a}^{+}_{\gamma}(E')\hat{a}_{\delta}(E'+\hbar\omega')\right\rangle - \left\langle \hat{a}^{+}_{\alpha}(E)\hat{a}_{\beta}(E+\hbar\omega)\right\rangle\left\langle \hat{a}^{+}_{\gamma}(E')\hat{a}_{\delta}(E'+\hbar\omega')\right\rangle \\ = \delta_{\alpha\delta}\delta_{\beta\gamma}\delta(E-E'-\hbar\omega')\delta(E+\hbar\omega-E')f_{\alpha}(E)[1-f_{\beta}(E+\hbar\omega)],\end{aligned} \tag{16}$$

which leads to:

$$\left\langle \Delta\hat{I}(\omega)\Delta\hat{I}(\omega')\right\rangle = \frac{e^{2}}{\hbar}\delta(\omega+\omega')\int dE \sum_{\alpha,\beta=1,2} A^{2}_{\alpha\beta} f_{\alpha}(E)[1-f_{\beta}(E+\hbar\omega)]. \tag{17}$$

This general expression takes a simple form at zero frequency. Using the definition (12), and taking into account the spin degeneracy, the spectral density of current fluctuations at zero frequency, denoted S_I, is:

$$S_I = \frac{4e^{2}}{h}\int dE \sum_{\alpha,\beta=1,2} A^{2}_{\alpha\beta} f_{\alpha}(E)[1-f_{\beta}(E)]\,. \tag{18}$$

This can be expressed as a function of the transmission probability τ :

$$S_I = 2G_0\left[\tau\int dEf_1(E)(1-f_1(E)) + f_2(E)(1-f_2(E)) + \tau(1-\tau)\int dE(f_1(E)-f_2(E))^{2}\right]. \tag{19}$$

The two integrals involving Fermi functions are respectively equal to $2k_BT$ and to $(eV\coth[eV/2k_BT]-2k_BT)$. The final result is:

$$S_I = 2G_0\tau(1-\tau)eV\coth\left[\frac{eV}{2k_BT}\right] + 4k_BTG_0\tau^{2}. \tag{20}$$

In the multichannel case, the spectral density for a given mesoscopic code $\{\tau_1,...,\tau_N\}$ is thus equal to:

$$S_I = 2G_0 eV\sum_{i=1}^{N}\tau_i(1-\tau_i)\coth\left[\frac{eV}{2k_BT}\right]+4k_BTG_0\sum_{i=1}^{N}\tau_i^2. \tag{21}$$

At low voltage or high temperature, i.e. when $eV/2k_BT \ll 1$, Exp. (21) reduces to the Johnson-Nyquist spectral density $S_I = 4k_BTG_0\sum_{i=1}\tau_i$. In the opposite limit $eV/2k_BT \gg 1$, the spectral density depends linearly on the average current. In this regime, the shot noise is reduced from its poissonian value by the so-called Fano factor $F(\{\tau_1,...,\tau_N\}) = 1-\sum_{i=1}^{N}\tau_i^2/\sum_{i=1}^{N}\tau_i < 1$:

$$S_I(V,T,\tau) \simeq 2e\langle I(t)\rangle F(\{\tau_1,...,\tau_N\}) \quad (eV/2k_BT \gg 1). \tag{22}$$

A.5 Shot noise: wave packet approach

In the previous section, we derived the spectral density of shot noise in a quantum coherent conductor within the framework of the scattering theory using second quantification [5]. In this formalism, the Pauli exclusion principle is taken into account through the commutation relations of creation and annihilation operators. Martin and Landauer [6] have proposed another more transparent way to take into account the Pauli principle, the wave-packet approach to the scattering problem.

The scattering problem is treated using a well chosen scattering state basis for the 1D electronic transport. Electrons are visualized as traveling through the leads under the form of orthonormal wave-packets. The authors emphasize that within the energy range $[E-\Delta E, E+\Delta E]$, the equally time-shifted wave-packets defined as:

$$\psi^{(n)}(x,t) = \int_{E-\Delta E}^{E+\Delta E} dE'\frac{1}{\Delta E}\left(\frac{1}{2\pi}\frac{dk}{dE'}\right)^{1/2} e^{ik(E')x-iE'(t+n\Delta t)/\hbar}, \tag{23}$$

where x is the coordinate of the 1D transport, $k(E)$ the wave vector, $\Delta t = 2\pi\hbar/\Delta E$ the time shift and n an integer, provide a complete orthonormal basis [7] for the scattering problem.

The occupations of these orthonormal states is restricted as usual: they can be occupied at most by a pair of opposite spin electrons.

Let us consider the single channel case. Wave-packets incoming on the scatterer are either transmitted or reflected, and the occupation of the outgoing states fluctuates randomly. If g denotes the random variable counting the number of electrons transferred during any period Δt (g can be equal to –1, 0 or 1), the contribution of the wave-packets in the energy interval $\left[E-\Delta E/2, E+\Delta E/2\right]$ to the spectral density ΔS_I is equal to [6]:

$$\Delta S_I = 2G_0 \Delta E \left(\left\langle g^2\right\rangle - \left\langle g\right\rangle^2\right)(E). \qquad (24)$$

This contribution depends only on the fluctuations of g, that are determined by the average value and by the fluctuations of the wave-packet occupations, and by the scattering process itself.

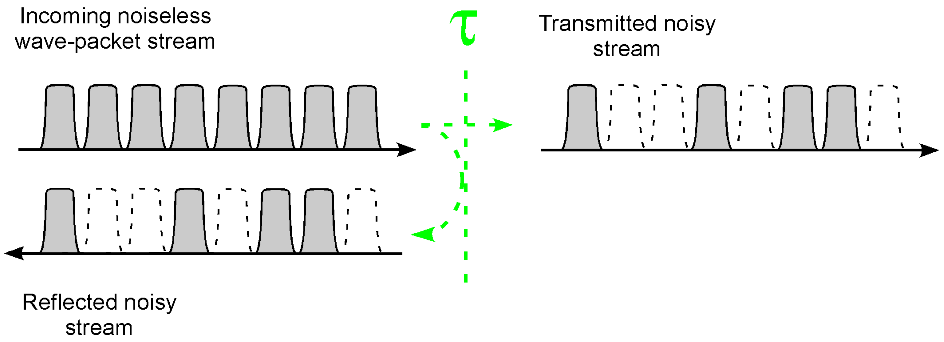

Figure 2: Schematic representation of the noiseless steady stream of orthonormal wave-packets emitted by charge reservoirs at zero temperature, partitioned into two noisy transmitted and reflected streams by the scatterer. Note that, in reality, the orthonormal state wave-functions strongly overlap.

At zero temperature, because of Pauli principle, all wave-packets in the left and right leads with energy lower than the chemical potential (denoted respectively μ_L and μ_R) are occupied with probability one. Assuming that $\mu_L - \mu_R = eV > 0$, the current through the channel is made up of electrons within the energy range $\left[\mu_L - eV, \mu_L\right]$ crossing the channel from the left to the right. For a perfect transmission $\tau = 1$, $g = 1$ with probability one within this energy range and zero elsewhere. The number of transferred electrons g does not fluctuate and consequently the spectral density is zero. The incoming wave-packets form a noiseless perfectly correlated stream which is not disturbed by the scatterer. For an arbitrary transmission however, the wave-packet stream is randomly partitioned between a transmitted and a reflected stream (see Figure 2). Denoting $r = 1 - g$ the random variable counting the number of reflected electrons during any pulse period Δt , the fluctuations of g within the energy range $[\mu_L - eV, \mu_L]$ are given by [6]:

$$\langle g^2 \rangle - \langle g \rangle^2 = \langle g(1-r) \rangle - \langle g \rangle^2 = \langle g \rangle - \langle gr \rangle - \langle g \rangle^2 . \tag{25}$$

Because wave-packets are either transmitted or reflected, one has $\langle gr \rangle = 0$, and thus:

$$\langle g^2 \rangle - \langle g \rangle^2 = \langle g \rangle - \langle g \rangle^2 = \tau(1-\tau) , \tag{26}$$

leading to a non vanishing spectral density:

$$S_I = 2G_0 eV\tau(1-\tau) = 2eI(1-\tau). \tag{27}$$

At small transmissions $\tau \ll 1, (1\text{-}\tau) \simeq 1$ and $S_I = 2eI$. One recovers the poissonian shot noise, since electrons are seldomly transmitted, like electrons emitted in vacuum diodes.

At finite temperature, the occupation numbers in the leads fluctuate, which contributes to fluctuations of g . At a given energy E , the variance of g is then given by [6]:

$$\langle g^2 \rangle - \langle g \rangle^2 = \tau \left(f_L(E) + f_R(E) - 2 f_L(E) f_R(E) \right) - \left(f_L(E) - f_R(E) \right)^2 \tau^2 , \tag{28}$$

where $f_L(E)$ and $f_R(E)$ are respectively the Fermi function in the left and in the right lead. The spectral density at a given voltage V and temperature T is thus given by:

$$S_I(V,T,\tau) = 2eVG_0\tau(1-\tau)\coth\left(\frac{eV}{2k_B T} \right) + 4k_B T G_0 \tau^2 , \tag{29}$$

in agreement with the prediction of the previous approach. The multichannel case can also be treated along the same lines.

References of Appendix A

[1]R. Landauer, IBM J. Res. Dev. **1**, 223 (1957); Philos. Mag. **21**, 863 (1970).

[2] S. Datta in *Electronic Transport in Mesoscopic Systems,* Cambridge University Press (1995) Sec. 2.1.

[3] M. Büttiker, Phys. Rev. B **46**, 12485 (1992).

[4] L.D. Landau and E.M. Lifshitz, *Statistical Physics* (Pergamon, Oxford, 1959), p. 354.

[5] M. Büttiker, Phys. Rev. Lett. **65**, 2901 (1990).

[6] Th. Martin and R. Landauer, Phys. Rev. B **45**, 1742 (1992).

[7] R. Landauer, Physica D **38**, 226 (1987); K.W.H. Stevens, J. Phys. C **20**, 5791 (1987); C.E. Shannon, Proc. IRE **37**, 10 (1949).

Appendix B Mesoscopic superconductivity

In this appendix, we sketch the calculation of the current-phase relationship and of the current-voltage characteristic of a short[1] quantum coherent conductor connecting two superconducting electrodes. Historically, the first theoretical approach to these problems was formulated in terms of the tunneling hamiltonian. Treating this hamiltonian to first order in perturbation theory, Josephson derived in 1962 the famous sinusoidal current-phase relationship of a tunnel junction connecting two BCS electrodes. The voltage biased case was also addressed to first order, but for a long time, the higher processes turned out to diverge. Only in the middle on the nineties, the divergences were corrected by carrying the perturbative treatment up to infinite order [1].

A second approach was introduced in 1982 by Blonder, Tinkham, and Klapwijk [2,3] to explain the subharmonic gap structure and excess current observed in the current-voltage characteristics of superconducting weak links[2]. Roughly speaking, it generalizes the Landauer scattering formalism to the superconducting state. The central concept is the Andreev

---

[1] Short means that the length of the coherent scatterer is much smaller than the superconducting coherence length ξ_0 and thus can be considered as zero.

[2] See references in [2].

reflection whereby an electron incident on a superconducting electrode is partially or completely reflected as a hole at the same energy [4]. This approach leads to a simple physical picture of transport through Josephson junctions and thus we adopt it in the following.

To formally separate the Andreev scattering mechanism from the scattering by the coherent conductor, normal leads connecting the superconducting reservoirs to the coherent scatterer are usually introduced (see Figure 1). It should be stressed that this is just an artifice convenient for the calculations. For atomic contacts, the length of this region is actually zero. Andreev reflections occur at the two normal lead-superconducting reservoir (NS) interfaces. As Andreev reflection does not mix up conduction channels [5], the problem can be treated in terms of the independent conduction channels defined in Appendix A, and we restrict ourselves to the one channel case.

The derivation is organized as follows: first, we introduce a representation of the quasiparticles in the superconducting state, which we think clarifies the usual semiconductor representation [6]. Then, the Andreev reflection probability amplitude at an NS interface is calculated and subsequently used as the basic ingredient to calculate the current-phase and current-voltage characteristics for SNS structures.

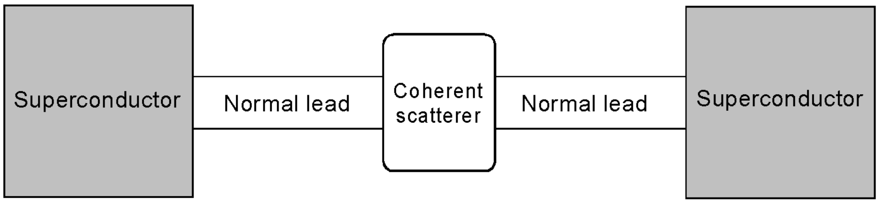

Figure 1: Modelization of a quantum coherent conductor connecting two superconducting electrodes.

B.1 The quasiparticles of a BCS superconductor

The transport through a conduction channel is one-dimensional and thus we restrict ourselves to a 1D problem along the $x-\text{axis}$. Let us denote $c^{+}_{k,\uparrow(\downarrow)}$ and $c_{k,\uparrow(\downarrow)}$ respectively the creation and annihilation operators of the independent quasiparticles of the electrode in the normal state with spin up (down), and ξ_k the quasiparticle energy with respect to chemical potential μ. In the non-diffusive regime we are concerned with, the quasiparticles wave-functions are well described by the eigenstates of a free electron hamiltonian:

$$\hat{H}_N = (-\frac{\hbar^2}{2m^*}\frac{\partial^2}{\partial x^2} - \mu),$$

where m^* is an effective mass. The label k corresponds in this case to the wave vector of the free wave eigenstates of $\hat{H}_N$ denoted $\psi^e_{k,N}$ and called "electronic states" in the following.

The hamiltonian describing the superconducting state with homogeneous pairing potential $\Delta = -V\left\langle c_{-k,\downarrow}c_{k,\uparrow}\right\rangle$, $V > 0$ being the attractive electron-electron interaction term, can be written within the mean field approximation [6]:

$$\hat{H}_S = \sum_k \xi_k (c^+_{k,\uparrow}c_{k,\uparrow} + c^+_{k,\downarrow}c_{k,\downarrow}) - \Delta\, c^+_{k,\uparrow}c^+_{-k,\downarrow} - \Delta^* c_{-k,\downarrow}c_{k,\uparrow}$$

where $\uparrow$ and $\downarrow$ represent respectively the up and down spin states. This single particle Hamiltonian is not of the usual form corresponding to all the operators products being of the type $c^+_q c_k$. However, this structure can be recovered by writing the hamiltonian in terms of the operators $b_k = c^+_{-k,\downarrow}$ for the spin down states and $c_k = c_{k,\uparrow}$ for spin up ones. In this new formulation, the spin labels are not necessary any longer as non ambiguously the operators c are related to spin up while b operators concern spin down. Before presenting this rewriting of $\hat{H}_S$, we discuss the implication of this change in point of view in the normal case.

B.1.1 "Hole description" of the spin down normal quasiparticles

The hamiltonian in the normal state is:

$$\hat{H}_N = \sum_k \xi_k (c^+_{k,\uparrow}c_{k,\uparrow} + c^+_{k,\downarrow}c_{k,\downarrow}).$$

Using the anti-commutation relation for the conjugated fermionic operators b^+_k and b_k: $b_k b^+_k + b^+_k b_k = 1$, $\hat{H}_N$ in terms of the operators c_k and b_k is equal to:

$$\hat{H}_N = \sum_k \xi_k (c^+_k c_k - b^+_k b_k) + \sum_k \xi_k .$$

The states associated to the operators b_k^+ and b_k, subsequently called “hole states” and denoted $\psi_{k,N}^h$, have an energy $-\xi_k$: Contrary to the corresponding electronic states, their energy is larger than the Fermi energy if k is smaller than the Fermi wave vector k_F and smaller otherwise (see Figure 2).

This leads to a new vacuum state, obtained by taking the occupation number of all electron and hole states equal to zero. Note that this corresponds in the electron representation to taking all electronic spin down states occupied, the spin up states remaining unoccupied (see Figure 3). Any creation operator b_k^+ then removes an electron from this fully occupied band and the associated wave function is thus that of a hole in the semiconductor sense, which justify our appellation. The hole states $\psi_{k,N}^h$ verify the eigenvalue equation:

$$\hat{H}_N \psi_{k,N}^h = -\xi_k \psi_{k,N}^h$$

and carry a positive charge $+e$. Note however that the ground state, corresponding to all electronic and hole states being occupied up to the Fermi level, is the same in the two representations. Indeed, having all hole states with energy smaller than E_F occupied correspond in the electronic representation to all states above the Fermi level being unoccupied.

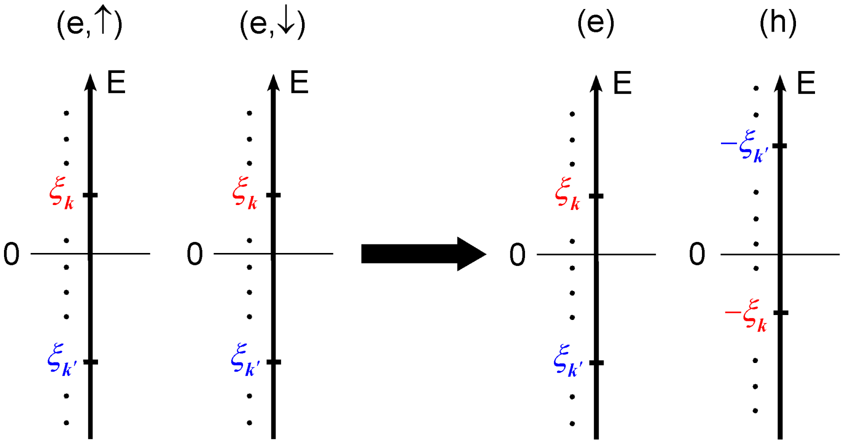

Figure 2: Schematic of the change of representation from electron to hole for the spin down states. To an electronic state characterized by the wave vector k with energy ξ_k corresponds an hole state with the same wave vector but with opposite energy $-\xi_k$ (the zero of energy is taken at the Fermi energy).

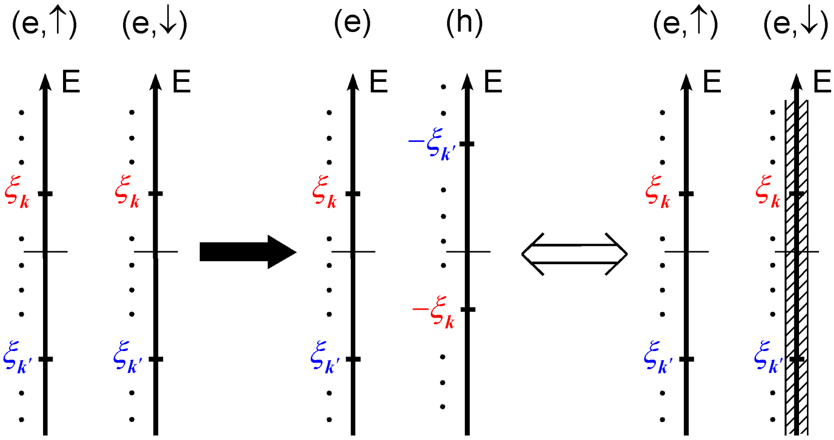

Figure 3: In the vacuum state of the initial formulation, the spin up and down electronic states are unoccupied (left). In the new representation, the vacuum corresponds to all the electron states and hole states being unoccupied (middle) which corresponds to unoccupied spin up electronic states and fully occupied spin down electronic states (right) (the hatches symbolize occupied states).

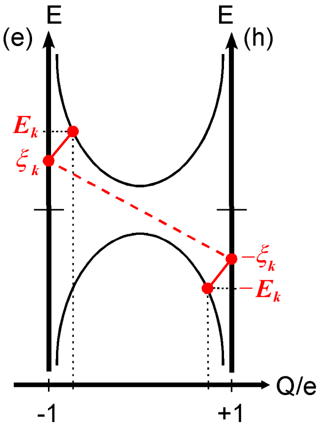

Figure 4: The coupling of electron and hole states corresponding to the same wave vector k but with opposite energy, respectively ξ_k and $-\xi_k$ results in two quasiparticles states with energies E_k and $-E_k$ larger in absolute value than $|\xi_k|$ and charge strictly smaller in absolute value than e (x-axis).

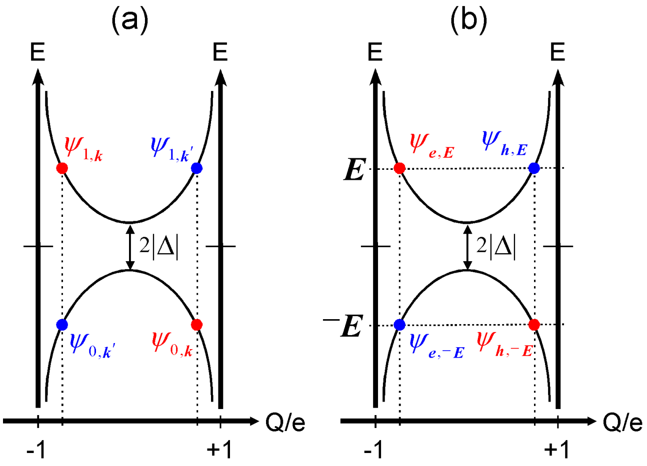

Figure 5: Labeling of the solutions of the Bogoliubov-de Gennes equation resulting from the coupling of electron and hole states corresponding to the same wave vector k (red: same as in Figure 4), or k' (blue) with k and k' being symmetric with respect to the Fermi wave vector so that $\xi_k = -\xi_{k'}$. (a) Wave vector labeling. (b) Energy labeling.

B.1.2 Quasiparticles in the superconducting state

In the electron-hole representation the superconducting hamiltonian writes[3]:

$$\hat{H}_S = \sum_k \xi_k (c_k^+ c_k - b_k^+ b_k) - \Delta\, c_k^+ b_k - \Delta^*\, b_k^+ c_k \tag{1}$$

In this representation, the effective electron-electron interaction responsible for superconductivity corresponds to the electron and hole states of the same wave vector k being coupled through the pairing potential Δ. This hamiltonian can be diagonalized using an unitary Bogoliubov transformation [6,7]:

$$\begin{cases} c_k = u_k^* \gamma_{k1} + v_k \gamma_{k0} \\ b_k = -v_k^* \gamma_{k1} + u_k \gamma_{k0} \end{cases} \Leftrightarrow \begin{cases} \gamma_{k1} = u_k c_k - v_k b_k \\ \gamma_{k0} = v_k^* c_k + u_k^* b_k \end{cases} \tag{2}$$

where γ_{k0} and γ_{k1} are new fermionic operators and the coefficients u_k and v_k verify $|u_k|^2 + |v_k|^2 = 1$.

In terms of these new operators, the hamiltonian is given by:

$$\hat{H}_S = \sum_k E_k (\gamma_{k1}^+ \gamma_{k1} - \gamma_{k0}^+ \gamma_{k0}) + \eta_k \gamma_{k1}^+ \gamma_{k0} + \eta_k^* \gamma_{k0}^+ \gamma_{k1},$$

with

$$\begin{cases} E_k = \xi_k (|u_k|^2 - |v_k|^2) + \Delta\, u_k v_k^* + \Delta^*\, u_k^* v_k \\ \eta_k = 2\xi_k u_k v_k - \Delta\, u_k^2 + \Delta^* v_k^2 \end{cases}.$$

The diagonalization condition is $\eta_k = 0$. Imposing that $E_k > 0$, and taking $u_k \in \mathbb{R}^+$ yields:

$$u_k = \frac{1}{\sqrt{2}} \left(1 + \frac{\xi_k}{E_k} \right)^{1/2},\ |v_k| = \frac{1}{\sqrt{2}} \left(1 - \frac{\xi_k}{E_k} \right)^{1/2},\ \frac{v_k}{|v_k|} = \frac{\Delta}{|\Delta|},$$

and $E_k = +\sqrt{\xi_k^2 + |\Delta|^2}$. The coupling repulses the electron and hole energy levels opening a gap $|\Delta|$ in the quasiparticle spectrum. The superconducting quasiparticles are coherent superpositions of electron and hole normal quasiparticles with probability amplitudes related to the coefficients u_k and v_k in accordance with Exp. (2). In the high energy limit $\xi_k \gg |\Delta|$, one recovers the normal state quasiparticles: $(u_k, v_k) \to (1,0)$ that leads to $(\gamma_{k1}, \gamma_{k0}) \to (c_k, b_k)$, while for $\xi_k = 0$ the quasiparticles are an equally weighted superposition of electron and hole

---

[3] The constant terms are ignored.

normal quasiparticles. The charge they carry varies continuously between ±e (for $|\xi_k| \gg |\Delta|$) and zero (at $\xi_k = 0$). The energy spectrum as a function of the quasiparticle charge is sketched in Figure 4.

The space representation of the quasiparticles states associated to the operators γ_{k1} and γ_{k0} are two component column vectors denoted respectively $\psi_{1,k}$ and $\psi_{0,k}$ that verify the Bogoliubov-de Gennes equations[4]:

$$\begin{bmatrix} \hat{H}_N & -\Delta^* \\ -\Delta & -\hat{H}_N \end{bmatrix} \psi_{1,k} = E_k \psi_{1,k}, \text{ and } \begin{bmatrix} \hat{H}_N & -\Delta^* \\ -\Delta & -\hat{H}_N \end{bmatrix} \psi_{0,k} = -E_k \psi_{0,k} \tag{3}$$

and that write:

$$\psi_{1,k}(x) = \begin{bmatrix} u_k \\ -v_k \end{bmatrix} e^{ikx} \text{ and } \psi_{0,k}(x) = \begin{bmatrix} v_k^* \\ u_k^* \end{bmatrix} e^{ikx} \tag{4}$$

Note that the vector components can be directly written from the expression of the operators γ_{k1} and γ_{k0} given in (2). The wave functions $\psi_{1,k}$ and $\psi_{0,k}$ are the complete set of solutions of the Bogoliubov-de Gennes equation (3) for energies larger in absolute value than $|\Delta|$.

There are also solutions for energies $|E| < |\Delta|$, which can be expressed in the same way as in (4) by introducing complex wave vectors. However, as Andreev reflection conserve energy but strictly speaking not momentum, it is more convenient to express all the solutions of (4) in terms of their energy.

At a given energy E, there are four solutions corresponding to electron or hole-like quasiparticles with both propagating directions:

$$\psi_{e,E}^{\pm} \equiv \begin{bmatrix} \alpha(E) \\ \beta(E) e^{i(\phi+\pi)} \end{bmatrix} e^{\pm i k_e(E) x} \text{ and } \psi_{h,E}^{\pm} \equiv \begin{bmatrix} \beta(E) \\ \alpha(E) e^{i(\phi+\pi)} \end{bmatrix} e^{\pm i k_h(E) x}.$$

In this expression, ϕ is the phase of the order parameter: $\Delta = |\Delta| e^{i\phi}$, and the wave vectors $k_e(E)$ and $k_h(E)$ satisfy the dispersion relations:

$$k_e(E) = \frac{1}{\hbar}\left[2m(\mu + \mathrm{sign}(E)\sqrt{E^2 - |\Delta|^2}) \right]^{1/2}, \tag{5}$$

---

[4] This matrix equation can be directly derived from the expression (1) of the superconducting hamiltonian.

and

$$k_h(E) = \frac{1}{\hbar}\left[2m(\mu - \mathrm{sign}(E)\sqrt{E^2 - |\Delta|^2})\right]^{1/2},$$

with the convention $\sqrt{E^2 - |\Delta|^2} = +i\sqrt{|\Delta|^2 - E^2}$ if $|E| < |\Delta|$. For $|E| > |\Delta|$, the coefficients $\alpha(E)$ and $\beta(E)$ are equal to:

$$\alpha(E) = \frac{1}{\sqrt{2}}\left(1 + \frac{\sqrt{E^2 - |\Delta|^2}}{|E|}\right)^{1/2}, \text{ and } \beta(E) = \frac{1}{\sqrt{2}}\left(1 - \frac{\sqrt{E^2 - |\Delta|^2}}{|E|}\right)^{1/2}. \qquad (6)$$

For $|E| < |\Delta|$, $\alpha(E)$ and $\beta(E)$ have the same modulus and are equal to:

$$\alpha(E) = \mathrm{sign}(E)\sqrt{\left|\frac{E}{2\Delta}\right|}\left(1 + i\,\mathrm{sign}(E)\frac{\sqrt{|\Delta|^2 - E^2}}{E}\right)^{1/2}, \qquad (7)$$

and

$$\beta(E) = \sqrt{\left|\frac{E}{2\Delta}\right|}\left(1 - i\,\mathrm{sign}(E)\frac{\sqrt{|\Delta|^2 - E^2}}{E}\right)^{1/2}.$$

B.2 Andreev reflection

The Andreev reflection mechanism was first pointed out by Andreev in 1964 [8] in a paper on heat flow through normal-superconducting interface. Nowadays, it has taken a central role in the description of transport properties in systems involving one or several superconducting electrodes. Here, we treat the case of a normal-BCS superconductor interface whose pairing potential profile is depicted in Figure 6 (the sharp step corresponds to neglecting proximity effects).

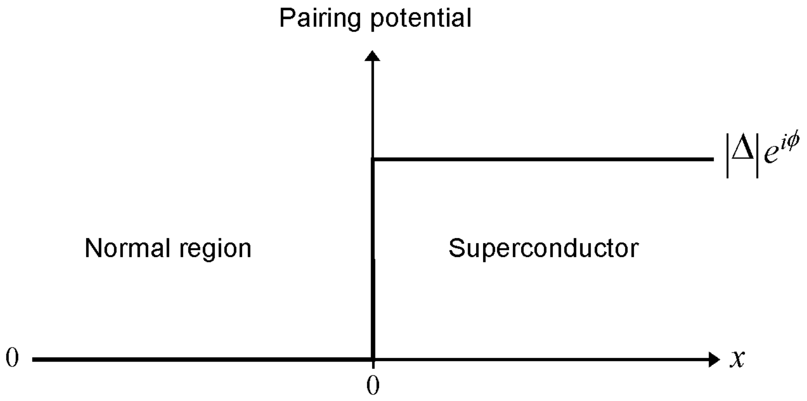

Figure 6: Pairing potential as a function of position at a normal-superconducting interface ($x = 0$).

An electron incident from the normal electrode is Andreev reflected off the pair potential discontinuity generating an electron-like wave in the superconducting electrode propagating in the same direction and an hole wave travelling in opposite direction in the normal electrode. The Andreev reflection amplitude $a(E,\phi)$ is obtained by matching at the interface $x = 0$ the wave functions of both electrodes[5]:

$$\lambda \begin{bmatrix} 1 \\ 0 \end{bmatrix} + \mu \begin{bmatrix} 0 \\ 1 \end{bmatrix} = \nu \begin{bmatrix} \alpha(E) \\ \beta(E) e^{+i(\phi+\pi)} \end{bmatrix}$$

that leads to $a(E,\phi) = \mu / \lambda = \beta(E) e^{+i(\phi+\pi)} / \alpha(E)$.

Using (6) and (7), the Andreev reflection amplitude of an electron as a hole is then equal to:

$$\boxed{a(E,\phi) = \begin{cases} \dfrac{1}{|\Delta|}\left(E - \operatorname{sign}(E)\sqrt{E^2 - |\Delta|^2}\right) e^{i(\phi+\pi)} & \text{for } |E| > |\Delta| \\ \dfrac{1}{|\Delta|}\left(E - i\,\operatorname{sign}(E)\sqrt{|\Delta|^2 - E^2}\right) e^{i(\phi+\pi)} & \text{for } |E| < |\Delta| \end{cases}}. \qquad (8)$$

---

[5] Only the wave functions are matched here and not their derivative. This is equivalent to not taking into account the mismatch of the wave vectors in the normal and in the superconducting electrodes. This approximation is valid as long as $|\Delta| \ll \mu$ (see [9]).

The modulus square and the phase of $a(E,\phi)$ are plotted in Figure 7. For $|E| < |\Delta|$, the modulus is one which means that the electron is Andreev reflected with probability one and the phase varies continuously between ϕ and $\phi + \pi$. For $|E| > |\Delta|$, the modulus falls off rapidly while the phase remains constant. The probability amplitude for a hole to be reflected as an electron is the same as in (8), except for the $e^{i(\phi+\pi)}$ factor that has to be changed by $e^{-i(\phi+\pi)}$.

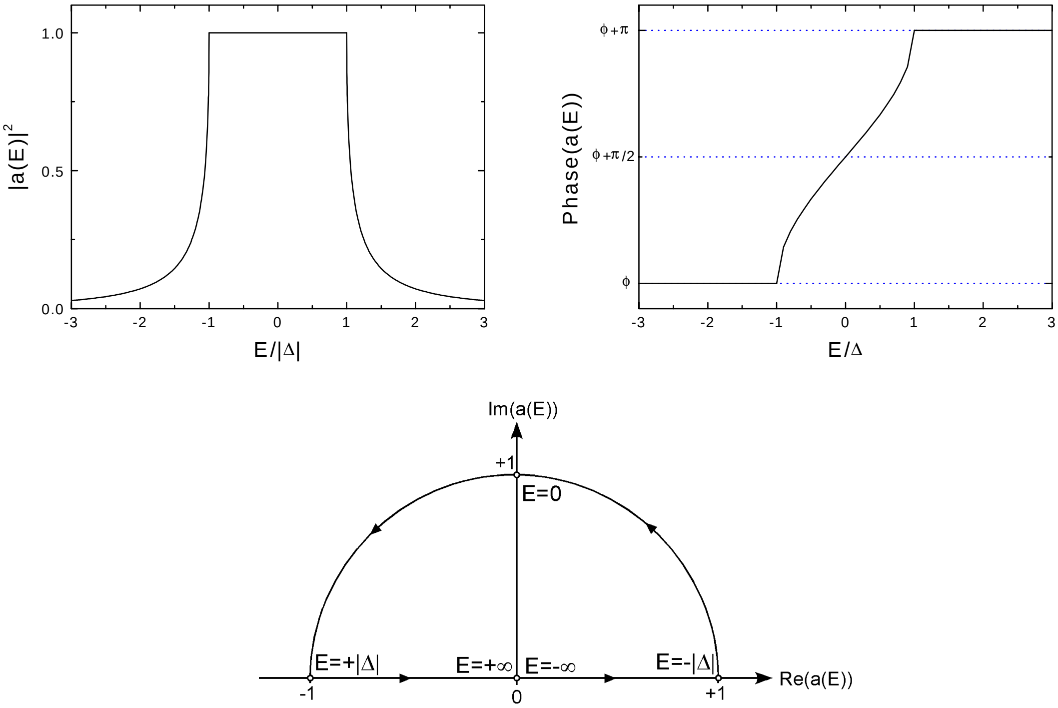

Figure 7: Andreev reflection probability (top-left) and phase of the probability amplitude (top-right) as a function of the quasiparticle energy in units of $|\Delta|$. ϕ is the phase of the superconducting gap. Bottom: Parametric representation of the Andreev reflection probability amplitude for $\phi = 0$, the parameter being the energy.

B.3 Andreev bound states: phase biased Josephson junctions

In the superconductor-conduction channel-superconductor junction, two scattering mechanism are used to describe the electrical transport: The Andreev reflections at both NS interfaces whose probability amplitudes are given by (8), and the normal scattering in the channel described by the matrix

$$S = \begin{bmatrix} -ir & t \\ t & -ir \end{bmatrix}$$

for electrons (see Appendix A) and its conjugated for holes (see Figure 8).

When a phase difference $\delta = \phi_L - \phi_R$ is applied between the superconductors, the electronic waves functions (as well as the hole ones) that are reflected at both interfaces interfere producing resonant states. These so-called Andreev bound states are localized inside the channel and carry the supercurrent between the two superconductors.

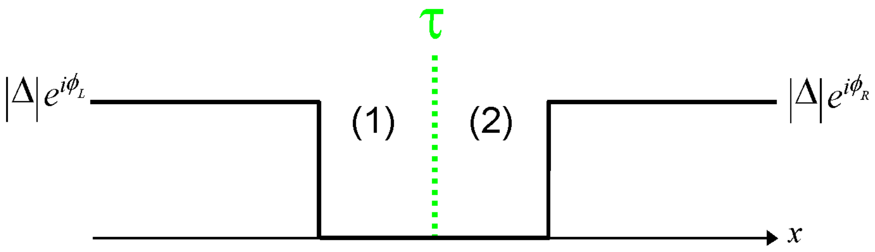

Figure 8: Schematic representation of the pair potential profile of superconductor-single channel-superconductor junction. Two parts that are connected through the normal scattering mechanism are distinguished in the channel.

B.3.1 The ballistic Andreev bound states

Let us first considered the simplest case of a ballistic channel ($\tau = 1$). An electron with energy E smaller in absolute value than $|\Delta|$ moving to the right in the normal region is Andreev reflected with probability one by the right superconductor into a left moving hole, leaving an extra charge 2e in the superconductor. The hole is in turn reflected back into a right moving electron, taking a charge 2e from the left superconductor. During this cycle, the electron wave function acquires a phase shift $2\arctan(-(|\Delta|^2 - E^2)^{1/2} / |E|) - \delta$: $\arctan(-(|\Delta|^2 - E^2)^{1/2} / |E|) + \phi_R + \pi$ for the reflection at the right electrode and

$\arctan(-(|\Delta|^2 - E^2)^{1/2}/|E|) - \phi_L - \pi$ for the second one (see Exp. (8)), and a charge 2e is transferred from the left to the right electrode. The same cycle exists starting from a left going electron that transfer charges in opposite direction. A resonance occurs for energies that verify:

$$\arctan\left(-\frac{\sqrt{|\Delta|^2 - E^2}}{|E|} \right) = -\frac{\delta}{2},$$

which leads to:

$$E = \pm|\Delta|\cos\left(\frac{\delta}{2}\right).$$

There are thus two Andreev bound states whose spectrum cross each other at $\delta = \pi$. As expected, they carry supercurrent in opposite direction, and for that reason we denote them $B_{\rightarrow}$ and $B_{\leftarrow}$. Their current phase relationship are:

$$I(\delta) = \varphi_0^{-1}\frac{dE}{d\delta} = \begin{cases} +\frac{e|\Delta|}{\hbar}\sin\left(\frac{\delta}{2}\right) \text{for } \mathrm{B}_{\rightarrow} \\ -\frac{e|\Delta|}{\hbar}\sin\left(\frac{\delta}{2}\right) \text{for } \mathrm{B}_{\leftarrow} \end{cases},$$

where $\varphi_0 = \hbar/2e$ is the reduced flux quantum.

B.3.2 Andreev bound states in a channel with arbitrary transmission probability τ

For a channel with arbitrary transmission, the supercurrent is still carried by bound states localized in the channel. Now, electrons (holes) have a finite probability to be reflected into electrons (holes), a mechanism that couples the two ballistic states $B_{\rightarrow}$ and $B_{\leftarrow}$. On both side of the scattering region (see Figure 8), the bound state wave function is the sum of electron and hole wave functions with right and left propagating direction. Keeping the same notation as in Appendix 1 to distinguish between the waves coming in, or outgoing from the scatterer, the wave function can be written:

$$\psi(x)=\begin{cases} a_1^e\begin{bmatrix}1\\0\end{bmatrix}e^{+ik_e^N x}+b_1^e\begin{bmatrix}1\\0\end{bmatrix}e^{-ik_e^N x}+a_1^h\begin{bmatrix}0\\1\end{bmatrix}e^{-ik_h^N x}+b_1^h\begin{bmatrix}0\\1\end{bmatrix}e^{+ik_h^N x} & \text{(region 1)}\\ a_2^e\begin{bmatrix}1\\0\end{bmatrix}e^{-ik_e^N x}+b_2^e\begin{bmatrix}1\\0\end{bmatrix}e^{+ik_e^N x}+a_2^h\begin{bmatrix}0\\1\end{bmatrix}e^{+ik_h^N x}+b_2^h\begin{bmatrix}0\\1\end{bmatrix}e^{-ik_h^N x} & \text{(region 2)}\end{cases}$$

where $k_e^N(k_h^N)$ corresponds to $k_e(k_h)$ defined in (5) taking $\Delta=0$. The coefficients corresponding to the electron (hole) wave functions are linked together by the scattering matrix S:

$$\begin{bmatrix}b_1^e\\b_2^e\end{bmatrix}=S\begin{bmatrix}a_1^e\\a_2^e\end{bmatrix}\text{and}\begin{bmatrix}b_1^h\\b_2^h\end{bmatrix}=S^*\begin{bmatrix}a_1^h\\a_2^h\end{bmatrix}. \qquad (9)$$

Furthermore, the electron and hole coefficients are related by the Andreev reflection probability amplitude:

$$\begin{cases}a_2^h=a(E,\phi_R)b_2^e\\ a(E,-\phi_R)b_2^h=a_2^e\end{cases}\text{(right interface), and}\begin{cases}a_1^h=a(E,\phi_L)b_1^e\\ a(E,-\phi_L)b_1^h=a_1^e\end{cases}\text{(left interface)}^{6}. \qquad (10)$$

Using Expr. (9) and (10), the following eigenvalue equation is obtained:

$$M\begin{bmatrix}a_1^e\\a_2^e\end{bmatrix}=\begin{bmatrix}a_1^e\\a_2^e\end{bmatrix}\text{with } M=\begin{bmatrix}a(E,-\phi_L) & 0\\ 0 & a(E,-\phi_R)\end{bmatrix}S^*\begin{bmatrix}a(E,\phi_L) & 0\\ 0 & a(E,\phi_R)\end{bmatrix}S$$

This matrix equation has a non-zero solution if:

$$\det(M-Id)=1+\gamma(E)^4-\gamma(E)^2(2r^2+2t^2\cos(\delta))=0, \qquad (11)$$

where $\gamma(E)=(E-i(|\Delta|^2-E^2)^{1/2})/|\Delta|=a(E,\phi)e^{+i\phi}$. Solving Eq. (11) for E leads to the energy spectrum of the two Andreev bound states:

$$E_\pm(\delta)=\pm|\Delta|\left[1-\tau\sin^2(\delta/2)\right]^{1/2}.$$

They carry a supercurrent equal to:

$$I_\pm(\delta)=\pm\frac{e\tau\Delta}{2\hbar}\frac{\sin(\delta)}{\sqrt{1-\tau\sin^2(\delta/2)}}.$$

In Chapter 3 section 3.1.2, the current-phase relationship of tunnel junctions, diffusive wires and a particular atomic size-contact are derived from this expression.

---

[6] As the channel is considered dimensionless, the phase accumulated during the travel through the normal part is zero.

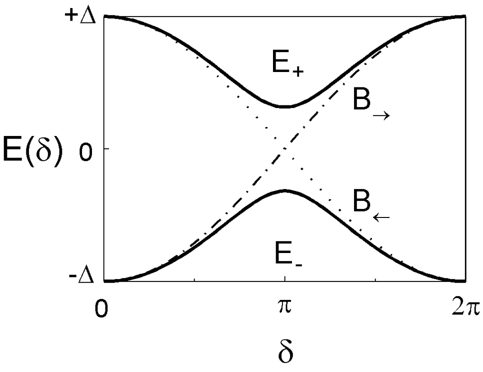

Figure 9: Andreev spectrum for a ballistic channel (dotted and dash dotted lines) and for a channel with transmission probability $\tau = 0.9$ (full lines). The coupling of the two ballistic bound states through the normal scattering mecanism in the channel opens a gap at the level crossing ($\delta = \pi$).

B.4 Multiple Andreev reflections: voltage biased Josephson junctions

When a voltage bias V is applied between the two superconductors, electrons and holes gain or lose an energy eV each time they cross the conduction channel. Consequently, a quasiparticle with energy E incident from the left superconductor, which produces an electron in the normal region with probability $J(E) = [1 - |a(E,0)|^2]^{1/2}$, generates an infinite series of Andreev reflections at energies: $E + 2neV$ for the left interface, and $E + (2n+1)eV$ for the right one.The wave function in the normal regions is as a result a sum of electron and hole wave functions with energies shifted by $2eV$, which in region 1 can be written [10]:

$$\psi^{(1)}(E,x) = \begin{bmatrix} \sum_{n\in\mathbb{N}} [(a_{2n}A_n + J(E)\,\delta_{n0})e^{+ik_e^N x} + B_n e^{-ik_e^N x}]e^{-i(E+2neV)t/\hbar} \\ \sum_{n\in\mathbb{N}} [A_n e^{+ik_h^N x} + a_{2n}B_n e^{-ik_h^N x}]e^{-i(E+2neV)t/\hbar} \end{bmatrix},$$

and in region 2:

$$\psi^{(2)}(E,x) = \begin{bmatrix} \sum_{n\in\mathbb{N}} [C_n e^{+ik_e^N x} + a_{2n+1}D_n e^{-ik_e^N x}]e^{-i(E+(2n+1)eV)t/\hbar} \\ \sum_{n\in\mathbb{N}} [a_{2n+1}C_n e^{+ik_h^N x} + D_n e^{-ik_h^N x}]e^{-i(E+(2n+1)eV)t/\hbar} \end{bmatrix},$$

where $a_k = a(E + keV, 0)$.

These expressions translate the fact that in region 1 (2), right (left) going electrons and holes result from the Andreev reflection of left (right) going holes and electrons respectively[7]. The coefficient A_n (B_n) is the probability amplitude to find a left going hole (electron) in region 1 with energy $E+2neV$ while C_n (D_n) is the probability amplitude associated to a right going electron (hole) with energy $E+(2n+1)eV$ in region 2. The coefficients in region 1 are related to those in region 2 by the scattering matrix. For the electronic waves, the relation is [10]:

$$\begin{bmatrix} B_n \\ C_n \end{bmatrix} = S \begin{bmatrix} a_{2n} A_n + J\delta_{n0} \\ a_{2n+1} D_n \end{bmatrix},$$

and for the hole waves:

$$\begin{bmatrix} A_n \\ D_{n-1} \end{bmatrix} = S^* \begin{bmatrix} a_{2n} B_n \\ a_{2n-1} C_{n-1} \end{bmatrix}.$$

The coefficients $A_n, B_n, C_n, \text{and } D_n$ are calculated from these four coupled recurrence equations.

The wave functions $\psi^{(1)}$ and $\psi^{(2)}$ should be thought of as the eigenstates of the time dependent Hamiltonian describing the system. They carry the same current given by:

$$\left\langle \psi^{(1)}(E) \middle| \hat{I} \middle| \psi^{(1)}(E) \right\rangle,$$

where $\hat{I}$ is the current operator. It has Fourier components at all multiples of the Josephson frequency $\omega_J = 2eV/\hbar$. The total current is obtained by summing up the contribution of all eigenstates weighted by the Fermi occupation factors. The DC component at zero temperature writes in terms of the coefficients A_n and B_n [10]:

$$I(V) = \frac{2e^2}{h}\left[V - \frac{1}{e}\int dE \left(J(E) a_0 (A_0^* + A_0) + \sum_n \left(1 + |a_{2n}|^2\right)(|A_n|^2 - |B_n|^2) \right)\right]$$

The numerical evaluation of this expression leads to the highly non linear current-voltage characteristics that were presented and described in the introduction (p.5).

---

[7] Except for the source term $J(E)\,\delta_{n0}$.

References of Appendix B

---

[1] J.C. Cuevas, A. Martin-Rodero, and A. Levy Yeyati, Phys. Rev. B **54**, 7366 (1996).

[2] T.M. Klapwijk, G.E. Blonder, and M. Tinkham, Physica **109&110B**, 1657 (1982).

[3] G.E. Blonder, M. Tinkham, and T.M. Klapwijk, Phys. Rev. B **25**, 4515 (1982).

[4] A.F. Andreev, Zh. Eksp. Teor. Fiz. **46**, 1823 (1964) [Sov. Phys. JETP **19**, 1228 (1964)].

[5] A. Bardas and D.V. Averin, Phys. Rev. B **56**, R8518 (1997).

[6] M. Tinkham in "*Introduction to Superconductivity*" (McGraw-Hill international editions, New York, 1985).

[7] N.N. Bogoliubov, Soviet Physics JETP **34**, 41 (1958).

[8] A.F. Andreev, Zh. Eksp. Teor. Fiz. **46**, 1823 (1964) [Sov. Phys. JETP **19**, 1228 (1964)].

[9] Magnus Hurd and Göran Wendin, Phys. Rev. B **49**, 15258 (1994).

[10] D. Averin and A. Bardas, Phys. Rev. Lett. **75**, 1831 (1995).